

# **DESIGN AND ANALYSIS OF PHOTONIC CRYSTAL FIBER FOR SENSING APPLICATIONS**

**Thesis Submitted  
in Partial Fulfillment of the Requirements  
for the Degree of**

## **DOCTOR OF PHILOSOPHY**

**by**

**VISHAL CHAUDHARY  
(Enrollment No.: 2K21/PHDEC/14)**

**Under the supervision of  
Dr. SONAL SINGH  
Assistant Professor, ECE Department, DTU, Delhi**



**To the  
Department of Electronics and Communication Engineering**

**DELHI TECHNOLOGICAL UNIVERSITY**

**(Formerly Delhi College of Engineering)**

**Shahbad Daultapur, Main Bawana Road, Delhi-110042, India  
March, 2026**

**© DELHI TECHNOLOGICAL UNIVERSITY, DELHI, 2026  
ALL RIGHTS RESERVED**

## ACKNOWLEDGEMENTS

“Your thoughts will define your actions, and your actions will define your destiny.”

--A.P.J. Abdul Kalam

At the outset, I would like to extend my sincere gratitude and appreciation to everyone who has been by my side through all the highs and lows since the very beginning of this dissertation journey. Your constant support has made me feel truly fortunate and blessed. Looking back, I see not just the conclusion of a chapter, but the beginning of a new one—making this entire journey both memorable and deeply enriching.

First and foremost, I express my heartfelt gratitude to the Almighty for His blessings, the gift of life, good health, and the positive energy that has guided me through every stage of my journey. Without His divine support, none of this would have been possible.

I take the opportunity to humbly submit my sincere and heartfelt thanks to my supervisor, **Dr. Sonal Singh** from the Department of Electronics and Communication Engineering, Delhi Technological University, Delhi, for her invaluable guidance, enthusiastic encouragement, and persistent support. I am truly grateful from the core of my heart for her meticulous approach, wonderful assistance of her perspective, and fruitful discussions on my research topic. Her immense contribution and rare dedication in providing the much-needed guidance, is worth of highest honor. Her careful supervision and personal attention have given me a lot of confidence and enthusiasm, during the different stages of my doctoral investigations. I invariably fall short of words to express my sincere gratitude for her patience and motivation.

I extend my sincere appreciation to the members of my doctoral committee for their insightful comments and thoughtful suggestions that have enhanced the quality of this thesis. I am extremely thankful to **Prof. Neeta Pandey**, Head of the Department of Electronics and Communication Engineering, Delhi Technological University, Delhi, and other faculty members for their endless support and cooperation throughout

this dissertation. I am thankful to all staff members of the department of Electronics and Communication Engineering for their kind help and support during the entire period of my research. I am grateful to the management of Delhi Technological University, Delhi, for providing the necessary resources, facilities, and a conducive research environment for my research work.

I would also like to extend my heartfelt gratitude to **Dr. Dharmendra Kumar** and **Dr. Vijay Shanker Chaudhary**, whose insightful guidance and enriching discussions over the years have greatly contributed to my academic and personal growth. Their support and wisdom have been truly invaluable throughout this journey.

My appreciation also goes to my colleagues and friends in the Department of Electronics and Communication Engineering, Delhi Technological University, Delhi, as well as those beyond the university, for their constant support, encouragement, and assistance especially **Ms. Kirti, Ms. Asbah, Mrs. Himanshi, Mr. Arjun, Mr. Ankit, Mr. Anil, Dr. Shivani, Mrs. Aapurva, Mrs. Divya, Dr. Palak, Mr. Vijay, Ms. Tanvika, Mr. Rohit, Ms. Rimika, Mr. Satish, Mr. Mayank, Mr. Rahul, Mr. Prateek, Mr. Aashish, Mr. Abhishek, Mr. Amit, Mr. Mohnish, Mr. Saurabh.**

I dedicate this thesis to my parents, sister and brother for their endless love, support, encouragement, and blessings throughout my life. My parents, **Mr. Jagdish Prasad Chaudhary, Mrs. Urmila Devi**, my younger sister, **Mrs. Vaishali Chaudhary** and my younger brother, **Mr. Shivam Chaudhary** for their undeterred faith in me, and being the biggest pillar of strength who supported me all the way till the end.

Last but not least, I would like to express my sincere gratitude to everyone who, directly or indirectly, contributed to my journey.

**VISHAL CHAUDHARY**



**DELHI TECHNOLOGICAL UNIVERSITY**

*Formerly Delhi College of Engineering*

Shahbad Daultpur, Main Bawana Road, Delhi -42

## CANDIDATE'S DECLARATION

I Vishal Chaudhary hereby certify that the work which is being presented in the thesis entitled **Design and Analysis of Photonic Crystal Fiber for Sensing Applications** in partial fulfillment of the requirements for the award of the Degree of Doctor in Philosophy, submitted in the **Department of Electronics and Communication Engineering**, Delhi Technological University, India, is an authentic record of my own work carried out during the period from **August 2021** to **March 2026** under the supervision of **Dr. Sonal Singh**.

The matter presented in the thesis has not been submitted by me for the award of any other degree of this or any other Institute.

**Vishal Chaudhary**  
**(2K21/PHDEC/14)**

**Date:** 05-03-2026

**Place:** Delhi, India

This is to certify that the student has incorporated all the corrections suggested by the examiners in the thesis and the statements made by the candidates is correct to the best of our knowledge.

**Signature of Supervisor**

**Signature of External Examiner**



# DELHI TECHNOLOGICAL UNIVERSITY

*Formerly Delhi College of Engineering*

Shahbad Daulatpur, Main Bawana Road, Delhi –42

---

## CERTIFICATE BY THE SUPERVISOR

Certified that **Vishal Chaudhary** (Enrollment No.: 2K21/PHDEC/14) has carried out their research work presented in this thesis entitled “**Design and Analysis of Photonic Crystal Fiber for Sensing Applications**”, for the award of **Doctor of Philosophy** from the Department of Electronics and Communication Engineering, Delhi Technological University, under my guidance and supervision. The thesis embodies results of original work, and studies are carried out by the student himself and the contents of the thesis do not form the basis for the award of any other degree to the candidate or to anybody else from this or any other University/Institution.

**Dr. Sonal Singh**

Supervisor

Department of ECE

Delhi Technological University,

Delhi –110042, India

**Date:** 05-03-2026

***Dedicated to my Parents, Sister and Brother***

*For their endless love,  
support and encouragement*

## ABSTRACT

Over the past few years, photonic crystal fibers (PCFs) have emerged as a promising class of optical fibers, offering immense potential across a wide range of applications, particularly in telecommunications and sensing technologies. Initially, research on PCFs was mainly focused on enhancing key optical characteristics such as dispersion, nonlinearity, confinement losses, and birefringence. However, with ongoing advancements in fiber fabrication techniques, PCF-based sensors have gained increasing attention, especially in the domain of sensing. A notable development in this field is the rapid progress of surface plasmon resonance (SPR)-based sensing technologies. Traditional prism-based SPR sensors, known for their label-free detection and real-time monitoring capabilities, are becoming less favorable due to limitations such as low sensitivity, bulky configurations, and high manufacturing costs. In response, PCF-based sensors have been introduced as a more efficient alternative, offering compact design and improved performance while eliminating the need for extensive experimental setups. This thesis explores the design and analysis of PCF-based sensors tailored for both physical and biological sensing applications. By carefully optimizing the structural parameters of the PCF-based refractive index (RI) sensor, it is possible to achieve high sensitivity, a broad sensing range, and simplified fabrication processes.

This thesis begins by providing a concise overview of the development of fiber-optic sensors. Optical fibers serve as effective sensing elements by continuously monitoring variations in the surrounding analyte. While traditional optical fibers are applicable for SPR sensing, their structural and optical limitations hinder further advancement in this area. To overcome these challenges, PCFs have been introduced as an innovative class of fibers that integrate the benefits of both optical fibers and photonic crystals. PCFs exhibit unique features that surpass the capabilities of conventional fibers. Among their many applications, PCF-based RI sensors have shown remarkable adaptability in diverse sensing domains, including physical, biological, and chemical detection.

The following chapter presents a comprehensive literature review on PCF-based RI sensors for physical and biomedical applications. The review begins with an overview of the fundamental concepts, including mode coupling theory, birefringence, and wavelength sensitivity. It then provides a concise explanation of the suitability of PCFs for RI-based sensing applications, followed by an in-depth discussion on PCF-based SPR sensors. Key areas covered in the discussion include temperature monitoring, analysis of blood components, malaria detection, and sensing of various fluid analytes.

The next chapter examines a circular-shaped hollow-core PCF filled with ethanol. The study focuses on analyzing key optical properties such as dispersion, effective mode area, confinement loss, and nonlinear coefficient across a wavelength range of 800 nm to 1600 nm. The primary objective is to attain a near-zero dispersion wavelength (ZDW) using the finite element method (FEM). By varying the filling configuration, air in the entire ring, ethanol in the central ring, and ethanol in the entire ring, ZDW values of approximately 880 nm, 1220 nm, and 1250 nm are achieved,

respectively. This type of PCF holds significant potential for applications in sensing, nonlinear optics, laser systems, and telecommunications.

The following chapter presents a detailed study of a twin-core photonic crystal fiber (TC-PCF) structure designed for temperature and chemical sensing applications. The proposed design features two solid cores separated by a vertically aligned elliptical air hole, which allows for independent light propagation in each core and results in high birefringence. The sensing mechanism is based on mode coupling between the two cores, which significantly enhances sensitivity. The performance of the TC-PCF sensor has been evaluated through simulations using the FEM. The findings demonstrate the sensor's high sensitivity and its suitability for both temperature and chemical detection. Numerical simulations reveal that the 3 cm long TC-PCF sensor has been optimized to exhibit a high temperature sensitivity of approximately 21.5 pm/°C across a broad temperature range of 0 to 1200 °C. Additionally, for chemical sensing, a sensor with a fiber length of just 0.03 cm achieves a maximum sensitivity of 6667 nm/RIU. This chapter covers the theoretical background, structural design, and performance analysis, emphasizing the real-world applicability of TC-PCF-based sensors.

Next chapter focuses on the design and investigation of advanced biosensing methods utilizing PCFs for the early identification of a range of diseases, such as multiple forms of cancer, essential blood constituents, and malaria. The research employs FEM simulations conducted in the terahertz (THz) frequency range to analyze mode coupling behaviour in TC-PCF structures, aiming to achieve superior sensitivity and accuracy in biomedical sensing applications. By thoroughly examining key design parameters of PCF, the proposed sensors demonstrate exceptional sensitivity and performance in identifying diseases, thereby supporting progress in biomedical diagnostics and enhancing healthcare technologies.

The following chapter introduces a SPR-based PCF sensor specifically designed for the detection of diabetes. Gold is employed as the plasmonic material and is incorporated in a layered structure to enhance the sensor's overall performance. The design is analyzed using FEM simulations to assess its capability in identifying diabetic conditions. In this sensor configuration, two concentric layers of air holes are organized in a hexagonal lattice, and a thin layer of gold is coated onto the fiber to enable the excitation of the SPR effect. This effect arises when the surface plasmon polariton (SPP) mode interacts with the core-guided mode under phase-matching conditions. Diabetes-related samples, each characterized by a distinct RI, are introduced into the fiber structure. Variations in RI between normal and diabetes-affected samples cause a measurable shift in the SPR resonance wavelength during confinement loss analysis. The sensor achieves a sensitivity of 2400 nm/RIU, as determined by tracking changes in the loss spectrum. With its simple sensing approach, the proposed SPR-PCF sensor offers a practical and cost-efficient solution for diabetes monitoring.

## LIST OF PUBLICATIONS

### Published Journal Papers

1. **Vishal Chaudhary** and Sonal Singh, “Twin core photonic crystal fiber based temperature sensor with improved sensitivity over a wide range of temperature,” *Optical and Quantum Electronics*, vol. 55, no. 1, 2023, doi: 10.1007/s11082-022-04304-4 (Springer, SCI Journal, Impact Factor: 4.0).
2. **Vishal Chaudhary** and Sonal Singh, “Highly sensitive twin core photonic crystal fiber for hazardous cancer cell detection in THz frequency regime,” *Optical and Quantum Electronics*, vol. 55, pp. 1–17, 2023, doi: 10.1007/s11082-023-05462-9 (Springer, SCI Journal, Impact Factor: 4.0).
3. **Vishal Chaudhary**, Sonal Singh, Vijay Shanker Chaudhary and Dharmendra Kumar “Design and Optimization of Terahertz Based D-shaped Photonic Crystal Fiber for Blood Component Detection,” *IEEE Sensors Journal*, vol. 24, no. 18, pp. 28768-28775, 2024, doi: 10.1109/JSEN.2024.3437245 (IEEE, SCI Journal, Impact Factor: 4.5).
4. **Vishal Chaudhary** and Sonal Singh, “Design and optimization of a terahertz photonic crystal fiber based biosensor to detect malaria disease,” *Journal of Computational Electronics*, vol. 24, no. 1, 2025, doi: 10.1007/s10825-024-02255-5 (Springer, SCI Journal, Impact Factor: 2.5).
5. **Vishal Chaudhary** and Sonal Singh, “Design of photonic crystal fiber-based plasmonic sensor for diabetes detection,” *Journal of Computational Electronics*, vol. 25, p. 29, 2026, doi: 10.1007/s10825-025-02475-3 (Springer, SCI Journal, Impact Factor: 2.5).

### Published Conference Papers

1. **Vishal Chaudhary** and Sonal Singh, “Effect of selectively-filled-ethanol on dispersion characteristics of circular shaped Hollow Core Photonic Crystal Fiber”

4th International Conference on Communication, Computing and Electronics Systems 2022 Lecture Notes in Electrical Engineering 977, pp. 429–437, 2023, doi: 10.1007/978-981-19-7753-4\_33.

2. **Vishal Chaudhary** and Sonal Singh, “Hexagonal lattice twin core photonic crystal fiber based chemical sensor” 10th International Conference on Signal Processing and Integrated Networks pp. 164-167, 2023, doi: 10.1109/SPIN57001.2023.10117365.
3. **Vishal Chaudhary** and Sonal Singh, "Dual-core Photonic Crystal Fiber for Blood Cancer Detection in THz Frequency Regime," 2024 International Symposium on Electrical, Electronics and Information Engineering (ISEEIE), Leicester, United Kingdom, 2024, pp. 283-286, doi: 10.1109/ISEEIE62461.2024.00059.

## TABLE OF CONTENTS

ACKNOWLEDGEMENTS	iii
CANDIDATE’S DECLARATION	v
CERTIFICATE BY THE SUPERVISOR	vi
ABSTRACT	viii
LIST OF PUBLICATIONS	x
TABLE OF CONTENTS	xii
LIST OF TABLES	xv
LIST OF FIGURES	xvi
LIST OF ABBREVIATIONS	xxii
<b>CHAPTER 1: INTRODUCTION</b>	<b>1</b>
1.1 Introduction to Optical Fiber Systems	1
1.1.1 Wavelength Windows Used in Fiber-Optic Communication	1
1.1.2 A Brief Overview of Fiber Optic Sensors	2
1.1.3 Block Diagram of Fiber Optic Sensors	3
1.1.3.1 Classification of Fiber Optic Sensors	3
1.2 Overview of Conventional Optical Fiber	7
1.3 Photonic Crystal Fiber	8
1.3.1 Classifications of PCF Based on Structural Design	8
1.3.2 Classifications of PCF Based on Propagation of Light	11
1.4 Overview of Single, Dual, and Multi-Core PCF Architectures	14
1.5 PCF Lattice Configurations: Hexagonal, Circular, and Square Structures	15
1.6 Applications of Photonic Crystal Fiber	16
1.7 Problem Statement	17
1.8 Motivation	17
1.9 Research Gaps	18
1.10 Research Objective	18
1.11 Organization of the Thesis	19
<b>CHAPTER 2: LITERATURE REVIEW</b>	<b>21</b>
2.1 PCF-Enabled Sensing Technologies	21

2.1.1 Temperature Sensor	21
2.1.2 Refractive Index Sensor	25
2.1.3 PCF-Based Biosensors	31
2.1.4 PCF based Chemical Sensor	38
2.2 Summary	41
<b>CHAPTER 3: EFFECT OF SELECTIVELY-FILLED-ETHANOL ON DISPERSION CHARACTERISTICS OF CIRCULAR SHAPED HOLLOW CORE PHOTONIC CRYSTAL FIBER</b>	<b>42</b>
3.1 Introduction	42
3.2 PCF Design	42
3.3 Results and Discussion	44
3.4 Summary	47
<b>CHAPTER 4: DESIGN AND ANALYSIS OF TWIN CORE PHOTONIC CRYSTAL FIBER FOR TEMPERATURE AND CHEMICAL SENSING APPLICATION</b>	<b>48</b>
4.1 Twin core photonic crystal fiber based temperature sensor with improved sensitivity over a wide range of temperature	48
4.1.1 Introduction	48
4.1.2 PCF structure and result analysis	49
4.1.3 Impact of diameter variation on sensitivity	55
4.1.4 Summary	56
4.2 Hexagonal lattice twin core photonic crystal fiber based chemical sensor	57
4.2.1 Introduction	57
4.2.2 PCF design and result analysis	57
4.2.3 Summary	62
<b>CHAPTER 5: DESIGN AND ANALYSIS OF ADVANCED BIOSENSING METHODS UTILIZING PCF FOR THE EARLY IDENTIFICATION OF A RANGE OF DISEASES, SUCH AS MULTIPLE FORMS OF CANCER, ESSENTIAL BLOOD CONSTITUENTS AND MALARIA IN TERAHERTZ FREQUENCY REGIME</b>	<b>63</b>
5.1 Twin core photonic crystal fiber for hazardous cancer cell detection with improved sensitivity in terahertz (THz) frequency regime	63
5.1.1 Introduction	63
5.1.2 PCF sensor design	64
5.1.3 Results simulation and discussion	65
5.1.4 Impact of diameter variation on sensitivity	71

5.1.5 Summary	72
5.2 Design and Optimization of Terahertz Based D-shaped Photonic Crystal Fiber for Blood Component Detection	73
5.2.1 Introduction	73
5.2.2 Design Methodology	75
5.2.3 Results analysis and discussion	77
5.2.4 Effect of pitch variation on sensitivity	82
5.2.5 Summary	83
5.3 Design and optimization of terahertz photonic crystal fiber based biosensor to detect malaria disease	83
5.3.1 Introduction	83
5.3.2 Sensor design	84
5.3.3 Results and discussion	85
5.3.4 Impact of pitch variation on sensitivity	88
5.3.5 Summary	90
<b>CHAPTER 6: DESIGN OF PHOTONIC CRYSTAL FIBER BASED PLASMONIC SENSOR FOR DIABETES DETECTION</b>	<b>91</b>
6.1 Introduction	91
6.2 Sensor design	92
6.3 Results Analysis	94
6.4 Summary	97
<b>CHAPTER 7: CONCLUSION, FUTURE SCOPE AND SOCIAL IMPACT</b>	<b>98</b>
7.1 Summary of the Work Done in the Thesis	98
7.2 Future Scope and Social Impact	99

## LIST OF TABLES

Table 2.1	Performance parameters of some PCF-based temperature sensors	24
Table 2.2	Performance analysis of previously reported RI sensor	30
Table 2.3	Performance characteristics of different PCF based RI sensor for detection of blood component	34
Table 2.4	Performance characteristics of different PCF based RI sensor for malaria detection	37
Table 2.5	Performance characteristics of some other PCF sensors for chemical detection	41
Table 3.1	Comparison of changes in parameters with and without ethanol filling the holes	46
Table 4.1.1	Performance comparison of different PCF sensors with our proposed PCF sensor	55
Table 4.1.2	Comparison of sensitivity of proposed TC-PCF with different diameters	56
Table 4.2.1	Comparison of the performance of various PCF sensors, including the PCF sensor proposed in this study	62
Table 5.1.1	Comparison between the sensor sensitivity and structure of the proposed and previous reported sensors	70
Table 5.2.1	Comparison of proposed PCF biosensor with recently reported biosensors	82
Table 5.3.1	Refractive index of analyte at different stages	85
Table 5.3.2	Comparison of the sensitivity between the sensor presented in this study and sensors reported in prior research	90
Table 6.1	Design parameters used for the proposed pcf biosensor	93
Table 6.2	Sellmeier coefficients values	93
Table 6.3	Drude–lorentz model parameters	93
Table 6.4	RI of healthy person and a diabetic person	93
Table 6.5	Comparison of the sensitivity of the sensor proposed in this study with that of sensors reported in previous research	97

## LIST OF FIGURES

Fig. 1. 1	Relationship between attenuation and wavelength for optical window The Endeavor to create VLSI Circuit Design	2
Fig. 1. 2	Block model of FOS	3
Fig. 1. 3	Classification of Fiber-Optic Sensor	4
Fig. 1. 4	Block diagram of intrinsic FOS	4
Fig. 1. 5	Block diagram of Extrinsic FOS	5
Fig. 1. 6	Conventional optical fiber (a) Cross-sectional view (b) 3-D view	8
Fig. 1. 7	Cross-sectional structures of SMF and MMF	8
Fig. 1. 8	Schematic Cross-sectional view of PCF	9
Fig. 1. 9	3-D view of solid core PCF	9
Fig. 1. 10	3-D view of hollow core PCF	10
Fig. 1.11	Photonic bandgap fibers with different type of hollow-core [40]	11
Fig. 1.12	Classification and naming of PCF	12
Fig. 1.13	Cross-sectional view of air-guiding PCF	13
Fig. 1.14	Schematic cross-section view of a low index core PCF	13
Fig. 1.15	Cross-sectional view of a Bragg PCF	14
Fig. 1.16	Design of PCF using (a) Single-core, (b) Dual-core, and (c) multi-core	15
Fig. 1.17	Design of PCF using (a) Hexagonal (b) Circular, and (c) Square lattice-structures modelling	15
Fig. 1.18	Application of PCF in various field	16
Fig. 2.1	(a) Cross-section view of TC-PCF (b) Transmission spectrum of TC-PCF (c) x-polarized even and odd mode (d) y-polarized even and odd mode [60]	22
Fig. 2.2	Cross-sectional view of the SPR-based PCF temperature sensor, (b) field distribution of the y-polarized core mode, (c) field distribution of the y-polarized SPP mode, (d) loss spectra of the core modes along with dispersion relations for the y-polarized core and plasma modes at $-5^{\circ}\text{C}$ , (e) variation of loss spectra with wavelength [61]	23
Fig. 2.3	(a) Cross-sectional view of temperature sensor (b) Structure of the Stacked preform of sensor (c) Loss spectrum in y-polarized core mode (d) Experimental setup of PCF sensor (e) At different temperature variation of FOM and FWHM [62]	24
Fig. 2.4	(a) 3-D view of PCF (b) Cross-sectional view of PCF (c)	25

	Experimental set-up of PCF (d) The impact of changing air-hole spacing $\Lambda$ on the loss spectrum (e) Field distribution in x-polarized (f) field distribution in y-polarized (g) The effect of gold nanowire diameter $d_3$ on the loss spectrum [65].	
Fig. 2.5	(a) Cross-sectional view of dual-core PCF, Field distribution (b) x-even polarized (c) x-odd polarized (d) y-even polarized (e) y-odd polarized (f) Transmission spectrum [73]	26
Fig. 2.6	(a) Cross-sectional view of C-PCF (b) Meshing of C-PCF (c) Transmission spectrum (d) Experimental set-up (e) Transmittance spectra of C-PCF [74]	27
Fig. 2.7	(a) Cross-section view of D-shaped PCF (b) Field distribution y-polarized core mode (c) SPP mode (d) Coupling mode (e) Loss curve and dispersion curve versus wavelength (f) Loss change with different diameters of air holes for $n_a=1.38$ (g) Loss variation at different thickness of gold layer [75]	28
Fig. 2.8	(a) Schematic illustration of the PCF sensor, (b) stacked preform of the fiber, (c) field distribution of the core mode for $n_a = 1.36$ , (d) SPP mode, (e) resonance condition, (f) loss curves for varying Ag layer thickness, (g) loss curve variations with $\text{TiO}_2$ thickness, (h) amplitude sensitivity [76].	29
Fig. 2.9	(a) 3-D view of D-shape biosensor (b) Cross-section of the PCF's stacked preform (c) Confinement loss curve (d) Linear fitting for the resonance wavelength dependency on the sample RI [81]	30
Fig. 2.10	(a) Cross-section view of blood component sensor (b) Mode profile of RBCs (c) HB (d) WBCs (e) plasma (f) water at operating wavelength $7 \mu\text{m}$ (g) Relative sensitivity versus wavelength (h) Confinement loss of different blood component [89]	31
Fig. 2.11	(a) Cross-section view of biosensor (b) coarse mesh of the biosensor (c) field distribution x-polarized RBC (d) y-polarized RBC (e) Effective material loss curve (f) Relative sensitivity curve (g) Numerical Aperture curve [90]	32
Fig. 2.12	(a) Cross-sectional view of sensor (b), (c) field distribution of fundamental mode and SPP mode for x-polarized (d) field distribution of fundamental mode (e) SPP mode for y-polarized (f) Confinement loss for x-pol (g) Amplitude sensitivity for x-pol (g) Loss for y-pol (h) Amplitude sensitivity for y-pol [91]	33
Fig. 2.13	Cross-sectional view of PCF (b) Electric field strength for core-mode (c) Electric field strength for SPP mode (d) At wavelength of $1032 \text{ nm}$ for RBC samples normalised electric field along the radial x-direction (e) Variation of core-mode confinement loss and ERI of core and SPP mode [92]	34
Fig. 2.14	(a) Cross-sectional view of the biosensor (b) Meshing arrangement of the biosensor (c) Transmission spectrum versus wavelength (d)	35

	Electric field distribution of x-even (e) y-even (f) x-odd (g) y-odd super modes of malaria biosensor at $\lambda=1.30 \mu\text{m}$ for normal RBC (h) Coupling length between normal and infected RBCs during cells during different stage of the parasite [99]	
Fig. 2.15	(a) Cross-sectional layout of the PCF biosensor, (b) experimental setup for the PCF-based SPR sensor, (c) x-polarized core mode field distribution, (d) y-polarized core mode field distribution, (e) x-polarized surface plasmon polariton (SPP) mode, (f) y-polarized SPP mode at a 932 nm resonance wavelength for the malaria ring stage, and (g) variation of peak loss in the y-polarized mode with different gold layer thicknesses [100]	37
Fig. 2.16	(a) Cross-sectional view of SPR sensor (b) Stacking and drawing method for fabrication of PCF (c) Chemical vapor deposition method for vapor deposition (d) Loss characteristics curve and dispersion relation between core mode and SPP mode for RI =1.36 [101]	38
Fig. 2.17	(a) Cross-section view of sensor (b) Birefringence with wavelength (c) Transmission curve versus wavelength (d) Field distribution odd x-polarized (e) odd y-polarized (f) even x-polarized (g) even y-polarized [109]	39
Fig. 2.18	(a) Cross-sectional view of octagonal PCF (b) RS versus frequency for $\pm 2 \%$ variations for x and y polarized (c) x-polarized field circulation (d) y-polarized field circulation (e) CL versus frequency for different chemicals [110]	40
Fig. 2.19	2.19 (a) Cross-sectional view of THz PC-PCF sensor with enlarged core (b) Field distribution x-polarized for water (c) Field distribution y-polarized for water (d) Relative sensitivity for x-polarization (e) Birefringence as a function of frequency (f) Effective area as a function of frequency [111]	41
Fig. 3.1	Geometry of proposed Circular shaped hollow core PCF	43
Fig. 3.2	Electric field profile for the basic modes of PCF (a) air is poured into the entire hole ring (b) ethanol is poured into the middle hole ring (c) ethanol is poured into the entire hole ring, at $\lambda = 1500 \text{ nm}$	44
Fig. 3.3	Effective refractive index variation with wavelength	45
Fig. 3.4	Effective area variation with wavelength (a) air is poured into the entire hole ring (b) ethanol is poured into the middle hole ring (c) ethanol is poured into the entire hole ring	45
Fig. 3.5	Nonlinear coefficient variation with wavelength (a) air is poured into the entire hole ring (b) ethanol is poured into the middle hole ring (c) ethanol is poured into the entire hole ring	46
Fig. 3.6	Dispersion graph of the circular shaped hollow core PCF when (a) air is poured into the entire hole ring (b) ethanol is poured into the	47

	middle hole ring (c) ethanol is poured into the entire hole ring	
Fig. 4.1.1	Geometry of proposed twin core PCF	49
Fig. 4.1.2	Electric field vector and amplitude distribution of the four super-modes: (a) x-polarization even (b) x-polarization odd (c) y-polarization even and (d) y-polarization odd	50
Fig. 4.1.3	Schematic of PCF sensing set up for temperature sensor	50
Fig. 4.1.4	Variation in $n_{eff}$ with wavelength	51
Fig. 4.1.5	Variation in $\Delta n_{eo}$ with wavelength	51
Fig. 4.1.6	Coupling length variation with wavelength	52
Fig. 4.1.7	Variation in birefringence with (a) wavelength (b) temperature applied ( $^{\circ}\text{C}$ )	53
Fig. 4.1.8	TC-PCF transmission curve with a length of 3 cm	53
Fig. 4.1.9	Transmission spectrum peak wavelength (nm) with applied temperature ( $^{\circ}\text{C}$ )	54
Fig. 4.1.10	Numerical line fitting for various wavelength shift values for a 3 cm long TC-PCF at wide temperature range of 0 to 1200 $^{\circ}\text{C}$	55
Fig. 4.1.11	TC-PCF transmission curve with different diameter of d, (a) 1.2 $\mu\text{m}$ (b) 1.4 $\mu\text{m}$ and (c) 1.6 $\mu\text{m}$	56
Fig. 4.2.1	Cross-section of proposed twin-core PCF	58
Fig. 4.2.2	The distribution of the amplitude and vector of the electric field for four super-modes: (a) and (b) are x-polarization with even and odd symmetry, respectively, while (c) and (d) are y-polarization with even and odd symmetry, respectively	58
Fig. 4.2.3	TC-PCF sensing arrangement for chemical sensor	58
Fig. 4.2.4	Variation in $n_{eff}$ with wavelength	59
Fig. 4.2.5	Variation in $\Delta n_{eo}$ with wavelength	59
Fig. 4.2.6	The variation of coupling length with wavelength	60
Fig. 4.2.7	The variation of birefringence with wavelength	61
Fig. 4.2.8	The transmission characteristics of TC-PCF, with a specific length of 0.03 cm	61
Fig. 5.1.1	(a) Cross-sectional view and (b) geometrical meshing statistics of proposed twin-core PCF sensor	65
Fig. 5.1.2	General representation of the PCF sensing setup for cancer cell detection	66
Fig. 5.1.3	Electric field distribution of (a) x-even, (b) x-odd, (c) y-even and (d) y-odd mode at a frequency of 0.75 THz	66

Fig. 5.1.4	Variation of $\Delta n_{eo}$ with frequency for normal and cancerous cell (a) HeLa and Jurkat (b) MDA-MB-231 and PC12 (c) Basal and MCF-7	67
Fig. 5.1.5	Variation of birefringence with frequency for normal and cancerous cell (a) HeLa and Jurkat (b) MDA-MB-231 and PC12 (c) Basal and MCF-7	68
Fig. 5.1.6	Variation of coupling length with frequency for normal and cancerous cell (a) HeLa and Jurkat (b) MDA-MB-231 and PC12 (c) Basal and MCF-7	69
Fig. 5.1.7	Transmission curve with frequency for normal and cancerous cell (a) HeLa (b) Jurkat (c) PC12 (d) Basal (e) MDA-MB-231 and (f) MCF-7	70
Fig. 5.1.8	Transmission curve with different diameter of D, for HeLa cell (a) 466 $\mu\text{m}$ (b) 468 $\mu\text{m}$ and (c) 470 $\mu\text{m}$	71
Fig. 5.1.9	Transmission curve with different diameter of D, for Jurkat cell (a) 466 $\mu\text{m}$ (b) 468 $\mu\text{m}$ and (c) 470 $\mu\text{m}$	72
Fig. 5.1.10	Transmission curve with different diameter of D, for PC 12 cell (a) 466 $\mu\text{m}$ (b) 468 $\mu\text{m}$ and (c) 470 $\mu\text{m}$	72
Fig. 5.1.11	Transmission curve with different diameter of D, for Basal cell (a) 466 $\mu\text{m}$ (b) 468 $\mu\text{m}$ and (c) 470 $\mu\text{m}$	72
Fig. 5.1.12	Transmission curve with different diameter of D, for MDA-MB-231 cell (a) 466 $\mu\text{m}$ (b) 468 $\mu\text{m}$ and (c) 470 $\mu\text{m}$	72
Fig. 5.1.13	Transmission curve with different diameter of D, for MCF-7 cell (a) 466 $\mu\text{m}$ (b) 468 $\mu\text{m}$ and (c) 470 $\mu\text{m}$	73
Fig. 5.2.1	Design of the proposed PCF sensor with dual solid cores: (a) 2D cross section view and (b) Fine mesh statistics	76
Fig. 5.2.2	Fabrication technique for proposed PCF using capillary stacking	76
Fig. 5.2.3	Representation of experimental setup for blood component detection	77
Fig. 5.2.4	Electric field distribution within a symmetric core, showcasing four distinct modes: (a) even x-polarization (b) odd x-polarization (c) even y-polarization and (d) odd y-polarization	78
Fig. 5.2.5	3-D view of Electric field distribution for four distinct modes: (a) even x-polarization (b) odd x-polarization (c) even y-polarization and (d) odd y-polarization	78
Fig. 5.2.6	Change in refractive index difference varies with different frequency	79
Fig. 5.2.7	Change in birefringence with respect to different frequency	80
Fig. 5.2.8	Change in coupling length with respect to different frequency	80
Fig. 5.2.9	Transmission curve of a DC-PCF with a length of 0.2 m	81

Fig. 5.2.10	Transmittance curve of DC-PCF for primary blood components	81
Fig. 5.2.11	Transmittance curve with different pitch ( $\Lambda$ ), for five primary blood constituents (a) 498 $\mu\text{m}$ (b) 500 $\mu\text{m}$ and (c) 502 $\mu\text{m}$	82
Fig. 5.3.1	Configuration of proposed DC-PCF based biosensor (b) Fine mesh statistics	84
Fig. 5.3.2	Fabrication method for the suggested DC-PCF utilizing capillary stacking	85
Fig. 5.3.3	Experimental setup of proposed sensor	86
Fig. 5.3.4	Distribution of electric field (a) even x-polarization, (b) odd x-polarization, (c) even y-polarization, and (d) odd y-polarization	87
Fig. 5.3.5	3-D view of Electric field distribution for four distinct modes: (a) even x-polarization, (b) odd x-polarization, (c) even y-polarization, and (d) odd y-polarization	87
Fig. 5.3.6	Variations in $\Delta n_{eo}$ with respect to frequency for different stages of RBCs	88
Fig. 5.3.7	Variations in coupling length with respect to frequency for different stages of RBCs	88
Fig. 5.3.8	Transmission curve with respect to frequency for (a) X and (b) Y-polarized light	89
Fig. 5.3.9	Transmission curve with different pitch ( $\Lambda$ ), for various stages of malaria infected RBCs under x polarization (a) 498 $\mu\text{m}$ (b) 500 $\mu\text{m}$ and (c) 502 $\mu\text{m}$	89
Fig. 5.3.10	Transmission curve with different pitch ( $\Lambda$ ), for various stages of malaria infected RBCs under y polarization (a) 498 $\mu\text{m}$ (b) 500 $\mu\text{m}$ and (c) 502 $\mu\text{m}$	90
Fig. 6.1	(a) Geometry illustration of the proposed PCF (b) schematic of the experimental setup for diabetes detection using the PCF-based SPR sensor	94
Fig. 6.2	Distributions of electric field at the resonance wavelength of 596 nm for various polarization modes: (a) core mode with x-polarization, (b) core mode with y-polarization, (c) SPP mode with x-polarization, and (d) SPP mode with y-polarization	95
Fig. 6.3	3D view of electric field profile for four distinct modes (a) core mode with x-polarization, (b) core mode with y-polarization, (c) SPP mode with x-polarization, and (d) SPP mode with y-polarization	96
Fig. 6.4	ERI and confinement loss curve corresponding to healthy and diabetic samples	97

## LIST OF ABBREVIATIONS

<b>AFF</b>	Air filling fraction
<b>BD</b>	Beam divergence
<b>BLS</b>	Broadband light source
<b>BSF</b>	Band-stop filter
<b>COC</b>	Cyclic olefin copolymer
<b>CT</b>	Crosstalk
<b>CVD</b>	Chemical vapor deposition
<b>DANCE</b>	Density alteration in non-physiological cells
<b>DCDHF</b>	Dual-core dual-hole fiber
<b>DC-PCF</b>	Dual-core photonic crystal fiber
<b>DECPCF</b>	Dual elliptical core photonic crystal fiber
<b>ERI</b>	Effective refractive index
<b>FBG</b>	Fiber Bragg grating
<b>FCM</b>	Flow cytometry
<b>FEM</b>	Finite element method
<b>FSS</b>	Fiber specklegram sensor
<b>GMF</b>	Grapefruit microstructured fiber
<b>HB</b>	Hemoglobin
<b>H-DCPCF</b>	Hybrid-dual-core photonic crystal fiber
<b>HiBi PCF</b>	High birefringence photonic crystal fibers
<b>H-PCF</b>	Hybrid photonic crystal fiber
<b>IgG</b>	Immunoglobulin G
<b>IgM</b>	Immunoglobulin M
<b>ITO</b>	Indium tin oxide
<b>LAMP</b>	Loop-mediated isothermal amplification
<b>LDMS</b>	Laser desorption mass spectrometry
<b>LPG</b>	Long-period grating
<b>LPG</b>	Long period grating

<b>LSPP</b>	Localized surface plasmon polariton
<b>MMF</b>	Multi-mode fiber
<b>MS</b>	Mass spectrophotometry
<b>MSS</b>	Marcuse spot size
<b>NA</b>	Numerical aperture
<b>NLC</b>	Nematic liquid crystal
<b>O-PCF</b>	Octagonal photonic crystal fiber
<b>OSA</b>	Optical spectrum analyzer
<b>PBG</b>	Photonic bandgap
<b>PCF</b>	Photonic crystal fiber
<b>PCR</b>	Polymerase chain reaction
<b>PF</b>	Power fraction
<b>PML</b>	Perfectly matched layer
<b>PM-PCF</b>	Polarization-maintaining photonic crystal fiber
<b>POFBG</b>	Polymer optical fiber Bragg grating
<b>PQF</b>	photonic quasi-crystal fiber
<b>QBC</b>	Quantitative buffy coat
<b>Q-PCF</b>	Quasi-photonic crystal fiber
<b>RBC</b>	Red blood cell
<b>RCPCF</b>	Rectangular core photonic crystal fiber
<b>RDT</b>	Rapid diagnostic test
<b>RI</b>	Refractive index
<b>SHDC-PCF</b>	Side-hole dual-core photonic crystal fiber
<b>SMF</b>	Single mode fiber
<b>SMSP- PCF</b>	Single-mode single-polarization photonic crystal fiber
<b>SPP</b>	Surface plasmon polariton
<b>SPR</b>	Surface plasmon resonance
<b>TIR</b>	Total internal reflection
<b>TC-PCF</b>	Twin-core photonic crystal fiber
<b>WBC</b>	White blood cell

# CHAPTER 1

## INTRODUCTION

### 1.1 Introduction to Optical Fiber Systems

In recent years, the field of optical fiber technology has undergone rapid evolution, serving as a catalyst for numerous emerging technologies and advanced applications. This progression has been driven by the unique characteristics of optical fibers, which, when combined with optoelectronic components, have given rise to highly effective sensing systems. One such development is the Fiber Optic Sensor (FOS), which benefits from the inherent advantages of optical fibers such as geometric flexibility, environmental compatibility and high sensitivity. Operating at frequencies far beyond those used in microwave technologies, optical devices support significantly higher bandwidths. As a result, optical waveguides enable much faster data transmission compared to microwave waveguides. Conventional optical fibers are composed of two concentric layers: a core and a surrounding cladding. The core has a higher refractive index than the cladding, which ensures that light signals are confined within the core through the mechanism of total internal reflection (TIR). There are certain structural restrictions, such as modal cut-off wavelength, a limited material selection and a limited core diameter in the single-mode domain in conventional optical fiber, despite excellent performance in telecom and non-telecom applications.

The concept of Photonic Crystal Fiber (PCF) was first introduced by Pochi Yeh in 1978 [1], where he proposed a structure featuring alternating layers of high- and low-refractive-index materials surrounding a low-index core. This type of configuration, known as a Bragg grating, represents a one-dimensional (1D) photonic crystal structure. Later, in 1992, Philip Russell developed a more advanced form of PCF using a two-dimensional (2D) photonic crystal structure incorporating an air core. The potential of PCFs to overcome the limitations of conventional optical fibers gained recognition in 1996 [2], marking their formal entry into optical fiber research. These fibers, often referred to as microstructured or holey fibers [3], are typically fabricated using undoped silica embedded with arrays of tiny air holes. A standard PCF comprises a core and a cladding. The core is usually formed by omitting the central air hole, while the cladding is made up of a periodic arrangement of air holes surrounding the core along the fiber length. PCFs represent a novel class of optical fibers that merge the guiding principles of traditional fibers with the photonic bandgap effects of photonic crystals, offering capabilities that are unattainable with standard fiber designs. The design of PCFs can be tailored extensively by adjusting parameters such as the diameter of the air holes, the pitch (distance between adjacent holes), the refractive index of the material, hole shape, and lattice geometry. Due to the PCF's design flexibility, an enormously single-mode fiber can be formed over the optical spectrum and they do not have a cut-off wavelength.

#### 1.1.1 Wavelength Windows Used in Fiber-Optic Communication

A In the optical spectrum, fiber-optic communication windows are specific wavelength ranges where optical fibers show the small amount of dispersion and attenuation (signal loss), which makes them perfect for long-distance and high-speed data transfer. These windows, which are generally in the near-infrared (NIR) spectrum, are classified according to the transmission

characteristics of the fiber shown in Figure 1.1. Signal attenuation is lowest in the following three optical windows.

**a) Short wavelength band (First Window):** The first optical window has a minimum signal loss of  $4 \text{ dBkm}^{-1}$  and wavelength ranges from 800-900 nm. For optical fiber communication, this band was the first to be used in the 1970s and early 1980s.

**b) Medium wavelength band (Second Window):** The second optical window, often known as the O-band, is centred at 1310 nm and provides  $0.5 \text{ dBkm}^{-1}$ . This band came into use in the mid 1980s. Now a days long distance communications system operates in this band.

**c) Long wavelength band (Third Window):** The third optical window has a loss of  $0.2 \text{ dBkm}^{-1}$  and is centred at 1550 nm, popularly known as the C-band. Almost all new communications technologies in the late 1990s functioned in this band. Because it provides the least amount of signal attenuation among all the optical windows, the 1550 nm wavelength is therefore the best choice when making optical system for long distance communication.

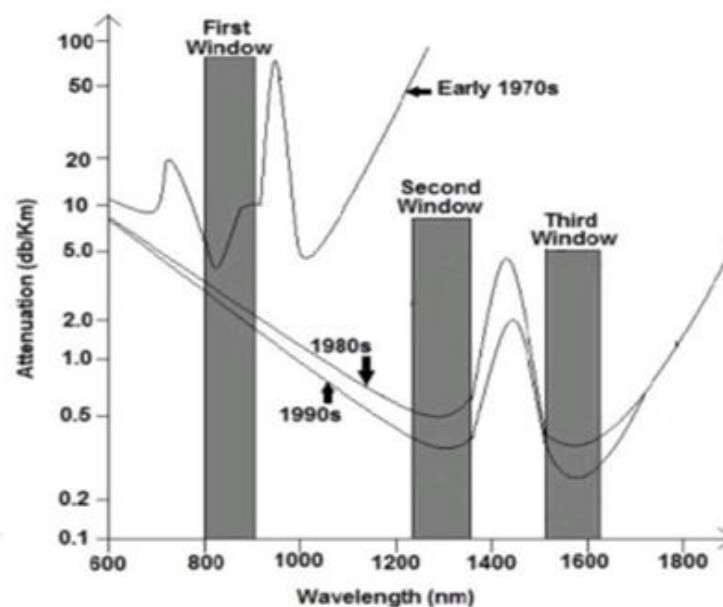


Figure 1.1 Relationship between attenuation and wavelength for optical window [2]

### 1.1.2 A Brief Overview of Fiber-Optic Sensors

Sensors that employ optical fibers to find changes in environmental parameter such as pressure, strain, temperature, or chemical composition are known as fiber optic sensors (FOS). Fiber optic communication technology development has been strongly connected with the development of fiber optic sensors. Because of their multiple sensing potentials such as absence of electric current conductivity, limit to radio frequency, high sensitivity, ease of combination with different structure and constituents, portability, and cylindrical shape, the FOS are superior to electrical sensors for analysing and changes in the environment can be detected [4, 5].

### 1.1.3 Block Diagram of Fiber Optic Sensors

Figure 1.2 represents block model of a FOS that include an Optical source such as a Laser or LED, optical fiber, a transducer for sensing, a detector such as a PIN or Avalanche Photodiode

and electronic processing such as an oscilloscope, optical spectrum analyser and wave analyser. The optical fiber carries the light that the optical source produces. The optical fiber transmits light generated by the optical source. As the light passes through the sensing region, its characteristics are altered in response to the measured parameters. It then continues through the fiber to a detector, which captures these changes. Finally, electronic processing devices interpret and display the resulting data [5]. Increasing advancements in research and development have directed to the expansion of FOS devices used in a variation of technological areas, including as military, industrial, agricultural, medical, civic and food. FOS is used to measure the concentrations of biomolecules and bio samples in the biomedical area. FOS is used to detect torsion, rotation, displacement, acceleration, and strain. Temperature, Gas, Chemical composition, and pressure have been measured by FOS in the context of environmental monitoring [6].

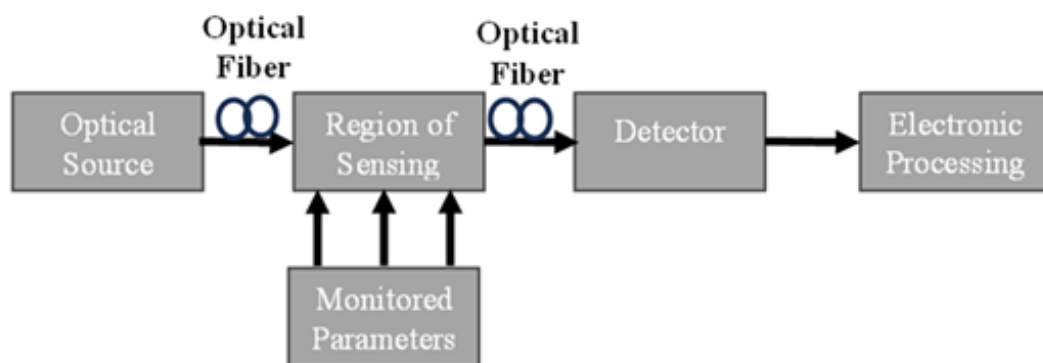


Figure 1.2 Block model of fiber optic sensors

### 1.1.3.1 Classification of Fiber Optic Sensors

The detailed classification of FOS, based on their sensing locations, operating principles of light and application is shown in Figure 1.3. Based on sensing locations, FOS are mainly classified into two part which is known as intrinsic FOS (IFOS) and Extrinsic FOS (EFOS).

a) A block diagram of IFOS is shown in Figure 1.4. In IFOS, the modulator works as element within the fiber, where the sensing occurs. The fiber's physical characteristics endure the changes that will take place, which is accomplished by a portion of the fiber link. The physical characteristics are phase, intensity, polarisation, and frequency can emerge in any form. Detector measures changes in the characteristics of light transmitted within the fiber if any additional changes made to the fiber's outside. The main advantages of intrinsic sensors are that they produce scattered sensing across long range distances. IFOS provide the best performance and can be used to replacement for sensing physical parameters such as pressure, temperature, and curvature [7].

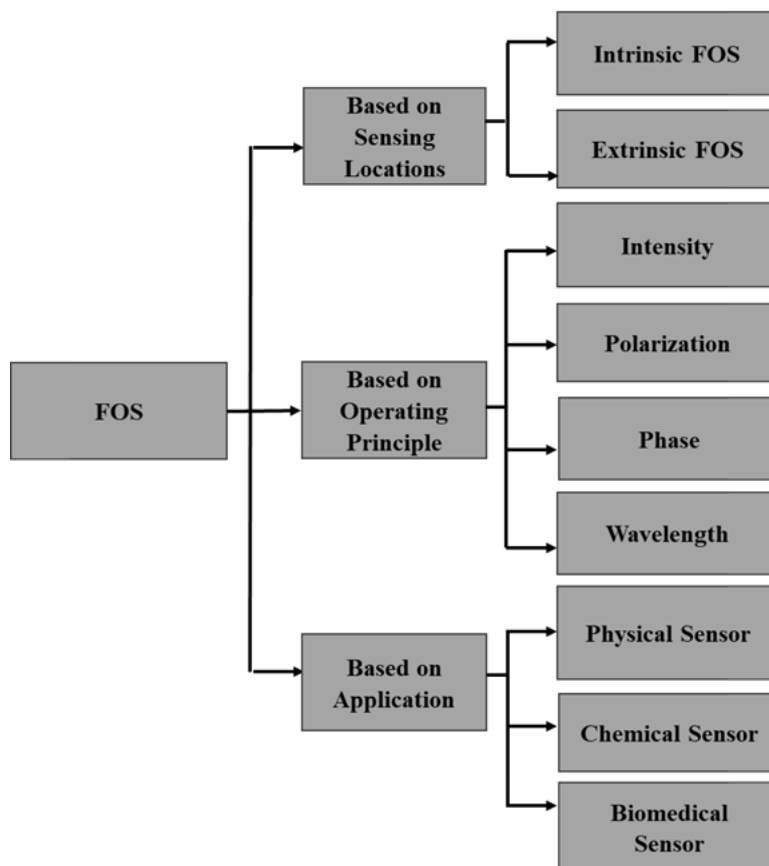


Figure 1.3 Classification of Fiber-Optic Sensor

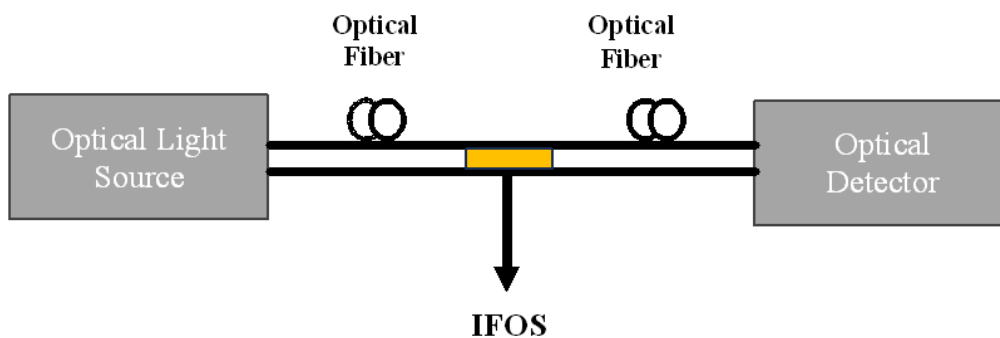
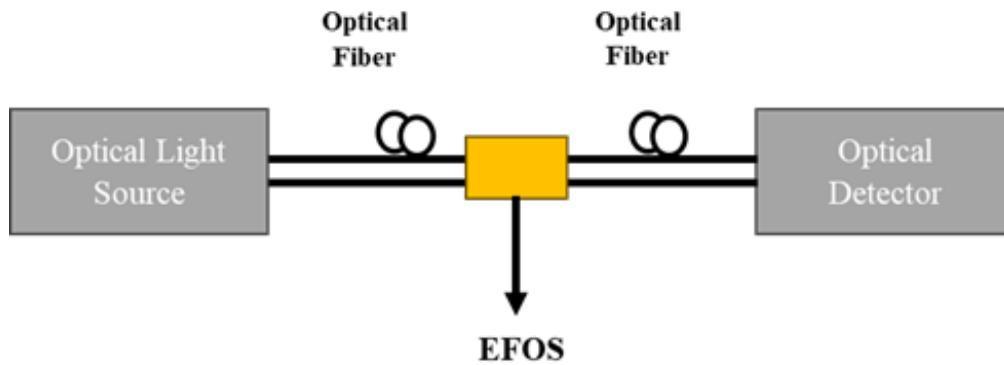


Figure 1.4 Block diagram of intrinsic FOS

b) The block diagram of EFOS is shown in Figure 1.5. The fiber in the EFOS just works as a carrier from the sensing region that transports light information from and to the optical device, it does not involve in any sensing. The transducer, that is separate from the fiber link, modifies the light in these kinds of sensors. Other external environmental factors are regulating and changing the light. The ability to reach remote locations and remarkable protection against noise distortion of the measurement signals are the main benefits of these sensors.



**Figure 1.5 Block diagram of Extrinsic FOS**

Based on operating principle of light FOS are mainly classified into four types known as Intensity, Polarization, Phase and Wavelength and their detailed explanation is given below.

**a) Intensity:** The intensity-based FOS measures change in light intensity as it propagates through the fiber. This type of sensors requires more light, hence fibers with large diameter of cores are generally used. These types of sensors have several important benefits such as affordability, ability to multiplex, dispersed sensor functionality and ease of use. These sensors are classified into two groups based on their principles: evanescent wave sensors, which are used to detect chemical and biological sensors and microband sensors, which are used to detect physical characteristics like pressure, temperature, and displacement.

**b) Polarization:** The sensors that only transfer and retain one polarization state are known as polarization dependent FOS. There exist three different polarization state: linear, circular, and elliptical. The direction and angle of the electric field component of the light determine the polarization of the light field. It is called the linear state of polarization when the electric field path remains in the same direction during the propagation of light. An ellipse is formed in the elliptical state, where the electric field vector terminates then the path of electric field changes. Two perpendicular linear components with identical amplitudes and a phase of  $\pi/2$  make up the electric field of light. For a circular, the resultant electric field will move in a circular motion. These sensors' polarization state gets affected by external factors such as stress or strain are applied. As a result, the external parameters may be identified when the polarization output state changes. Polarimetric sensor is the best example for polarization dependent FOS.

**c) Phase:** The changes in phase of light after it has been transmitted through the fiber link are used to measure and observe the phase-based FOS. The field is changing the phase as it propagates through the fiber for identification. Phase modulation will be detected using interferometric techniques, which compare and measure the phase of light in a position fiber to that of light in the signal fiber. Several interferometers, including the Mach-Zehnder, Michelson, Sag-nac, and Fabry-Perot models, are used to sense and detect phase modulation. Certain characteristics, such as fiber length, geometric fiber measures and RI affect the phase of light. Phase-based FOS works as a sensor element and achieves high sensitivity, among other characteristics that are necessary for single mode fiber and laser. Fiber gyroscopes, hydrophones, and multimode gauges are examples of these kind of sensors evolved throughout the previous few decades as the most efficacious technology in the Micro-Electronics industry. To cater to the requisition of continuous improvement at both device and performance level, device-scaling approach has been persistently adapted over the generations of technology.

**d) Wavelength:** Because of the different environmental conditions and considerations, the FOS dependent wavelength sensors are planned to sense different wavelengths of light. It is highly hypothesised that these sensor devices are the best option for measuring temperature, humidity, and viscosity of fluorescent-based fiber. The Bragg grating sensor, fluorescence sensor, and black body sensor are the best examples of these kind of sensors.

The FOS are classified into three categories according to their application which is known as chemical, biomedical and physical sensors.

**a) Chemical Sensors:** The element that FOS is a device that converts chemical sample data into a physical signal that can be calculated and is related with the concentration of specific chemical species. They are an important analyser component. The analyser consists of two components, the transducer and the receptor, and works according to a sample strategy. The receptor converts the chemical sample data into an energy signal that the transducer can measure. A transducer converts the signal from the chemical sample data into diagnostic signal. For gas analysis, pH level analysis and determining the chemical amount in a sample, the chemical FOS is used. Furthermore, recent studies have focused on using PCF to detect chemicals such as ethanol, methane, acetylene.

**b) Biomedical Sensor:** The electronic devices known as biomedical FOS are crucial to health care research because they convert the non-electrical factor found in the biomedical area into electrical parameters that are simple to detect and measure. They are very helpful in collecting and storing human physiological and pathological information. Portability, flexibility, miniaturisation, and the possibility of remote access are the key advantage of these sensors, the human body is not subjected to electrical interactions. Blood flow assessment, pulse monitoring, and glucose content valuation are just a few of the uses for biomedical FOS. Furthermore, in the biomedical field, PCFs have been broadly studied and scrutinised in recent years for the precise exposure of biomolecules including Deoxyribonucleic acid (DNA), proteins, and other blood components.

**c) Physical Sensor:** The physical FOS sensors are made to offer the specifics of physical properties based on their physical nature and effects. Many physical factors, including displacement, stress, velocity, torsion, and others, are calculated and measured by the physical FOS sensors. Many other sensing techniques may be used to study and control these characteristics. Tunnels, dams, pipelines, bridges, and buildings are examples of civil compositions that need constant review and monitoring to avoid initial collisions and accidents. Assistance is required under structural supervision of health for even transversal, bend, and strain loads. Metal restricts photoelectric sensor, strain sensor, and piezoelectric sensors are popular names for various kind of physical FOS.

Long-period grating (LPG) optical fibers are special fiber for identification of direction [8]. Fiber Bragg grating (FBG)-based fiber-optic sensors significantly increases performance, efficiency, and dependability across a wide range of industries, including aerospace, telecommunications, automotive and energy. Variations in fiber temperature, static pressure, mechanical tension, and compression can all affect FBGs. By adjusting the center wavelength of the light emitting source FBG-based fiber-optic sensors can be made more efficient [9]. Light propagation in the core of optical fiber is based TIR principle and the cladding has almost zero propagation loss. This is crucial for optical communication, but it limits the application of light for sensing because light does not interact with the environment. Some methods have been planned for modification of light propagation and improve light interaction with sensing materials, such as polishing, bending, chemical etching, tapering, and femtosecond grating

inscription. Optical fibers are only able to sense some number of analytes due to their zero selectivity and low sensitivity, that limits their development and applications, particularly for biosensors that need to be both highly sensitive and highly selective. Using respective materials, which may adjust their properties such as conductivity, RI, absorption, when surrounding environment (analytes) changes. Fiber-optic biosensors and chemical sensors can be made using several sensing materials, including carbon nanotubes, quantum dots, metal oxides, metals, polymers, nanowires, graphene, and many more to the fast development of functional material in recent years. To achieve optical fiber sensing purposes, the optical fibers would thus record and examine the changes in the sensing analytes. In recent years, a number of fiber-optic chemical sensors and biosensors have been designed and proposed [10].

## 1.2 Overview of Conventional Optical Fiber

Figure 1.6 shows the basic construction of a conventional optical fiber, which includes an outer cylindrical fiber core cladding with a slightly lower refractive index encircling an inner cylindrical fiber core with a high refractive index. For both the core and cladding fused silica is commonly used with different dopants are added to slightly change the refractive index [11]. A germanium-doped core and a pure silica cladding made fiber for long distance communication. There are some dopants which increases silica's RI such as aluminum, nitrogen and Phosphorus and some dopants decreases silica's refractive index such as fluorine and boron [12]. For making low-index cladding over pure silica cores, index-lowering dopants are used. TIR phenomenon is used for propagation of light within the core of conventional optical fiber [13]. When light falls on the boundary with materials having different refractive indices then some part of light is refracted and some part of light is reflected. When light in a material with a high RI reaches the boundary with a lower RI, known as the critical angle, refracted light moves along the boundary. The material reflects all light when the incidence angle between the normal and the boundary is greater than critical angle. Because of this, optical fibers use a low-index cladding and high-index core to achieve TIR guiding throughout the length. Two dimensionless parameters are used to study the guide mechanism of light in optical fibers are the normalised frequency  $V$ , which provide information about number of modes and the relative RI difference  $\Delta$ , which defines the relative RI difference between the core and cladding. The parameters  $\Delta$  and  $V$  is defined as [14].

$$\Delta = \frac{n_1 - n_2}{n_1} \quad 1.1$$

$$V = \frac{2\pi}{\lambda} \times a \times \sqrt{n_1^2 - n_2^2} \quad 1.2$$

where,  $n_1$  and  $n_2$  are the RI of core and cladding respectively,  $a$  is the radius of fiber core and  $\lambda$  is operating wavelength.

According to Eq. 1.2, optical fibers with  $V < 2.408$  represents single mode fiber (SMF), which means they are only capable of supporting a fundamental mode and not higher order modes. The fibers allow multi-mode transmission if  $V \gg 2.408$ . Because multi-mode fiber (MMF) propagation modes are closely random, the mode distribution at different incidence angles is unstable [15]. SMFs are typically employed for long-distance communication but are challenging and expensive to fabricate. In contrast, MMFs are mainly utilized for short-range communication and are comparatively easier to fabricate. Value of  $\Delta$  should be lower for SMF and higher for MMF. MMF suffer from modal dispersion. Figure 1.7 illustrates the cross-sectional structures of both single-mode and multimode fibers.

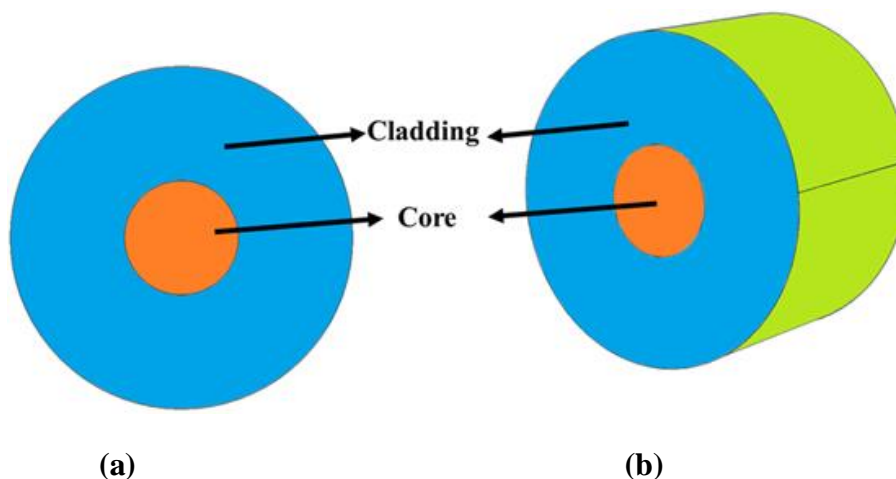


Figure 1.6 Conventional optical fiber (a) Cross-sectional view (b) 3-D view

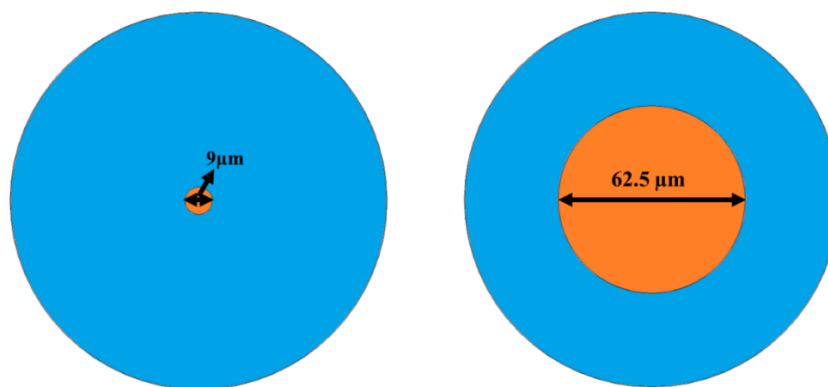


Figure 1.7 Cross-sectional structures of SMF and MMF

### 1.3 Photonic Crystal Fiber

A photonic crystal fiber is a novel type of optical fiber characterized by a cladding structure containing a periodic arrangement of air holes. The cross-sectional structure of the PCF is illustrated in Figure 1.8. To achieve desired characteristics such as high birefringence, large mode area, endlessly single-mode behaviour and tailorable dispersion, the PCF's structural parameters, like diameter of the cladding air holes ( $d$ ) and the distance between the two air holes called lattice constant or pitch  $\Lambda$  can be engineered [16]. PCFs are also known as micro structured or holey fiber, which are the advanced technology of optical fiber. Micro-structured air holes in PCF cladding provide a great arrangement of design adaptability which allows the PCF to achieve unique properties such as high birefringence [17], high nonlinearity [18], low dispersion [19], infinitely single mode [20], large mode area [21], low loss [22]. Russell's research team created the first solid core PCF in 1996 and after three-year, Russell's group was the first to create hollow core PCF. Later, PCF provide a variety of individual optical properties that are challenging to achieve with conventional fiber and because it creates new opportunities in related research field [23].

#### 1.3.1 Classifications of PCF Based on Structural Design

The two types of PCFs are referred to as solid core and hollow core PCF. Their detail explanation is given below.

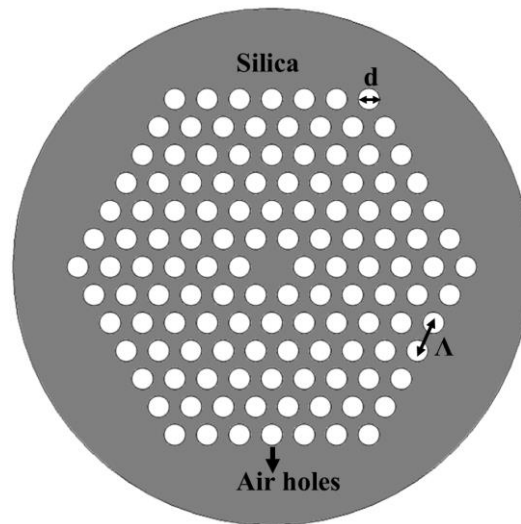


Figure 1.8 Schematic Cross-sectional structure of PCF

**a) Solid Core PCF:** The solid core is also known as high index fiber. Solid core has high refractive material (silica) at its center surrounded by low RI material of microscopic air holes known as the cladding region. Figure 1.9 shows 3-D view of solid core PCF with a triangular lattice arrangement. The cladding region includes air holes with diameter ( $d$ ), pitch ( $\Lambda$ ) which is separation between two air holes. For more desirable optical properties, PCFs structural geometrical parameters including pitch and diameter can be adjustable. The PCF has been built in several shapes like Equiangular spirals [24], squares, circles, and triangles [25].

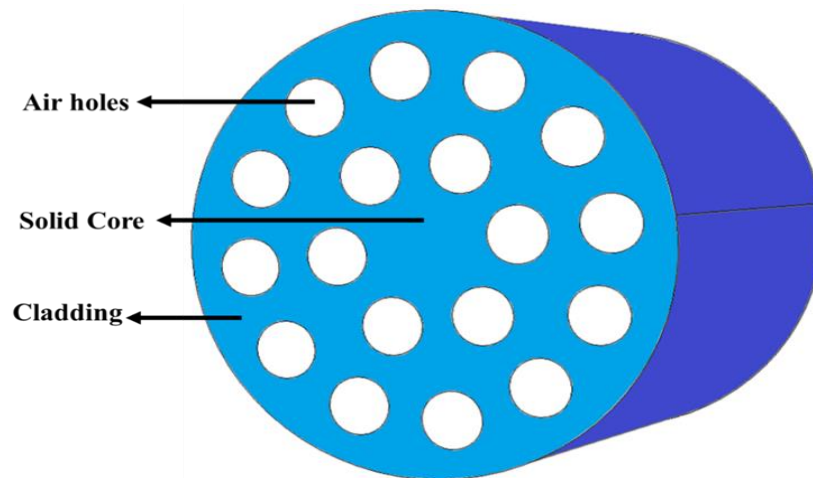


Figure 1.9 3-D view of solid core PCF

With a propagation constant  $\beta$ , the light beam travel along the axis of fiber in core as guided mode. In an infinite homogeneous media, the maximum value of  $\beta$  is  $n\kappa_0$ , where  $\kappa_0$  is the free space propagation constant and  $n$  is the refractive index of the homogeneous medium. Guided light in a solid core PCF with silica core has an effective refractive index ( $n_{eff}$ ) that meets the criterion  $n_s > n_{eff} = \frac{\beta}{\kappa_0} > n_{FSM}$ , where  $n_s$  is the high index silica core and  $n_{FSM}$  is the first cladding mode in the infinite periodic cladding structure also known as the fundamental space-filling mode (FSM).

**b) Hollow Core PCF:** In hollow core PCF, a photonic band (PBG) mechanism is used in propagation of light in the low index region at a particular wavelength. Figure 1.10 illustrates the 3D view of the hollow-core PCF. The section of air-filling is highly vital, which describe the hollow core PCF. Knight et al. discussed the air filling fraction and is defined as

$$a_{ff} = \frac{\pi}{\sqrt{3}} \frac{d_h^2}{\Lambda^2} \quad 1.3$$

where  $d_h$  the diameter of air hole capillary and  $\Lambda$  is lattice constant. Air-filling fraction  $a_{ff}$  is large for easy propagation in air,  $\frac{\beta}{\kappa_0} < 1$  must be present for guided modes [26].

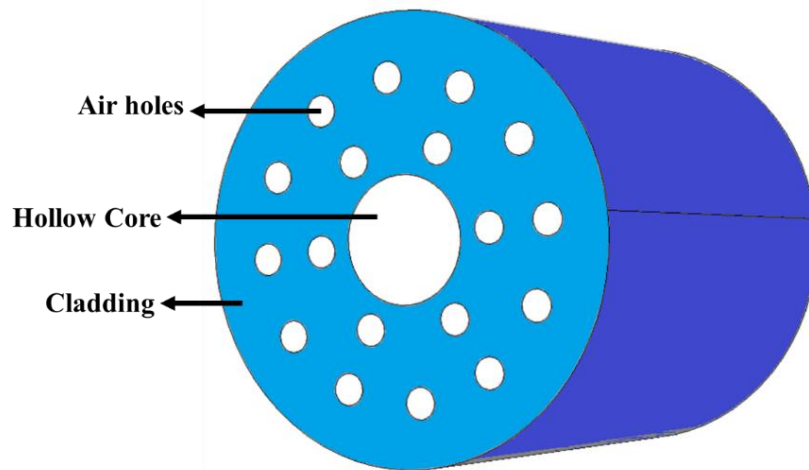


**Figure 1.10 3-D view of hollow core PCF**

Hollow-core PBG fibers are a new kind of optical fiber, Figure 1.11 (a) shows regularly organised micron-sized air holes [27, 28], Figure 1.11 (b) shows a PBG fibers can have rings of air holes spaced by nano support [29, 30], Figure 1.11 (c) shows a periodic sequence of micron-sized layers of various material with different RI [31, 32]. PBG fibers are now offered in speciality soft glass, polymer, and silica glass applications. The main role of such types of fibers to focus light into hollow cores that have a refractive index lower than the surrounding cladding material. Instead of using TIR, PBG fibers use the photonic bandgap effect to confine light in their hollow cores. In practical terms, bandgaps are described as frequency regions of improved fiber transmission that arises from destructive interference of core-guided light within the fiber micro structured cladding. PBG fibers primarily operate in a single mode over extended propagation distances, enhancing the quality of the transmitted light beam. This results from the significant variation of radiation losses of a PBG fiber's core-guided modes, with just a limited number of low-order modes having low propagation losses. The modes with the lowest losses will remain till the fiber end when many modes are excited at the fiber input end. Before the progress of all-dielectric PBG fibers, hollow-core fiber guiding was shown in the accompanying of metal-coated capillaries [33, 34]. The main benefits of hollow-core PBG fibers provide for sensing applications are discussed in detail. In such type of sensors, one must discriminate two modes of operation. Analyte absorption, or the change in the imaginary part of the analyte's RI, is first sensed by looking for and identifying small absorption bands in the fiber transmission spectrum. This is the most basic, non-resonant use of hollow PBG fibers for optical sensing, where the strong optical field overlap with the analyte is the only benefit. The sensitivity of these sensors and the signal intensity resulting from analyte absorption are closely correlated with the sensor length. Many experimental applications of these absorption-based

sensors have recently studied [35-39]. Detecting variations in the fiber bandgap position allows a PBG fiber-based sensor to detect changes in the real part of the analyte's RI, which is second mode of operation. Functioning within the resonant region, this type of sensor exhibits sensitivity that remains nearly independent of its length.

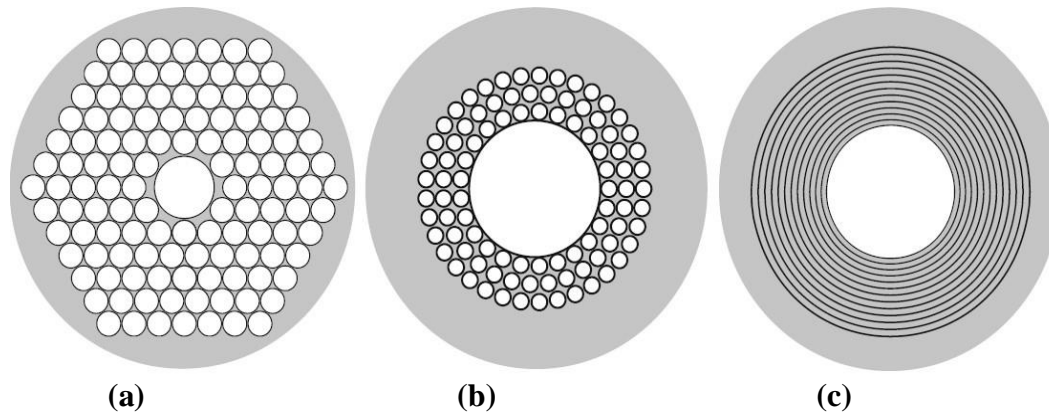


Figure 1.11 Photonic bandgap fibers with different type of hollow-core [40]

### 1.3.2 Classifications of PCF Based on Propagation of Light

The classification and naming of several PCF types is shown in Figure 1.12. Based on the light propagation method used, PCFs are broadly categorized as index guiding fibers and photonic bandgap fibers. TIR causes light to travel through index-guiding fibers. Index-guiding fiber is further subdivided into highly nonlinear fiber, large mode area fiber, high numerical aperture fiber and random hole PCF.

**a) Highly Nonlinear Fiber:** The HNL PCF, has a large index difference between the air-filled micro structured cladding and the solid silica core. This allows for tight mode confinement in the core, which leads to a high nonlinear coefficient and a low effective area [41]. Larger air holes or a smaller core size that forces light to stay confined within the silica core produce higher effective index difference [42].

**b) Large Mode Area fiber:** Core diameters of large mode area fibers are significantly bigger, over 50 times that of free-space wavelengths [43]. The fiber cross-section's geometrical characteristics can be changed to make this type of PCF.

**c) High Numerical Aperture Fiber:** A central core region surrounded by a ring of comparatively large air-hole cladding makes up a high numerical aperture fiber. For certain purposes, the numerical aperture can be modified by changing the number of air holes and their sizes in the cladding region. With a numerical aperture greater than 0.9, high numerical aperture fibers may therefore collect light with an unusually low loss [44]. The loss may be reduced to less than 0.1 dB/km with the use of larger air holes [45]. As a result of their great light-collecting capabilities, HNA PCFs have very low loss.

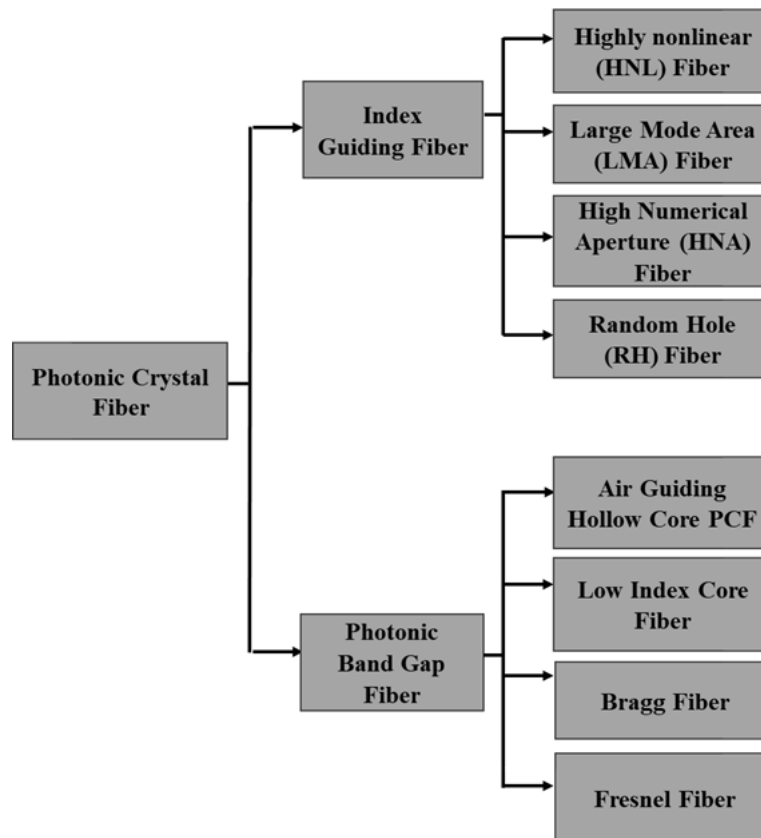
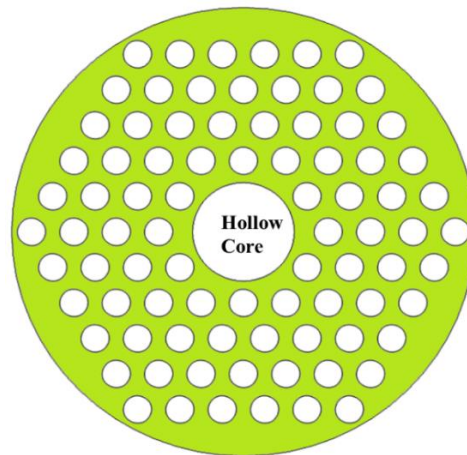


Figure 1.12 Classification and naming of PCF

**d) Random Hole (RH) Fiber:** The random hole PCF, has holes that are spread at random across the fiber length to guide light. These fibers are made up of silica. The central area is without any air holes. Random air holes around this, making the cladding region with the lower effective refractive index [46]. Because the holes in RH PCFs are randomly distributed, the hole-pitch is an uncertain size, and the distribution of holes must be described by a probability density function. Like periodic holey fibers, this area serves as the core when there are no air holes within the hole-pitch form in the center of fiber. Furthermore, the air holes cannot be found too near to one another. Two important parts of these fibers are the hole-size and the wavelength to typical hole spacing ratio.

The PBG effect causes light to travel in photonic band gap fibers. Photonic bandgap fiber is further divided into air guiding hollow core fiber, low index core fiber, Bragg fiber and Fresnel fiber

**a) Air Guiding Hollow Core PCF:** Light may flow through the hollow core of the air guiding hollow core fiber without leaking since it contains air. Figure 1.13 illustrates the cross-section of the air-guiding core PCF. The cladding region is formed by periodic microstructure air-holes in the silica background, which act as photonic crystal. Further an important advantage of this fiber over solid-core fibers is that its performance is less dependent on the absorptive interaction between the guided light and the fiber's solid core material. It facilitates stimulated Raman and Brillouin effects by allowing the propagation of light corresponding to supported signal wavelengths and power levels that are not possible in traditional solid-core optical fibers [47].



**Figure 1.13** Cross-sectional view of air-guiding PCF

**b) Low Index Core Fiber:** Low index liquids, chemicals, or gases are deliberately transferred into the hollow core of low index core fiber. Cross-sectional view of low index core is shown in Figure 1.14. Light enters the fiber core through the PBG effect. Even though the liquid's RI is lower than silica, the fundamental mode may however guide light through the liquid core for formation of a suitable range of waveguide parameters. In a particular wavelength range, this improves the interaction between light and liquid. Since most chemical or biological solutions consist of water and alcohols, they are the most basic and common liquids for these types of applications [48].

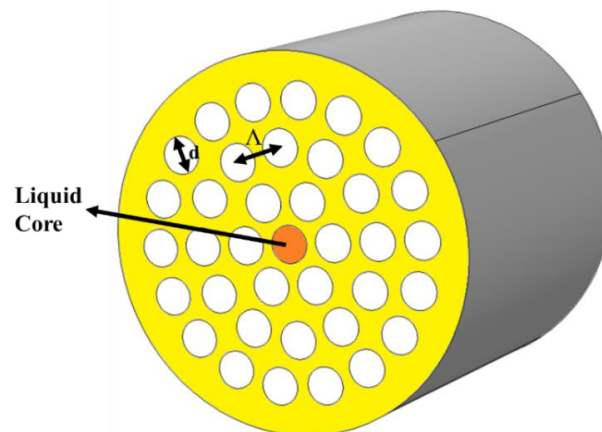


**Figure 1.14** Schematic cross-section view of a low index core PCF

**c) Bragg Fiber:** The Bragg fiber has a ring structure with alternating lower and higher index regions which is shown in Figure 1.15. Therefore, these fibers are different from other kinds of fibers that have holes in the cladding region. This structure differs from the other PCF structures previously mentioned in that it is made up of two solid materials arranged so that the RI only fluctuates in a radial direction. This type of index change is useful because it makes it simple to yield PBG-guidance in the hollow core fiber due to the single periodicity involved. However, the thermal and thermochemical characteristics of the two solid materials must be well-matched. Large PBGs and omnidirectional reflections are the results of this specific fiber's hollow core surrounded by a solid multilayer structure with a high refractive index difference.

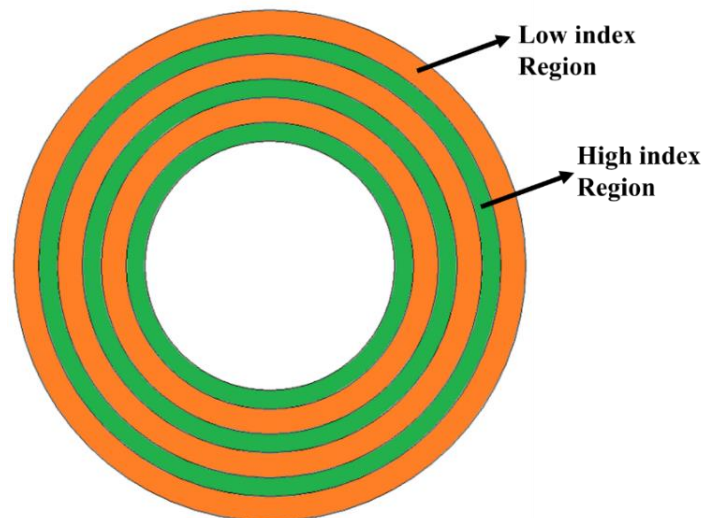


Figure 1.15 Cross-sectional view of a Bragg PCF

**c) Fresnel Fiber:** A ring with a higher index approaches the central hole of the Fresnel fiber, as shown in Fig. In a radial direction, this supports waves, which may be defined as Gaussian. Through superposition, the peak intensity is higher in the low-index air region rather than the high index ring when the field distribution is appropriate. According to published research, a Fresnel PCF supports a mode at 1550nm with peak intensity in the center hole [49]. By changing its width, the structure may be optimised to transmit a remote extensive spectrum of light down the middle hole. The dispersion may be changed to modify the Fresnel fiber's propagation characteristics. The existing works also reports a water-core Fresnel PCF, which portions guiding characteristics with the air-hole guiding Fresnel fiber. However, there is a noticeable loss edge at around  $0.9 \mu\text{m}$  [50]. This represents that the band gap, which is associated with Fresnel guidance, has shifted to longer wavelength.

#### 1.4 Overview of Single, Dual, and Multi-Core PCF Architectures

In recent years, PCF with single, dual and multi core configurations has been broadly studied by researchers. The basic design of a single, dual and multi core PCF using a hexagonal lattice is shown in Figure 1.16 (a)-(c). In order to make one, two, and more than two core regions, particular air holes have been removed from the lattice. The number of guiding channels in a single, dual, or multi-core PCF type is one, two, or several, accordingly. To improve each probable optical property of a PCF, dual-core PCFs are now frequently used. Removing the air holes close to the PCF's central air hole permits for the formation of a dual-core PCF. It has recently been discovered that dispersion correction is the primary advantage of using dual-core PCF [51, 52]. A dual-core PCF has important advantage for refractometric and biosensing applications. Significant interaction between core guided waves and sensing samples is made possible by its dual guiding channel. Dual-core PCF is also useful for beam splitting, frequency tuning, and optical switching. Multi-core fiber was introduced in 2009. With its extensive scaling in the mode field size and nominal change to the dispersion characteristics, multi-core PCFs have countless potential for high power supercontinuum construction [53, 54].

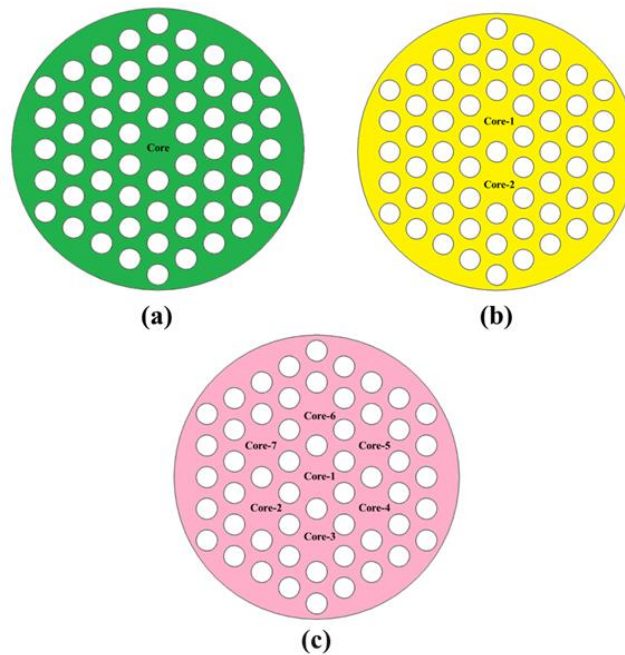


Figure 1.16 Design of PCF using (a) Single-core, (b) Dual-core, and (c) multi-core

### 1.5 PCF Lattice Configurations: Hexagonal, Circular, and Square Structures

Different lattice patterns of air holes, such as hexagonal, circular, and rectangular, may be used to design PCF, as shown in Figure 1.17 (a)-(c).

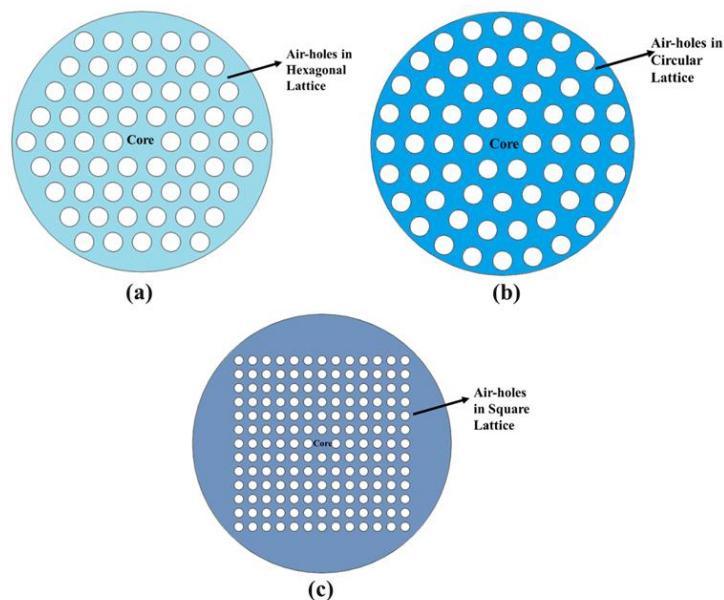


Figure 1.17 Design of PCF using (a) Hexagonal (b) Circular, and (c) Square lattice-structures modelling

PCF also uses different lattice structures, including octagonal, star, triangular and honeycomb. Several materials including silica, Zeonex and TOPAS are used as base material for design of PCF. Many optical characteristics, including as confinement loss, dispersion, birefringence, non-linearity, numerical aperture, and sensitivity are influenced by the varied effective refractive indices of PCF structures with different background materials. Different PCF lattice

structures have been used in biosensing, liquid sensing, chemical sensing, and gas sensing, among other applications in recent years [55-58].

### 1.6 Applications of Photonic Crystal Fiber

In addition to low-loss communication, PCF is showing its adaptability in a variety of other applications, including dispersion compensation, high-power beam delivery, infinitely single-mode fiber, Physical sensor, Supercontinuum Generation, Biochemical sensor, Refractive index sensor as shown in Figure 1.18.

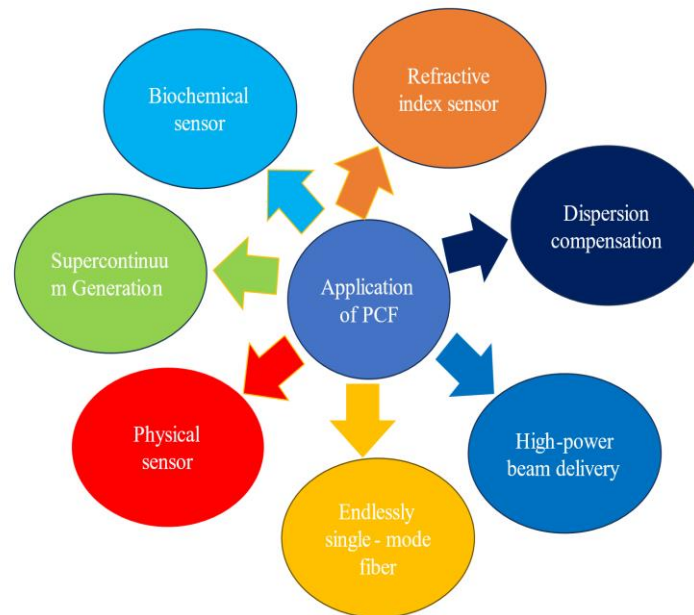


**Figure 1.18 Application of PCF in various field**

The use of PCF to study different physical potential is a combination of engineering and optics. Because of high sensitivity, adaptability in design, small size, and durability of PCF sensor makes superior than conventional optical fiber and electrical sensing systems. Due to unique nature of PCF, there is a lot of attention for research. The supercontinuum generation (SCG) is the formation of extensive continuous spectra when one injects almost perfectly monochromatic light from a laser source. This occurs because high strength pulses propagate through nonlinear mediums. The parameter that determines SCG are the pulse length, peak power, and the nonlinear medium's dispersion in relation to the pumping wavelength. A unique nonlinear phenomenon that can have a spectral width more than two octaves for lengthy pulses and comparatively modest intensities is the formation of an ultrabroadband continuum. With a broad variety of pump pulse durations and pump wavelengths in the visible or near-infrared spectrum, this effect has been seen in PCFs and shaped fibers [59]. Physical sensor can fill analytes to interact with light due to their interior structure and flexibility. For several applications such as in health monitoring, biomedical sensing, remote sensing, physical sensors are mainly used to measure desired parameters like pressure, torsion, RI, electric field, magnetic field, temperature, displacement, stress, and strain. Some sensors are used to identify chemicals that exist such as gases, vapours, or liquids. They are employed in the chemical industry to sense a range of substances to identify chemical density and leakage. In the medical field, blood components and hazardous compounds in the body are identified. Food ingredients are also sensed to identify potentially harmful additives. The RI of a material is measured by

refractive index sensor, which supports in determining its density, composition, and concentration. Environmental monitoring, food safety, chemical analysis, and biological diagnostics all make extensive use of these sensors. The process of forming single mode fiber is general and achieving a core radius as small as a few micrometres is challenging. However, there is problem of intermodal dispersion by utilising single mode fiber. Thus, a fiber with an infinitely single mode larger radius is required. Only single mode propagation is discovered to be maintained when the ratio of hole size to hole spacing exceeds a certain amount. Any wavelength can accommodate core sizes ranging from extremely small to very big. Thus, it is feasible to build a fiber with a core size of tens microns. High-power beam delivery in PCFs is an important field of research for applications such as in biomedical and defence technology. Dispersion is a significant phenomenon that requires consideration and compensation. In general, there are two kinds of dispersion. One is intra-modal or chromatic dispersion and other is inter-model dispersion. Chromatic means colour, and this kind of dispersion occurs because light of several colours travels at different speeds. This is classified into two category one is waveguide dispersion and other is material. The whole dispersion must be zero since waveguide dispersion has a negative dispersion coefficient. The zero dispersion for standard fiber is at 1.3  $\mu\text{m}$ . At operational frequency, chromatic dispersion can be compensated for zero wavelengths dispersion. There are multiple paths of transportation within the fiber each has different velocity and hence reaching at the receiver at a different time, cause intermodal dispersion. This kind of dispersion may be compensated by infinitely single mode fiber.

### **1.7 Problem Statement**

Conventional optical fibers send data across long distances at high speeds in the form of short light pulses. It has a few advantages and utilised in several non-telecom applications. Even yet, they show some limits in the sensing area because of several problems, including low detection accuracy, a restricted capability to tune for desired optical properties and a more complex design for high-sensitivity devices. To reduce this, a sensor based on PCF is proposed.

### **1.8 Motivation**

Optical fiber technology has played an important role in the development of modern telecommunication and sensing systems since its discovery in 1966 by Charles K. Kao. Optical fiber sensors are widely used because they provide high sensitivity, compact size, and immunity to electromagnetic interference. Conventional optical fibers have been successfully used in communication and sensing applications; however, their performance is limited by the material properties of silica and their fixed structure. In conventional fibers, it is difficult to control important optical parameters such as dispersion, birefringence, effective area, and nonlinearity. These limitations reduce their efficiency for advanced sensing applications. To overcome these problems, Photonic Crystal Fiber (PCF) was introduced in 1996. PCF contains a microstructured arrangement of air holes in the cladding, which provides greater flexibility to control the optical properties of the fiber. Due to their special structure, PCFs can provide high birefringence, adjustable dispersion, high nonlinearity, and strong light-matter interaction. Because of these advantages, PCFs are widely used in different sensing applications such as chemical, biological, and temperature sensing. In addition, integrating plasmonic materials with PCF structures can further improve the sensing performance. However, several challenges still exist, such as improving parameters like effective area, birefringence, dispersion, and nonlinearity, achieving high sensitivity over a wide temperature range, developing compact PCF designs for chemical sensing, studying PCF sensors in the terahertz frequency range, and exploring plasmonic sensing using optical fibers. Therefore, the main motivation of this research is to design and analyze PCF-based sensors with high

sensitivity, low confinement loss, and compact size in order to address the identified research gaps.

## 1.9 Research Gaps

Based on the literature survey, the following research gaps were identified:

- There is a scope of improvement in performance parameters of conventional fibers such as effective area, birefringence, dispersion and nonlinearity.
- High sensitivity of PCF-based temperature sensors over wide detection range of temperature is still lacking.
- Lack of optimized fiber designs that can deliver PCF-based chemical sensors with high sensitivity and compactness.
- Limited research found on frequency variation in THz regime-based PCF sensors.
- Not enough research has been found on conventional fiber-based plasmonic sensors for sensing applications.

## 1.10 Research Objective

The aim of this thesis is to begin a theoretical study into the modelling, simulation, and classification of fabricable PCF sensors for physical and biochemical analytes with different refractive indices, as well as to explore their sensing abilities. PCF-based physical sensor measures physical quantity such as (temperature and refractive index) and convert it into a signal which can be ready by an observer. Furthermore, PCF based biochemical sensor can convert a chemical (or biological) quantity into an electrical signal. Biochemical sensors are useful in human health monitoring that includes blood component detection, malaria detection and fluid analyte sensing, The primary focus of the research area is the designing and analysis of PCF-based sensors with improved sensitivity, large sensing range, compactness, lower confinement loss, high birefringence, and other characteristics, which will result in improved sensing performance in a suitable detection system. The overall objective of this work can be described as follows:

- Design and analysis of ethanol filled circular shaped hollow core photonic crystal fiber to enhance performance characteristics.
- Design and analysis of Twin core photonic crystal fiber based temperature sensor with improved sensitivity over a wide range of temperature.
- Design a compact and highly sensitive hexagonal lattice dual core photonic crystal fiber based chemical sensor.
- To study the effect of frequency variation in THz regime on sensitivity of Twin Core PCF based sensors.
- Design a surface plasmon resonance based photonic crystal fiber for sensing application.

## 1.11 Organization of the Thesis

In this thesis, the PCF based sensors are simulated and examined with COMSOL Multiphysics software, which employs the finite element method (FEM). Based on the variations of the fiber

structure parameters, the obtained effective RI data sets with their corresponding wavelengths for different analytes are used to calculate important parameters such as sensitivity, confinement loss, detection range, transmission spectrum, and sensing performance, which can be used to determine the sensing ability of a PCF sensor. This thesis is arranged into seven chapters. Hence, the chapter layout with brief summaries of each is clearly explained below.

**Chapter 1** provides the research background of fiber-optic sensors, research flow, PCF description, research objectives, and an outline of the entire thesis based on a comprehensive literature review concerning PCF-based sensors.

**Chapter 2** reviews the detail history and previous works on this research in past few years. Fundamental concepts of PCF as well as the operation of a PCF-based sensor are also introduced, described, and explored. Finally, at the end of this chapter, the finite element method, which is a numerical methodology for determining the effective refractive index required in solving the wave equation, is explained.

**Chapter 3** proposes a circular shaped ethanol-filled hollow core photonic crystal fiber. The optical properties, like dispersion and effective area of the proposed hollow core PCF have been studied for the wavelength range from 800 nm to 1600 nm. The main focus of this research work is to achieve nearly zero dispersion wavelength (ZDW) by using finite-element method. This kind of PCF is useful in sensing applications, non-linear applications, laser technologies and telecommunication.

**Chapter 4** provides an overview of twin-core photonic crystal fiber (TC-PCF) designed for temperature and chemical sensing applications. The proposed TC-PCF structure consists of twin solid cores separated by a vertical elliptical air hole, enabling independent waveguiding and high birefringence. The sensor operates on the principle of mode coupling between the two fiber cores, enhancing its sensitivity. Finite element method (FEM)-based simulations have been conducted to analyze the performance of the proposed sensors. The results confirm the effectiveness of TC-PCF in achieving high sensitivity for both temperature and chemical sensing. This chapter presents the theoretical foundation, design, and performance evaluation of TC-PCF-based sensors, highlighting their practical implementation potential.

**Chapter 5** presents the design and analysis of advanced photonic crystal fiber (PCF)-based biosensing techniques for the early detection of various diseases, including different types of cancer, primary blood components, and malaria. The study utilizes finite element method (FEM)-based simulations in the terahertz (THz) frequency range to explore mode coupling in twin-core PCFs, ensuring high sensitivity and precision in biosensing applications. Through rigorous analysis of various PCF parameters, the proposed sensors exhibit superior sensitivity and efficiency in disease detection, contributing to advancements in biomedical diagnostics and healthcare applications.

**Chapter 6** introduces a photonic crystal fiber (PCF) based surface plasmon resonance (SPR) biosensor for early detection of diabetes. In the designed PCF structure, two layers of air holes are arranged in a hexagonal lattice, and a thin gold coating is applied to facilitate the excitation of surface plasmon resonance (SPR). The SPR phenomenon is triggered when the surface plasmon polariton (SPP) mode couples with the core mode under phase-matching conditions. The sensor design is analyzed and optimized using COMSOL Multiphysics, which is based on the finite element method (FEM). This configuration demonstrates potential as an effective technique for the early detection of diabetes.

**Chapter 7** summarizes the key findings of the research presented in this thesis and explores future directions in the field of fiber sensors. The discussion focuses on advancements in both solid and hollow core fiber sensor technologies, highlighting their potential for further development and applications.

## CHAPTER 2

### LITERATURE REVIEW

#### 2.1 PCF-Enabled Sensing Technologies

PCFs have involved the care of several research organisations due to their interesting properties. The PCFs have air holes, samples of liquids or gases can be filled into them. This permits interaction between confined light and sensing samples, opening novel sensing applications that would not have been possible with conventional optical fiber. In sensing field, applications of PCFs are categorized into physical sensors and biochemical sensors, depending on the specific parameter they are designed to detect. The physical properties that physical sensor include are temperature, pressure, torsion, vibration, displacement, electric field, and refractive index. On the other hand, biochemical sensor, can detect chemical and biological substance (such as antibody, cell, bacteria, blood component, enzymes, virus, nucleic acid, etc.). Key element of biochemical sensors is to measure chemical refractive index. Chemical sensor and biosensor are frequently referred to as biochemical sensors because of their close interrelation. Some of the main advantages of PCF-based sensors are as follows:

- Different lattice structures can be employed to give adaptability in the sensor design.
- By adjusting structural parameters such as air-hole diameter  $d$ , lattice constant called pitch  $\Lambda$ , and lattice structure shape sensitivity and sensing range can be controlled.
- In the sensing process, a hollow air-core can be employed as an analyte sensing channel.

##### 2.1.1 Temperature Sensor

Most commonly, a PCF temperature sensor is referred to as a PCF-based temperature sensor. Temperature variation is detected by these sensors using the special characteristics of PCFs, which are optical fibers with a microstructure arrangement of air holes running along their length. Using optical methods like interferometry or Bragg gratings, one may calculate how temperature variation affects the PCF's RI.

For temperature sensing, a twin-core PCF (TC-PCF) with two solid cores separated by an air hole is used is shown in Figure 2.1 (a). As the light travels through the fiber, it couples between the two waveguides after being injected into one core. The transmission spectrum of the TC-PCF is sensitive to temperature variations due to changes in the RI of the base material. Maximum achieved sensitivity is found to be 18.5 pm/°C with 6 cm long TC-PCF that can sense temperature range of 0°C to 600°C [60]. Figure 2.1 (b) shows the transmission spectrum which is measured between 1540 and 1560 nm, exhibits a sinusoidal pattern at different temperature. Figure 2.1(c) illustrates the electric field vector and magnitude distribution for the x-polarized even and odd modes, while Figure 2.1(d) presents the corresponding distributions for the y-polarized even and odd modes, based on the principles of mode coupling theory.

A very sensitive D-shaped PCF temperature sensor based on surface plasmon resonance (SPR) is discussed in this study. A gold layer is applied on the smooth, polished surface to improve sensitivity of the PCF and ethanol, chloroform are temperature sensitive material. Under phase-matching conditions, the core mode couples with the surface plasma mode. The maximum

achieved sensitivity is  $6.36 \text{ nm}/^\circ\text{C}$  throughout a  $-5$  to  $60 \text{ }^\circ\text{C}$  range [61]. The sensor's great manufacturing feasibility and outstanding linearity ( $R^2 = 0.9981$ ) make it a good choice for biochemical and biomedical application. Figure 2.2 (a) represents the cross-sectional structure of SPR-based temperature sensor including two layers of cladding air holes with diameters  $d$ ,  $d_1$ ,  $d_2$  arranged in hexagon shape and pitch of lattice is  $\Lambda$  and optimized values of these parameters are  $d = 2 \text{ }\mu\text{m}$ ,  $d_1 = 1.5 \text{ }\mu\text{m}$ ,  $d_2 = 0.75 \text{ }\mu\text{m}$ ,  $d_3 = 1.8 \text{ }\mu\text{m}$ ,  $r = 6.5 \text{ }\mu\text{m}$ ,  $\Lambda = 2.5 \text{ }\mu\text{m}$ ,  $h = 3.5 \text{ }\mu\text{m}$  and  $t = 30 \text{ nm}$ . Figure 2.2 (b)–(c) depicts the electric field distribution for the y-polarized core modes and the y-polarized SPP mode. Figure 2.2 (d) represents the y-polarized core mode and plasmon mode loss spectra and dispersion relations at  $-5 \text{ }^\circ\text{C}$ . The y-polarized core mode shows significant loss with peak between  $0.82$  and  $0.9 \text{ }\mu\text{m}$ . The y-polarized mode is the ideal mode for sensing because of its better sensitivity and stronger interaction with the SPP mode. The real part of the ERI for the SPP and core mode coincides at  $0.8568 \text{ }\mu\text{m}$  with a maximum loss peak  $317.51 \text{ dB/cm}$ . Figure 2.2 (e) represents the variation of temperature ( $T$ ) and resonance wavelength ( $\lambda_{\text{peak}}$ ), from which sensitivity can be calculated. The sensor outperforms several previously reported PCF-based temperature sensors, surpassing their maximum sensitivity of  $6.36 \text{ nm}/^\circ\text{C}$  at  $-5 \text{ }^\circ\text{C}$ .

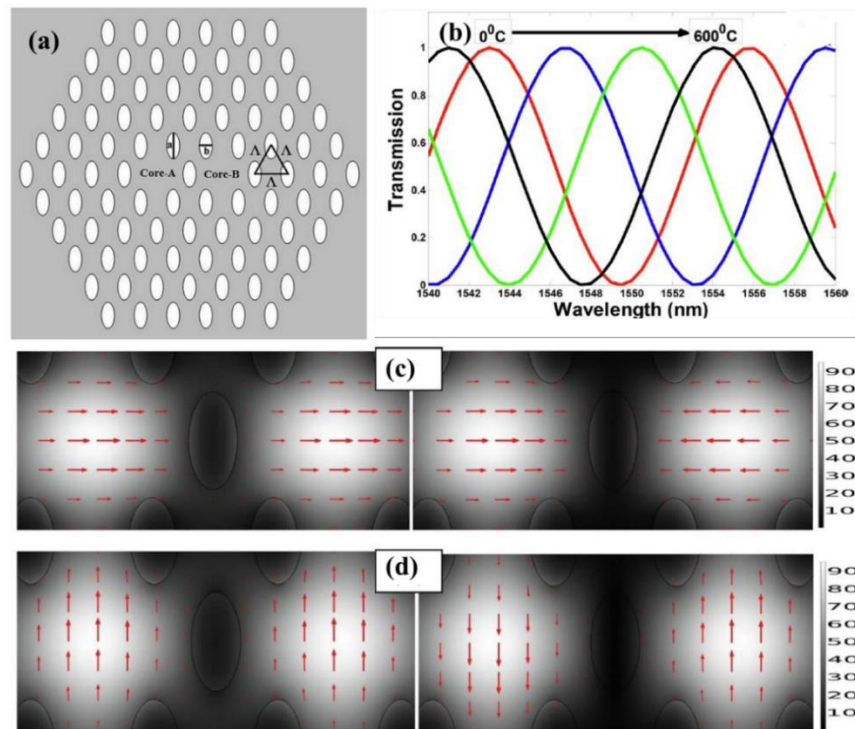


**Figure 2.1 (a) Cross-section view of TC-PCF (b) Transmission spectrum of TC-PCF (c) x-polarized even and odd mode (d) y-polarized even and odd mode [60]**

SPR in a PCF is the basis for an extremely sensitive temperature sensor is studied. Ethanol and toluene are filled into the central hole and the gold-coated air holes, respectively, to produce SPR. The sensor provides high sensitivity through the optimization of the air hole's size and orientation. From the analysis maximum achieved temperature sensitivity is found to be  $7.13 \text{ nm}/^\circ\text{C}$  and Figure of merit (FOM) is  $0.1169/^\circ\text{C}$  in the range of  $0^\circ\text{C}$ – $70^\circ\text{C}$ . This sensor represents a lot of potential for applications requiring exact temperature sensing [62]. The cross-section of the PCF-based temperature sensor, comprising three cladding layers, is illustrated in Figure 2.3 (a). The diameter of second layer arranged in hexagonal is  $d_2$  allowing for modifications to the mode field and coupling, while the core air hole has a diameter  $d_1$ . The

thickness of gold film is  $t$  and  $d_3$ ,  $d_4$  have the diameter of outer layer. In  $d_3$ , a golden ring is seen in the air hole. To examine how different factor affects temperature sensing

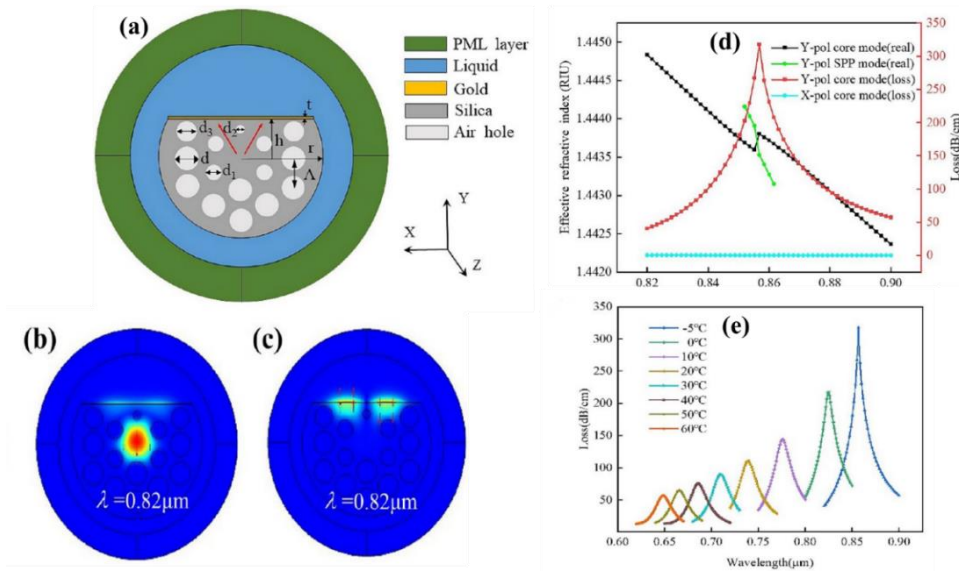


**Figure 2.2** (a) Cross-sectional view of the SPR-based PCF temperature sensor, (b) field distribution of the y-polarized core mode, (c) field distribution of the y-polarized SPP mode, (d) loss spectra of the core modes along with dispersion relations for the y-polarized core and plasma modes at  $-5^{\circ}\text{C}$ , (e) variation of loss spectra with wavelength [61]

performance, the following parameters are set as  $d_1 = 2\ \mu\text{m}$ ,  $d_2 = 1.8\ \mu\text{m}$ ,  $d_3 = 3\ \mu\text{m}$ ,  $d_4 = 3\ \mu\text{m}$ ,  $p = 3\ \mu\text{m}$ ,  $t = 37\ \text{nm}$  and  $r = 10\ \mu\text{m}$ . For simulation, a perfect matched layer (PML) is put at the uppermost layer. Methods for stacking and stretching is used to form PCF as shown in Figure 2.3 (b). Before the preforms are layered, fiber preforms are first formed. Solid rods, thick-walled capillaries, and thin-walled capillaries are placed one after the other to create air holes and guide cores. The prefabricated rods are then placed and pulled with a conventional pulling tower [63, 64]. The loss spectrum of the y-polarized core mode in the temperature range of  $0^{\circ}\text{C}$  to  $70^{\circ}\text{C}$  is shown in Figure 2.3 (c). This explains how the loss raises and the loss spectrum redshift as the temperature rises and this is because when the temperature rises, the filling liquid's RI changes. The temperature sensor's experimental setup and three-dimensional construction are shown in Figure 2.3 (d). Broadband light is produced by lasers. The optical spectrum analyser (OSA) is then connected to the sensor through a single-mode fiber once it has been introduced to it. Finally, the optical spectrum analyzer measures the optical spectrum. The change in FOM and FWHM values at different temperatures is shown in Figure 2.3 (e) and it is observed that the FOM value rises as the FWHM value falls.

Using the finite element approach for design optimization, a D-type PCF temperature sensor containing a gold nanowire is studied. To improve performance, important variables such as air hole width, nanowire size, and spacing were adjusted. Maximum sensitivity achieved is found to be  $-19.0\ \text{nm}/^{\circ}\text{C}$  that can sense  $10$  to  $50^{\circ}\text{C}$ . Its minimal manufacturing complexity and straightforward structure make it very promising for temperature sensing applications [65]. A schematic of D-shaped PCF in three dimensions is shown in Figure 2.4 (a). The simplified square air hole distribution of the PCF-based SPR temperature sensor contrasts with the traditional hexagonal air hole arrangement. A single layer of air holes in the sensor's makes manufacturing simple shown in Figure 2.4 (b). The diameter of larger air holes is  $d_1 = 3.2\ \mu\text{m}$ , while the smaller air holes have diameter of  $d_2 = 1.2\ \mu\text{m}$ , with pitch of  $\Lambda = 3\ \mu\text{m}$ . The operation

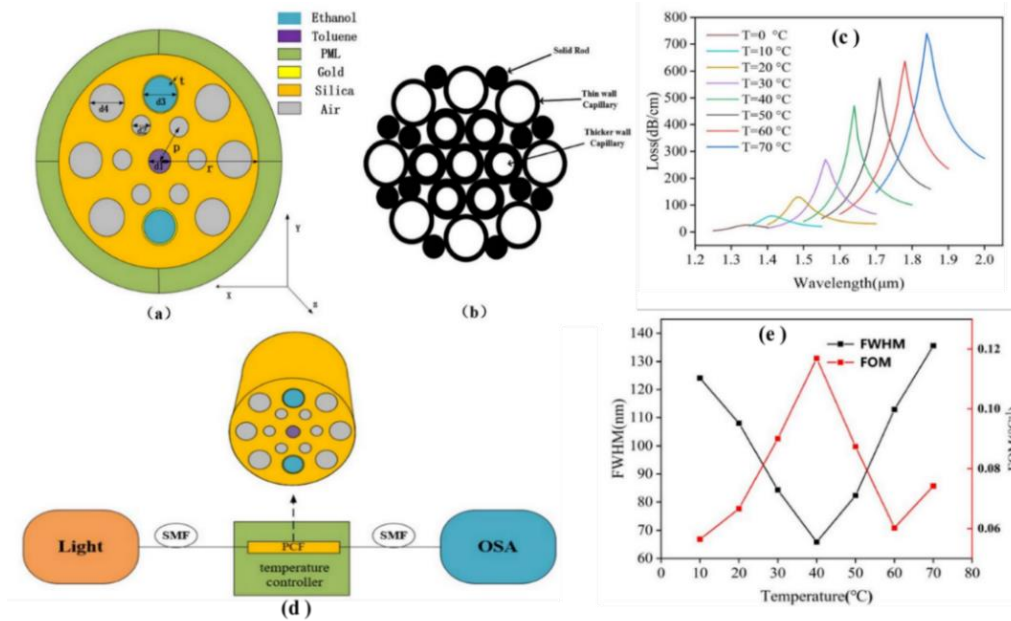


**Figure 2.3** (a) Cross-sectional view of temperature sensor (b) Structure of the Stacked preform of sensor (c) Loss spectrum in y-polarized core mode (d) Experimental setup of PCF sensor (e) At different temperature variation of FOM and FWHM [62]

of the sensor, illustrated in Figure 2.4(c), involves a broadband light source (BBS), a single-mode fiber (SMF), an X-direction polarization controller, the D-shaped PCF-SPR temperature sensor, a temperature-sensitive material (PDMS), and an optical spectrum analyzer (OSA). The impact of the air hole spacing on the loss spectrum is shown in Figure 2.4 (d). As the air-hole spacing raises from 2.8  $\mu\text{m}$  to 3.2  $\mu\text{m}$ , the resonance wavelength shifts to blue. This is because the energy is contained within the core by the air holes that surround it. The leakage channel for fiber core energy expands as  $\Lambda$  rises. Field distribution is shown in Figure 2.4 (e)-(f). The performance of sensor is significantly influenced by the size of the gold nanowire. Figure 2.4 (g) illustrates how different gold nanowire diameter ( $d_3$ ) affects the loss spectrum. To examine the impact of the gold nanowire characteristics on the sensor's performance, the diameters of gold nanowires  $d_3$  were measured at 400, 500, 600, 700 and 800 nm, respectively.

A several more temperature sensors are included in Table 2.1

**Table 2.1** Performance parameters of some PCF-based temperature sensors.

Ref.	Sensor Structure	Temperature Sensitivity( $\text{nm}/^\circ\text{C}$ )	Sensing Range
[66]	Hexagonal PCF	5	$30^\circ\text{C} - 60^\circ\text{C}$
[67]	Side Throw PCF	-4.09	$20^\circ\text{C} - 50^\circ\text{C}$
[68]	D-shaped PCF	6.1	$0^\circ\text{C} - 60^\circ\text{C}$
[69]	Ultracompact	2.82	$0^\circ\text{C} - 100^\circ\text{C}$
[70]	Sag-nac interferometer	1.65	$25^\circ\text{C} - 33^\circ\text{C}$
[71]	LPG	1.356	$20^\circ\text{C} - 50^\circ\text{C}$
[72]	Polarization-maintaining PCF(PM-PCF)	2.58	$25^\circ\text{C} - 42^\circ\text{C}$

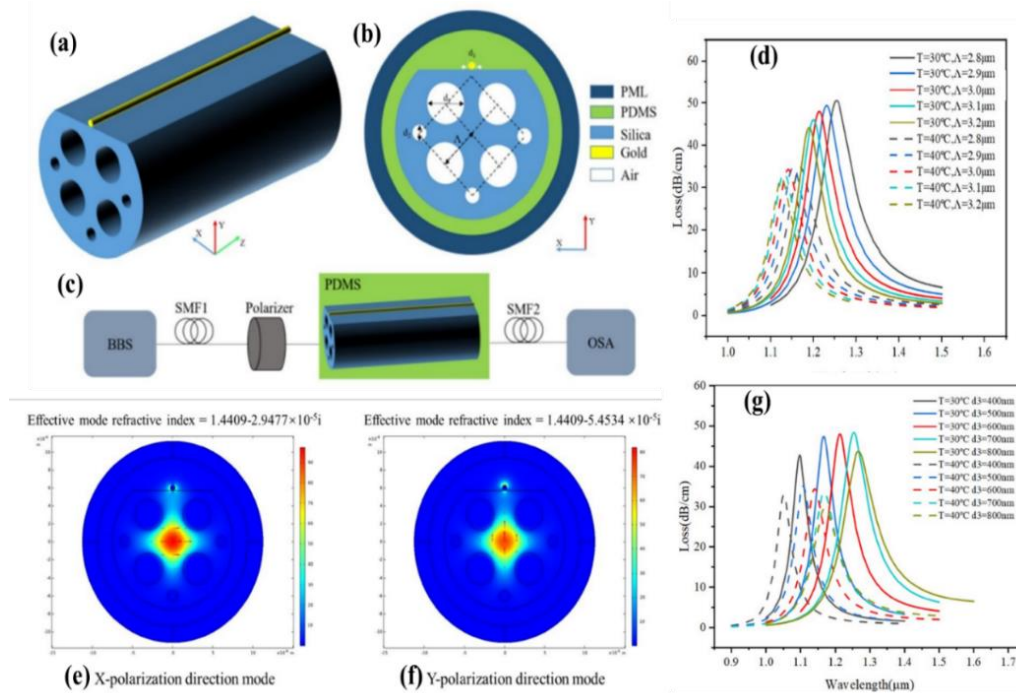


**Figure 2.4 (a) 3-D view of PCF (b) Cross-sectional view of PCF (c) Experimental set-up of PCF (d) The impact of changing air-hole spacing  $\Lambda$  on the loss spectrum (e) Field distribution in x-polarized (f) field distribution in y-polarized (g) The effect of gold nanowire diameter  $d_3$  on the loss spectrum [65]**

## 2.1.2 Refractive Index Sensor

A refractive index sensor based on PCF is an optical sensor that uses unique properties of PCFs to recognize changes in the RI of an infiltrated or surrounding medium. Strong light confinement and improved evanescent field interaction with the material are made possible by the micro structured arrangement of air holes in PCFs. These sensors are particularly sensitive for use in chemical detection, environmental monitoring, and biological sensing since they work based on concepts like surface plasmon resonance (SPR), interferometry, or modal analysis.

A refractive index sensor based on liquid-infiltrated dual-core PCF is studied, in which two fiber cores are separated by an air hole and filled with analyte liquid form independent waveguides. For sensor's performance a numerical analysis is done by using mode coupling theory reveals an immense sensing range. Maximum achieved sensitivity is found to be of  $-65,166.10 \text{ nm/RIU}$  at a wavelength of  $1.25 \text{ }\mu\text{m}$  for a 1cm long PCF. The wavelength shift is observed on the transmission spectra by mode coupling between the cores that uses different RI and it can sense low RI as 1.30 [73]. A single microfluidic analyte channel ( $n_a$ ) is placed between two solid core is shown in Figure 2.5 (a) that contains triangular array of low index air holes of diameter  $d = 3\mu\text{m}$  and the two cores are spaced by two times of pitch  $2\Lambda$ . Hole-to-hole distance is pitch ( $\Lambda$ ) =  $5 \mu\text{m}$  in this study. Using COMSOL Multiphysics software, which is based on FEM, the fundamental modes (x-even, x-odd, y-even and y-odd transmission super modes) is shown in Figure 2.5 (b)-(e). The power transmission of dual core PCF in both polarized modes (x-polarized and y-polarized) is shown in Figure 2.5 (f) when the analyte RI  $n_a = 1.3$  is placed into center hole and nature of transmission spectra is sinusoidal.

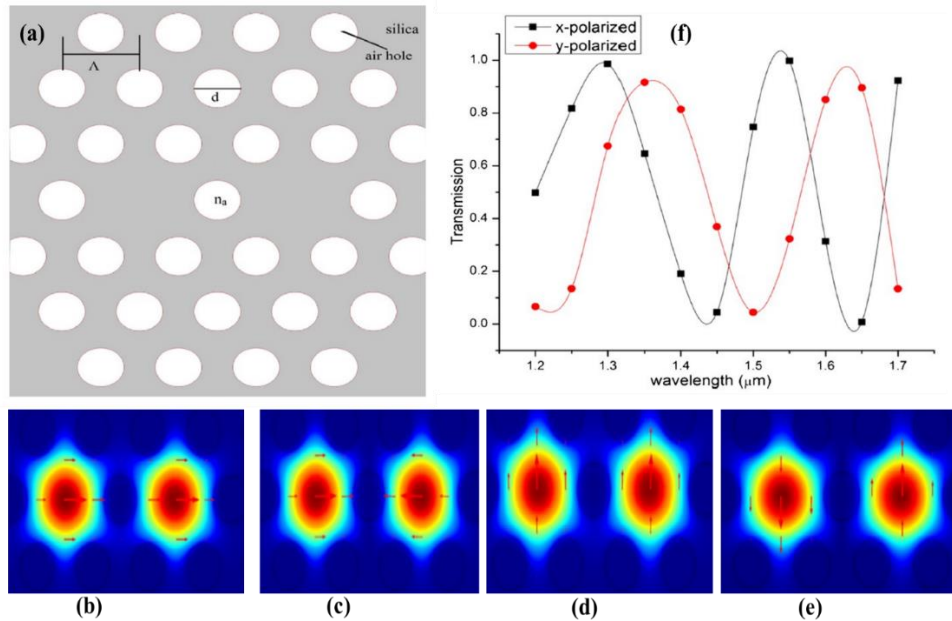


**Figure 2.5** (a) Cross-sectional view of dual-core PCF, Field distribution (b) x-even polarized (c) x-odd polarized (d) y-even polarized (e) y-odd polarized (f) Transmission spectrum [73]

Based on SPR, a plasmonic material-coated circular-shaped PCF fiber (C-PCF) sensor is studied for RI sensing in the range of 1.7-3.7  $\mu\text{m}$ . By selectively infiltrating the liquid, a twin resonance coupling profile is shown by finite element method (FEM) simulations. A magnesium fluoride ( $\text{MgF}_2$ ) coating on fused silica is applied to a nano-ring gold layer in the sensor to improve performance. A transmission dip of -34 dB, a resolution of  $3.70094 \times 10^{-5}$  RIU, a birefringence of  $3.9 \times 10^{-4}$ , and a high sensitivity of 27,958.49 nm/RIU are achieved from analysis. With its superior RI sensing abilities, the C-PCF sensor is a promising option for next-generation biosensing application [74]. A schematic diagram of cross-sectional view of C-PCF is shown in Figure 2.6 (a). For effective loss profile calculation, the simulation uses a circular perfectly matched layer (C-PML) as a boundary condition. The diameter  $d_1 = 1 \mu\text{m}$  for circular one-layer air holes, denoted in white with pitch of  $\Lambda_1 = 3.95 \mu\text{m}$  and positioned inside the gold layer ring. Diameter  $d_2 = 1 \mu\text{m}$  with pitch  $\Lambda_2 = 6.05 \mu\text{m}$  are the holes outside the  $\text{MgF}_2$  layer ring into which analyte is filled. The thickness of  $\text{MgF}_2$  and gold layers are 40 nm and 50 nm, respectively. To solve Maxwell's equations, the FEM splits the sensor into homogeneous triangular or quadrilateral subspaces which is known by mesh analysis is shown in Figure 2.6 (b). Using FEM, the sensor is divided into 578 vertex elements, 27,978 elements, and 4,071 boundary elements. Figure 2.6 (c) shows the transmission spectra of the C-PCF for RI between 1.32-1.38. The nature of power is sinusoidal and vary from 0 to 1. The output spectrum has a delay as the RI rises because the curve gets thicker. From the analysis, the spectrum for RI of 1.38 represents the most lag, whereas the spectrum for RI 1.32 represents most forward. Figure 2.6 (d) represents a schematic representation of experimental set-up of C-PCF based sensor. The polarization controller, single-mode (SM) fiber, optical spectrum analyser (OSA), and optical tuneable source (OTS) are the main part of this configuration. Figure 2.6 (e) represents the transmittance spectra for RI = 1.32-1.38. For RI = 1.38, the maximum transmittance of 34 dB is attained. Compared to the lower RI analyte, which showed a sharp downward peak, the higher RI analyte had a denser curve. Therefore, analytes with higher RIs of 1.38 and 1.37 two different downward peaks, respectively while other showed just ones. Additionally, the analyte with  $n = 1.38$  had the most lag in its transmittance profile, whereas the one with  $n = 1.32$  had the most forward.

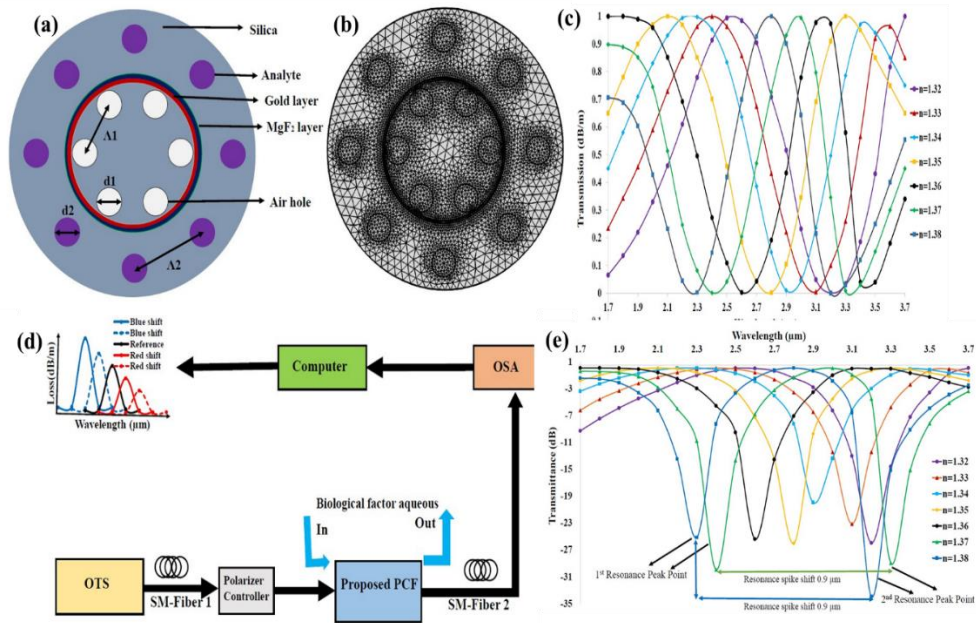
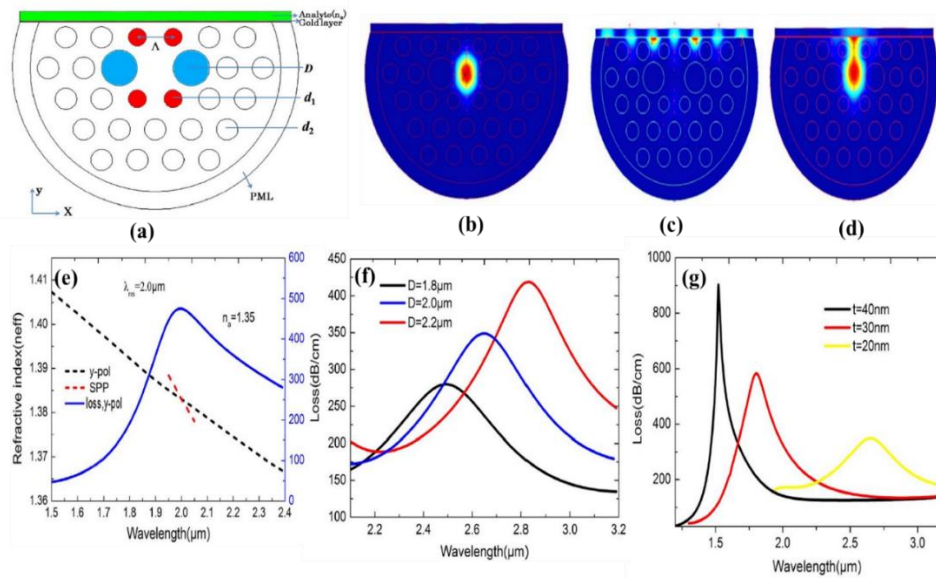


Figure 2.6 (a) Cross-sectional view of C-PCF (b) Meshing of C-PCF (c) Transmission spectrum (d) Experimental set-up (e) Transmittance spectra of C-PCF [74]

A D-shaped PCF refractive index (RI) sensor featuring a wide detection range and exceptionally high sensitivity is investigated. A layer of gold is placed on the polished surface of the design, which makes manufacture simple by avoiding coating within air gaps. The sensor's properties are examined and achieved maximum sensitivity of 31,000 nm/RIU and detection range of 1.32 to 1.40 for refractive index. The structure makes it extremely good for sensing applications by improving sensing performance and allowing for further optimization through the adjustment of structural parameters or the thickness of the gold layer [75]. D-shaped SPR-based sensor is made up of three layers of different size air holes in a triangle lattice is shown in Figure 2.7 (a). By taking advantage of gold's ductility and resistance to oxidation, the top portion of the PCF is polished carefully and gold layer is applied to the polished surface to stimulate surface plasmons. The diameter  $d_1 = 1.0 \mu\text{m}$  of four smaller red air holes placed in vertical direction and  $d_2 = 1.2 \mu\text{m}$  is diameter of other air holes.  $D = 2.0 \mu\text{m}$  is the diameter of the largest air hole next to the fiber core. The green area above the gold layer represents the aqueous analyte. The mode field distribution for y-polarized, SPP, and coupling modes are shown in Figure 2.7 (b)-(d), where colour brightness denotes energy transmission and arrows show field direction. Energy moves from the core mode to the SPP mode when the core mode and SPP mode resonance, maximizing core mode loss. The study focuses on y-polarization loss because the coupling between the SPP and core modes is higher in y-polarization than in x-polarization. The dispersion relation and loss curve as the wavelength changes for analyte's RI is 1.35 is shown in Figure 2.7 (e). The effective RI curves for the SPP mode and core mode in y-polarization denoted by the red dashed line and black dashed line, respectively. The y-polarized core mode loss is shown by the blue solid line. The maximum loss is 474.32 dB/cm at  $2.0 \mu\text{m}$ . The core and SPP modes effective refractive curves intersect at the resonant wavelength at  $3 \mu\text{m}$ . The loss spectrum for 1.8, 2.0 and  $2.2 \mu\text{m}$  air hole sizes is shown in Figure 2.7 (f). At 280 dB/cm ( $2.49 \mu\text{m}$ ), 349 dB/cm ( $2.65 \mu\text{m}$ ), and 419 dB/cm ( $2.83 \mu\text{m}$ ), respectively, the loss rises as the diameter increases, indicating a red shift in resonance wavelength. This is explained by the air hole gap shrinking, which improves light confinement in the y-polarization and makes coupling with the SPP mode easier. The value of loss is strongly influenced by the thickness of the gold layer as shown in Figure 2.7 (g). At  $2.65 \mu\text{m}$

for 20 nm, loss rises to 349 dB/cm, 582 dB/cm at 1.8  $\mu\text{m}$  for 30 nm, and 902 dB/cm at 1.52  $\mu\text{m}$  for 40 nm. Loss peaks blue shift as thickness increases, but exact phase matching adjustments are made possible by a reduction in the space between peaks.



**Figure 2.7** (a) Cross-section view of D-shaped PCF (b) Field distribution y-polarized core mode (c) SPP mode (d) Coupling mode (e) Loss curve and dispersion curve versus wavelength (f) Loss change with different diameters of air holes for  $n_a=1.38$  (g) Loss variation at different thickness of gold layer [75]

To detect low refractive indices, a dual-core PCF-based SPR sensor that is extremely sensitive. For avoid of oxidation, a protective coating of titanium dioxide ( $\text{TiO}_2$ ) is applied on silver which plasmonic material. By outperforming previously published PCF-SPR sensors, the sensor achieves remarkable wavelength and amplitude sensitivities of 116,000 nm/RIU and 2452 RIU<sup>-1</sup>, with resolutions of  $8.62 \times 10^{-7}$  and  $5.55 \times 10^{-6}$  RIU, respectively. For range of 1.29-1.39, this sensor has strong Figure of merit (FOM) 2320 makes it ideal for organic chemical, biosensing, and pharmaceutical applications [76]. Figure 2.8 (a) represents two layers of air holes make up the square lattice structure of the sensor is studied. To improve the interaction between the surface plasmon polaritons (SPP) and core-guided modes, two air holes ( $d_2$ ) from the top of the first ring are shrunk. To make dual-core PCF, two air holes from the centre of first ring are also removed. The optimized parameters of the PCF are  $d_1 = 1.8 \mu\text{m}$ ,  $d_2 = 1.0 \mu\text{m}$ ,  $d_3 = 1.65 \mu\text{m}$ , pitch  $\Lambda = 3.3 \mu\text{m}$ , and thickness of the silver and  $\text{TiO}_2$  are 65nm, 10nm and opening of the microchannel is 1.75  $\mu\text{m}$ , respectively. Figure 2.8 (b) explains the method for formation of sensor. The fiber is formed by first stacking all of the capillaries and solid rods together, then drawing at a predetermined pace, a process known as the stack and drawn method [77]. The employment of solid rods, thin capillaries, and thick capillaries results in large, tiny, and no air holes, correspondingly [78]. Polishing is done after the completion of fiber manufacture [79]. Through a polishing procedure, the second ring's huge thin-walled capillary and a portion of the fiber will be polished, while the remaining capillary forms the microchannel. This is followed by the use of the chemical deposition technique [80] and to cover the fiber's polished surface with silver and  $\text{TiO}_2$ . The field distribution for the plasmonic and core-guided modes at RI of 1.36 is shown in Figure 2.8 (c)-(d). In plasmonic mode, the optical field is focused on the metal-coated sensing layer, whereas in the core guided mode, it stays contained within the core. Figure 2.8 (e) represents the field distribution at the resonance point. Figure 2.8 (f)-(g) analyse the effect of thickness of  $\text{TiO}_2$  and silver on loss spectra. There is blue shift with less propagation loss when the thickness of silver changes from 55 nm to 75

nm and a red shift with higher propagation loss occur as the thickness of TiO<sub>2</sub> layers changes from 5 nm to 15 nm due to changes in the phase matching condition caused by changes in effective RI of fundamental and SPP modes. The amplitude sensitivity of the sensor for the variation of analyte RI ranging from 1.34 to 1.39 is shown in Figure 2.8 (h).

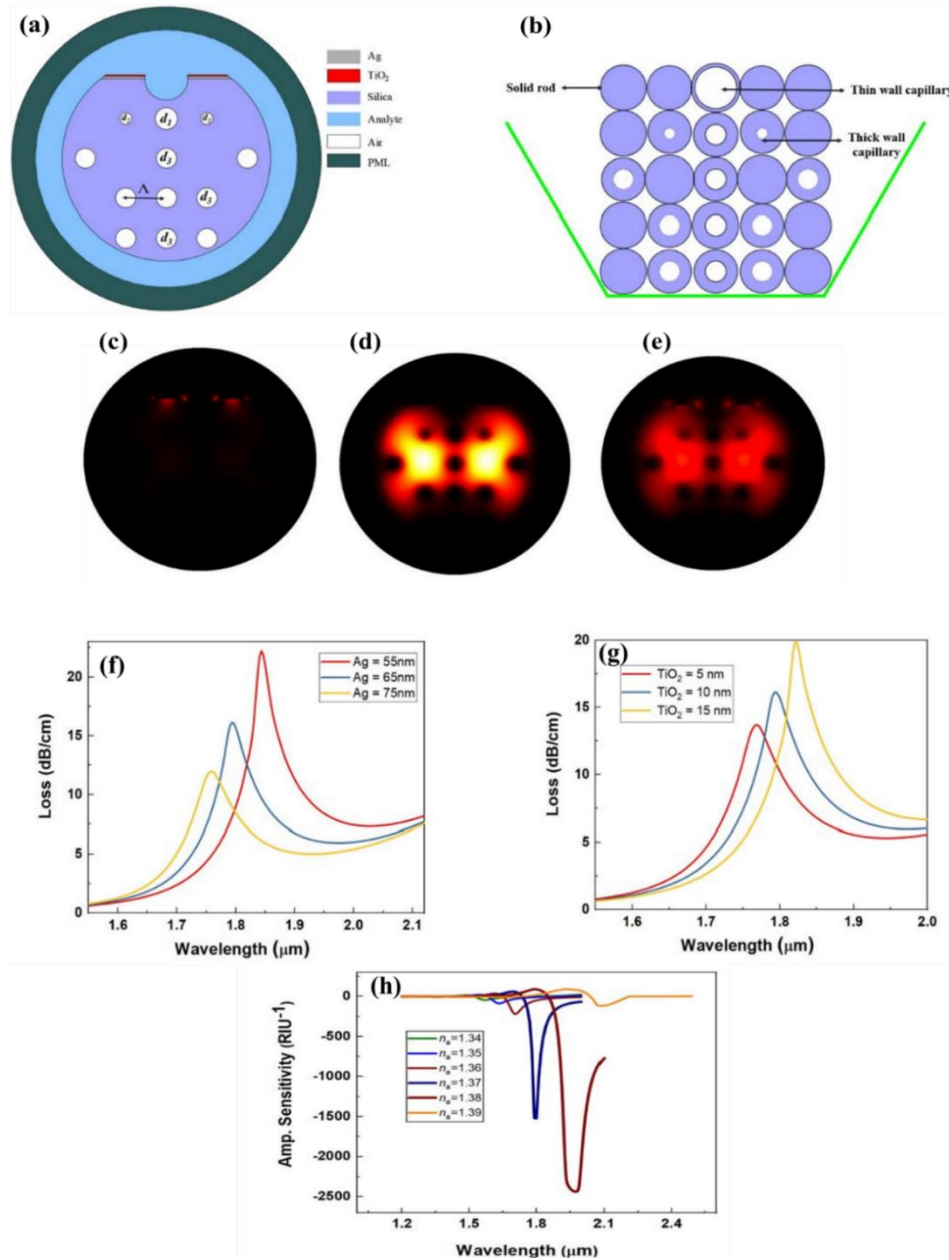


**Figure 2.8** (a) Schematic illustration of the PCF sensor, (b) stacked preform of the fiber, (c) field distribution of the core mode for  $n_a = 1.36$ , (d) SPP mode, (e) resonance condition, (f) loss curves for varying Ag layer thickness, (g) loss curve variations with TiO<sub>2</sub> thickness, (h) amplitude sensitivity [76]

The design, analysis, and fabrication of a highly sensitive D-shaped plasmonic PCF sensor for RI sensing have been studied. The sensor functions by linking the surface plasmon mode with the core-guided mode at the metallic-dielectric interface, where the resonance frequency vary between 1.33 to 1.354 in relation to the analyte RI. The final design is manufactured using the stack-and-draw approach after the sensor's geometrical characteristics are optimized to increase sensitivity using the FEM method. With a resolution of  $3.4 \times 10^{-4}$  RIU, the manufactured sensor has a high sensitivity of 294.11 nm/RIU. This sensor is a helpful in

biological sensing applications, especially for glucose concentration detection, as glucose levels impact the analyte's RI within the tested range [81]. The 3-D schematic representation of the biosensor is shown in Figure 2.9 (a). Based on a silica background material, the proposed PCF has an air hole diameter of  $d = 2.4 \mu\text{m}$  and a triangular lattice with pitch  $\Lambda = 2.8 \mu\text{m}$ . A horizontal etch is performed at a distance of  $2.9 \mu\text{m}$  from the core region to create the D-shaped surface. A solid silica rod is placed at the centre to form the core region shown in Figure 2.9 (b), which shows the stacked view of the biosensor. Figure 2.9 (c) represents the confinement loss of the quasi-TM core-guided mode and the wavelength dependency of the real part of the effective indices for both SP and quasi-TM core-guided modes. Under certain conditions, the study is carried out  $\Lambda = 2.8 \mu\text{m}$ ,  $d = 2.4 \mu\text{m}$ ,  $t = 40 \text{ nm}$ ,  $n_a = 1.33$ . The core-guided mode exhibits high confinement at  $\lambda = 1000 \text{ nm}$  because of the large difference in effective indices, which inhibits coupling. At the resonance wavelength  $\lambda = 1163 \text{ nm}$ , however, the effective indices of both modes equalise, leading to diminished confinement of the quasi-TM core-guided mode and facilitating maximum power transfer from the core mode to the SPP mode.

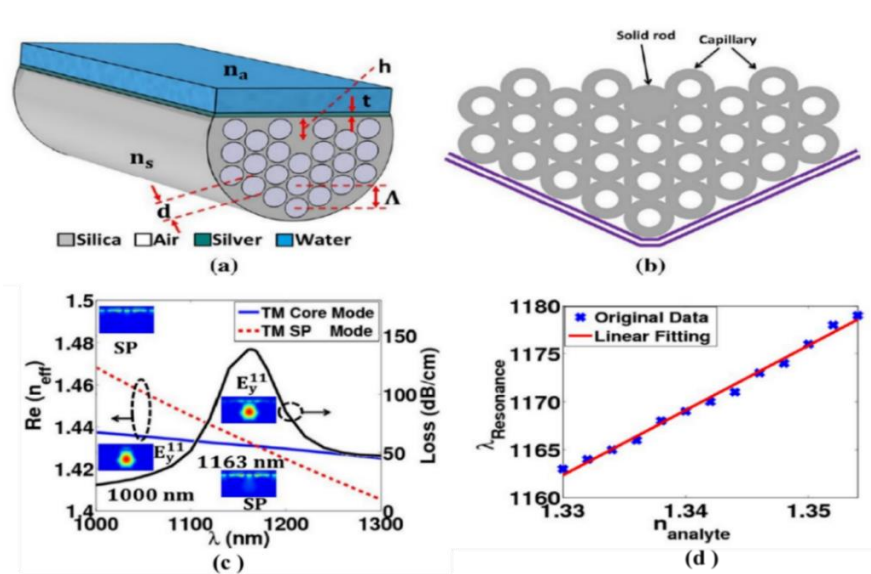


Figure 2.9 (a) 3-D view of D-shape biosensor (b) Cross-section of the PCF's stacked preform (c) Confinement loss curve (d) Linear fitting for the resonance wavelength dependency on the sample RI [81]

The suggested sensor's linearity across the RI range being studied is ensured by studying the resonance wavelength change with the analyte RI. With a step of 0.002, the linearity analysis is carried out within the RI range of 1.33 to 1.354. Figure 2.9 (d) represents that the proposed design has a high degree of linearity across the intended range, with a R-squared value of 0.98508. Table 2.2 includes some additional PCF-based RI sensor.

Table 2.2 Performance analysis of previously reported RI sensor

Ref.	Structures	Range of RI detection	Sensitivity (nm/RIU)
[82]	D-shaped PCF with solid core	1.33–1.38	7300
[83]	Two rings based hexagonal PCF	1.33–1.37	4000
[84]	D-shape PCF	1.35–1.41	8129
[85]	D-shaped PCF based on SPR	1.33–1.37	5200
[86]	Silver-graphene coated surface	1.46–1.49	3000
[87]	Spiral PCF	1.33–13.8	4600
[88]	Hollow-core silver coated PCF	1.33–1.37	4200

### 2.1.3 PCF-Based Biosensors

A biosensor is a diagnostic device that detects certain biological molecules (such as proteins, DNA, viruses, and blood component) by combination of transducer with a biological sensing element. Food safety, biotechnology, environmental monitoring, and medical diagnostics all make extensive use of biosensors. PCF-based biosensors have drawn a lot of interest among biosensing technologies because of their high sensitivity, small size, and ability to function under challenging conditions.

For identify blood components such as RBCs, WBCs, HB, plasma and water, a highly sensitive PCF-based sensor has been designed and studied. Numerical simulations using COMSOL Multiphysics proved the performance of sensor is outstanding with relative sensitivities of up to 99.89 % at wavelength 7  $\mu\text{m}$ . The sensor has a two-layer cladding structure with octagonal and circular air holes and an octagonal core, which confirms favourable propagation properties including controlled beam divergence and reduced confinement loss. Due to its sophisticated design, it may be used for optical communications as well as medical diagnostics, making it a viable tool for the biomedical and telecommunication industries [89]. A core, cladding, and perfectly matched layer (PML) include the cross-section view of blood component sensor with total diameter of 40.8  $\mu\text{m}$  is shown in Figure 2.10 (a). Two rings of air holes make up the cladding and an octagonal core hole surrounded by circular holes in the second ring and octagonal holes in the first ring. The core length  $l = 7.55 \mu\text{m}$  detects several blood components. The second ring has circular air holes with a diameter  $d = 7.6 \mu\text{m}$ . The mode distribution profile of different blood component within the fiber core at an operating wavelength of 7 $\mu\text{m}$  is shown Figure 2.10 (b)-(f). Relative sensitivity measures the interaction between optical light and detecting analytes, such as water, plasma, HB, WBCs, and RBCs shown in Figure 2.10 (g). Relative sensitivity rises in the lower wavelength range at first, but then falls as the wavelength rises. Confinement loss is the term used to explain the tendency of light signals to leakage from the fiber's core with respect to wavelength which is shown in Figure 2.10 (h). Confinement losses rise as the wavelength increases.

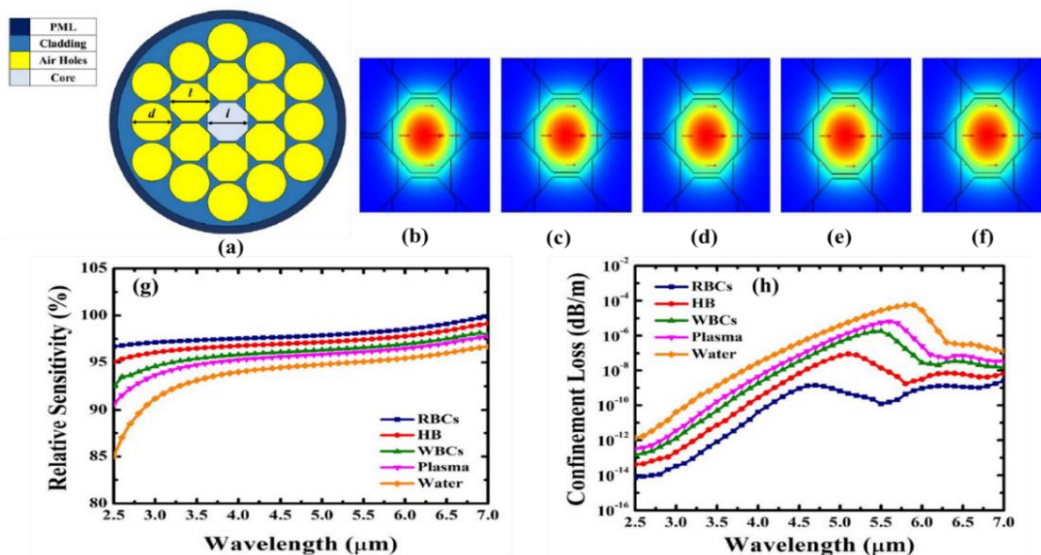
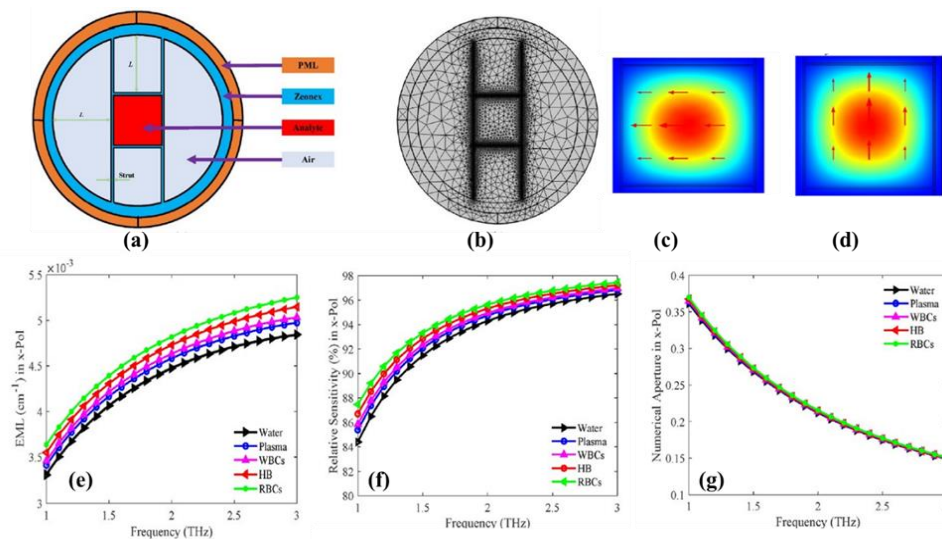


Figure 2.10 (a) Cross-section view of blood component sensor (b) Mode profile of RBCs (c) HB (d) WBCs (e) plasma (f) water at operating wavelength 7 $\mu\text{m}$  (g) Relative sensitivity versus wavelength (h) Confinement loss of different blood component [89]

The THz regime is used to detect blood components using a mono-rectangle based PCF biosensor that is built and analysed using FEM. Relative sensitivity of HB, WBCs, RBCs, water, and plasma at 2.2 THz exceeds 95 % which indicate the excellent sensitivity. Moreover, it shows little confinement loss ( $10^{-12} \text{ cm}^{-1}$ ) and low effective material loss ( $\sim 0.005 \text{ cm}^{-1}$ ). Fabrication possibility is confirmed by the biosensor's square-shaped core and circularly organised air cladding. This sensor is a viable choice for blood component detection since it provides high sensitivity with little losses in the operating range of 1-3 THz [90]. A square core ( $500 \mu\text{m} \times 500 \mu\text{m}$ ) and a suspended circular cladding with four air pieces make up the PCF structure shown in Figure 2.11 (a). To reduce light confinement in the fiber material, the cladding circle is  $L = 582.5 \mu\text{m}$  from the center of the core's square arm. The ideal size of strut is  $7.5 \mu\text{m}$ . The total radius of fiber is  $1050 \mu\text{m}$  which includes a PML of  $105 \mu\text{m}$ . Figure 2.11 (b) represents meshing analysis of PCF that contains 992 boundary element, 8344 domain elements. Figure 2.11 (c)-(d) represents the mode field distribution in x-polarized and y-polarized respectively at 2.2 THz for RBC. Effective material loss (EML) and confinement loss (CL) are the most common types of losses that any may experience when propagating in THz region. These loss characteristics have been measured. The EML measurement is shown in Figure 2.11 (e). The observed EML values for x-polarization for water, plasma, WBC, HB, and RBC blood component at 2.2 THz frequency are  $0.0046 \text{ cm}^{-1}$ ,  $0.0047 \text{ cm}^{-1}$ ,  $0.0049 \text{ cm}^{-1}$ ,  $0.0048 \text{ cm}^{-1}$ , and  $0.005 \text{ cm}^{-1}$ , respectively. The sensitivity of the sensor, which is its most critical design characteristics are carefully selected to provide a greater level of sensitivity performances. In the x-polarization direction, the sensitivity for water, plasma, WBC, HB, and RBC is around 94.97 %, 95.37 %, 95.87 %, 95.54 % and 96.17 % respectively at 2.2 THz regime as shown in Figure 2.11 (f). Figure 2.11 (g) represents the numerical aperture (NA) varied for the three struts of  $6.5 \mu\text{m}$ ,  $7.5 \mu\text{m}$  and  $10 \mu\text{m}$ . The different application areas determine the NA values. Based on analysis, the  $6.5 \mu\text{m}$  strut has a higher NA of 0.1963 in x-polarization. The x-polarization values for  $7.5 \mu\text{m}$  and  $10 \mu\text{m}$  struts are 0.1954, 0.1934, respectively.



**Figure 2.11 (a) Cross-section view of biosensor (b) coarse mesh of the biosensor (c) field distribution x-polarized RBC (d)y-polarized RBC (e) Effective material loss curve (f) Relative sensitivity curve (g) Numerical Aperture curve [90]**

PCF-based circular plasmonic biosensor studied in this work is proposed to detect different blood components in the visible and near-infrared range. The sensor exhibits excellent performance with a Figure of merit (FOM) of 325 in the  $HE_{y11}$  mode and a maximum amplitude sensitivity of  $5078.99 \text{ RIU}^{-1}$  using Al-doped ZnO as the plasmonic material and finite element

analysis. Furthermore, the design exhibits encouraging results in terms of optimising sensor length and resolution. The study includes discussion of the stack-and-draw method's fabrication feasibility and tolerance analysis, which shows great promise for developing medical biosensing [91]. To improve coupling between the core (fundamental) mode and the SPP mode, a sensor is designed whose cross-sectional view is shown in Figure 2.12 (a). Structure of PCF includes two different sizes ( $d_1$  and  $d_2$ ) air holes. The circular lattice is firmly empty of certain holes to balance the movement of the evanescent field. Between neighbouring holes, the pitch is  $P_1 = 2 \mu\text{m}$  and  $P_2 = 1.02 \mu\text{m}$ . The thickness of sensing channel ring  $t_s = 2 \mu\text{m}$  and width of plasmonic ring is  $W_{\text{AZO}} = 30 \text{ nm}$ . The electromagnetic field profiles of core mode and SPP mode for x-polarized and y-polarized is shown in Figure 2.12 (b)-(e). From Figure 3.4 (f) loss peak for higher RI analytes such as HB and WBC are shifting towards longer wavelengths. This is because the corresponding RI of the SPP mode also varies for higher RI analytes, which leads to the shifting of phase-matching points. Amplitude sensitivity (AS) of this sensor is shown in Figure 2.12 (g), where AS is also shifting to longer wavelengths and maximum AS is seen for HB-RBC. The CL and AS for the different blood components in  $HE_y^{11}$  are shown in Figure 2.12 (h)-(i). It is evident that compared to  $HE_x^{11}$ , the distances between neighbouring CL curves are greater.

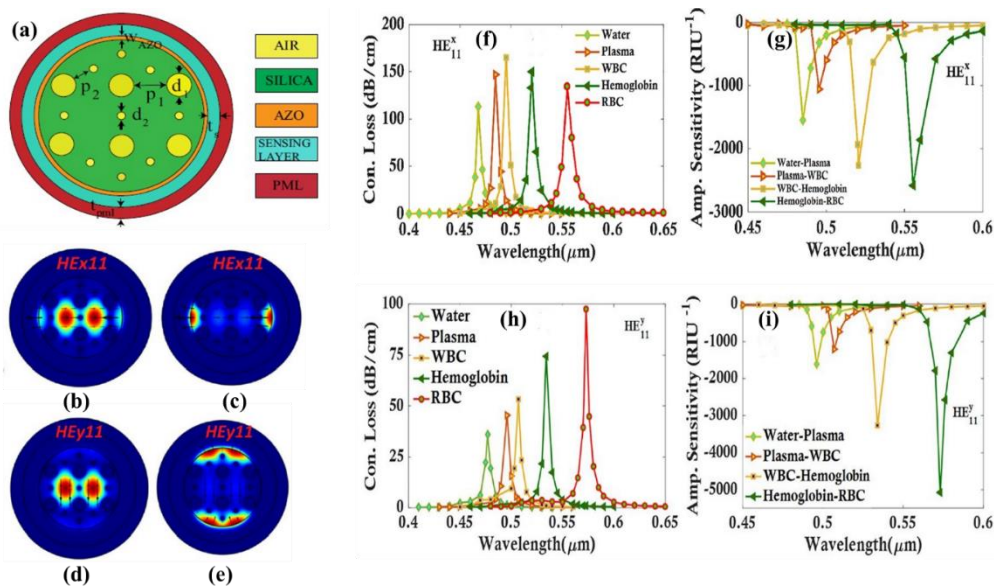


**Figure 2.12 (a) Cross-sectional view of sensor (b), (c) field distribution of fundamental mode and SPP mode for x-polarized (d) field distribution of fundamental mode (e) SPP mode for y-polarized (f) Confinement loss for x-pol (g) Amplitude sensitivity for x-pol (g) Loss for y-pol (h) Amplitude sensitivity for y-pol [91]**

To detect several blood components, including RBCs, HB, WBCs, plasma and water, this study offers a plasmonic biosensor based on PCF. Based on SPR theory, the sensor is simulated and measured using FEM. It has a titanium oxide layer for enhanced adhesion and a gold layer for plasmonic response. A very sensitive loss peak is produced when the sensor detects changes in the RI of blood components. It has an amplitude sensitivity of  $-574.3 \text{ RIU}^{-1}$ , a detection limit of 0.02, and a maximum wavelength sensitivity of  $12,400 \text{ nm/RIU}$ . The RI resolution ranges from  $8.06 \times 10^{-6}$  to  $5.0 \times 10^{-5} \text{ RIU}$ . These results suggest that they have a great arrangement of possible for application in medical diagnostics [92]. Figure 2.13 (a) shows a cross-sectional view of the PCF-based plasmonic biosensor coated with titanium dioxide and gold for the detection of different blood component. The two rings of circular air holes arranged in a

hexagonal arrangement with triangular lattice constant  $\Lambda=1.7 \mu\text{m}$  make up the cladding region. There are six tiny air holes with diameter  $d_0 = 0.2 \mu\text{m}$  in the first ring. Ten large air holes with diameter  $d= 1.36 \mu\text{m}$  and two microscopic ones with a diameter of  $d_c$  are located vertically in the second ring. The round surface of the PCF is covered with an exterior layer of titanium dioxide and gold, which have thickness of  $t_1=35 \text{ nm}$  and  $t_g=25 \text{ nm}$ , respectively. Figure 2.13 (b)-(c) represents the electric field strength during mode coupling. In core-mode propagation, the field is stronger in the core, whereas in SPP-mode propagation, it is stronger in the plasmonic area. This is because SPP-mode concentrates energy in the PCF plasmonic area, whereas core-mode confines most of the energy in the core. The distribution of the normalised electric field along the radial x-direction of the proposed PCF's cross-section is shown in Figure 2.13 (d). The PCF's cross-section's radial x-direction shows a gradual decrease in the electric field, which is strongest in the middle of the PCF core. The core mode CL and effective refractive index (ERI) of the core and SPP modes at different wavelengths for different blood components, such as RBCs, HB, WBCs, plasma, and water are shown in Figure 2.13 (e). Every component shows a unique loss peak at a particular resonance frequency when the core and SPP modes ERIs line up. Differences in the ERI for each blood component reason for the variance in peak loss values between the samples. Table 2.3 include some other PCF based RI sensor for detection of blood component.

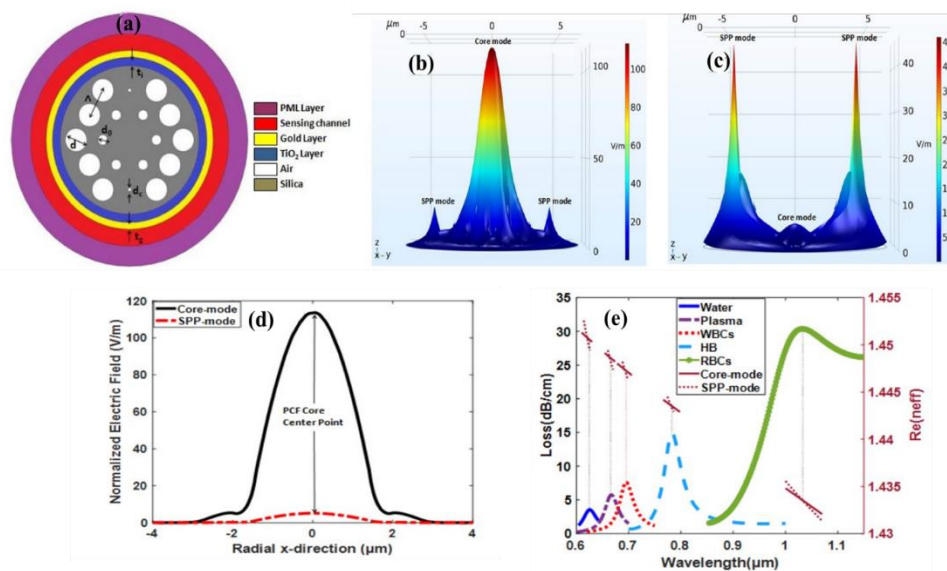


**Figure 2.13** Cross-sectional view of PCF (b) Electric field strength for core-mode (c) Electric field strength for SPP mode (d) At wavelength of 1032 nm for RBC samples normalised electric field along the radial x-direction (e) Variation of core-mode confinement loss and ERI of core and SPP mode [92]

**Table 2.3** Performance characteristics of different PCF based RI sensor for detection of blood component

Ref.	Structure	Relative sensitivity %				
		RBCs	HB	WBCs	Plasma	Water
[93]	Circular hollow ring	56.05	66.47	53.72	54.04	55.09
[94]	Benzene shaped core	--	--	--	77.84	--
[95]	Porous core	80.93	80.56	80.13	79.91	79.39
[96]	Rectangular hollow core	93.50	92.41	92.25	90.48	89.14
[97]	Circular hollow ring	55.83	58.05	62.72	65.05	66.47
[98]	Ring resonator	56.05	66.47	53.72	54.05	55.09

A highly sensitive and reasonably priced PCF sensor is designed to detect malaria by monitoring variations in RBCs RI across the sequence of the parasite's life cycle. With maximum sensitivity of 11,428.57, 9473.68 and 9655.17 nm/RIU, respectively. The sensor indicates spectral variations in transmission corresponding to the ring, trophozoite and schizont phase of malaria infection. It has a single elliptical channel that is filled with RBC samples. Due to simple design makes it a practical instrument for early malaria diagnosis because of number of benefits including mobility, environmental compatibility and simplicity of detection [99]. Circular air holes arranged hexagonally encircle the core elliptical channel PCF biosensor for detection of malaria infection using COMSOL Multiphysics software characterized by semi-major and semi-minor axes ( $a$  and  $b$ ) is shown in Figure 2.14 (a). These air holes, which represent the pitch of the biosensor, are placed at a distance  $P=2 \mu\text{m}$  with diameter  $d_a = 1.4 \mu\text{m}$ . The structure is covered with thick perfectly matched layer (PML) of  $1.3 \mu\text{m}$ . Total diameter of biosensor is  $8.8 \mu\text{m}$  including the PML. Figure 2.14 (b) represents the meshing arrangement for the sensor includes 8,944 boundary elements and 10,894 domain elements make up the whole mesh system. The final geometry of the biosensor has 132 borders, 33 domains, and 132 vertices. Figure 2.14 (c) shows the transmission spectra of different stage of malaria having different RI, due to this shift is observed based on the concept of mode coupling theory. Because of center horizontal elliptical channel present on which samples of RBC is placed and forms two fiber core. x-even, y-even, x-odd, and y-odd are the four even and odd super modes that result from mode pairing between the two cores. Figure 2.14 (d)-(g) represents how the electric fields are oriented towards these four super modes. The biosensor's coupling length as a function of operating wavelength is shown in Figure 2.14 (h).

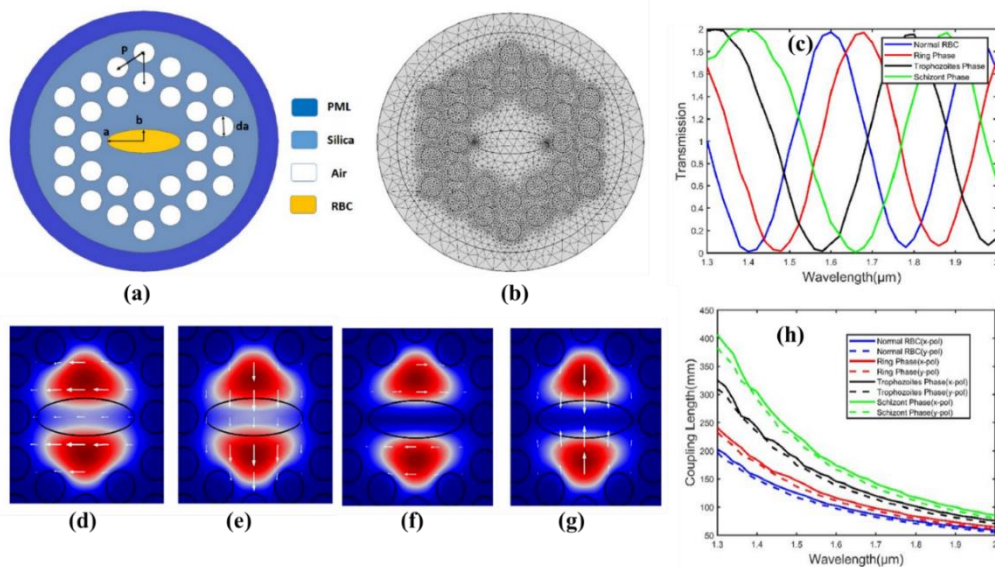


**Figure 2.14 (a) Cross-sectional view of the biosensor (b) Meshing arrangement of the biosensor (c) Transmission spectrum versus wavelength (d) Electric field distribution of x-even (e) y-even (f) x-odd (g) y-odd super modes of malaria biosensor at  $\lambda=1.30 \mu\text{m}$  for normal RBC (h) Coupling length between normal and infected RBCs during cells during different stage of the parasite [99]**

For x-polarization, the maximum coupling lengths were measured as 203.125 mm for healthy red blood cells (RBCs), while for the parasite-infected stages, the values increased to 240.740 mm, 325.000 mm, and 406.250 mm during the ring, trophozoite, and schizont phases, respectively. In the case of y-polarization, the coupling lengths were found to be 196.969 mm for normal RBCs and rose to 232.142 mm, 309.523 mm, and 383.352 mm for the ring,

trophozoite, and schizont stages, respectively. Additionally, it was observed that increasing the wavelength resulted in a reduction of the coupling length.

A SPR biosensor based on PCF is studied. It measures changes in RBCs to diagnose malaria early. SPR is made possible by the hexagonal arrangement of air hole PCF and gold coating, which link the core and SPP modes. The ring, trophozoite, and schizont phases of malaria can be detected by shifting the SPR resonance wavelength caused by malaria infected RBCs, which have different RI than healthy RBCs. High wavelength sensitivities and a low detection limit (0.029) make the sensor ideal for diagnosing malaria in its early stages. Maximum achieved wavelength sensitivity of this sensor is 13714.29 nm/RIU and 14285.71 nm/RIU for x-polarized and y-polarized respectively for ring phase [100]. Figure 2.15 (a) represents a cross-sectional view of the PCF biosensor for malaria detection. It is made up of two layers of air holes arranged hexagonally with a triangular lattice structure using silica as base material. There are tiny and big air holes in both layers with diameter  $d_0 = 0.2 \Lambda$  and  $d = 0.6 \Lambda$  respectively. The triangular lattice structure's lattice constant is  $\Lambda$ . The PCF's circular surface is covered with an exterior gold coating of thickness  $t_g = 40$  nm. To identify malaria, RBC samples are placed in a biochemical layer of thickness  $t_{RBC} = 1 \mu\text{m}$  that is applied over the gold layer. A circular PML with thickness  $t_{PML} = 1.2 \mu\text{m}$  and scattering boundary conditions has been added to absorb the radiation energy from the PCF's surface. Figure 2.15 (b) represents the experimental set-up of PCF that contain single mode fiber (SMF) that is connected to the sensor through splicing is used to transmit broadband light as part of the measurement setup for malaria detection using the PCF biosensor. RBC samples is controlled by a pump as they pass through a channel over a gold layer within a flow cell. The interaction between RBCs and ligands such as erythrocyte-binding antigen-175 (EBA-175), erythrocyte-binding ligand-1 (EBL-1), and erythrocyte-binding antigen-140 (EBA-140) causes a shift in the resonance wavelength due to changes in the ERI. A computer displays this shift once an OSA detects it. New samples are tested once the sensor has been cleaned with deionised water. Figure 2.15 (c)-(f) represents the simulated PCF biosensor, where the arrow indicates the direction of the electric field distribution and light is limited in the core mode and SPP mode. The x-polarized mode and y-polarized mode's core mode field are shown in Figure 2.15 (c)-(d), respectively. At a resonance wavelength of 932 nm. Figure 2.15 (e)-(f) represents the SPP mode in the x-polarized and y-polarized modes respectively. Resonance wavelengths of 762 nm, 806 nm, 836 nm, and 858 nm are measured at gold thickness of 30 nm, 35 nm, 40 nm, and 45 nm, respectively, with peak core losses of 14.05 dB/cm, 11.33 dB/cm, 8.322 dB/cm, and 5.838 dB/cm shown in Figure 2.15 (g). The resonance wavelength exhibits red shifts as gold thickness rises and blue shifts as gold thickness falls from the optimal value. Plasmon damping causes a broadening of the loss peak, which might result in inaccurate sensing, if the gold thickness is increased or decreased by an ideal 40 nm thickness. Therefore, for the best analysis, the thickness should be kept modest.

D-shaped PCF sensor based on SPR with a micro-rectangular hole is studied. By increasing interaction between the metal layer and the core-guided mode, the opening facilitates manufacturing and increases sensitivity. To efficiently create surface plasmons, gold is used as the plasmonic material. Compared to previous designs, the sensor outperforms them with a maximum wavelength sensitivity of 67,000 nm/RIU, a resolution of  $1.5 \times 10^{-6}$  RIU, and a Figure of merit of  $279.16 \text{ RIU}^{-1}$ . Furthermore, it is used to identify malaria, exhibiting unique sensitivity to various phases of RBCs [101]. The cross-sectional view of D-shaped PCF construction is shown in Figure 2.16 (a). The top portion with air holes is removed to form the D-shaped structure. The cladding, which has number of air holes, is made of silica as the substrate material. Three different kind of circular air holes with different sizes make up the

structure. The diameter of the greatest air hole  $D=2.4 \mu\text{m}$  next to the fiber core and the diameter of the four smaller air holes  $D_1$  in the vertical direction is  $1.2 \mu\text{m}$ . The diameter of the extra air holes  $D_2$  is  $1.4 \mu\text{m}$  and pitch  $\Lambda=2.2 \mu\text{m}$ . Figure 2.16 (b) shows the PCF sensor's serial manufacturing process. The stack and draw method is used to build the PCF [102]. This process

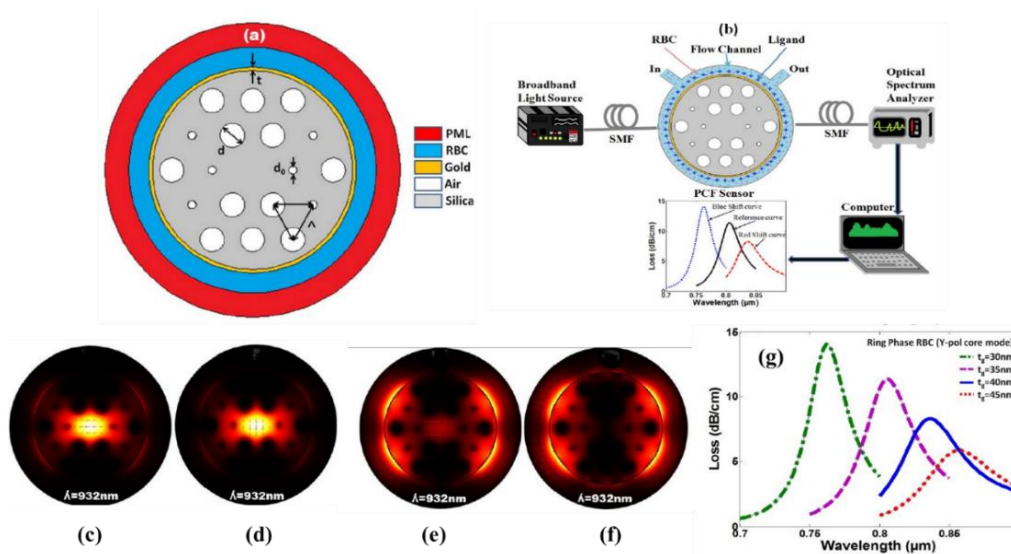


**Figure 2.15 (a) Cross-sectional layout of the PCF biosensor, (b) experimental setup for the PCF-based SPR sensor, (c) x-polarized core mode field distribution, (d) y-polarized core mode field distribution, (e) x-polarized surface plasmon polariton (SPP) mode, (f) y-polarized SPP mode at a 932 nm resonance wavelength for the malaria ring stage, and (g) variation of peak loss in the y-polarized mode with different gold layer thicknesses [100]**

involves piling the solid rods and capillaries, and adding thick and thin capillaries allows to adjust the size of air holes. The fiber's top half is polished to provide a smooth surface once the manufacturing process is finished. A rectangular micro-opening has been grooved into the fiber's smooth surface. Femtosecond laser micromachining or focused ion-beam milling can be used to generate the rectangular micro-opening [103]. A chemical vapour deposition process is used in this small rectangular aperture channel to coat the gold layers shown in Figure 2.16 (c). On a curved surface, the gold layer may also be precisely covered using the atomic layer deposition (ALD) technique [103]. The black and blue lines in Figure 2.16 (d) explains the wavelength-dependent changes in the ERI of the core and SPP modes, respectively. Where a phase matching condition permits maximum energy transfer between the core and SPP modes, these RIs intersect at the resonance wavelength ( $1.38 \mu\text{m}$ ). Propagation loss is shown by red curve, peaks at this resonance because of evanescent field penetration into the analyte and metal layers. Figure 2.16 (e) represents the loss curve for the sensor as the bio analyte RI changes in increments of 0.01 from 1.30 to 1.40. A higher interaction between core-guided and SPP modes is shown by the loss peak increasing from 1.30 to 1.36 with increasing RI values. Table 2.4 include some other PCF based RI sensor for identification of early stage of malaria at different stages. Some other PCF based RI sensor for malaria detection is studied in Table 2.4.

**Table 2.4 Performance characteristics of various PCF-based RI sensors utilized for malaria detection**

Ref.	Methods	Sensitivity %
[104]	Immuno-chromatographic test	97.6
[105]	Automated detection	93

[106]	Flow cytometry	91.26
[107]	Microscopic rapid diagnostic test	84.6
[108]	Quantitative buffy coat examination	96.92

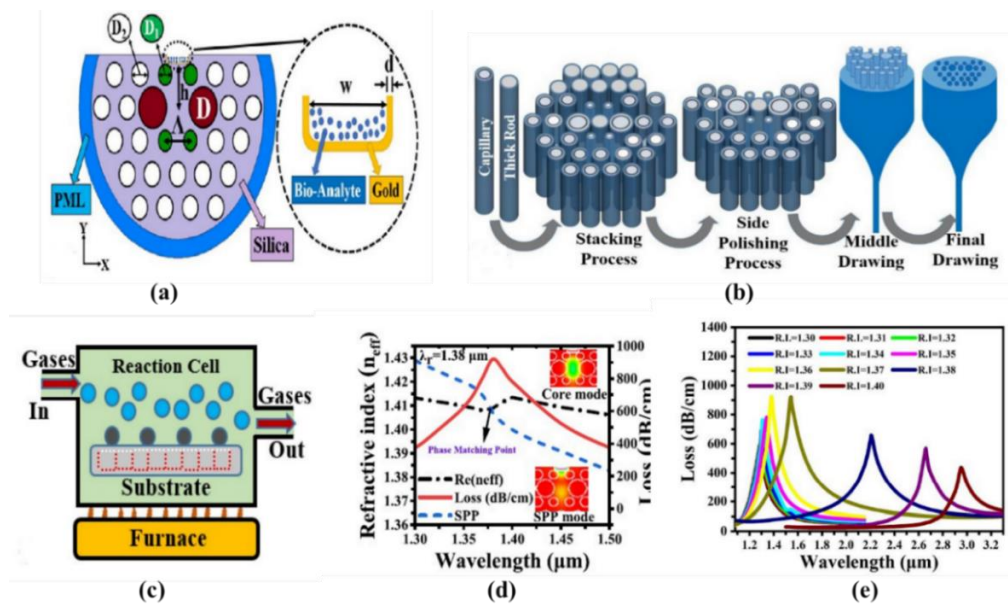


Figure 2.16 (a) Cross-sectional illustration of SPR sensor (b) Stacking and drawing method for fabrication of PCF (c) Chemical vapor technique for vapor coating (d) Loss characteristics curve and dispersion relation between core mode and SPP mode for RI =1.36 [101]

### 2.1.4 PCF based Chemical Sensor

PCF based chemical sensor is an optical sensor that tracks variations in behaviour of light to recognize chemical mixture using PCF. This sensor is having great sensitivity, small size, and ability to endure electromagnetic interference make them important. By changing the fiber's structure or covering it with material that respond with specific analytes, chemical detection is accomplished. Chemicals that meet the fiber's surface or enter its air holes influence light propagation by changing the RI. To determine and analysis the chemicals present, this change is measured.

A chemical sensor with a dual core PCF and hexagonal lattice structure is designed and examined using the FEM method in COMSOL Multiphysics software. Benzene, ethanol, and water are among the several chemicals that are contained within the two cores, which are divided by an air hole. At a wavelength of  $1.55 \mu\text{m}$ , numerical simulations show good optical characteristics with a maximum coupling length of  $0.45 \text{ mm}$ . The sensor achieves maximum wavelength sensitivity of  $9615 \text{ nm/RIU}$  with a fiber length of  $0.5 \text{ cm}$  [109]. The sensor's cross-sectional structure is depicted in Figure 2.17(a), incorporating perfectly matched layer (PML) boundary conditions. COMSOL Multiphysics software is used to analyse the sensor's guiding characteristics. This construction forms two cores in the PCF by removing two air holes. A change of substances, including ethanol, water, and benzene, are present in the central air hole that divides the fiber's two cores. The diameter of air holes and pitch are measured to be  $1.4 \mu\text{m}$  and  $2 \mu\text{m}$ , respectively. Figure 2.17 (b) shows the ERI difference changes for several compounds with respect to wavelength. As light tends to diffuse out of the core, the RI of the

fiber's basic mode with increasing wavelength. Therefore, Birefringence rises with wavelength. Figure 2.17 (c) represents the transmission spectrum curve for the x-polarized mode of the DC-PCF sensor of length 0.5 cm when the center hole is filled with chemicals. The DC-PCFs transmission curve is sinusoidal. By shifting the peaks with changes in the various RI of chemicals, the sensitivity of sensor can be determined. COMSOL Multiphysics software is used to examine the four basic modes of the fiber sensor shown in Figure 2.17 (d)-(g). The distribution of the electric field for each of the four odd and even modes is shown by the arrow diagram inside the core.

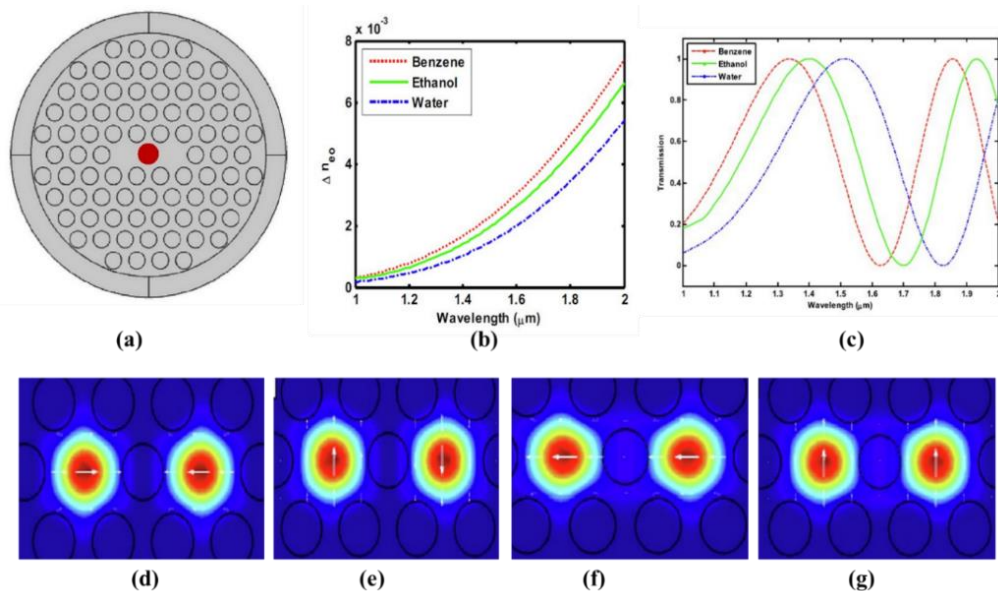


**Figure 2.17 (a) Cross-section view of sensor (b) Birefringence with wavelength (c) Transmission curve versus wavelength (d) Field distribution odd x-polarized (e) odd y-polarized (f) even x-polarized (g) even y-polarized [109]**

A new type of PCF sensor has been designed for the detection of chemical substances at terahertz (THz) frequencies. It includes a hexahedron core and an octagonal cladding. The performance of sensor is measured using relative sensitivity (RS), EML and CL. Air hole diameter and core size are two design parameters that are optimized using FEM simulations. At 1 THz the sensor has low confinement losses and high relative sensitivity of 91.25 % for ethanol, 93.80 % for benzene, and 89.95 % for water are observed. Because of this, it may be used in a variety of settings, such as THz communication systems, industrial quality control and physiological monitoring [110]. Figure 2.18 (a) represents geometrical structure of octagonal PCF including hexahedron core. The optimized parameter of core that contains two layers are core diameter  $d_c = 72 \mu\text{m}$ , two layers of core pitch  $P_c = 75 \mu\text{m}$ , five layers of cladding diameter  $d_1 = 260 \mu\text{m}$  and pitch of five-layer cladding  $P_1 = 350 \mu\text{m}$ . Depending on the changes of  $\pm 2$  percentage maximum value of sensitivity is obtained which shown in Figure 2.18 (b) for either the central air hole or the additive frequency stratification. The full light is clearly flowing across the middle region for the x and y polarized mode shown in Figure 2.18 (c)-(d). Figure 2.18 (e) represents the confinement loss which shows flat response across the frequency range of 2.10 THz to 3 THz. At 1 THz, the CL for chemical such as ethanol, water and benzene are  $7.75 \times 10^{-8}$ ,  $7.80 \times 10^{-8}$  and  $7.85 \times 10^{-8}$  dB/m, respectively.

A new type of porous core-PCF (PC-PCF) with a slotted rectangular core structure and Kagome cladding has been created for extremely sensitive terahertz chemical detection. To achieve high

birefringence, minimum confinement loss, near-zero dispersion, large effective area, high sensitivity and a high numerical aperture, the fiber's design was optimized using a complete FEM approach. The fiber's may be used in terahertz region that need polarization-preserving

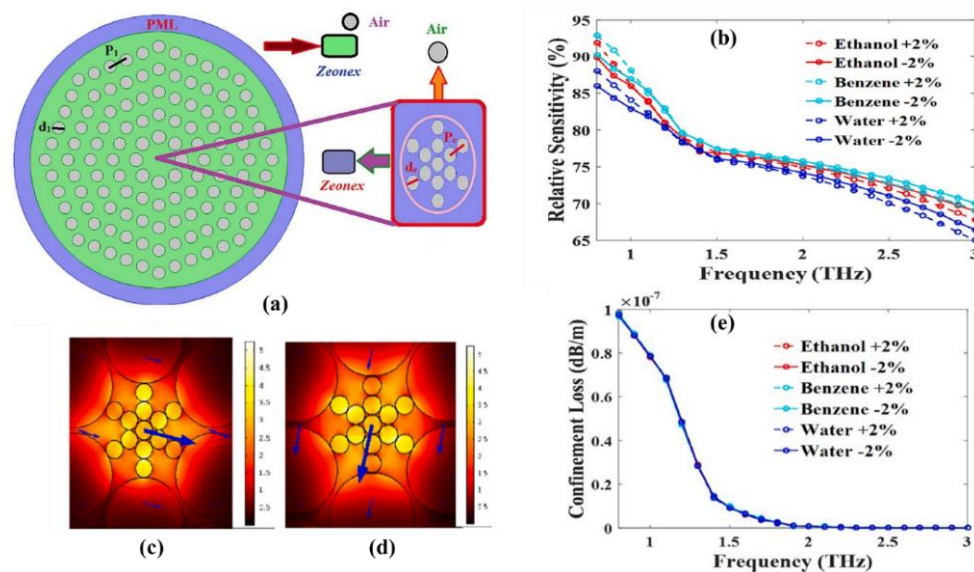


**Figure 2.18 (a) Cross-sectional view of octagonal PCF (b) RS versus frequency for  $\pm 2\%$  variations for x and y polarized (c) x-polarized field circulation (d) y-polarized field circulation (e) CL versus frequency for different chemicals [110]**

transmission and has great potential for commercial use in chemical and biological sensing. From analysis of simulation results maximum achieved sensitivity is 85.6 %, 85.7 % and 85.9 % and low confinement loss of  $4.5 \times 10^{-9} \text{ cm}^{-1}$ ,  $1.7 \times 10^{-9} \text{ cm}^{-1}$ , and  $1.02 \times 10^{-9} \text{ cm}^{-1}$  for water, ethanol, and benzene respectively in THz range [111]. The cross-section of the PCF is illustrated in Figure 2.19 (a).  $D_{core}$  represents the diameter of core,  $P_c$  is called core pitch represents center-to-center distance between two air holes in the core region,  $w$  represents the width of core air hole, and  $L$ ,  $L_1$ ,  $L_2$ ,  $L_3$ , and  $L_4$  denote the lengths of the core air holes, which are  $372 \mu\text{m}$ ,  $332 \mu\text{m}$ ,  $288 \mu\text{m}$ ,  $244 \mu\text{m}$ , and  $198 \mu\text{m}$ , respectively. The optimum value for  $D_{core}$ ,  $P_c$  and  $w$  is  $360 \mu\text{m}$ ,  $38.8 \mu\text{m}$ , and  $32.32 \mu\text{m}$ . In the Kagome region,  $d$  and  $d_1$  are the values of strut width and distance between parallel strut having values of  $195.38 \mu\text{m}$  and  $4 \mu\text{m}$  respectively. Figure 2.19 (b)-(c) explains the interaction of light strength with analyte water for x-polarized mode to explain the modal characteristics. It is evident that the core region is only traversed by the fundamental modes. Figure 2.19 (d) represents the relative sensitivity of the PC-PCF in the x-polarization mode. For numerical study, the length of the slotted holes in the core region remains constant. Sensitivity of this chemical sensor is studied using three different analyte such as water, ethanol and benzene having RI value 1.33, 1.354, 1.366 respectively. Due to higher RI of benzene compared to ethanol and water, it has the highest relative sensitivity. Furthermore, it can be observed that relative sensitivity rises with frequency up to 1.6 THz before beginning to fall. Figure 2.19 (e) represents the birefringence versus frequency. From observation it is found that birefringence is linear. The value of birefringence for water, ethanol and benzene are 0.0065, 0.005, and 0.0043 respectively at optimized design parameter. Figure 2.19 (f) shows how effective area varies as a function of frequency. When frequency increases, light pulses are narrowly noted in the porous core region, representing that the effective area shrinks with frequency. The corresponding effective areas for ethanol, benzene, and water are  $69800 \mu\text{m}^2$ ,  $71100 \mu\text{m}^2$ , and  $69300 \mu\text{m}^2$ , respectively. Some other PCF based chemical sensor is studied in Table 2.5.

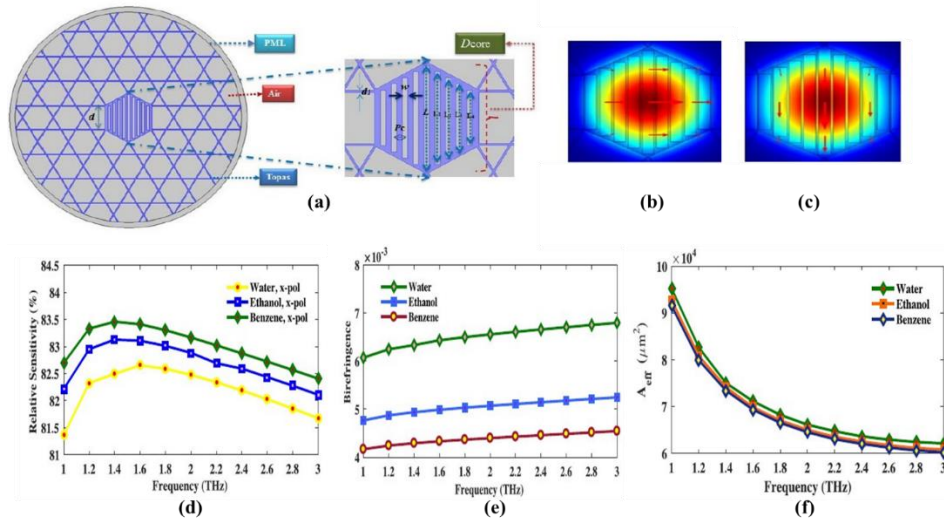


**Figure 2.19** (a) Cross-sectional view of THz PC-PCF sensor with enlarged core (b) Field distribution x-polarized for water (c) Field distribution y-polarized for water (d) Relative sensitivity for x-polarization (e) Birefringence as a function of frequency (f) Effective area as a function of frequency [111]

**Table 2.5** Performance characteristics of some other PCF sensors for chemical detection

Ref.	Structure	Operating region	Relative Sensitivity %
[112]	Hexagonal and octagonal PCF	$\lambda = 1.5 \mu\text{m}$	25.1
[113]	V-shaped PCF	$\lambda = 1.5 \mu\text{m}$	23.75
[114]	Hexagonal PCF	$\lambda = 1.33 \mu\text{m}$	49.17
[115]	Porous cored octagonal PCF	$\lambda = 1.33 \mu\text{m}$	67.66
[116]	Circular PCF	$\lambda = 1.33 \mu\text{m}$	29.25
[117]	Folded cladding PCF	$\lambda = 1.55 \mu\text{m}$	64.19

## 2.2 Summary

This chapter includes a literature review and contains basic information on the PCF sensor, concept of mode coupling theory, SPR concepts, PCF-based RI for physical, biomedical, and chemical sensing applications. There has been extensive discussion of different methods to improve the sensing capabilities of these sensors. Beginning with the fundamentals of PCF optic sensors, explain how a PCF can be used for sensing applications including physical, biomedical, and chemical substances. Section 2.1.1 covers PCF-based temperature sensor and explains how temperature variation affects the PCF's RI. Section 2.1.2 covers PCF-based RI sensor and explains how strong light confinement and improved evanescent field interaction with the material are made possible by the micro structured arrangement of air holes in PCFs. Section 2.1.3 covers PCF-based RI sensor for biomedical application to detect biological molecules such as proteins, DNA, viruses, and blood component and explains optical characteristics such as coupling length, birefringence and transmission spectrum changed with RI of biomolecules. Section 2.1.4 covers PCF-based RI sensor for chemical sensor and explains how chemicals that meet the fiber's surface or enter its air holes influence light propagation by changing the RI.

# CHAPTER 3

## EFFECT OF SELECTIVELY-FILLED-ETHANOL ON DISPERSION CHARACTERISTICS OF CIRCULAR SHAPED HOLLOW CORE PHOTONIC CRYSTAL FIBER

### 3.1 Introduction

In recent years, photonic crystal fibers (PCF) are garnered a lot of attention due to their unusual and remarkable features and properties [118]. PCF also known as Holey fibers or Micro structured fibers, represents one of the major applications of the photonic crystals [119, 120]. PCFs have the capability to control the light that enters the fiber, which was previously unfeasible due to their conventional design issues. By adjusting the number of liquid filled holes, pitch distance and air hole size of the PCF, the structural cross-section may exhibit unique properties such as controlled effective area, low confinement loss, dispersion control and higher nonlinearity [121]. However, some researchers have used the air holes filled PCF to regulate the optical and transmission characteristics of the PCF by filling them with other types of liquids like as water [122], ethanol [123], liquid crystals [124, 125] and polymers [126–128]. By suitably tailoring their optical characteristics, liquid-filled PCFs are employed for various sensing parameters such as temperature, magnetic field, refractive index (RI) and many other applications [129–132]. Using an asymmetric circular Dual Core-PCF, Md. Mahbub Hossain et al. demonstrated a PCF Chloroform infiltration temperature sensor in 2018 [133]. Shi et al. also demonstrated stress and temperature sensors with alcohol filled holes in their experiments [134]. Furthermore, theoretical PCF structures for water-ethanol [135], ethanol, benzyne and water [136] solutions are proposed. The researcher recently presented a liquid-filled PCFs-based tunable multiband pass filter [137].

Thus, the intention of this work is to design a selectively filled ethanol circular shaped hollow-core PCF for the zero-dispersion wavelength. The proposed PCF configuration is designed using the COMSOL software, which uses the full-vector finite element method (FV-FEM). For geometry statistics 38 domains, 152 boundaries, 152 vertices and for mesh statistics 14172 triangular elements, 1224 edge elements, 152 vertex elements are analyzed. This kind of PCF is useful in nonlinear applications, sensing applications, laser technologies and telecommunications.

### 3.2 PCF Design

The proposed circular shaped hollow core PCF geometry is shown in Figure 3.1. In this design, a diameter,  $d$  of  $0.22 \mu\text{m}$  and a pitch length,  $\Lambda$  of  $1.5 \mu\text{m}$  is chosen for circular holes with silica as the PCF background material. The RI of ethanol ( $n_{\text{etha}} = 1.352$ ) and air ( $n_{\text{air}} = 1$ ), are considered. Equation (3.1) gives the RI of silica ( $n_{\text{silica}}$ ) which is called Sellmeier equation.

$$n_{\text{silica}}^2(\lambda) = 1 + \frac{A_1\lambda^2}{\lambda^2 - B_1} + \frac{A_2\lambda^2}{\lambda^2 - B_2} + \frac{A_3\lambda^2}{\lambda^2 - B_3} \quad (3.1)$$

The operational wavelength in  $\mu\text{m}$  is denoted by  $\lambda$  and the Sellmeier coefficients are  $A_1 =$

0.696166300,  $A_2 = 0.407942600$ ,  $A_3 = 0.897479400$ ,  $B_1 = 4.67914826 \times 10^{-3} \mu\text{m}^2$ ,  $B_2 = 1.35120631 \times 10^{-2} \mu\text{m}^2$  and  $B_3 = 97.9340025 \mu\text{m}^2$ , respectively [129].

A Perfectly Matched Layer (PML) boundary condition is applied at the outer boundary to absorb the outgoing electromagnetic waves and prevent artificial reflections during simulation. Additionally, a fine mesh has been employed to ensure numerical accuracy and stability of the FEM-based simulation results.

The PCF effective mode area is an important characteristic that attracts a lot of attention in a vast area of applications. A PCF having a large effective mode area is highly useful in field of lasers and telecommunication devices, whereas a PCF having a small effective area is considered suitable for non-linear effects. The effective area,  $A_{eff}$  of the PCF is determined using the below equation

$$A_{eff} = \frac{(\iint |E|^2 dx dy)^2}{\iint |E|^4 dx dy} \quad (3.2)$$

where 'E' represents the fundamental modes of PCF transverse electric field [138, 139].

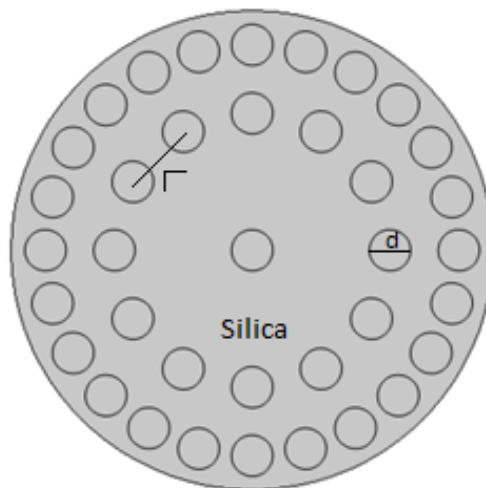


**Figure 3.1 Geometry of proposed Circular shaped hollow core PCF**

The effective area of the fiber is intimately linked to nonlinearity. The nonlinear coefficient can be determined using the below equation

$$\gamma = \left(\frac{2\pi}{\lambda}\right) \left(\frac{n_2}{A_{eff}}\right) \quad (3.3)$$

where  $n_2$  denotes the nonlinear refractive index of PCF,  $\lambda$  denotes the wavelength and  $A_{eff}$  denotes the effective area of PCF. For silica material ( $n_2 = 3.2 \times 10^{-20} \text{ m}^2/\text{W}$ ) is considered [138, 140].

Confinement loss ( $L_c$ ) is the term for the attenuation caused on by the waveguide geometry. This is a new type of loss that occurs in single material fibers especially in PCFs because they are generally made of silica and can be determined using the below equation

$$L_c = -20 \log_{10} \epsilon^{-k \text{Im}[n_{eff}]} = 8.686k \text{Im}[n_{eff}] \quad (3.4)$$

where  $k_0$  represents the propagation constant ( $k = 2\pi/\lambda$ ) in free space and  $Im[n_{eff}]$  denotes the imaginary part of the complex effective index [120].

The dispersion parameter, D of PCF is calculated by using equation (3.5)

$$D = -\frac{\lambda}{c} \frac{d^2 Re[n_{eff}]}{d\lambda^2} \quad (3.5)$$

where  $c$  denotes light velocity in vacuum and  $Re[n_{eff}]$  represents the real part of effective refractive index [121].

### 3.3 Results and Discussion

Figure 3.2 shows the basic mode's electric field profile of PCF with and without ethanol filling the holes. The FV-FEM mode solver is used to compute the effective refractive indices ( $n_{eff}$ ) of the proposed PCF basic guided modes. At transmission wavelength of 1500 nm,  $n_{eff}$  becomes 1.379906281, 1.333575804 and 1.417018929 when air is poured into the entire hole ring, ethanol is poured into the middle hole ring and ethanol is poured into the entire hole ring, respectively. The variation of  $n_{eff}$  with wavelengths is shown in Figure 3.3. According to the figure as wavelength increases, the  $n_{eff}$  of the proposed PCFs decreases.

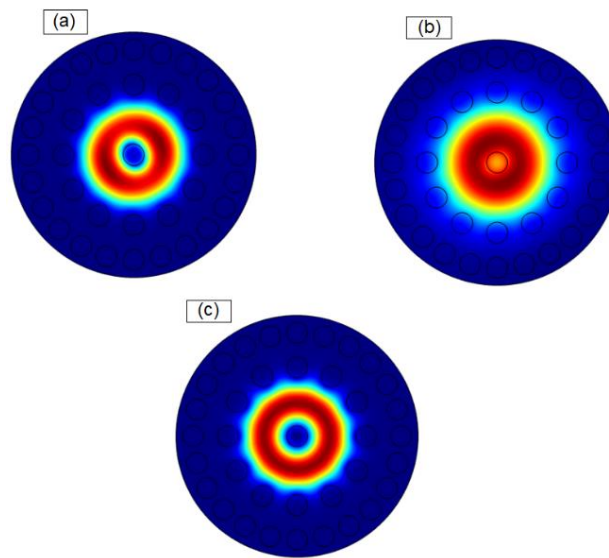


**Figure 3.2** Electric field profile for the basic modes of PCF (a) air is poured into the entire hole ring (b) ethanol is poured into the middle hole ring (c) ethanol is poured into the entire hole ring, at  $\lambda = 1500$  nm

After obtaining the effective refractive indices for various modes of the PCF, the effective area is calculated using equation (3.2). At transmission wavelength of 1500 nm, the effective area of the proposed PCF comes out to be  $4.36 \mu\text{m}^2$ ,  $4.91 \mu\text{m}^2$  and  $6.39 \mu\text{m}^2$  when air is poured into the entire hole ring, ethanol is poured into the middle hole ring and ethanol is poured into the entire hole ring, respectively. The effective mode area variation with wavelengths is shown in Figure 3.4. According to the graph, the  $A_{eff}$  of the proposed PCF increases as the wavelength increases and it can also be shown that pouring ethanol into the hole ring increases the effective mode area compared to pouring air into the hole ring.

The existence of ethanol in the cladding section increases the  $n_{eff}$  of the cladding section of

the PCF because ethanol has a higher refractive index than air. As a result, when compared to air-filled holes, the difference in RI between cladding and core region is smaller. When light passes through the ethanol-filled fiber's core, some of it leaks into the cladding region, increasing the effective area. As a result, the ethanol-filled PCF's effective mode area is larger than the air-filled PCF.

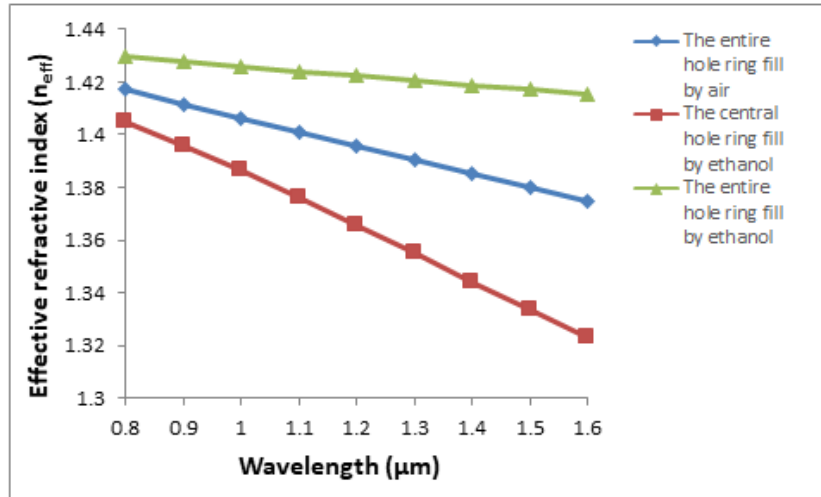


Figure 3.3 Effective refractive index variation with wavelength

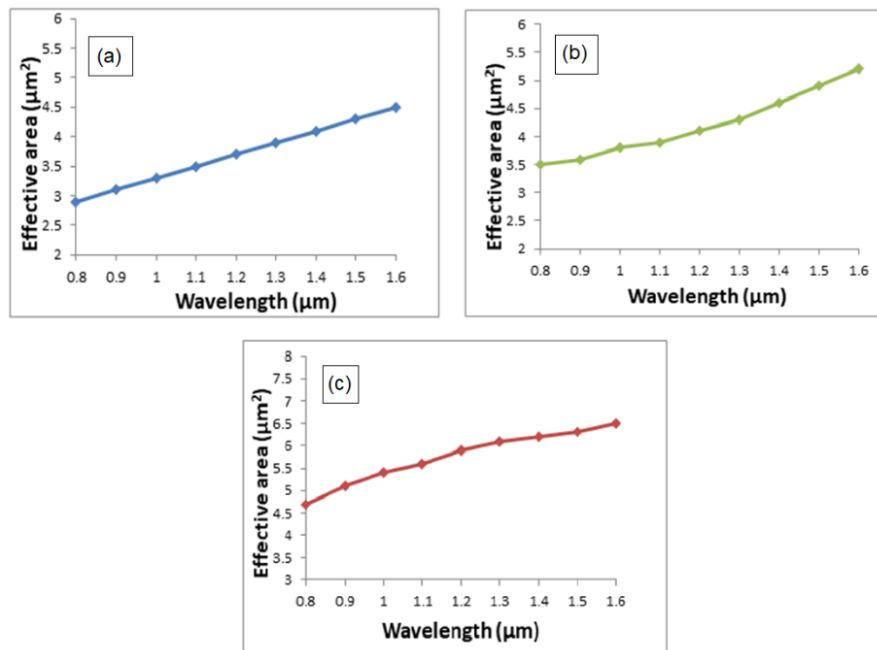
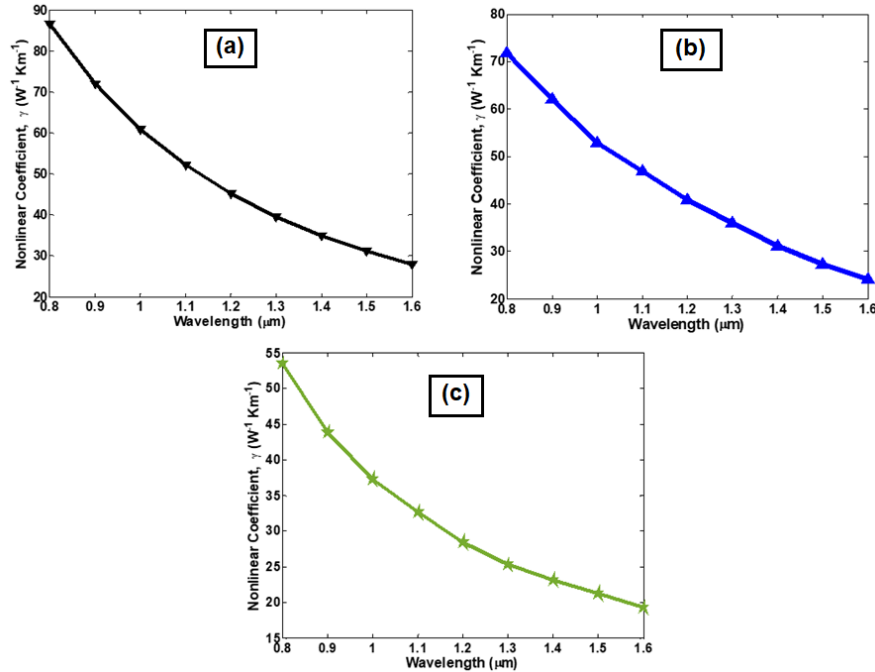


Figure 3.4 Effective area variation with wavelength (a) air is poured into the entire hole ring (b) ethanol is poured into the middle hole ring (c) ethanol is poured into the entire hole ring

After obtaining the  $A_{eff}$  of the PCF, the nonlinear coefficient is calculated using equation (3.3). At transmission wavelength of 1500 nm, the nonlinear coefficient of the proposed PCF comes out to be 31.17, 27.36 and 21.28 when air is poured into the entire hole ring, ethanol is poured into the middle hole ring and ethanol is poured into the entire hole ring, respectively. Figure 3.5 represents the variation of nonlinear coefficient with respect to wavelength of the proposed PCF. It can be seen that nonlinearity of the proposed PCF decreases as the wavelength increases.

The confinement loss of the proposed PCF is calculated using equation (3.4). At transmission wavelength of 1500 nm, the confinement loss of the proposed PCF comes out to be  $1.03878 \times 10^{-9}$  dB/m,  $9.18252 \times 10^{-6}$  dB/m and  $2.63927 \times 10^{-9}$  dB/m when air is poured into the entire hole ring, ethanol is poured into the middle hole ring and ethanol is poured into the entire hole ring, respectively.



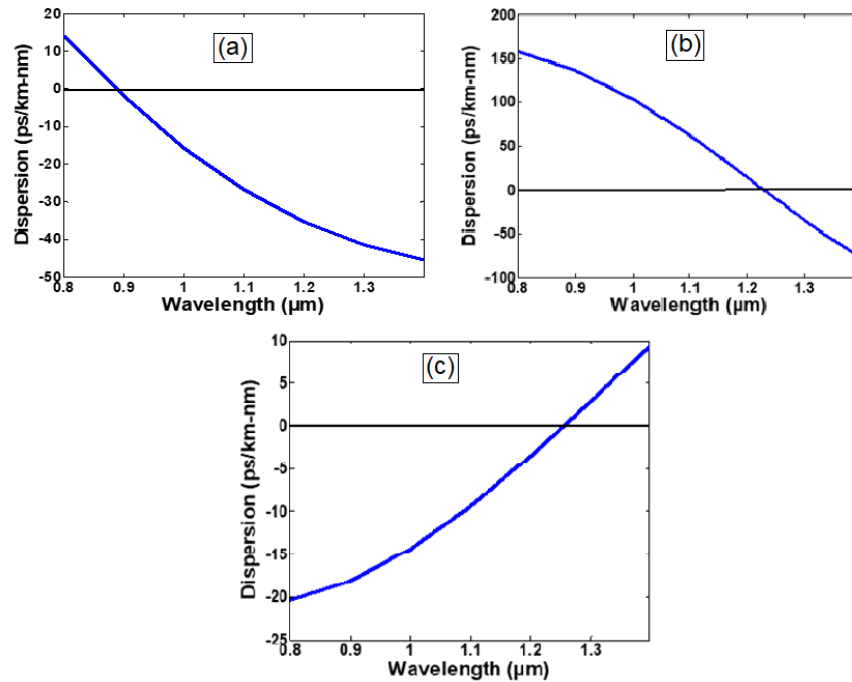
**Figure 3.5 Nonlinear coefficient variation with wavelength (a) air is poured into the entire hole ring (b) ethanol is poured into the middle hole ring (c) ethanol is poured into the entire hole ring**

Figure 3.6 represents the variation of dispersion parameter with respect to wavelength of the proposed circular shaped hollow core PCF as calculated from equation (3.5). The ZDW is determined to be 880 nm, 1220 nm and 1250 nm when air is poured into the entire hole ring, ethanol is poured into the middle hole ring and ethanol is poured into the entire hole ring, respectively. As indicated from the graph, when the number of hole rings filled with ethanol increases, a shift in zero dispersion towards higher wavelength is observed, as compare to hole-rings filled with air. As the value of dispersion is extremely sensitive to the fiber parameters and the doping level of the materials, like the difference between the refractive indices and core radius, dispersion can be changed by doping the silica with different materials and changing the  $n_{eff}$  values of the guided mode. Additionally, a rise in effective refractive indices can lead to an increase in dispersion. Since, the ZDW values achieved in our case are almost close and equal to the values of pump wavelength as required by the fiber laser devices, this kind of PCF is found useful in the area of laser technology as well, other than their already proven utilizations in the field of sensing, telecommunication and non-linear applications. Based on our research work, a comparison of optical parameters of PCF with and without ethanol filling the holes is presented in table 3.1. Highest effective area is achieved when ethanol is filled into the entire hole ring. ZDW is attained for all proposed PCFs with maximum wavelength reaching in PCF entirely filled with ethanol.

**Table 3.1 Comparison of changes in parameters with and without ethanol filling the holes**

Optical parameters	Air is poured into the entire hole ring	Ethanol is poured into the middle hole ring	Ethanol is poured into the entire hole ring
--------------------	---	---	---

Effective mode area at $\lambda=1500$ nm	$4.36 \mu\text{m}^2$	$4.91 \mu\text{m}^2$	$6.39 \mu\text{m}^2$
Zero Dispersion Wavelength	880 nm	1220 nm	1250 nm



**Figure 3.6** Dispersion graph of the circular shaped hollow core PCF when (a) air is poured into the entire hole ring (b) ethanol is poured into the middle hole ring (c) ethanol is poured into the entire hole ring

### 3.4 Summary

This research work proposes a circular shaped hollow core PCF designed by COMSOL software using finite element method. By regulating the number of hole rings poured with ethanol, the optical characteristics of the proposed PCF, such as effective area, confinement loss, dispersion and nonlinear coefficient have been investigated. This study clearly indicates that when the number of ethanol-filled hole rings increases, the zero dispersion wavelength can be shifted from 880 nm to 1250 nm, which lies in the near-infrared region. We may conclude from this research that ethanol has a considerable impact on the effective area and dispersion parameter. This kind of proposed PCF is very useful in non-linear applications, sensing applications, laser technology and telecommunication.

# CHAPTER 4

## DESIGN AND ANALYSIS OF TWIN CORE PHOTONIC CRYSTAL FIBER FOR TEMPERATURE AND CHEMICAL SENSING APPLICATION

This chapter is divided into two main sections. Section 4.1 focuses on the design and simulation of a TC-PCF for temperature sensing. The structure, featuring two solid cores separated by a vertical elliptical air hole, enables high birefringence and mode coupling, resulting in a temperature sensitivity of  $21.5 \text{ pm}/^\circ\text{C}$  over a range of 0 to  $1200^\circ\text{C}$ . The effect of air hole diameter variation on sensor performance is also analyzed.

Section 4.2 presents a TC-PCF-based chemical sensor, where the two cores are filled with chemicals like ethanol, benzene, and water. The unique elliptical hole arrangement enhances sensitivity, achieving a maximum of  $6667 \text{ nm}/\text{RIU}$  with a compact  $0.03 \text{ cm}$  fiber length. This design offers practical advantages in fabrication and aims to support industrial chemical detection applications.

### 4.1 Twin core photonic crystal fiber based temperature sensor with improved sensitivity over a wide range of temperature

#### 4.1.1 Introduction

Of late, optical fiber sensors have outshined traditional electronic sensors for multi-sensing capabilities such as pressure, stress, temperature, strain and acoustic signals as they offer a great number of advantages over latter such as light weight, high sensitivity, relatively inexpensive, immunity to radio frequency interference and their ability to multiplex sensor networks. In the field of photonics, photonic crystal fibers (PCFs) exhibit a great potential compared to conventional optical fibers. Physical characteristics of PCF's like refractive index, pressure, displacement, curvature, temperature, torsion, vibration, and electric field can be used to analyse optical sensors. Its endless single-mode feature and structural analysis make it a factor to consider for a variety of applications, including sensor, splitter [141]–[143], narrow band pass filter [144], photonic crystal fiber coupler [145], [146], and wavelength MUX and DEMUX [147]. A growing number of TC-PCF sensors have been created in recent years, such as pressure [141], Refractive Index (R.I.) [142], bio and temperature sensors [148], [149]. Many research groups have been actively involved in enhancing the temperature sensitivity of dual core-PCF. For ex. S. Revathi et. al investigated a pressure and temperature sensor based upon Dual-Core Photonic Quasi-Crystal Fiber in 2015 and obtained a temperature sensitivity of about  $20 \text{ pm}/^\circ\text{C}$  over the range of 0 to  $1000^\circ\text{C}$  [149]. Similar results have also been observed by S. Jegadeesan et. al over the same temperature range using different model of PCF [150]. D. Chen and group presented a Dual-Core PCF based pressure/temperature sensor in 2011 achieving a temperature sensitivity of around  $20.7 \text{ pm}/^\circ\text{C}$  over the range of 0 to  $1000^\circ\text{C}$  [151].

In this work, we propose a PCF with twin solid cores separated by single vertical elliptical air hole for a wide temperature sensing range of up to  $1200^\circ\text{C}$ . When optical light enters the TC-

PCF from first core, it travels along the TC-PCF from first core to second core. When temperature is applied to the TC-PCF, the optical light at the edge of output in second core is measured with the help of optical analyzer using the transmission graph. The shift in transmission curve of TC-PCF is observed due to change of R.I. of silica material which thus helps in determining the temperature sensitivity of the TC-PCF. COMSOL software, which is based on the Finite Element Method (FEM), is used to design the proposed TC-PCF setup.

#### 4.1.2 PCF structure and result analysis

The proposed TC-PCF is made up of twin-fiber cores separated by single vertical elliptical air hole. Figure (4.1.1) illustrates the geometry of the proposed TC-PCF. Two missing holes depicted as A and B represents the twin fiber cores of the PCF. Pitch ( $\Lambda$ ) is the center-to-center length between air holes. A diameter,  $d$  of  $1.4 \mu\text{m}$  and a pitch length,  $\Lambda$  of  $2 \mu\text{m}$  is chosen for air holes for the proposed PCF and pure silica is taken as a background material. The major-axis of the single elliptical hole in the proposed configuration is  $a = 1.4 \mu\text{m}$ , the minor axis,  $b = 0.9 \mu\text{m}$  and the R.I. of air,  $n_{\text{air}} = 1$  is considered. Equation (4.1.1) gives the R.I. of pure silica ( $n_{\text{silica}}$ ) which is called Sellmeier equation.

$$n_{\text{silica}}^2(\lambda) = 1 + \frac{c_1\lambda^2}{\lambda^2-d_1} + \frac{c_2\lambda^2}{\lambda^2-d_2} + \frac{c_3\lambda^2}{\lambda^2-d_3} \quad (4.1.1)$$

The operational wavelength in  $\mu\text{m}$  is denoted by  $\lambda$  and the Sellmeier coefficients are  $c_1=0.696166300$ ,  $c_2=0.407942600$ ,  $c_3=0.897479400$ ,  $d_1=4.67914826 \times 10^{-3} \mu\text{m}^2$ ,  $d_2=1.35120631 \times 10^{-2} \mu\text{m}^2$  and  $d_3 = 97.9340025 \mu\text{m}^2$ , respectively [152].

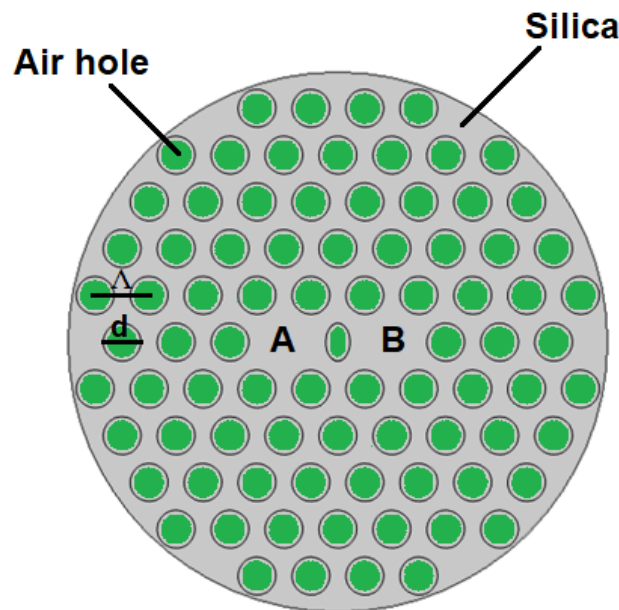
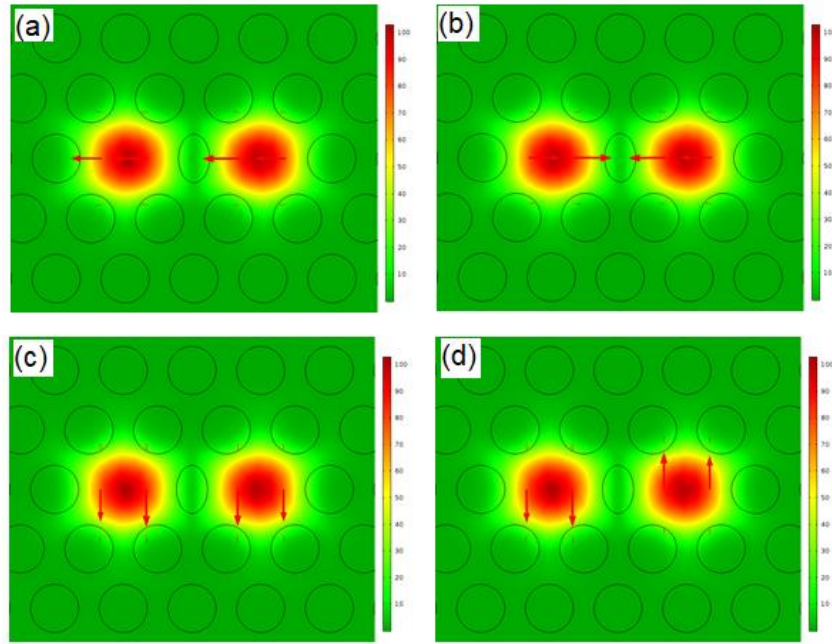


Figure 4.1.1 Geometry of proposed twin core PCF

In this work, due to small core-to-core length, twin fiber cores inside the PCF form two waveguides, each of which is independent (accompanying with coupling mode) to each other. At  $1550 \text{ nm}$ , Figure 4.1.2 depicts the electric field vector and amplitude distribution of the four polarized super-modes viz., the x-even, x-odd, y-even and y-odd. The coupling effect observed in TC-PCF is attributed to these super-modes based on FEM.



**Figure 4.1.2 Electric field vector and amplitude distribution of the four super-modes: (a) x-polarization even (b) x-polarization odd (c) y-polarization even and (d) y-polarization odd**

Figure 4.1.3 shows the schematic diagram of the PCF sensing set up. Broadband light source, temperature controller and optical spectrum analyzer are the essential tools. A single-mode fiber (SMF) can be used to feed light into the fiber core A of the proposed TC-PCF from a broadband light source. Through another SMF, the output signal can be seen from the fiber core B in an optical spectrum analyzer. The PCF's surrounding environment temperature can be adjusted using the temperature control chamber.

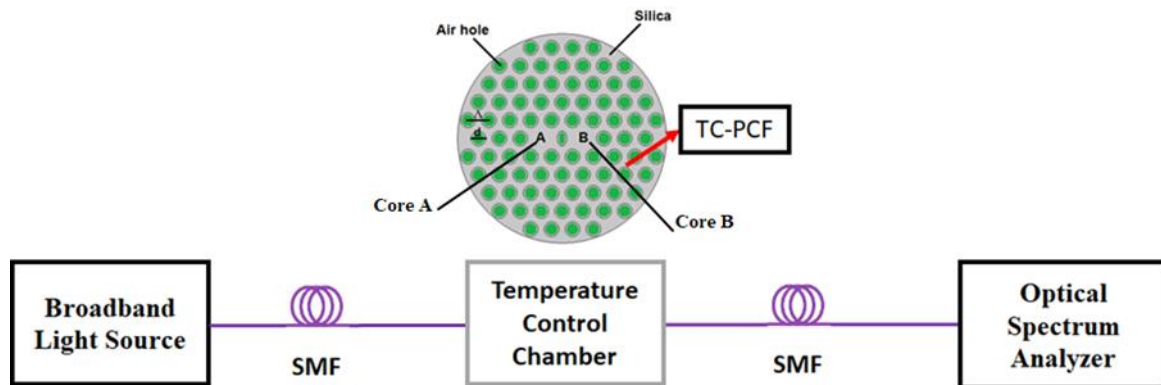


**Figure 4.1.3 Schematic of PCF sensing set up for temperature sensor**

At 1550 nm, the  $n_{eff}^x$  even and odd modes are 1.4013807059 and 1.4006623442, respectively and for  $n_{eff}^y$  even and odd mode are 1.4009086063 and 1.4001836831, respectively. Figure 4.1.4 demonstrates how the  $n_{eff}$  of the even and odd modes variation with wavelength for x-polarized and y-polarized modes. The effective refractive index falls as the wavelength increases.

The  $\Delta n_{eo}$  fluctuation, which is  $\Delta n_{eo} = |n_e - n_o|$ , for x and y polarized modes is depicted in Figure 4.1.5. As the effective index difference between the core and cladding increases, the

wavelength increases. The rise in  $\Delta n_{eo}$  of the TC-PCF implies that light is trapped more tightly in the core.

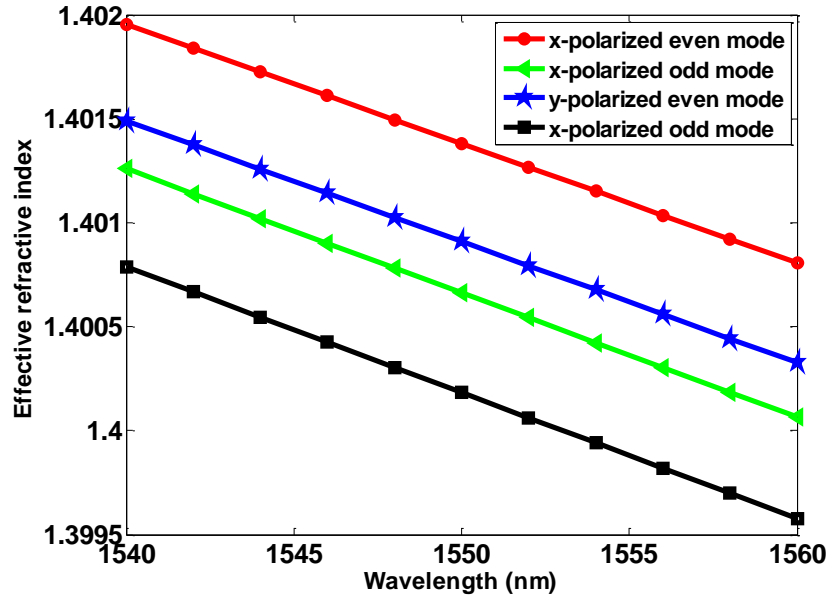


Figure 4.1.4 Variation in  $n_{eff}$  with wavelength

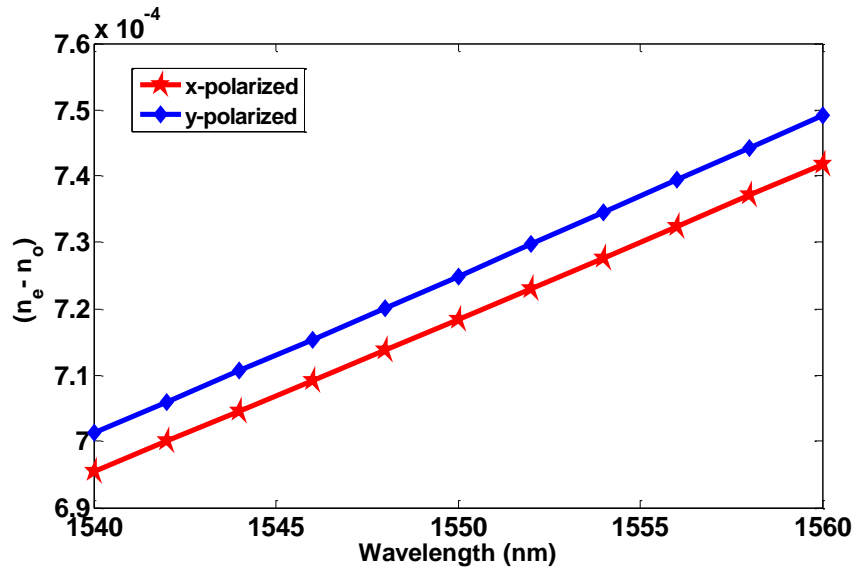


Figure 4.1.5 Variation in  $\Delta n_{eo}$  with wavelength

The TC-PCF coupling length is defined as

$$L_c = \frac{\pi}{|\beta_e^i - \beta_o^i|} = \frac{\lambda}{2|n_e^i - n_o^i|} \quad (4.1.2)$$

where  $i = x, y$ , the even and odd mode propagation constants of the TC-PCF are  $\beta_e^i$  and  $\beta_o^i$ , respectively. Even and odd mode effective refractive indices are represented by  $n_e^i$  and  $n_o^i$ , respectively [146], [153]. We first estimated the effective refractive indexes of x and y polarized modes, then calculated the difference in effective refractive indexes for x and y polarized modes and finally determined their coupling lengths using equation (4.1.2) for

different wavelength.

Figure 4.1.6 depicts the change in coupling length as a function of wavelength. To determine the value of Coupling length for different wavelength using Eq. (4.1.2), the  $n_{eff}$  of four super modes are first computed followed by the  $\Delta n_{eo}$  for x and y polarized mode. It should be noted that the y-polarized coupling length is smaller than that of x-polarized mode and that the coupling length reduces as the wavelength increases.

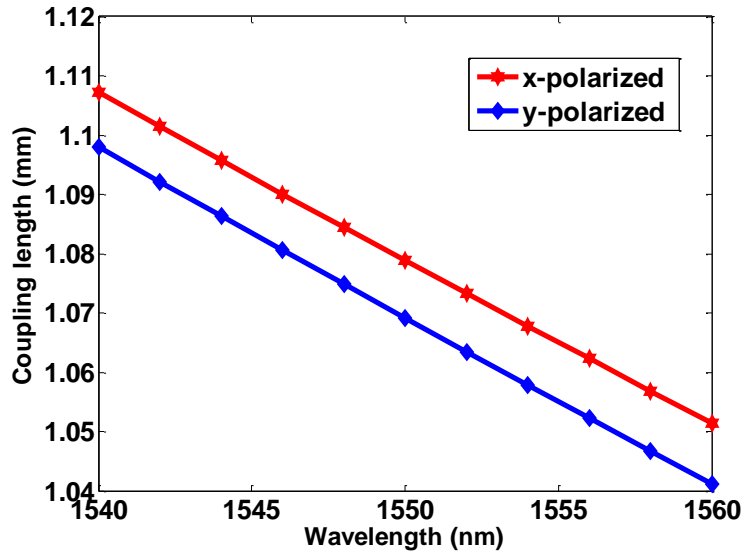


Figure 4.1.6 Coupling length variation with wavelength

Confinement loss is the term for the attenuation caused by the waveguide geometry. This type of loss occurs in single material fibers, especially in PCFs because they are generally made of silica and given by

$$\text{Confinement loss} = -20 \log_{10} \epsilon^{-k \text{Im}[n_{eff}]} = 8.686k \text{Im}[n_{eff}] \quad (4.1.3)$$

where  $k$  represents the propagation constant ( $k = 2\pi/\lambda$ ) in free space,  $\lambda$  denotes the wavelength and  $\text{Im}[n_{eff}]$  represents the imaginary part of the complex effective index [154].

The confinement loss of the proposed TC-PCF is calculated using equation (4.1.3). At transmission wavelength of 1550 nm, the low confinement loss of the proposed PCF comes out to be  $1.23 \times 10^{-14} \text{ dB/cm}$ ,  $2.14 \times 10^{-14} \text{ dB/cm}$ ,  $2.77 \times 10^{-14} \text{ dB/cm}$  and  $5.39 \times 10^{-15} \text{ dB/cm}$  for x-polarized even, x-polarized odd, y-polarized even and y-polarized odd modes, respectively.

Birefringence causes double refraction when a light ray strikes a birefringent material, polarization splits it into two different rays that travels in slightly different directions. The birefringence parameter,  $B$  of TC-PCF is calculated by using equation (4.1.4).

$$B = |\text{Re}(n_{eff}^x) - \text{Re}(n_{eff}^y)| \quad (4.1.4)$$

where the effective R.I. of x and y polarized modes are represented by  $n_{eff}^x$  and  $n_{eff}^y$ , respectively [155]. When birefringence is low, the x and y polarized coupling lengths are almost equal, making it tough to split the light. These two modes are excited because the proposed twin-core PCF structure supports mode coupling between the two cores. Among

these, the mode that shows higher sensitivity to changes in the sensing parameter is more suitable for sensing applications.

According to Figure 4.1.6, the x polarized coupling length of the proposed TC-PCF is larger than that of y-polarized mode. The high birefringence of  $4.721 \times 10^{-4}$  and  $4.787 \times 10^{-4}$  is achieved for even and odd mode, respectively at  $\lambda = 1550$  nm. The changes in birefringence with operational wavelength and at the applied temperature are shown in Figure 4.1.7.

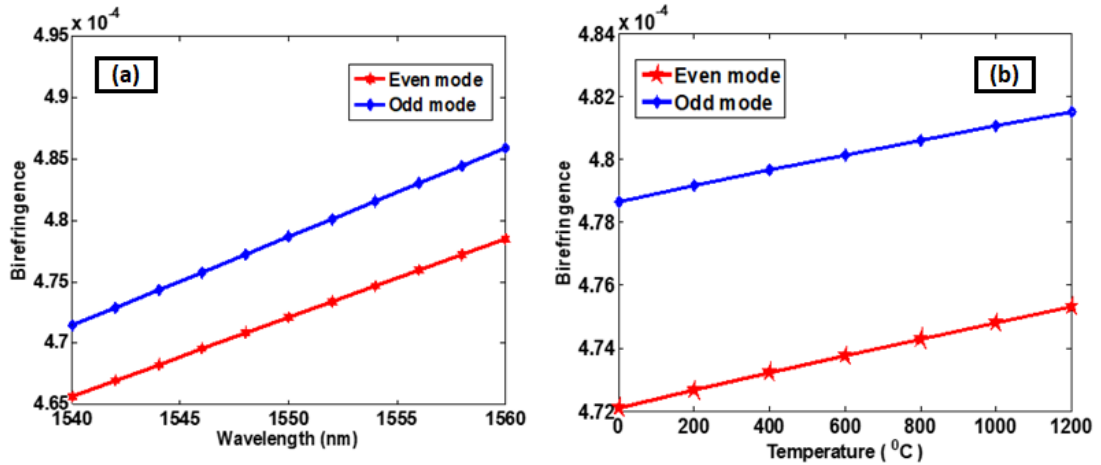


Figure 4.1.7 Variation in birefringence with (a) wavelength (b) temperature applied ( $^{\circ}\text{C}$ )

Following a length  $L$ , the TC-PCF power transfer is computed by using equation (4.1.5).

$$I(\lambda) = \sin^2\left(\frac{\pi}{\lambda} \Delta n_{eo} L\right) \quad (4.1.5)$$

The effective R.I. difference is denoted by  $(\Delta n_{eo})$  and effective R.I. of the even and odd modes are represented by the letters  $n_e^i$  and  $n_o^i$  respectively [146], [156].

Figure 4.1.8 illustrates the TC-PCF power transmission graph for x-polarized mode when the length is 3 cm at sensing temperature range of  $0^{\circ}\text{C}$  to  $1200^{\circ}\text{C}$ . It should be noted that the proposed TC-PCF power transmission curve is sinusoidal.

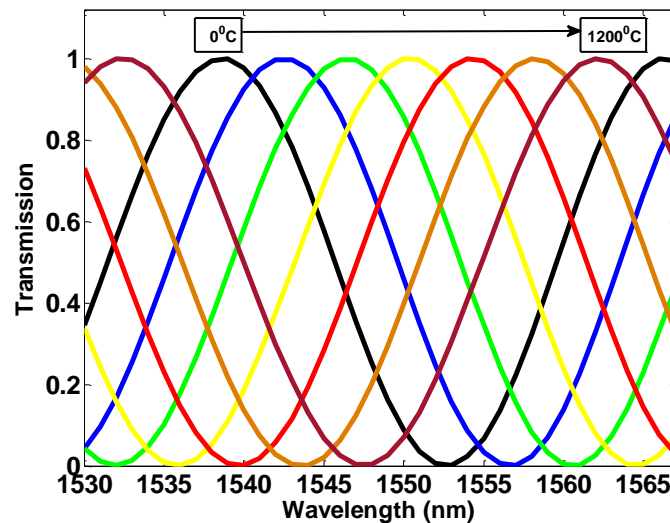


Figure 4.1.8 TC-PCF transmission curve with a length of 3 cm

The sensitivity of the proposed twin-core PCF for temperature sensing is determined by shifting of peaks with the rise in temperature detected across the wide range of 0 to 1200°C. The twin-core PCF temperature sensitivity is defined as

$$S_{\lambda}(nmRIU^{-1}) = \Delta\lambda_{peak}/\Delta T \quad (4.1.6)$$

where  $\Delta\lambda_{peak}$  represent the overall shift in wavelength peak due to fluctuation in temperature and  $\Delta T$  is the shift in temperature [157].

The R.I. value of the TC-PCF will vary very little above normal temperature due to the effect of thermo-optic, when heat is applied to the fiber. Due to its almost zero thermal expansion, silica is a ceramic with interesting uses as a filler in composites [158]. The relation between refractive index and applied temperature is determined by using equation (4.1.7).

$$n = n_0 + T \frac{dn}{dt} \quad (4.1.7)$$

where  $n_0$  denotes the R.I. of pure silica at zero degree celsius and the thermo-optic coefficient of silica is obtained by using the following formula [155]:

$$\frac{dn}{dt} = 10^{-5}(1/^{\circ}C) \quad (4.1.8)$$

For the sensing temperature range of 0°C to 1200°C, Figure 4.1.9 depicts the shift of the wavelength peak. The transmission graph is linear, shifting to a higher wavelength when the temperature rises.

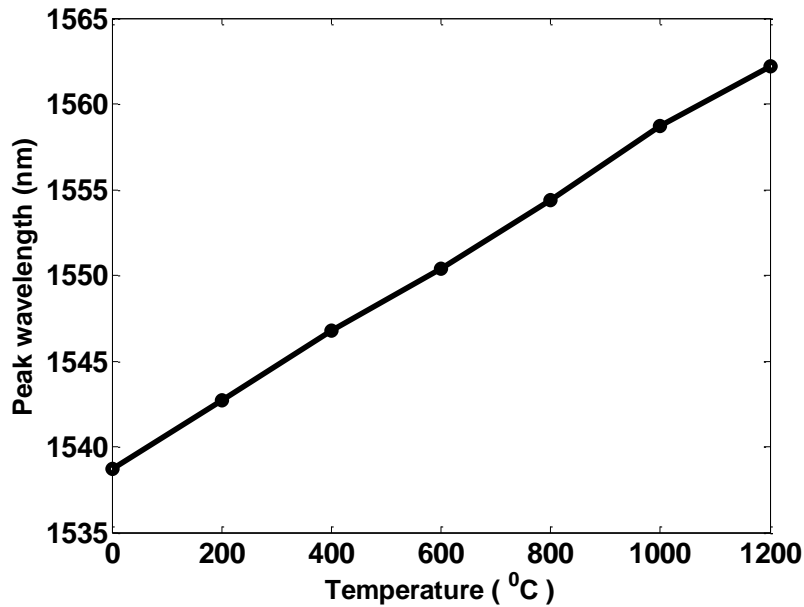


Figure 4.1.9 Transmission spectrum peak wavelength (nm) with applied temperature (°C)

Figure 4.1.10 depicts the numerical fitting line for shift in wavelength spots in the transmission curve of TC-PCF when the temperature is applied. For a 3 cm fiber, the twin-core PCF has a temperature sensitivity of 21.5 pm/°C.

The proposed sensor performance is summarized in Table 4.1.1. The presented sensor outperformed the recently published PCF sensors, as shown in Table 4.1.1.

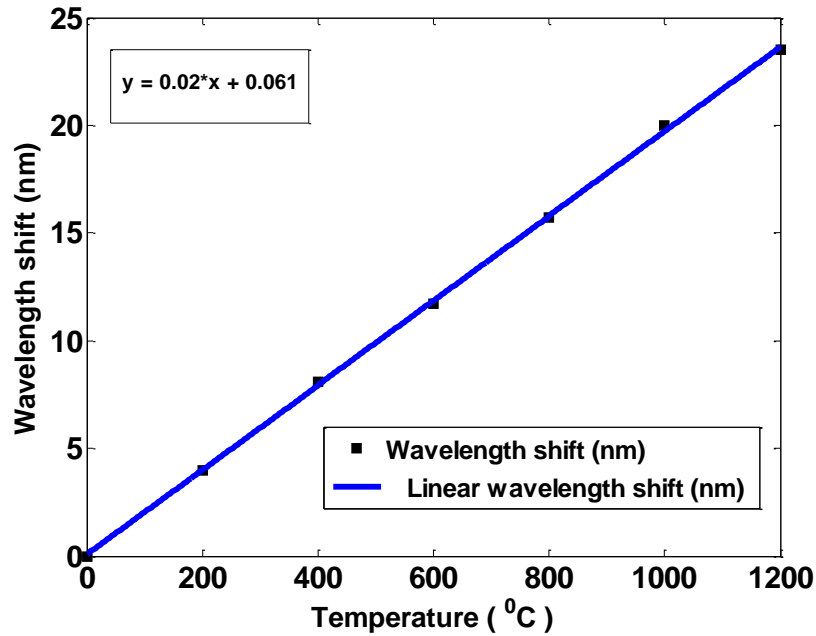


Figure 4.1.10 Numerical line fitting for various wavelength shift values for a 3 cm long TC-PCF at wide temperature range of 0 to 1200°C

Table 4.1.1 Performance comparison of different PCF sensors with our proposed PCF sensor

Reference	Sensitivity	Sensitivity Range
[149]	20 pm/°C	0°C to 1000°C
[150]	20 pm/°C	0°C to 1000°C
[151]	20.7 pm/°C	0°C to 1000°C
[159]	18.5 pm/°C	0°C to 600°C
[160]	15.61 pm/°C	300°C to 1200°C
Proposed PCF	21.5 pm/°C	0°C to 1200°C

### 4.1.3 Impact of diameter variation on sensitivity

Figure 4.1.11 shows the TC-PCF power transmission graph for the x-polarized mode with different diameters when the length is 3 cm at a sensing temperature range of 0°C to 1200°C. According to figures 4.1.11-a, 4.1.11-b and 4.1.11-c for a temperature sensing range of 0 to 1200°C, the twin-core PCF can achieve a temperature sensitivity of 20 pm/°C at  $d = 1.2 \mu\text{m}$ , 21.5 pm/°C at  $d = 1.4 \mu\text{m}$  and 20.5 pm/°C at  $d = 1.6 \mu\text{m}$ , respectively. As indicated from the graph, when the diameter of hole rings is taken as  $1.2 \mu\text{m}$ , a blue shift towards higher wavelength is observed, as compared to the diameter of hole rings taken as  $1.4 \mu\text{m}$  and when the diameter of hole rings is taken as  $1.6 \mu\text{m}$ , a red shift towards lower wavelength is observed,

as compared to the diameter of hole rings taken as  $1.4 \mu\text{m}$ . The variation of sensitivity of proposed TC-PCF with different diameter shown in Table 4.1.2.

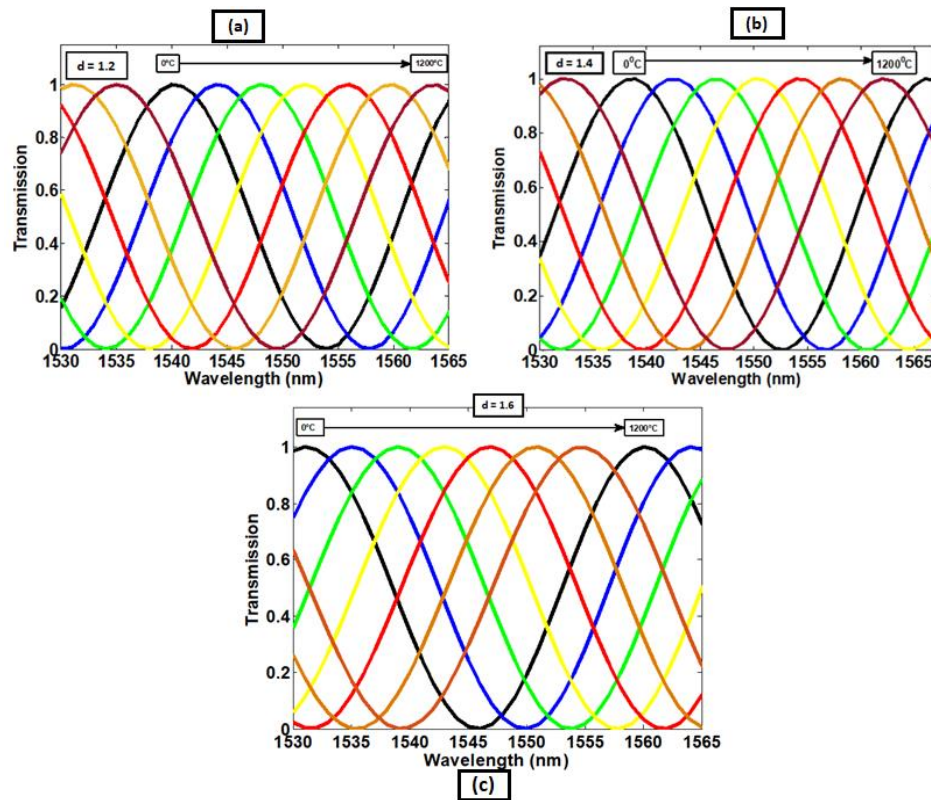


Figure 4.1.11 TC-PCF transmission curve with different diameter of  $d$ , (a)  $1.2 \mu\text{m}$  (b)  $1.4 \mu\text{m}$  and (c)  $1.6 \mu\text{m}$

Table 4.1.2 Comparison of sensitivity of proposed TC-PCF with different diameters

Diameter	Sensitivity
$d = 1.2 \mu\text{m}$	$20 \text{ pm}/^\circ\text{C}$
$d = 1.4 \mu\text{m}$	$21.5 \text{ pm}/^\circ\text{C}$
$d = 1.6 \mu\text{m}$	$20.5 \text{ pm}/^\circ\text{C}$

#### 4.1.4 Summary

Using the COMSOL software and the Finite Element Method, we have proposed a temperature-sensor based on twin-core PCF highly sensitive over a wide range of temperature. The high sensitivity is ascribed to the unique combination of circular and elliptical air holes arranged in our proposed structure. The R.I. of pure silica at different temperature is determined using the thermo-optic coefficient equation. Furthermore, the proposed PCF temperature sensitivity is evaluated using coupling length and transmission spectrum calculations. Under broad temperature sensing range of  $0$  to  $1200^\circ\text{C}$ , the twin-core PCF can achieve a temperature sensitivity of  $21.5 \text{ pm}/^\circ\text{C}$  for  $3 \text{ cm}$  fiber length with the diameter of  $1.4 \mu\text{m}$ . The key advantages of a TC-PCF based temperature sensor are its low cost, small size, and better stability. Using the current existing known PCF manufacturing techniques, facile fabrication of proposed TC-PCF is possible.

## 4.2 Hexagonal lattice twin core photonic crystal fiber based chemical sensor

### 4.2.1 Introduction

The development of photonic crystal fibers (PCFs), which have salient optical characteristics, has demonstrated the potential advantages of optical fibers in sensing applications [161]–[164]. These micro structured fibers stand out especially for chemical and biological sensing due to their exceptional qualities, including their tiny size and relative compatibility [165]–[167]. While in conventional fibers, designing is so difficult, the size of the core is constrained, selection of material is tough etc. Additionally, these geometry restrictions make the system less flexible to identify the characteristics of fibers, such as birefringence [166], confinement loss [168], dispersion [166], relative sensitivity [169] etc. PCF enables long-distance light propagation that was previously impossible. It is possible to control the characteristics of light propagation by modifying the air holes in the core and cladding region. In the areas of nonlinear optics [170], sensing [171] and optical communications [169], numerous research investigations have previously been conducted. It has been suggested to use a PCF refractive index (RI) sensor that is based on the surface plasmon resonance (SPR) phenomena. Because the inside side of the air holes in these fibers contains metal, they are particularly challenging to make. As a result, the use of fibers based on SPR has extremely few applications. Simple twin core PCF sensors are extremely effective because they have high sensitivity, easy fabrication, simple design and require less metal wires for their construction.

In this research work, we proposed a novel type of chemical sensing fiber with two solid cores separated by a vertical elliptical hole. The sensitivity of the TC-PCF can be determined by examining the variation in the transmission curve of the TC-PCF caused by changes in the refractive index of different chemicals, such as ethanol, benzene, and water. The proposed TC-PCF configuration is designed by the FEM-based COMSOL Multiphysics version 5.2a.

### 4.2.2 PCF design and result analysis

Figure 4.2.1 shows the configuration of a proposed hexagonal lattice twin core PCF chemical sensor. Two air holes are eliminated from this design, creating two PCF solid cores. The twin-fiber cores of the proposed TC-PCF are separated by a vertical elliptical hole and filled with different chemicals such as ethanol, benzene and water. The proposed Photonic Crystal Fiber will have elliptical air holes with a pitch length ( $\Lambda$ ) of 2  $\mu\text{m}$ . The minor axis of the elliptical hole is 0.9  $\mu\text{m}$ , while the major axis is 1.4  $\mu\text{m}$ . The background material selected is pure silica and its refractive index (R.I.) is determined by the Sellmeier equation [172] and R.I. of air ( $n_{\text{air}} = 1$ ) is considered. The refractive index of various analytes like ethanol ( $n = 1.354$ ), benzyne ( $n = 1.366$ ) and water ( $n = 1.33$ ) is considered [173]. When compared to other complex structures that have been previously published, this form of PCF structure is quite simple to fabricate. Here, a normal mode of Mesh analysis is chosen to investigate the proposed PCF using COMSOL Multiphysics software.

Four super modes in the x and y-polarization are possible according to the theory of PCF mode coupling [174]. Due to the distinct cores, these four super-modes are possible. The electric field profile distribution of the four super modes at 1.55  $\mu\text{m}$  are shown in Figure 4.2.2.

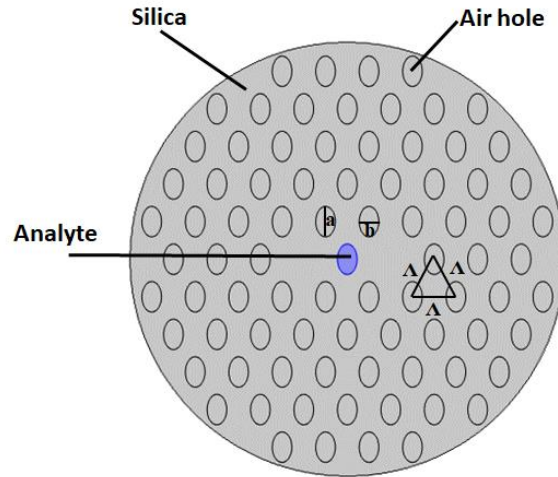


Figure 4.2.1 Cross-section of proposed twin-core PCF

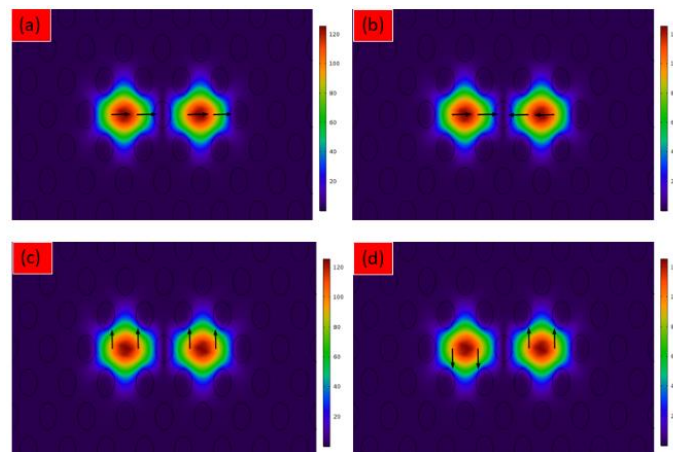


Figure 4.2.2 The distribution of the amplitude and vector of the electric field for four super-modes: (a) and (b) are x-polarization with even and odd symmetry, respectively, while (c) and (d) are y-polarization with even and odd symmetry, respectively

The PCF sensing setup, as illustrated in Figure 4.2.3, requires crucial equipment such as a temperature controller, broadband light source, and optical spectrum analyzer. Light can be introduced into the fiber-core A using a single-mode fiber (SMF) from the broadband light source, while the output signal can be observed from the fiber core B using another SMF and an optical spectrum analyzer.

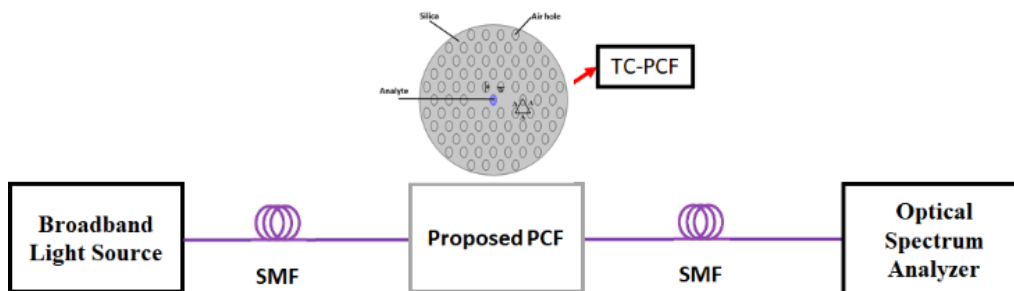


Figure 4.2.3 TC-PCF sensing arrangement for chemical sensor

The  $n_{eff}^x$  even and odd modes at  $1.55 \mu\text{m}$  are 1.410891625 and 1.407693967, respectively,

while the  $n_{eff}^y$  even and odd modes at 1.55  $\mu\text{m}$  are 1.411224356 and 1.408240529, respectively. Figure 4.2.4 shows how the  $n_{eff}$  of the even and odd modes for x-polarized and y-polarized vary with wavelength. As the wavelength increases, the  $n_{eff}$  decreases.

Figure 4.2.5 shows the  $\Delta n_{eo}$  fluctuation, where  $\Delta n_{eo} = |n_e - n_o|$ , for the x and y polarized modes. When there is an increase in the wavelength of light, the  $\Delta n_{eo}$  between the core and cladding of a fiber also increases. The increase in the  $\Delta n_{eo}$  of the proposed PCF indicates that the confinement of light in the core has become stronger.

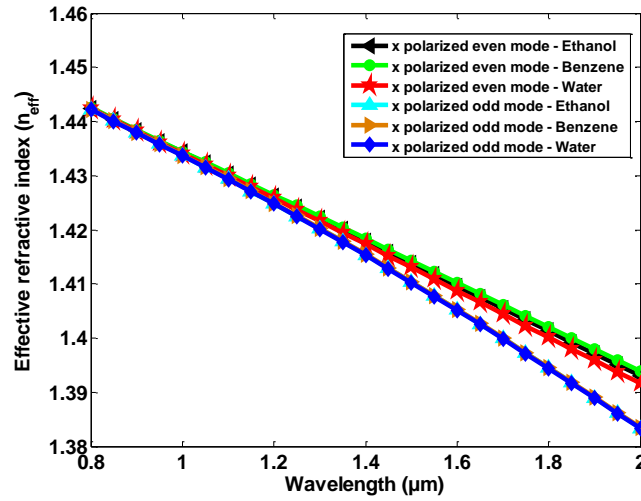


Figure 4.2.4 Variation in  $n_{eff}$  with wavelength

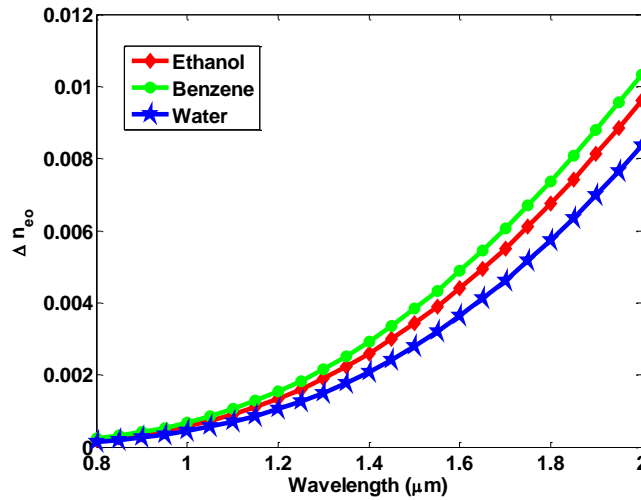


Figure 4.2.5 Variation in  $\Delta n_{eo}$  with wavelength

The coupling length of the proposed PCF is computed using Eq. (4.2.1).

$$L_c = \frac{\pi}{|\beta_e^i - \beta_o^i|} = \frac{\lambda}{2|n_e^i - n_o^i|} \quad (4.2.1)$$

The TC-PCF has even and odd mode propagation constants represented by  $\beta_e^i$  and  $\beta_o^i$ , respectively, where  $i$  is either  $x$  or  $y$ . Additionally, even and odd effective R.I. are denoted by  $n_e^i$  and  $n_o^i$ , respectively [175], [176]. We have determined the coupling length value for various wavelengths using Eq. (4.2.1). The coupling length variation as a function of wavelength when

the central hole of the TC-PCF is filled with different chemicals such as ethanol, benzene and water shown in Figure 4.2.6. It should be noticed that the coupling length decreases with increasing wavelength. The TC-PCF coupling length varies depending on the chemical used and when water is poured into the central hole of the TC-PCF, it can provide a maximum coupling length of 0.24 mm at a 1.55  $\mu\text{m}$  wavelength. Also, a small coupling length results in a greater mode coupling between the two fiber cores.

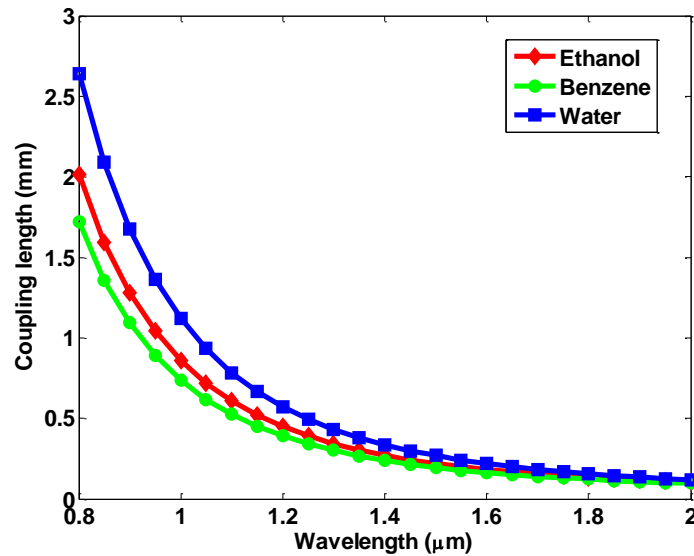


Figure 4.2.6 The variation of coupling length with wavelength

The birefringence of the proposed PCF, which is the cause of the double-refraction phenomenon, is computed using Eq. (4.2.2). In the presence of a birefringent material, the polarization of a light ray leads to its division into two rays, which propagate in separate directions.

$$B = |Re(n_{eff}^x) - Re(n_{eff}^y)| \quad (4.2.2)$$

Where the effective refractive indices of the x and y polarized modes is denoted as  $n_{eff}^x$  and  $n_{eff}^y$ , respectively [177]. At 1.55  $\mu\text{m}$  wavelength, the high birefringence of  $3.327 \times 10^{-4}$  and  $5.466 \times 10^{-4}$ , respectively is attained for the even and odd modes when water is poured into the central hole of the TC-PCF. Figure 4.2.7 illustrates how birefringence changes with operational wavelength.

Equation (4.2.3) is used to calculate the power transfer of the TC-PCF after a length L.

$$I(\lambda) = \sin^2\left(\frac{\pi}{\lambda} \Delta n_{eo} L\right) \quad (4.2.3)$$

In the given context, the effective refractive indices difference is denoted as ( $\Delta n_{eo}$ ) and the effective refractive indices of the even and odd modes are denoted as  $n_e^i$  and  $n_o^i$  respectively [175]. Figure 4.2.8 depicts the power transmission graph of TC-PCF for different chemicals when the PCF length is just 0.03 cm. The proposed power transmission graph for TC-PCF displays a sinusoidal pattern, which should be duly noted.

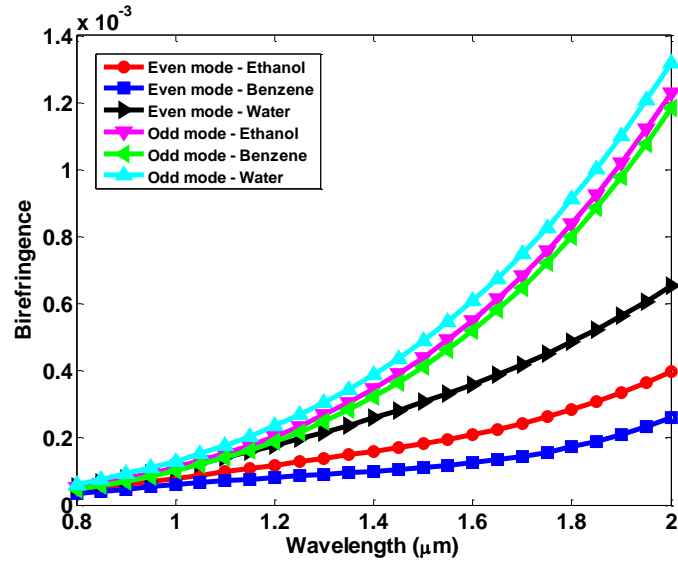


Figure 4.2.7 The variation of birefringence with wavelength

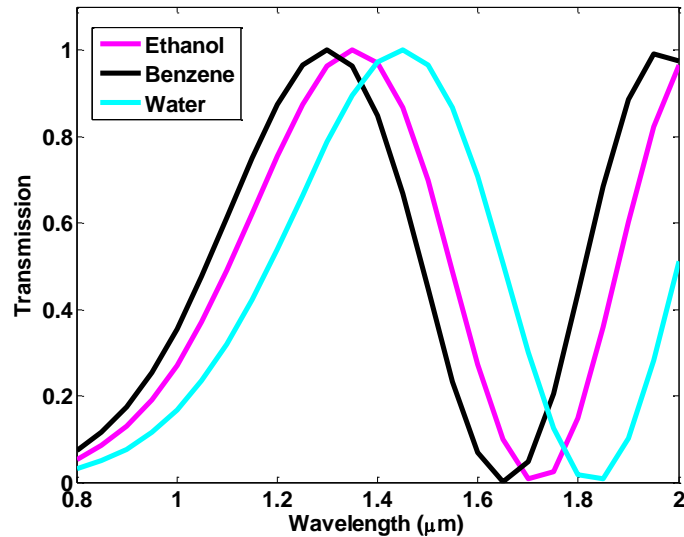


Figure 4.2.8 The transmission characteristics of TC-PCF, with a specific length of 0.03 cm

To evaluate the proposed TC-PCF sensitivity for chemical sensing, the shifting of transmission peaks is observed by changing the refractive index (RI) of different chemicals. The TC-PCF temperature sensitivity can be described as

$$S_{\lambda}(nmRIU^{-1}) = \Delta\lambda_{peak}/\Delta n_a \quad (4.2.4)$$

where  $\Delta\lambda_{peak}$  represent the overall shift in transmission curve and  $\Delta n_a$  is the shift in RI of different chemicals [178]. The sensitivity of the twin-core PCF, which is 6667 nm/RIU, is achieved for a fiber length of only 0.03 cm. With other published papers, we have compared the proposed design sensitivity response. Using a gold nanofilm coated photonic crystal fiber, Zhen-Kai Fan et al. demonstrated a SPR sensor in 2019 achieving a RI sensitivity of around 3978 nm/RIU [179]. In their study of a SPR sensor based on a PCF with large-sized microfluidic channels, P. Bing and group found that the sensor had a maximum wavelength sensitivity of 2000 nm/RIU for a RI detection range of 1.33 to 1.39 [180]. G. An et al. presented

a PCF-SPR sensor with a maximum wavelength sensitivity of around 3233 nm/RIU and an extra-wide RI detection range of 1.30 to 1.79 [181]. C. Liu et al. presented a SPR sensor in 2018 achieving a RI sensitivity of around 6300 nm/RIU [182]. The main benefits of a proposed chemical sensor based on TC-PCF are its inexpensive price, compact size and improved stability.

Table 4.2.1 summarizes the suggested sensor performance. Table 4.2.1 shows that the sensor presented in this study exhibited superior performance compared to the PCF sensors that were reported recently. The proposed twin-core photonic crystal fiber (TC-PCF) structure shows better performance than previously reported sensors due to several design advantages. The twin-core configuration enables strong optical coupling between the two cores, which significantly increases the sensitivity to refractive index variations of the analyte.

**Table 4.2.1 Comparison of the performance of various PCF sensors, including the PCF sensor proposed in this study**

Reference	Sensitivity
[179]	3978 nm/RIU
[180]	2000 nm/RIU
[181]	3233 nm/RIU
[182]	6300 nm/RIU
Proposed PCF	6667 nm/RIU

### 4.2.3 Summary

This research presents a chemical sensor based on twin-core photonic crystal fiber (PCF) with a hexagonal lattice structure. The sensitivity of the sensor is evaluated using the Finite Element Method and COMSOL software by analyzing the coupling length and transmission spectrum. The results demonstrate the potential of the proposed PCF sensor for chemical sensing applications. The highest sensitivity achieved for the proposed fiber sensor is 6667 nm/RIU when the fiber length is 0.03 cm. The result reveals that the size of the proposed TC-PCF chemical sensor is very compact, of simple design, and easy to fabricate when compared to other reported works. The small fiber length can help to overcome associated practical physical constraints during designing and achieve a less complex PCF architecture.

# CHAPTER 5

## DESIGN AND ANALYSIS OF ADVANCED BIOSENSING METHODS UTILIZING PCF FOR THE EARLY IDENTIFICATION OF A RANGE OF DISEASES, SUCH AS MULTIPLE FORMS OF CANCER, ESSENTIAL BLOOD CONSTITUENTS AND MALARIA IN TERAHERTZ FREQUENCY REGIME

This chapter is divided into three main sections. Section 5.1 presents a twin-core photonic crystal fiber (TC-PCF) designed for early cancer detection using the refractive index differences of normal and cancerous cells in the terahertz (THz) regime. The structure features a central elliptical hole for sample infiltration and achieves exceptionally high sensitivity (up to  $1.67 \times 10^6$  nm/RIU) for various cancer types, validated through FEM simulations.

Section 5.2 introduces a D-shaped dual-core PCF (DC-PCF) sensor aimed at detecting major blood components (RBCs, WBCs, plasma, water, and hemoglobin) in the THz range. The solid core design and mode coupling theory enable high sensitivity ( $1.49 \times 10^6$  nm/RIU) within an RI range of 1.33–1.4. The impact of air hole pitch on sensitivity is also analyzed.

Section 5.3 proposes a DC-PCF-based biosensor for early malaria detection by identifying different infection stages through variations in the refractive index of RBCs. The sensor demonstrates high sensitivity for the ring, trophozoite, and schizont stages, with values exceeding  $1.1 \times 10^6$  nm/RIU, making it a promising tool for biomedical diagnostics.

### **5.1 Twin core photonic crystal fiber for hazardous cancer cell detection with improved sensitivity in terahertz (THz) frequency regime**

#### **5.1.1 Introduction**

Photonic crystal fiber (PCF) has emerged as a promising potential for detection of gas and chemical due to its flexible architecture, low loss, large effective mode area, high birefringence and low dispersion [183]. PCF sensors are appropriate for biosensing applications since they do not require a lot of mechanical components [184]. They have recently been used in the detection of diseases such as oncovirus [185], cholesterol [186], DNA [187] and glucose [188]. More than 9.6 million people died worldwide in 2018 as a result of oncovirus [189], a virus that has been related to the emergence of cancer. The smaller size of the virus and how it diverges around the cell region define the effect of cancer existence. Early detection is essential for lowering mortality rates because cancer is one of the main causes of death around the globe. As a result, researchers are concentrating on finding new methods for detecting cancer cells before they spread, and PCF technology has emerged as an effective approach. Leland C. Clark used a biosensor to monitor blood glucose levels for the first time in 1962, as reported [190].

Various methods to detect cancerous cells have been developed throughout time, including microfluidic devices [191], immunocytochemistry [192], electrochemical methods [193], and Raman spectroscopy [194]. Particularly, spark fused tapers have been proposed for breast cancer detection using Raman spectroscopy [195], allowing early detection of cancerous cells at the molecular level. Using a plasmonic optical fiber, C. Ribaut et al. presented an immunosensor for lung cancer detection in 2017 [196], while N. Ayyanar et al. presented a novel PCF based sensor for detection of cancerous cell in 2018. The PCF sensor required cancerous cells to be injected into 0.6  $\mu\text{m}$  air holes, but in fact, this was found to be a challenging operation [197]. A nanocomposite material-coated photonic crystal based sensor was also presented that year, but it had a low sensitivity of just 43 nm/RIU [198].

A number of applications, including astrophysics, genetics, biomedical research, spectroscopy, sensing and telecommunications, are finding the terahertz (THz) band to be more attractive as a suitable frequency range [199]–[206]. This frequency band, which covers a broad range from 0.1 to 10 THz, offers a unique range of opportunities for different fields of study and technological advancements. Researchers have successfully developed chemical and biosensors that operate in the THz range using PCF technology. These sensors can detect on a wide range of chemical and biological elements, including salinity [207], cholesterol [208], blood components [203], and adulterated fuel [209]. PCF sensors, as compared to traditional fiber sensors, provide greater diversity and standard values for optical parameters, faster detection systems, and adjustable optical parameters with careful modification of the cladding and core hole of the PCF. PCF sensors also provide a number of advantageous characteristics, including improved sensitivity, low confinement loss, light weight and durability. The potential applications in chemical and biological sensing of PCF-based sensors have expanded due to the broad range of capabilities they provide. These include using surface plasmon resonance-based biosensors [210]–[212], investigating RNA and DNA [213]–[215], identifying cancerous cells [216]–[218], categorizing and detecting alcohol [219]–[223], and detecting formalin [224], [225]. The potential applications in chemical and biosensing of PCF-based sensors have increased as a result of these characteristics.

The proposed work demonstrates the design of a rapid cancer detection method based on a TC-PCF architecture in the terahertz (THz) frequency regime. Among the cancer cell types identified are those that cause blood cancer (Jurkat), cervical cancer (HeLa), cancer of the adrenal glands (PC12), skin cancer (Basal) and two forms of breast cancer (MDA-MB-231 and MCF-7). The FEM-based detection method assumes that the concentration of cancerous cell is to be 80% in the form of liquid. The finite element approach is used in a specifically designed PCF to examine the mode coupling of twin cores as part of the proposed method for early detection of different cancers. A significant difference was observed by comparing the changes in birefringence, coupling properties, and transmission between cancerous and normal cells using different refractive indices. The shift of the transmitted spectrum's largest wavelength dip is used to evaluate the sensitivity of the proposed TC-PCF sensor. This shows that a simple TC-PCF-based sensor could be used for the early detection of different cancerous cells.

### 5.1.2 PCF sensor design

The cancerous and normal cells, which is inserted within the PCF elliptical central hole, separates the two solid cores that make up the proposed TC-PCF, which is illustrated in Figure 5.1.1 (a). On the base material, the circular air holes are arranged in a hexagonal pattern with a pointed orientation. The air holes have a diameter ( $D$ ) of 470  $\mu\text{m}$  and a pitch ( $\Lambda$ ) of 500  $\mu\text{m}$

between any two adjacent air holes, which maintains the PCF over all air filling fraction (AFF) of 0.94. The PCF is suitable for operation at THz frequencies with low confinement loss owing to these dimensions and a constant refractive index of 1.53 for the base material (TOPAS), offering flexibility in fiber manufacture [226], [227]. FEM based COMSOL Multiphysics software is used to simulate and design the proposed PCF construction. There are two cores in the PCF named as Core A and Core B. As shown in Figure 5.1.1 (a), these cores are created by vertically eliminating two air holes that are located in the middle of the PCF. The elliptical hole in the center of the PCF is used for inserting a normal and cancerous cell to be detected. The major-axis of the elliptical hole in the proposed configuration is  $a = 260 \mu\text{m}$ , the minor axis,  $b = 140 \mu\text{m}$  is considered. According to Figure 5.1.1 (b), the geometrical meshing statistics required 3173 edge elements, 360 vertex elements and 24,222 triangular elements for the proposed PCF. The R.I. of the surroundings has a significant impact on the way light propagates in the core region of PCF. Therefore, both normal and cancerous cells exhibit a noticeable shift in the coupling length, transmission curve and birefringence. The R.I. and liquid percentage (%) of both normal and cancerous cells are obtained from [197], [228].

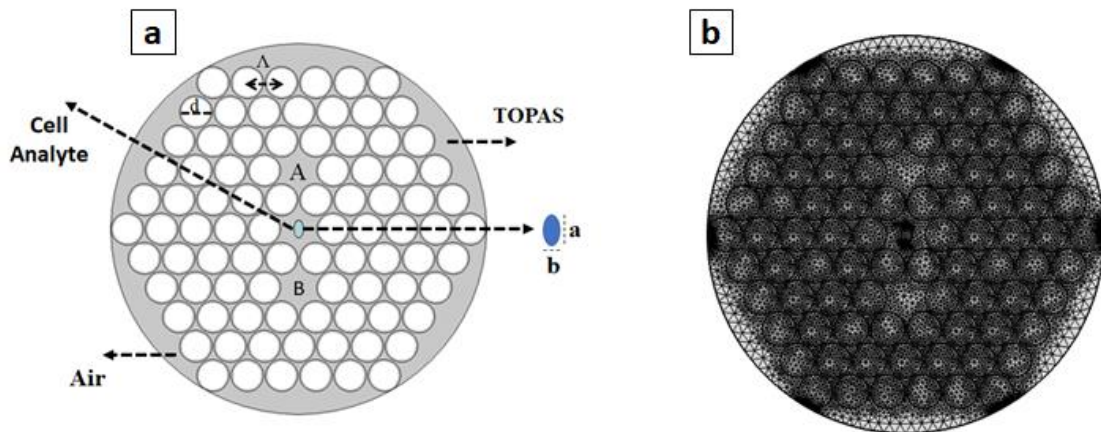


**Figure 5.1.1 (a) Cross-sectional view and (b) geometrical meshing statistics of proposed twin-core PCF sensor**

A general experimental setup to detect different cancerous cells is shown in Figure 5.1.2. A single mode fiber (SMF) is used in the setup to transmit light into the TC-PCF from a light source like laser or LED. An optical spectrum analyzer (OSA) can be used to see the output signal via another SMF. Between the TC-PCF and the SMF, a splice-free connecting approach can be used to reduce coupling losses. The OSA can be used to examine the shift in wavelength of the transmission spectra to detect the presence of cancerous cells. This procedure offers a simple and effective way to detect different cancerous cells.

According to coupling theory, the guided mode of a twin-core PCF contains four supermodes polarized in the X and Y directions that stand in for the even and odd modes at a frequency of 0.75 THz. The distribution of these four supermodes electric fields in the proposed PCF is illustrated in Figure 5.1.3.

### 5.1.3 Results simulation and discussion

The variation of effective refractive index difference between even and odd mode ( $\Delta n_{eo}$ ) for the x-polarized and y-polarized direction in Figure 5.1.4 show how the effective refractive index difference for different normal (30–70%) and cancerous cell (80%) decreases as the

frequency increases. A higher confinement of light within the core is implied by the decrease in  $\Delta n_{eo}$  with frequency seen in the proposed TC-PCF.

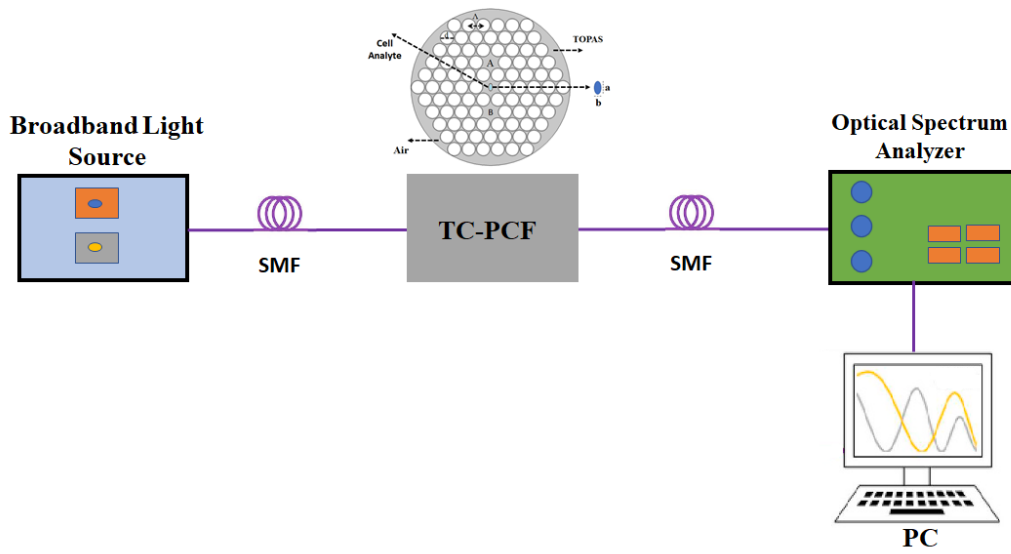


Figure 5.1.2 General representation of the PCF sensing setup for cancer cell detection

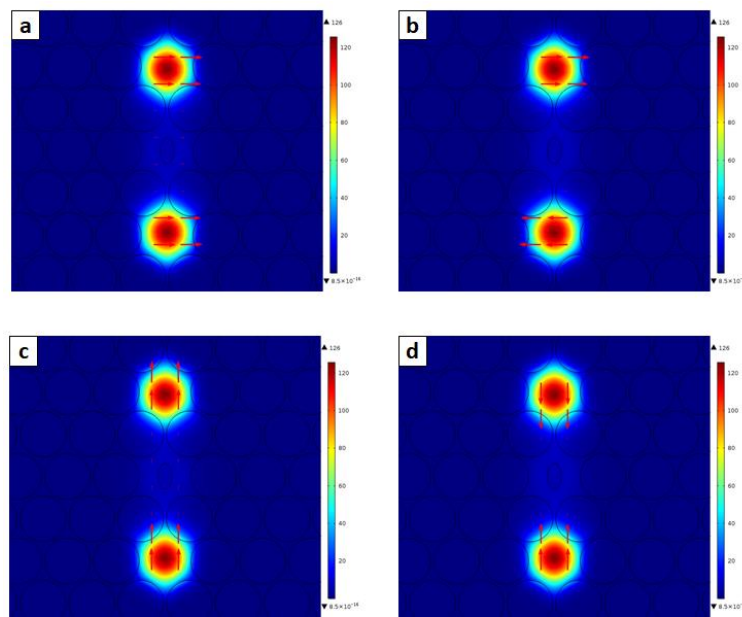


Figure 5.1.3 Electric field distribution of (a) x-even, (b) x-odd, (c) y-even and (d) y-odd mode at a frequency of 0.75 THz

A birefringent material can cause light to be divided into two separate rays that travel in different directions when it is subjected to polarization. Birefringence is the main cause of the optical phenomenon, known as double refraction. To calculate the TC-PCF birefringence parameter,  $B$ , equation (5.1.1) is used.

$$B = |Re(n_{eff}^x) - Re(n_{eff}^y)| \quad (5.1.1)$$

where the  $n_{eff}^x$  and  $n_{eff}^y$  symbols stand for the effective refractive indices of the x-polarized and y-polarized modes, respectively [228]. The total amount of variations in birefringence with changes in frequency is shown in Figure 5.1.5 for both cancerous (80%) and normal cell (30-

70%). The maximum range of birefringence, which exhibits a downward trend, is between 0.0026 and 0.0015. The sensitivity and coupling length of the proposed geometry are directly correlated with its birefringence. The proposed sensor birefringence starts at 0.0026 and decreases linearly as the frequency increases until it achieves a low birefringence value of 0.0015.

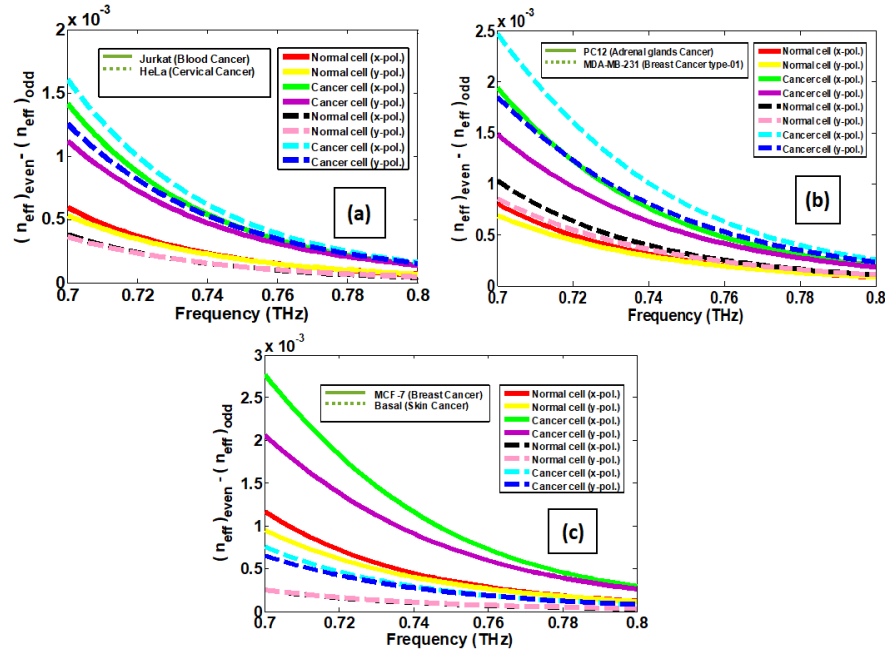


**Figure 5.1.4** Variation of  $\Delta n_{eo}$  with frequency for normal and cancerous cell (a) Helia and Jurkat (b) MDA-MB-231 and PC12 (c) Basal and MCF-7

The smallest length at which the maximum transmission of light can efficiently pass through the core for a PCF is known as the coupling length. This is applicable to both X and Y polarization and can be calculated by using equation (5.1.2).

$$L_c = \frac{\pi}{|\beta_e^i - \beta_o^i|} = \frac{\lambda}{2|n_e^i - n_o^i|} \quad (5.1.2)$$

where  $\beta_e^i$  and  $\beta_o^i$  respectively, are used to denote the propagation constants of the even and odd supermodes with  $i = x, y$  polarization, symbol  $\lambda$  represents the wavelength and the symbols  $n_e^i$  and  $n_o^i$ , respectively, denote the effective refractive indices for the even and odd mode [229]. The coupling length gradually varies as the frequency changes for both normal cells (30-70%) and cancerous cells (80%), as seen in Fig. 5.1.6. The graph indicates that the maximum coupling length that can be achieved lies between 0.8435 m and 6.013 m, with an upward curving trend.

The amount of optical power that is transferred between cores in a TC-PCF varies with the PCF length (L), according to the mode-coupling theory. The following expression can be used to describe this:

$$I_i(\lambda) = \sin^2\left(\frac{\pi}{\lambda}\Delta n_{i,eo}L\right), \text{ with } i = x, y \quad (5.1.3)$$

where symbol  $\Delta n_{i,eo}$ , denotes the effective refractive index difference for the even and odd modes [229].

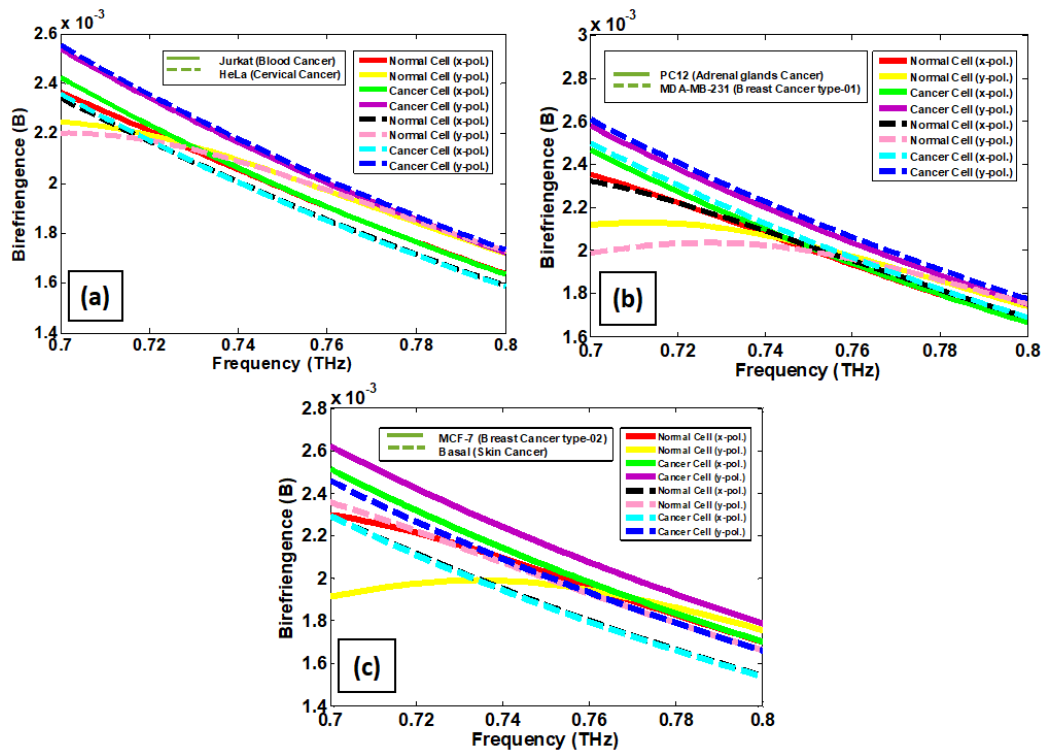


**Fig. 5.1.5** Variation of birefringence with frequency for normal and cancerous cell (a) HeLa and Jurkat (b) MDA-MB-231 and PC12 (c) Basal and MCF-7

By incorporating both x and y polarized light, the TC-PCF displays the total intensity of the operating light as output. The total output can be determined by taking into consideration the unique properties of the orthogonal x and y polarized light [230].

$$I(\lambda) = I_x + I_y \quad (5.1.4)$$

Equation (5.1.3) and equation (5.1.4) can be used to determine the total output intensity.

$$I(\lambda) = 1 - \cos\left[\frac{\pi(\Delta n_x + \Delta n_y)L}{\lambda}\right] \cdot \cos\left[\frac{\pi(\Delta n_x - \Delta n_y)L}{\lambda}\right] \quad (5.1.5)$$

The output intensity spectra for both normal and cancerous cells is illustrated in Figure 5.1.7 using fibers with varied lengths and frequency between 0.7 and 0.8 THz. The maximum dips observed for different cancerous cells (80%) were at wavelengths of  $3.963 \times 10^5$  nm,  $3.994 \times 10^5$  nm,  $3.968 \times 10^5$  nm,  $3.963 \times 10^5$  nm,  $3.973 \times 10^5$  nm and  $3.984 \times 10^5$  nm for HeLa, Jurkat, PC12, Basal, MDA-MB-231 and MCF-7, respectively with corresponding fiber lengths of 1.0 m, 1.0 m, 0.8 m, 2.0 m, 0.6 m, 0.5 m, respectively. In contrast, different normal cells (30–70%) showed their maximum dips at  $4.207 \times 10^5$  nm,  $4.207 \times 10^5$  nm,  $4.189 \times 10^5$  nm,  $4.237 \times 10^5$  nm,  $4.207 \times 10^5$  nm and  $4.195 \times 10^5$  nm for HeLa, Jurkat, PC12, Basal, MDA-MB-231 and MCF-7, respectively with corresponding fiber lengths of 1.0 m, 1.0 m, 0.8 m, 2.0 m, 0.6 m, 0.5 m, respectively.

The wavelength shift in the transmission spectra caused by change in cancerous and normal cells is used to determine the proposed sensor's sensitivity. The proposed TC-PCF sensitivity for cancerous cell is defined as

$$S_{\lambda}(nmRIU^{-1}) = \Delta\lambda_{Dip}/\Delta n_i \quad (5.1.6)$$

where  $\Delta\lambda_{Dip}$  represents the overall shift in maximum wavelength dip and  $\Delta n_i$  is the difference in R.I. for normal and cancerous cell [228].

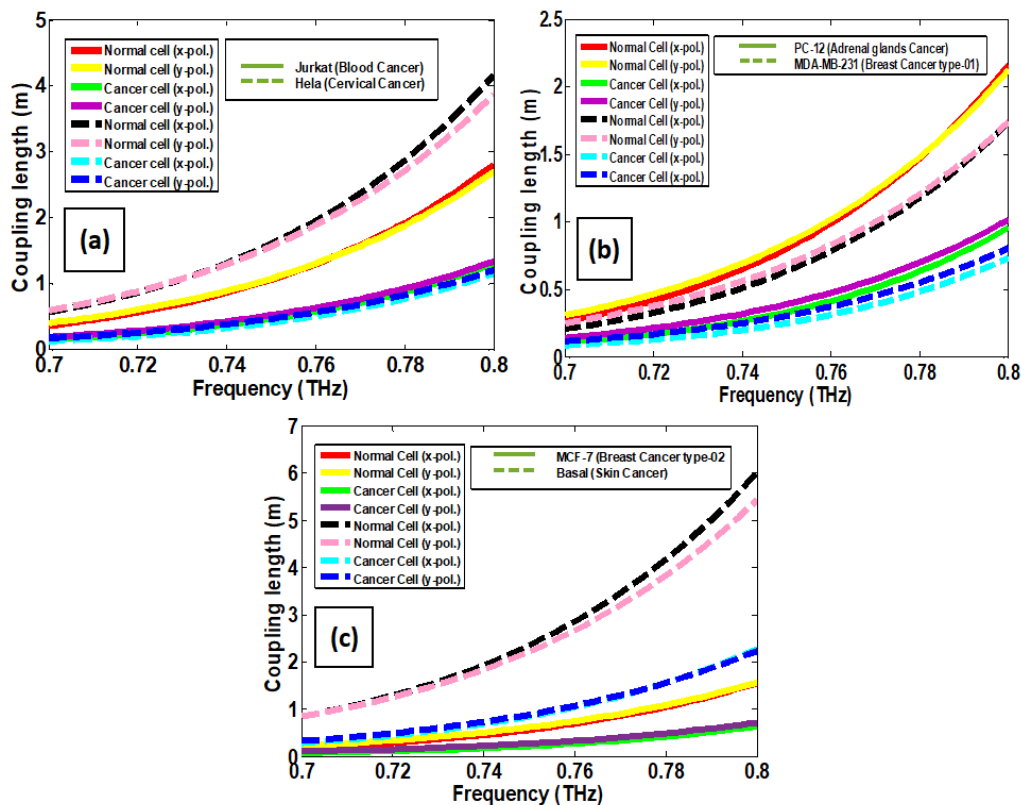


**Fig. 5.1.6** Variation of coupling length with frequency for normal and cancerous cell (a) Helia and Jurkat (b) MDA-MB-231 and PC12 (c) Basal and MCF-7

The proposed sensor has a sensitivity of 1016666.67 nm/RIU, 1521428.57 nm/RIU, 1578571.42 nm/RIU, 1370000 nm/RIU, 1671428.57 nm/RIU and 1507142.85 nm/RIU for Helia, Jurkat, PC12, Basal, MDA-MB-231 and MCF-7 cancerous cells, respectively, as obtained by using Equation (5.1.6). A comparison of the sensitivity between the proposed sensor and the sensor reported in the reference [185], [197], [228], [231]–[233] is shown in Table 5.1.1. The findings show that our proposed TC-PCF sensor has higher sensitivity over the currently available sensors, to the best of our knowledge. Previous models had a drawback in that they only evaluated the performance of individual cancer cells in relation to that of nearby cancer cells. They didn't compare cancerous cells to normal cells while making their evaluation. The proposed method aims to get over this limitation by detecting various cancerous cell bio-samples in contrast to normal cells. This method is considered to be the most effective one for detecting cancer.

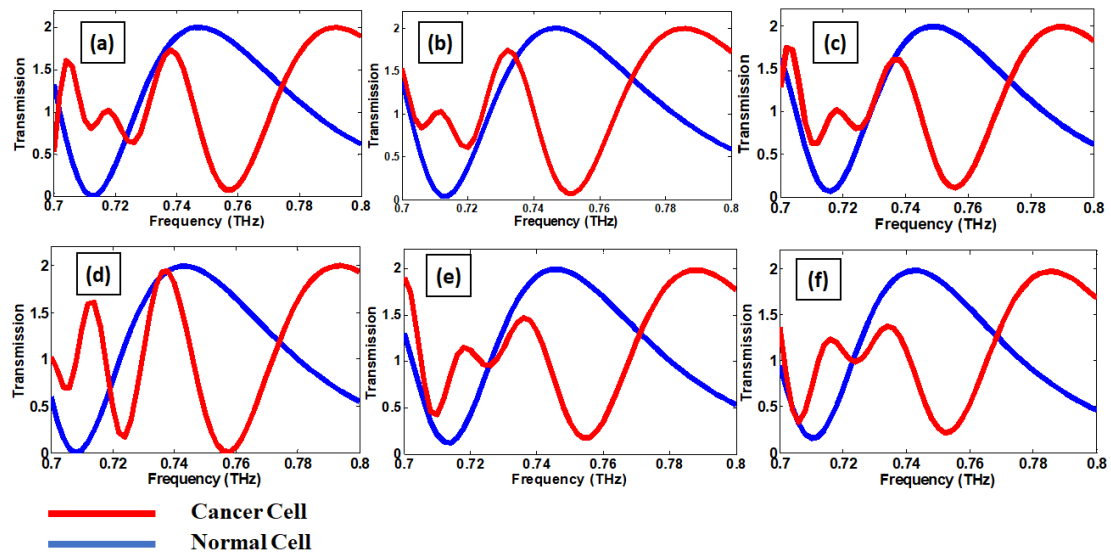


**Fig. 5.1.7** Transmission curve with frequency for normal and cancerous cell (a) HeLa (b) Jurkat (c) PC12 (d) Basal (e) MDA-MB-231 and (f) MCF-7

**Table 5.1.1** Comparison between the sensor sensitivity and structure of the proposed and previous reported sensors

Reference	PCF Structure	Cell Name	Sensitivity (nm/RIU)	Background Material
[228]	Side polished PCF	Cervical cancer (HeLa) Blood cancer (Jurkat) Adrenal glands cancer (PC12) Skin cancer (Basal) Breast cancer (MDA-MB-231) Breast cancer (MCF-7)	10208.33 10714.28 10000 17500 17857.14 18071.42	Silica
[197]	Dual-core PCF	Cervical cancer (HeLa) Skin cancer (basal) Breast cancer (MDA-MB-231)	7083.33 6000 7857.14	Silica
[185]	Triangular shape PCF	Blood cancer (Jurkat)	8571.43	Silica
[231]	Bottom-Side Polished PCF	Cervical cancer (HeLa) Blood cancer (Jurkat) Adrenal glands cancer (PC12) Skin cancer (Basal) Breast cancer (MDA-MB-231) Breast cancer (MCF-7)	20000 22857 20714 20000 21428 25000	Silica
[232]	Heart-shaped PCF	Cervical cancer (HeLa) Blood cancer (Jurkat) Adrenal glands cancer (PC12) Breast cancer (MDA-MB-231) Breast cancer (MCF-7)	7916.67 8571.43 9285.71 10000 10000	Silica

[233]	Side tapered PCF	Cervical cancer (HeLa) Blood cancer (Jurkat) Adrenal glands cancer (PC12) Skin cancer (Basal) Breast cancer (MDA-MB-231) Breast cancer (MCF-7)	4333.33 4642.86 5500 3150 6428.57 7142.86	Silica
Proposed Structure	Twin-Core PCF	Cervical cancer (HeLa) Blood cancer (Jurkat) Adrenal glands cancer (PC12) Skin cancer (Basal) Breast cancer (MDA-MB-231) Breast cancer (MCF-7)	1016666.67 1521428.57 1578571.42 1370000 1671428.57 1507142.85	TOPAS (cyclic olefin copolymer)

#### 5.1.4 Impact of diameter variation on sensitivity

Figure (5.1.8), (5.1.9), (5.1.10) (5.1.11), (5.1.12) and (5.1.13) illustrates the TC-PCF transmission curve with different diameters for HeLa, Jurkat, PC 12, Basal, MDA-MB-231 and MCF-7 cell, respectively with corresponding fiber lengths of 1.0 m, 1.0 m, 0.8 m, 2.0 m, 0.6 m, 0.5 m, respectively. Figure (5.1.8-a), (5.1.8-b) and (5.1.8-c) shows the proposed TC-PCF can obtain a sensitivity of 1008323.56 nm/RIU at  $D = 466 \mu\text{m}$ , 1012334.34 nm/RIU at  $D = 468 \mu\text{m}$  and 1016666.67 nm/RIU at  $D = 470 \mu\text{m}$ , respectively for HeLa cell. Figure (5.1.9-a), (5.1.9-b) and (5.1.9-c) indicates the proposed TC-PCF can obtain a sensitivity of 1507142.85 nm/RIU at  $D = 466 \mu\text{m}$ , 1514285.71 nm/RIU at  $D = 468 \mu\text{m}$  and 1521428.57 nm/RIU at  $D = 470 \mu\text{m}$ , respectively for Jurkat cell. Figure (5.1.10-a), (5.1.10-b) and (5.1.10-c) illustrates the proposed TC-PCF can obtain a sensitivity of 1576757.37 nm/RIU at  $D = 466 \mu\text{m}$ , 1578486.50 nm/RIU at  $D = 468 \mu\text{m}$  and 1578571.42 nm/RIU nm/RIU at  $D = 470 \mu\text{m}$ , respectively for PC 12 cell. Figure (5.1.11-a), (5.1.11-b) and (5.1.11-c) shows the proposed TC-PCF can obtain a sensitivity of 1360157.89 nm/RIU at  $D = 466 \mu\text{m}$ , 1363654.15 nm/RIU at  $D = 468 \mu\text{m}$  and 1370000 nm/RIU nm/RIU at  $D = 470 \mu\text{m}$ , respectively for Basal cell. Figure (5.1.12-a), (5.1.12-b) and (5.1.12-c) indicates the proposed TC-PCF can obtain a sensitivity of 1662471.65 nm/RIU at  $D = 466 \mu\text{m}$ , 1666757.37 nm/RIU at  $D = 468 \mu\text{m}$  and 1671428.57 nm/RIU nm/RIU at  $D = 470 \mu\text{m}$ , respectively for MDA-MB-231 cell. Figure (13-a), (13-b) and (13-c) illustrates the proposed TC-PCF can obtain a sensitivity of 1498258.96 nm/RIU at  $D = 466 \mu\text{m}$ , 1502324.65 nm/RIU at  $D = 468 \mu\text{m}$  and 1507142.85 nm/RIU nm/RIU at  $D = 470 \mu\text{m}$ , respectively for MCF-7 cell. Diameter optimization indicates the proposed TC-PCF sensor has superior sensitivity at  $D = 470 \mu\text{m}$ .

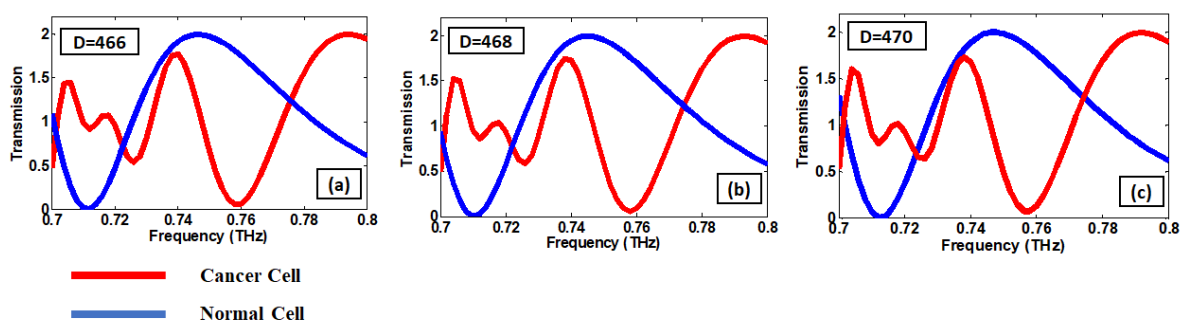


Fig. 5.1.8 Transmission curve with different diameter of  $D$ , for HeLa cell (a)  $466 \mu\text{m}$  (b)  $468 \mu\text{m}$  and (c)  $470 \mu\text{m}$

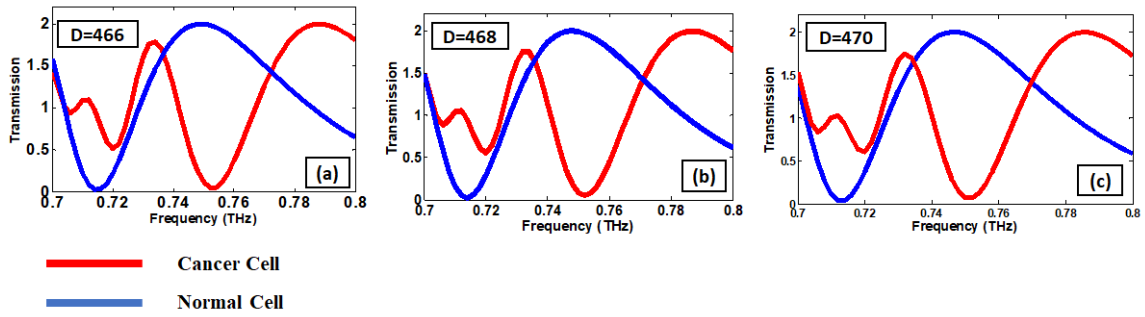


Fig. 5.1.9 Transmission curve with different diameter of D, for Jurkat cell (a) 466 μm (b) 468 μm and (c) 470 μm

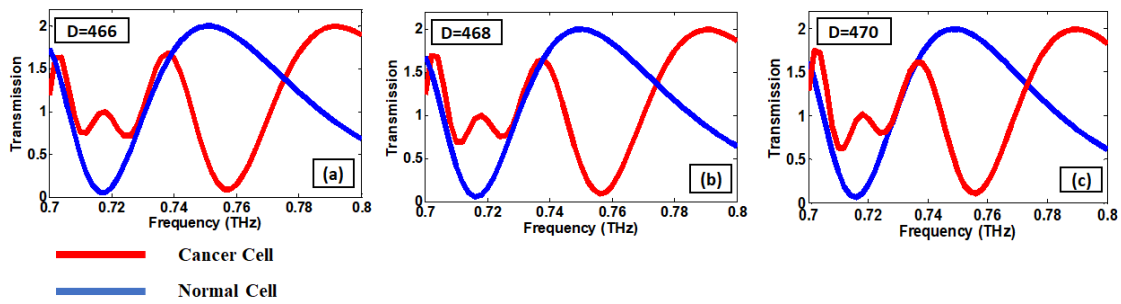


Fig. 5.1.10 Transmission curve with different diameter of D, for PC 12 cell (a) 466 μm (b) 468 μm and (c) 470 μm

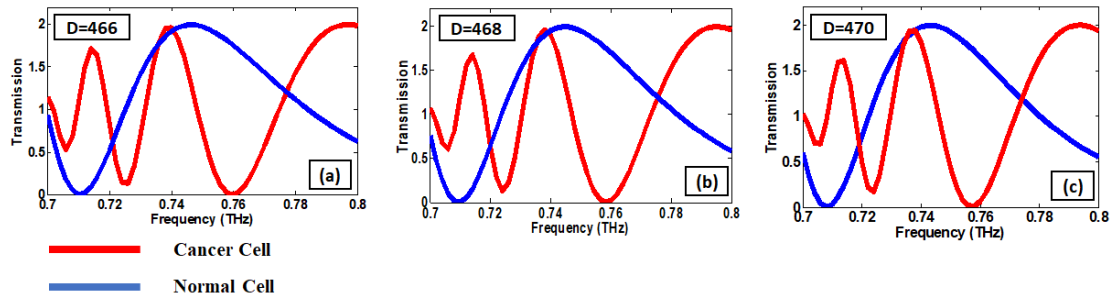


Fig. 5.1.11 Transmission curve with different diameter of D, for Basal cell (a) 466 μm (b) 468 μm and (c) 470 μm

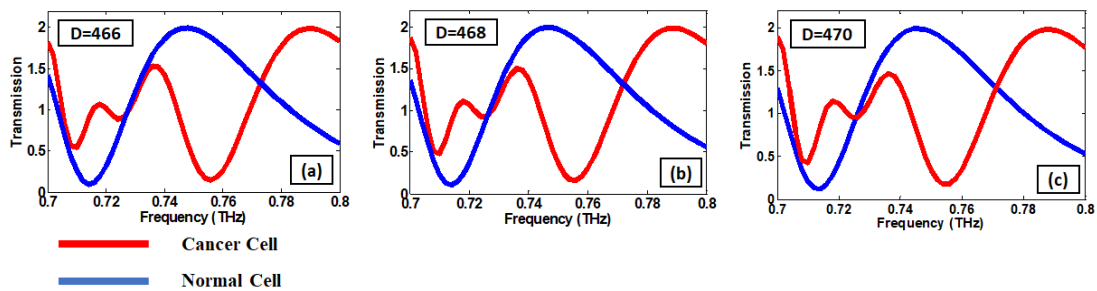
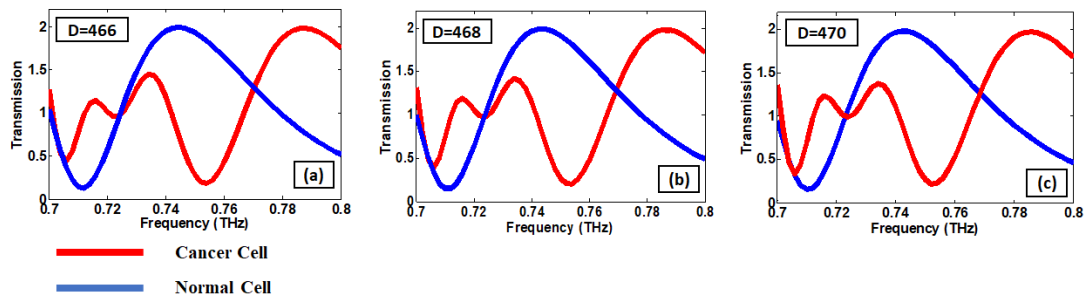


Fig. 5.1.12 Transmission curve with different diameter of D, for MDA-MB-231 cell (a) 466 μm (b) 468 μm and (c) 470 μm



**Fig. 5.1.13** Transmission curve with different diameter of  $D$ , for MCF-7 cell (a) 466  $\mu\text{m}$  (b) 468  $\mu\text{m}$  and (c) 470  $\mu\text{m}$

### 5.1.5 Summary

In this work, for the early detection of different cancerous cells, a novel type of sensor based on TC-PCF technology has been introduced by using the Finite Element Method and the COMSOL software. Our proposed sensor comprises injecting the sample cell (normal or cancerous) in the form of fluid, which interacts with the electric field during the propagation of light between the two cores of the TC-PCF, into the central elliptical hole of the structure. The guiding characteristics of transmission, are strongly influenced by the R.I. of the sample cell. As a result of the different R.I. values between normal and cancer cells, the proposed TC-PCF displays distinct optical properties for both types of cells. The proposed sensor can achieve a high sensitivity of 1016666.67 nm/RIU, 1521428.57 nm/RIU, 1578571.42 nm/RIU, 1370000 nm/RIU, 1671428.57 nm/RIU and 1507142.85 nm/RIU for Hela, Jurkat, PC12, Basal, MDA-MB-231 and MCF-7 cancerous cells, respectively based on numerical analysis. Our proposed sensor exhibits great potential for the detection of different cancerous cells in the future because of its simple design and sensing technique.

## 5.2 Design and Optimization of Terahertz Based D-shaped Photonic Crystal Fiber for Blood Component Detection

### 5.2.1 Introduction

Biosensors are devices that employ biological components like antibodies, enzymes and nucleic acids to detect the presence of certain biological components or substances. RBCs, hemoglobin, WBCs, plasma, and water are among the components of human blood that are able to be detected using photonic crystal fiber (PCF) based biosensors [234]. Human blood is an intricate fluid that composed of over 4000 functional elements [235]. It is essential for supplying nutrients and oxygen to body cells while aiding in the removal of waste. Blood is thicker than water because it contains numerous cells and proteins. The average quantity of blood within a human body is 5 liters (7%) of blood. This blood volume contains 55% plasma, a liquid portion of which comprises 99% water and the remaining blood volume contains various components [236]. Protein is an essential part of plasma, playing crucial roles in promoting blood clotting and facilitating the transportation of diverse substances within the blood. Blood also contains glucose and variety of dissolved nutrients. Approximately 45% of the total blood volume is made up of blood cells, with white blood cells engaging in infection defense, red blood cells are specialized cells responsible for oxygen delivery to tissues and dedicated to transporting respiratory gases [237]–[239], and platelets aiding in the clotting process. Analyzing blood samples is an essential part of the diagnostic process to identify the presence of numerous disorders associated with blood such as thalassemia, anaemia, myeloma and haemophilia [234].

By using PCF technology, the sensor not only addresses the limitations of conventional systems but also enhances optical properties with greater diversity. Moreover, it boasts quicker detection of biological analytes compared to conventional methods. The PCF-based sensor's standout achievement is its ability to adjust optical properties by fine-tuning the arrangement, dimensions, and configurations of its air holes. Furthermore, these sensors built on PCF technology guarantee elevated sensitivity, compactness, affordability, resilience, and heightened versatility. This is accomplished by offering effective remedies for a wide array of environmental and industrial challenges [240]. In recent years, the PCF-based sensor has emerged as an intelligent component within fiber optic technology, showcasing its substantial potential across various applications. These encompass chemical sensing [241]–[243], alcohol sensing [244]–[246], genetic diagnostics [247][14], time domain spectroscopy [248], [249], cancer detection [250]–[253], medical diagnosis [254], RNA analysis [248], DNA analysis [255], [256] etc. particularly within the terahertz frequency range. This frequency band, spanning from 0.1 to 10 THz, occupies the space between microwave and infrared frequencies within the electromagnetic spectrum. Of particular note, terahertz-based photonic biosensors have garnered significant attention for their applications in sensing and detection, notably within the realm of biomedical sensing [257].

However, the benefits of photonic crystal fibers (PCF) provide researchers with the opportunity to investigate diverse models for detecting various analytes within the THz range. For instance, a noteworthy achievement in chemical sensing was demonstrated by Asaduzzaman et al., who attained a sensitivity of 49% at a wavelength range from 0.7 to 1.7  $\mu\text{m}$  [258]. Several studies have been conducted to detect substances like water, benzene, and ethanol. Sen. et al. introduced a model with a hexagonal structure that achieved relative sensitivities of 57%, 57.27% and 57.18% for water ( $n = 1.33$ ), benzene ( $n = 1.366$ ) and ethanol ( $n = 1.354$ ), respectively [259]. Additionally, Kanmani et al. proposed a PCF model that achieved remarkable relative sensitivities of 77.23%, 77.18% and 77.08% for water ( $n = 1.33$ ), ethanol ( $n = 1.354$ ) and benzene ( $n = 1.366$ ), respectively [260]. In 2019, Podder et al. developed a PCF sensor that exhibited a relative sensitivity of 63.4% in detecting sulfuric acid for the maximum concentration of  $\text{H}_2\text{SO}_4$  at a wavelength range from 0.8 to 1.8  $\mu\text{m}$  [261]. Another notable example is the circular PCF designed for sensing blood components presented, where a maximum sensitivity of 66.49% was achieved at a wavelength range from 0.7 to 1.4  $\mu\text{m}$ . The primary aim of this proposed work is to detect numerous human diseases and play a crucial role in medical science [234]. Further advancements were made by Ahmed et al. in 2018, achieving an even higher sensitivity of approximately 80.93% for RBCs, 80.56% for hemoglobin, 80.13% for WBCs, 79.39% for water, and 79.91% for plasma in the THz frequency range from 1.5 THz to 3.5 THz [236]. In 2020, a novel hollow rectangular core photonic crystal fiber (RCPCF) was specifically designed for detecting crucial blood components. This innovative fiber structure features six rectangular air holes arranged in a horizontal configuration, forming the cladding. Topas was chosen as the primary bulk material due to its remarkable properties in the THz range. The sensor operational range spans from 0.8 THz to 1.8 THz, offering significant advantages such as a high mode area, minimal confinement loss, and exceptional relative sensitivity. At the high-frequency end of 1.8 THz, the RCPCF demonstrates exceptional relative sensitivity results of 94.38% for RBCs, 93.72% for hemoglobin, 92.94% for WBCs, 90.8% for water, and 92.14% for plasma [262]. Recently in 2023, Vijayalakshmi et al. developed a bi-core PCF sensor that exhibited a maximum sensitivity of 6930 nm/RIU in detecting blood component such as RBCs, hemoglobin, WBCs, plasma, and water, covering the refractive index range of 1.33 to 1.40 [263]. These discussions clearly indicate that there exists significant potential for enhancing the sensing properties of PCF-based models.

In this study, a DC-PCF has been proposed for detecting primary blood components such as RBC, WBC, water, plasma and hemoglobin. The proposed sensor has demonstrated superior sensitivity, achieving 1487500 nm/RIU with a fiber length of 0.2 m in the frequency range from 0.7 THz to 0.8 THz. The achieved high sensitivity of the designed sensor is attributed to a thorough analysis of diverse PCF parameters, thereby rendering it highly applicable for a wide range of applications in the field of biosensing. Operating effectively within a refractive index (RI) range spanning from 1.33 to 1.40, the sensor distinguishes itself by achieving remarkable sensitivity without resorting to the use of any plasmonic materials. A comprehensive exploration of various PCF parameters has been undertaken, encompassing factors like RI difference, birefringence, coupling length, transmission spectrum and transmittance curve. By closely monitoring spectral shifts of the transmittance curve aligned with their corresponding refractive indices, the distinctive components present in blood can be accurately discerned and identified. The proposed sensor presented here is designed using COMSOL Multiphysics software. The proposed biosensor has the potential to be a highly sensitive and selective option for detecting blood compositions.

### 5.2.2 Design Methodology

Figure 5.2.1 (a) depicts the design configuration of the proposed THz PCF sensor, which is constructed using TOPAS material, alongside a detailed depiction of the D-shape structure. We opt for a solid core due to its ability to facilitate the operation of light across a wide range of wavelengths. The central elliptical hole of the PCF is utilized for the insertion of blood components, with the aim of their detection. Different analytes, including RBC, WBC, water, plasma, and hemoglobin have a distinct refractive index (RI), with values of 1.40 for RBC, 1.36 for WBC, 1.33 for water, 1.35 for Plasma and 1.38 for hemoglobin. To enhance sensitivity, we have removed one air hole on each side from the central elliptical hole. This results in the creation of a dual-core structure for the sensor, where light confinement occurs between these two cores. In the proposed configuration, the elliptical hole's major axis (a) is 340  $\mu\text{m}$  and minor axis (b) is 190  $\mu\text{m}$  are taken into consideration. The air holes, with a diameter (d) of 470  $\mu\text{m}$  and spaced at a pitch ( $\Lambda$ ) of 500  $\mu\text{m}$  between any two consecutive holes, ensure a consistent air filling fraction (AFF) of 0.94 throughout the PCF. A fine mesh is employed during simulation, whereas a parametric sweep is applied to vary the operating frequency. As depicted in Figure 5.2.1 (b), the geometric meshing statistics for the proposed PCF included 2,016 edge elements, 203 vertex elements, and 14,556 triangular elements. TOPAS has been selected as the background material for the proposed structure due to its remarkable optical properties, including exceptional transparency, strong resistance to acids and alkalis, nice biocompatibility, a wide range of adjustable deflection temperatures, a constant refractive index ( $n = 1.53$ ) across a broad frequency range, impressive strength, excellent heat resistance, outstanding water vapor barrier characteristics, significant light transmission (91%), suitability for high humidity conditions, and minimal material dispersion [240], [264] To date, various fabrication methods have been documented, including capillary stacking, sol-gel, extrusion, and 3D printing. Capillary stacking and the sol-gel technique are commonly employed for manufacturing circular and elliptical holes [265], while asymmetric hole structures (rectangular) have been successfully fabricated through extrusion [266] and 3D printing [267]. Consequently, the capillary stacking and sol-gel methods are recommended for fabricating the proposed DC-PCF sensor structure. The method prototype, depicted in Figure 5.2.2, involves stacking small span capillaries of fixed diameters into a glass tube of larger diameter to achieve completion. The proposed sensor introduced here is constructed using COMSOL Multiphysics Software, which is affiliated with the numerical approach known as the finite element method (FEM).

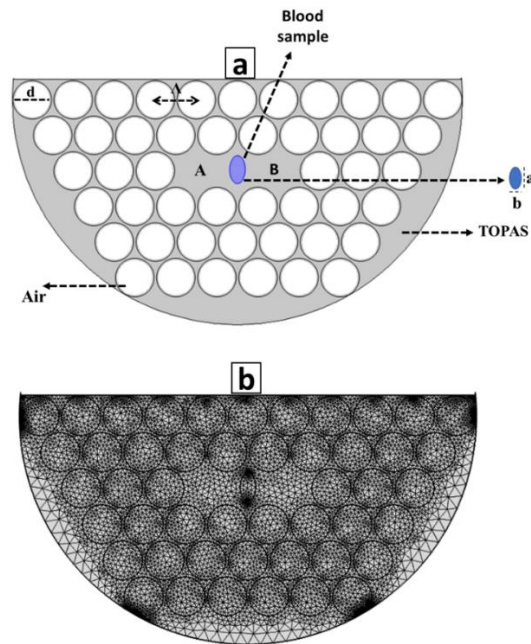


**Fig. 5.2.1** Design of the proposed PCF sensor with dual solid cores: (a) 2D cross section view and (b) Fine mesh statistics

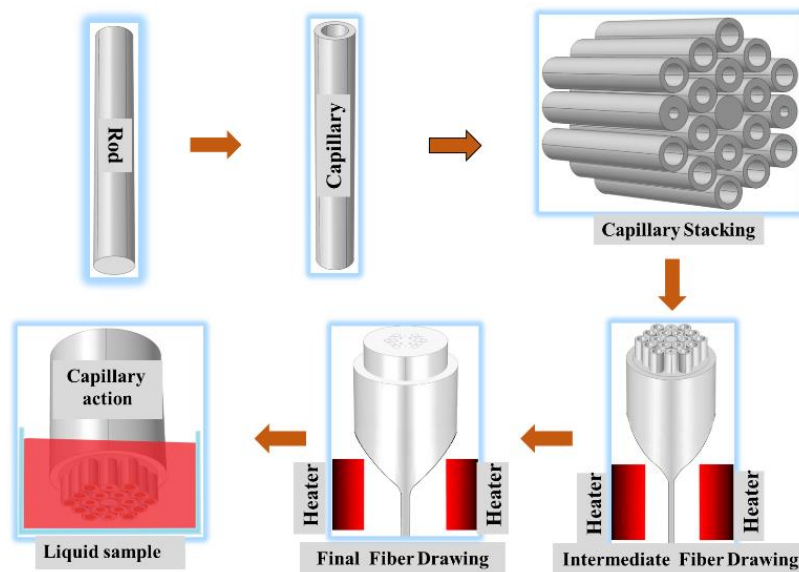


**Fig. 5.2.2** Fabrication technique for proposed PCF using capillary stacking

The experimental setup for assessing the accuracy of identifying blood components using the proposed PCF biosensor is depicted in Figure 5.2.3. A broadband light source (BLS) is used to transmit optical light via a single-mode fiber (SMF). The SMF can be connected to the biosensor using the Fujikura Splicer splicing method. Various blood components are positioned in the sensing channel. Prior to measuring new samples, the PCF biosensor probes are required to undergo washing with deionized water. Changes occur in blood component samples as they react with ligands inside the sensing channel. The interaction between ligands and target molecules induces changes in the optical properties (wavelength shift in the transmittance spectrum) of the guided mode in the DC-PCF sensor. These optical changes are detected and analyzed to quantify the various blood components. The optical spectrum analyzer (OSA)

captures the focused light through the SMF. In the end, the computer connected to the OSA generates the final spectrum.

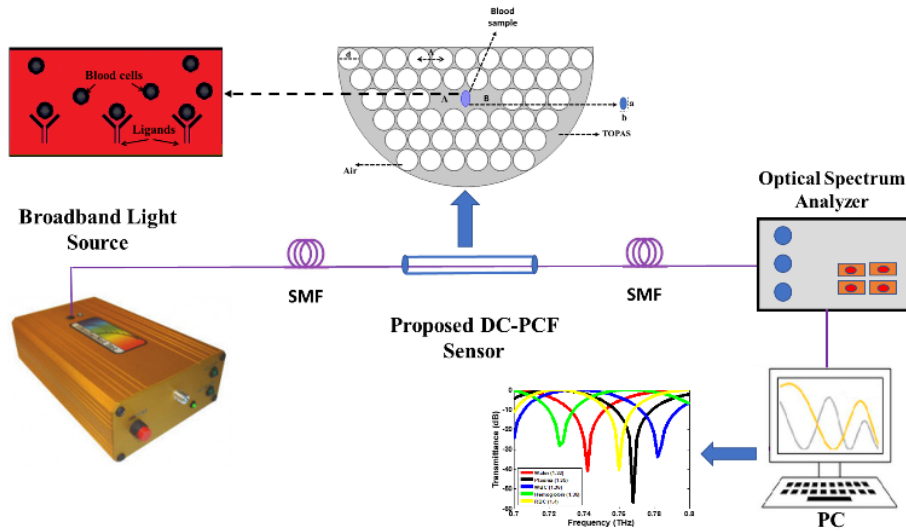


Fig. 5.2.3 Representation of experimental setup for blood component detection

### 5.2.3 Results analysis and discussion

In the cross-sectional view, there are two fiber cores that establish separate waveguides, and within PCFs, mode coupling can occur. In DC-PCF sensors, mode coupling describes the interaction and transfer of optical power between the modes of the two fiber cores. This phenomenon is influenced by factors such as core separation, wavelength, and external perturbations like temperature, pressure, and strain. The strength of mode coupling, quantified by the coupling coefficient, is critical for the sensor's performance and sensitivity [268]. According to the theory of mode coupling, the interaction in a dual-core fiber can be explained through the description of four super modes, encompassing both even (x-even and y-even) and odd (x-odd and y-odd) modes.

These super-modes arise from the inherent modes of the individual cores, showcasing symmetric and anti-symmetric field distributions, respectively. Figure 5.2.4 shows the distribution of the electric field among the dual core for the x and y polarized super-modes at a frequency of 0.75 THz. Figure 5.2.5 depicts a three-dimensional (3-D) visualization showcasing the electric field strength across various modes.

The initial estimation of the difference in effective refractive indices between the even and odd super-modes serves as a starting point for calculating the other parameters. It is evaluated by

$$\Delta n_{eo} = |n_e - n_o| \quad (5.2.1)$$

where,  $n_e$  and  $n_o$  represent the effective refractive indices for even and odd modes, respectively.

The graph in Figure 5.2.6 illustrates how the effective refractive index difference ( $\Delta n_{eo}$ ) between even and odd modes varies for x-polarized directions. It demonstrates that as the frequency increases, the effective refractive index difference decreases for primary blood components.

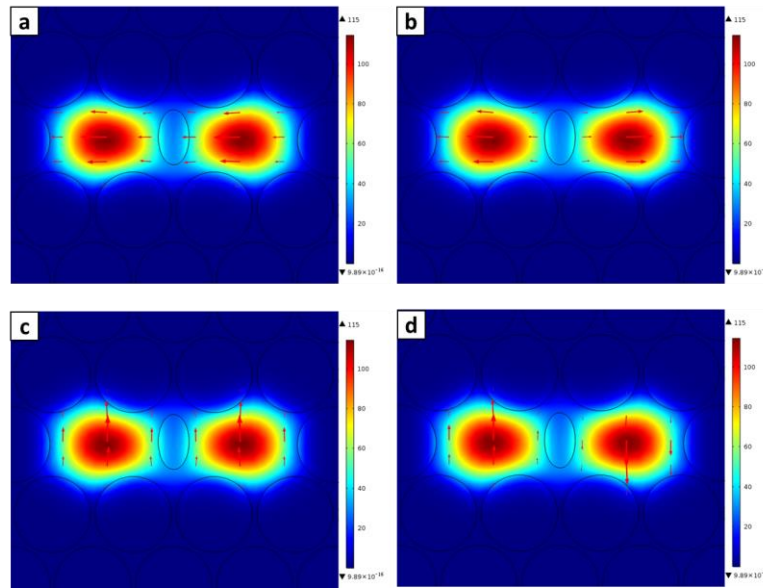


**Fig. 5.2.4 Electric field distribution within a symmetric core, showcasing four distinct modes: (a) even x-polarization (b) odd x-polarization (c) even y-polarization and (d) odd y-polarization**

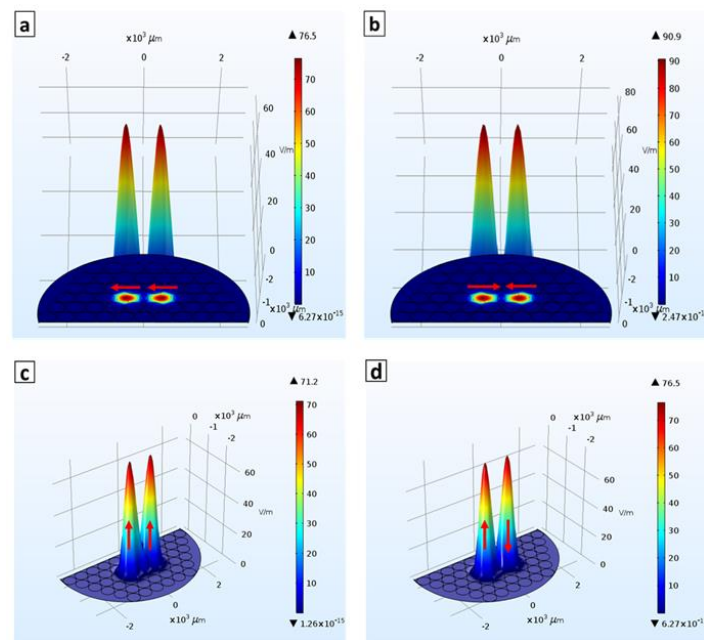


**Fig. 5.2.5 3-D view of Electric field distribution for four distinct modes: (a) even x-polarization (b) odd x-polarization (c) even y-polarization and (d) odd y-polarization**

Birefringent materials can induce the phenomenon of double refraction, wherein light is split into two distinct rays traveling in different directions upon polarization. The calculation of the birefringence parameter,  $B$ , specific to DC-PCF, involves employing equation (5.2.2).

$$B = |Re(n_{eff}^x) - Re(n_{eff}^y)| \quad (5.2.2)$$

where, the symbols  $n_{eff}^x$  and  $n_{eff}^y$  represent the effective refractive indices corresponding to the x and y-polarized modes, respectively [261]. Figure 5.2.7 illustrates the overall variation in birefringence with frequency changes. Within the frequency range of 0.0062 to 0.0035, there

is a discernible descending trend in the maximum range of birefringence. The sensitivity and coupling length of the proposed design exhibit a direct correlation with its birefringence. The initial birefringence of the proposed sensor is 0.0062, and it undergoes a linear decrease with increasing frequency until it reaches a minimal birefringence value of 0.0035.

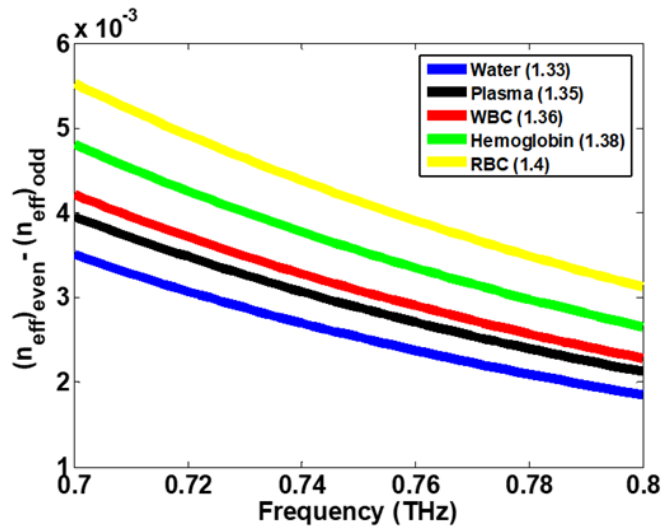


Fig. 5.2.6 Change in refractive index difference varies with different frequency

The coupling length, defined as the minimum length at which optimal light transmission occurs through the core of a PCF. It can be determined by using equation (5.2.3).

$$L_c = \frac{\pi}{|\beta_e^i - \beta_o^i|} = \frac{\lambda}{2|n_e^i - n_o^i|} \quad (5.2.3)$$

where,  $\beta_e^i$  and  $\beta_o^i$  represent the propagation constants of the even and odd supermodes with  $i = x, y$  polarization,  $\lambda$  is the wavelength, and  $n_e^i$  and  $n_o^i$  denote the effective refractive indices for the even and odd modes, respectively [269]. The coupling length changes gradually with the frequency, as depicted in Figure 5.2.8. The graph reveals that the maximum achievable coupling length falls within the range of 0.0387 m to 0.1011 m, exhibiting an upward-curving trend.

To detect blood constituents in a sample analyte, the coupling mode theory is employed, where power is transmitted between the two cores. The power transferred from first core to another in the designed DC-PCF is computed by utilizing equation (5.2.4).

$$I(\lambda) = \sin^2\left(\frac{\pi}{\lambda} \Delta n_{eo} L\right) \quad (5.2.4)$$

where, symbol L represents the length of the fiber, and  $\lambda$  denotes the wavelength [270]. Figure 5.2.9 depict the transmission curve achieved for the primary blood constituents for x polarized light with corresponding fiber length of 0.2 m. These graphs cover the refractive index range of 1.33 to 1.4. It is worth noting that the power transmission graph of the proposed DC-PCF follows a sinusoidal pattern.

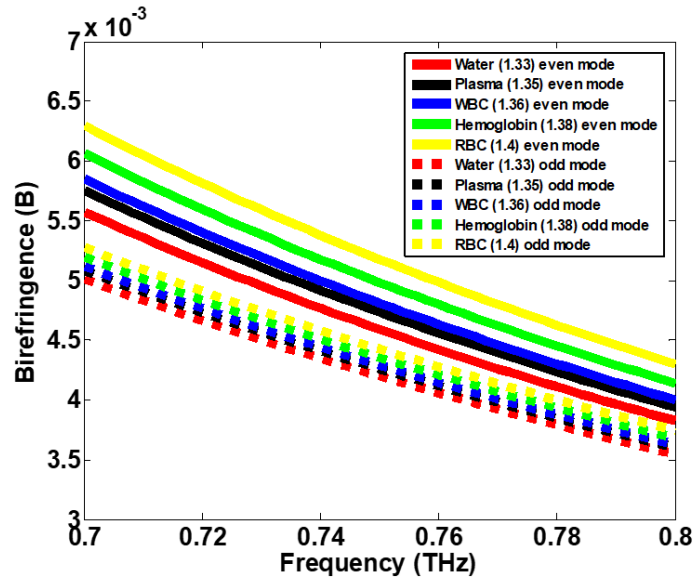


Fig. 5.2.7 Change in birefringence with respect to different frequency

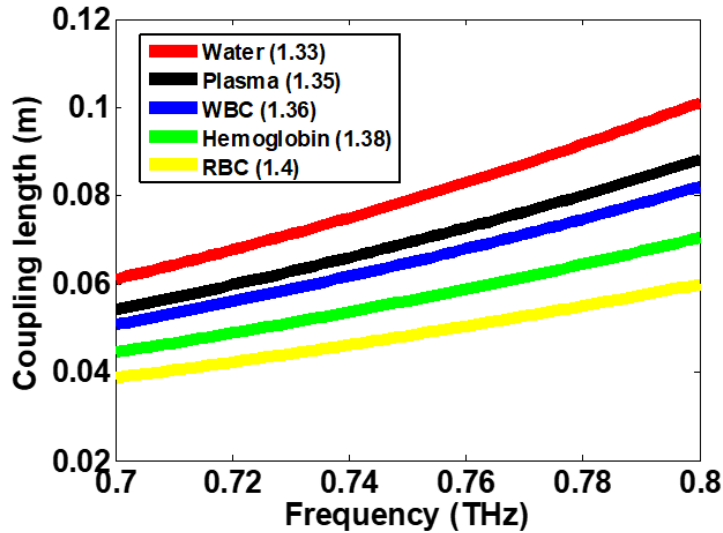


Fig. 5.2.8 Change in coupling length with respect to different frequency

Moreover, when taking into account the optical light entering the initial core, the transmittance can be determined by using equation (5.2.5).

$$T_r = 10 \log_{10} \frac{P_{out}}{P_{in}} \quad (5.2.5)$$

here, we consider  $P_{in}$  as the maximum power of  $P_{out}$  [263].

Figure 5.2.10 display the transmittance curve for the five main blood constituents, covering the refractive index range of 1.33 to 1.4, for x polarized light with corresponding fiber length of 0.2 m. By monitoring the shift in refractive index (RI), it is possible to sense and detect the corresponding blood component. The frequency peaks ( $f_{peak}$ ) observed for major blood constituents, like water, plasma, WBC, Hemoglobin and RBC at 0.74 THz, 0.766 THz, 0.78 THz, 0.724 THz and 0.758 THz, respectively.

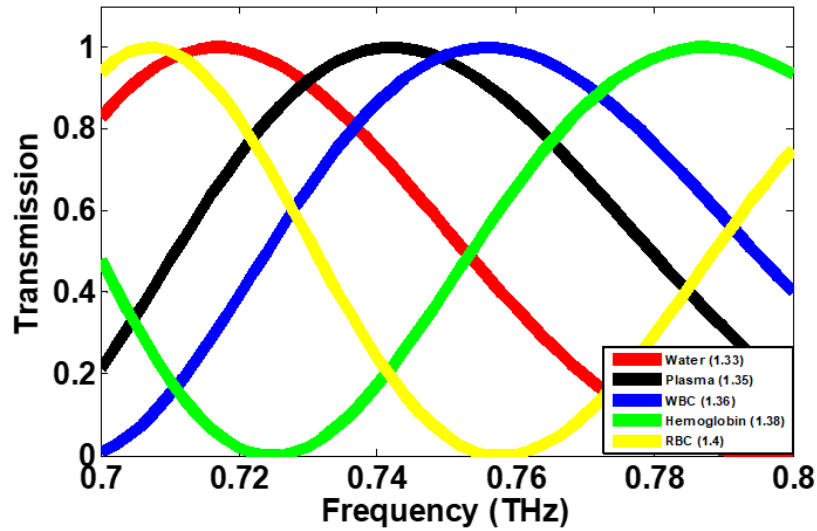


Fig. 5.2.9 Transmission curve of a DC-PCF with a length of 0.2 m

Sensitivity is a crucial parameter used to evaluate the performance of PCF sensor. It is determined by examining the peak shift in response to changes in the refractive index of the blood constituent. This is articulated as follows;

$$S_{\lambda}(nmRIU^{-1}) = \Delta\lambda_{peak}/\Delta n_a \quad (5.2.6)$$

where,  $\Delta\lambda_{peak}$  represents the shift in wavelength peak,  $\Delta n_a$  denotes the difference in RI of the blood samples and  $\left(\lambda_{peak} = \frac{\text{speed of light } (c)}{f_{peak}}\right)$  [271]. The maximum sensitivity determined for the main blood constituents, spanning from 1.33 to 1.4, is 1487500 nm/RIU. Table 5.2.1 depicts a thorough examination of the anticipated outcomes of the proposed PCF biosensor study alongside a recently reported sensor with a similar sensing range. The analysis reveals that the sensitivity of the proposed PCF significantly exceeds that of the other PCF biosensor. This technique is recognized as the simple and most effective approach for blood components detection.

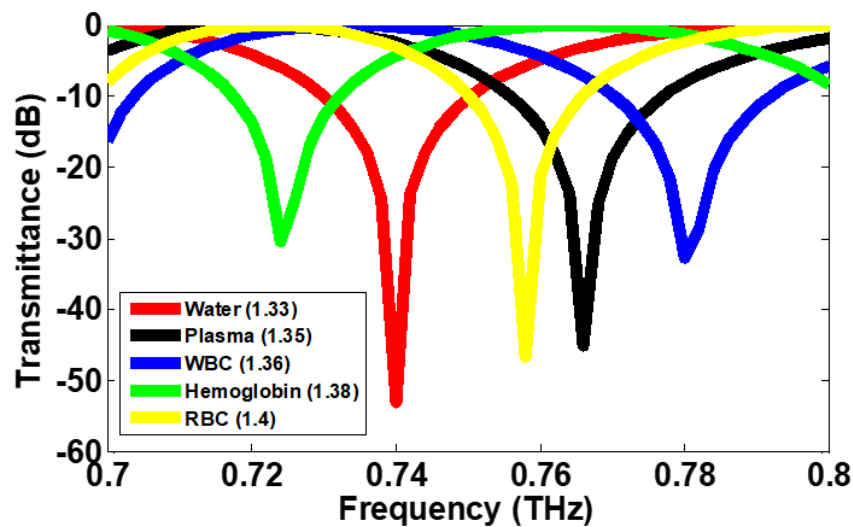


Fig. 5.2.10 Transmittance curve of DC-PCF for primary blood components

**Table 5.2.1**  
**Comparison of proposed PCF biosensor with recently reported biosensors**

Reference	Design of sensor structure	Sensing range	Sensitivity (nm/RIU)
[272]	D-shape PCF with pyramid grating	1.355-1.385	5200
[273]	AZO-coated plasmonic PCF nano sensor	1.33-1.40	1950
[274]	D-shaped PCF RI sensor	1.33-1.354	294.11
[275]	D-shape open-loop PCF temperature sensor	1.35-1.40	3300
[263]	Bi-core PCF	1.33-1.40	6930
Proposed structure	THz based D-shape DC-PCF	1.33-1.40	1487500

#### 5.2.4 Effect of pitch variation on sensitivity

Figure 5.2.11 demonstrates the pitch variation in the transmittance curve of DC-PCF for the five primary blood constituents with corresponding fiber length of 0.2 m. Figure (5.2.11-a), (5.2.11-b), and (5.2.11-c) reveal that the proposed DC-PCF achieves a sensitivity of 1479500 nm/RIU at pitch ( $\Lambda$ ) = 498  $\mu\text{m}$ , 1487500 nm/RIU at pitch ( $\Lambda$ ) = 500  $\mu\text{m}$ , and 1483500 nm/RIU at pitch ( $\Lambda$ ) = 502  $\mu\text{m}$ , respectively. Optimizing the pitch demonstrates that the proposed DC-PCF sensor achieves maximum sensitivity at  $\Lambda = 500 \mu\text{m}$ .

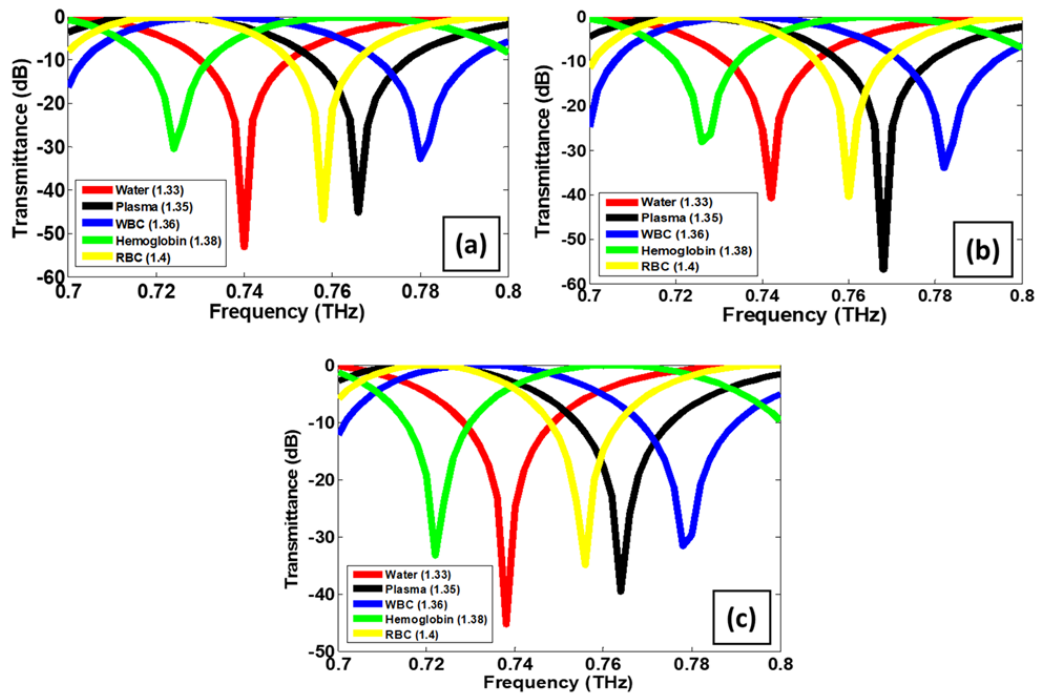


**Fig. 5.2.11** Transmittance curve with different pitch ( $\Lambda$ ), for five primary blood constituents (a) 498  $\mu\text{m}$  (b) 500  $\mu\text{m}$  and (c) 502  $\mu\text{m}$

### 5.2.5 Summary

In this manuscript, a highly sensitive DC-PCF based biosensor is presented using COMSOL Multiphysics Software and FEM method, encompassing a frequency range from 0.7 to 0.8 THz. The proposed sensor is designed to operate within a refractive index (RI) range of 1.33 to 1.4, facilitating the detection of main components in blood. The blood constituents analyzed include water, plasma, WBC, hemoglobin and RBC. Detection and sensing of these components are achieved through coupling mode theory involving the transfer of power between the twin cores. A comprehensive investigation of various PCF parameters has been carried out, including refractive index difference, birefringence, coupling length, transmission spectrum, and transmittance curve. Our research reveals that the sensor reaches its highest sensitivity, measuring 1487500 nm/RIU, when utilizing a 0.2 m long fiber at pitch ( $\Lambda$ ) = 500  $\mu\text{m}$ . The simplicity in structure ensures an easy fabrication process for the proposed biosensor. For the fabrication of the proposed DC-PCF sensor structure, it is recommended to utilize capillary stacking and sol-gel methods. The exceptional sensing proficiency and straightforward design of this proposed biosensor establish it as a valuable contender for utilization in both industrial and medical applications.

## 5.3 Design and optimization of terahertz photonic crystal fiber based biosensor to detect malaria disease

### 5.3.1 Introduction

Photonic crystal fiber (PCF) based sensors are suitable for biosensing applications due to their minimal need for mechanical components [276]. They have been recently used in detecting various diseases, including oncovirus [277], cholesterol [278], DNA [279], glucose [280] and malaria [281]. When mosquito bites a human, it injects a parasite in its sporozoite stage into the human tissues, initiating the malarial infection process. Within red blood cells (RBCs), this parasite goes through three stages like ring stage, trophozoite stage and schizont stage. Each stage has different refractive indices (R.I.) for the infected RBCs. The initial cycle of malaria is known as ring stage, during which merozoites enter the RBCs and change into uninucleate trophozoites. Subsequently, multinuclear cells transition from trophozoites to schizonts during the schizont stage. An important parameter for malaria identification is the R.I. difference between normal human RBCs and malaria infected human RBCs [282].

The terahertz (THz) band is increasingly gaining attention as a frequency range for many fields, such as astrophysics, genetics, biomedical research, spectroscopy, sensing, and telecommunications [283]–[290]. Stretching across 0.1 to 10 THz, this frequency band provides a diverse range of possibilities for various areas of research and technological progress. Compared to conventional fibre sensors, PCF sensors offer increased diversity and standardized optical parameters, fast detection systems, and the ability to regulate optical parameters via precise modifications to the core and the cladding arrangement of the PCF.

In this study, through the observations of human RBCs interacting with the malaria parasites (i.e., *Plasmodium falciparum*), as they progress through various stages of the intraerythrocytic cycle including ring, trophozoite, and schizont stages, we have proposed a R.I. biosensor using DC-PCF for the malaria detection. It employs finite element analysis in a specially constructed DC-PCF to investigate the mode coupling of dual cores as part of the suggested approach to detect the malaria disease. Notable distinctions were observed when changes in effective R.I., coupling characteristics, and transmission curve of the DC-PCF were compared for normal

human RBCs and malaria infected human RBCs. The shift of the peak wavelength in the transmission curve is used for sensitivity calculations of the proposed DC-PCF based biosensor to detect malaria.

### 5.3.2 Sensor design

The design configuration of the proposed THz DC-PCF based biosensor, which is constructed using TOPAS material, is shown in Figure 5.3.1 along with a detailed representation of the hexagonal shape structure. In the DC-PCF, there are two cores referred to as Core A and Core B, and these cores are formed by removing one air hole on each side from the middle elliptical hole. The middle elliptical hole of the DC-PCF is utilized to insert analyte, having different R.I. shown in Table 5.3.1, aiming for their detection. It has a  $470\ \mu\text{m}$  diameter ( $D$ ) and a  $500\ \mu\text{m}$  pitch ( $\Lambda$ ) between neighboring air holes. The DC-PCF maintains an overall air filling fraction (AFF) of 0.94. This configuration, combined with a constant R.I. of 1.53 for the background material (TOPAS), makes the DC-PCF suitable for THz frequency operation with minimal confinement loss, providing manufacturing flexibility [291]. In the proposed configuration, the elliptical hole has a major axis of  $1200\ \mu\text{m}$  and a minor axis of  $240\ \mu\text{m}$ .

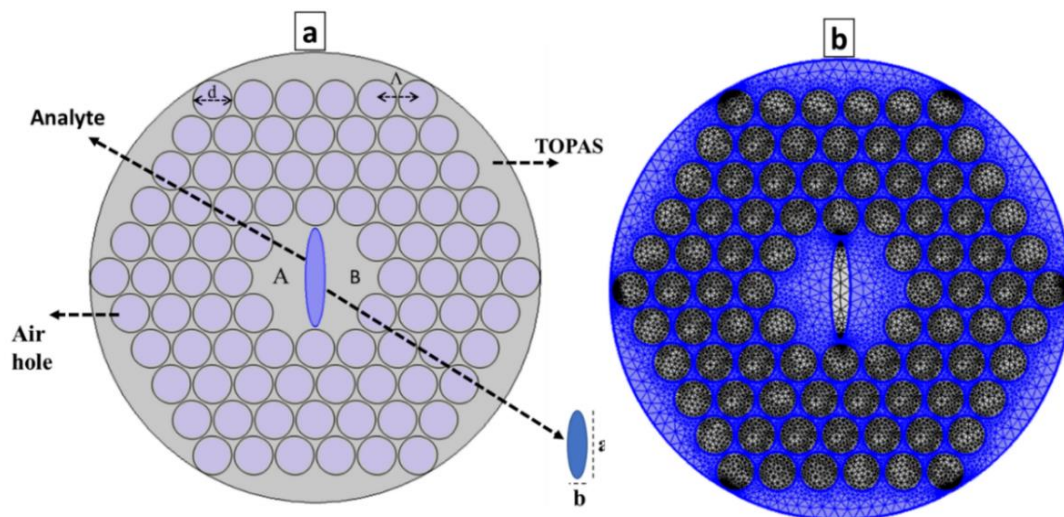


Fig. 5.3.1 (a) Configuration of proposed DC-PCF based biosensor (b) Fine mesh statistics

Several fabrication techniques, including capillary stacking, sol-gel, extrusion, and 3D printing, have been reported till date. Sol-gel and capillary stacking are frequently utilized in the fabrication of circular and elliptical holes [292], while asymmetric hole structures (rectangular) have been manufactured successfully by extrusion [293] and 3D printing [294]. Thus, for the fabrication of the suggested DC-PCF sensor structure, capillary stacking and sol-gel techniques are recommended. The method prototype is shown in Figure 5.3.2 and consists of stacking tiny span capillaries with fixed diameters into a bigger diameter glass tube in order to complete the process. The proposed PCF construction is simulated and designed using COMSOL Multiphysics software, which is based on FEM. During simulation, a fine mesh is used, and a parametric sweep is utilized to vary the frequency. The geometrical mesh statistics for the proposed DC-PCF consist of 3,079 edge elements, 344 vertex elements, and 23,644 triangular elements.

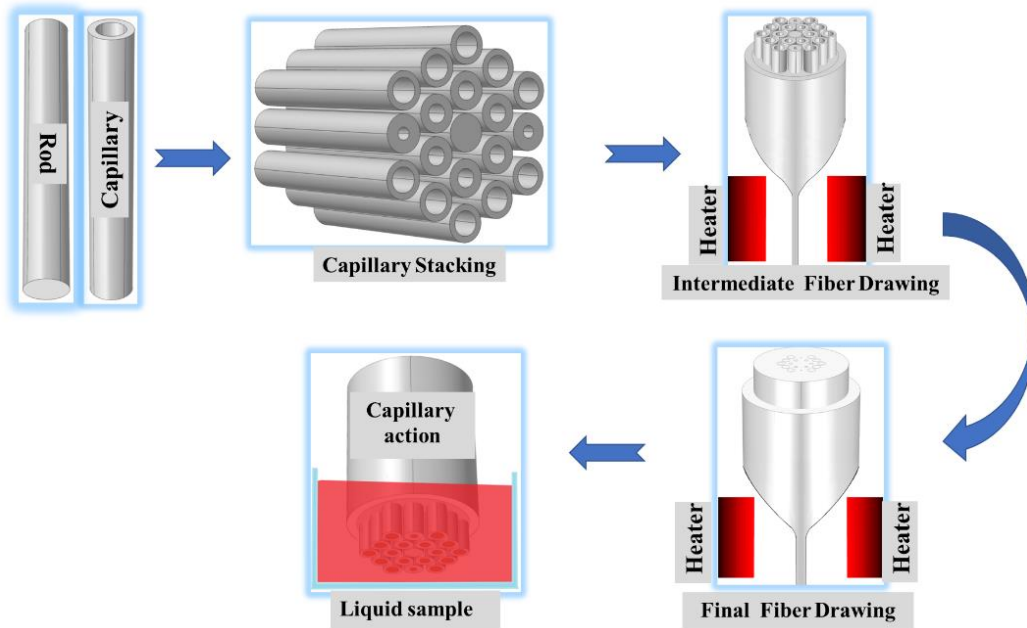


Fig. 5.3.2 Fabrication method for the suggested DC-PCF utilizing capillary stacking

Table 5.3.1 Refractive index of analyte at different stages

Different stages of RBCs	Refractive Index	References
Normal human	1.402	[282, 295, 296]
Infected human at ring stage	1.395	
Infected human at trophozoite stage	1.383	
Infected human at schizont stage	1.373	

The experimental configuration for evaluating the precision of malaria disease identification using the suggested PCF biosensor is illustrated in Figure 5.3.3. A broadband light source (BLS) is employed to propagate optical light over a single-mode fiber (SMF). The Fujikura Splicer splicing technique connects the SMF to the biosensor. The refractive index of various analytes at different stages of RBC is located in the sensing channel. Before taking measurements on new samples, it is necessary to wash the PCF biosensor probes with deionized water. Various transformations take place at various stages of RBC samples when they interact with ligands inside the sensing channel. Using the SMF, the optical spectrum analyzer (OSA) detects focused light. Ultimately, the computer connected to the OSA generates the final spectrum.

### 5.3.3 Results and discussion

In DC-PCF sensors, mode coupling refers to the interaction and transfer of optical power between the modes of the two fiber cores. This process is influenced by factors such as core separation, wavelength, and external deviations like pressure, temperature and strain. The effectiveness of mode coupling, measured by the coupling coefficient, is essential for the sensor's performance and sensitivity [297]. Coupling theory states that the guided mode in a

DC-PCF comprises of four supermodes. These supermodes are polarized along the X and Y directions, representing odd and even modes, respectively, at a frequency of 0.75 THz. Figure 5.3.4 illustrates the electric field distribution of the four supermodes. Figure 5.3.5 illustrates a three-dimensional (3-D) visualization of the electric field intensity across several modes.

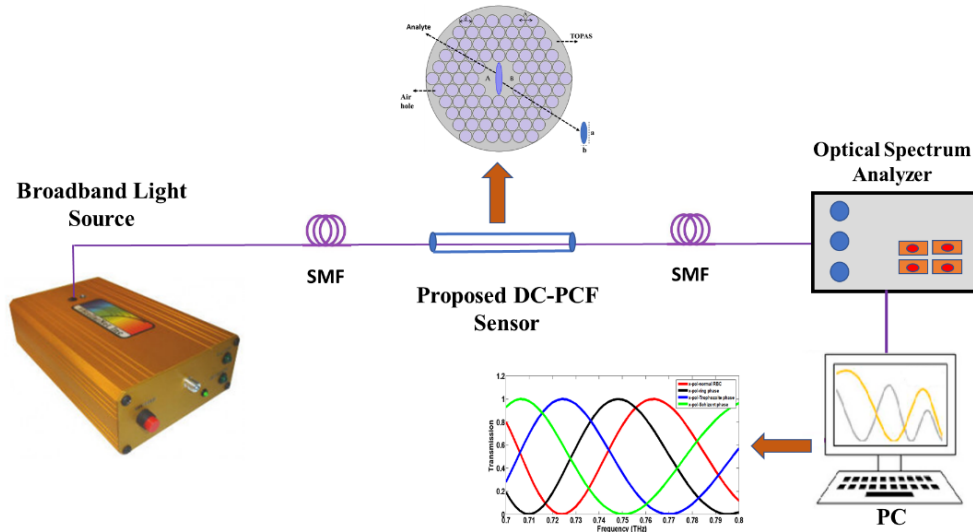


**Fig. 5.3.3 Experimental setup of proposed sensor**

Figure 5.3.6 illustrates the change in the effective refractive index difference ( $\Delta n_{eo}$ ) for both X and Y-polarized directions, indicating a decrease in  $\Delta n_{eo}$  as the frequency rises.

The coupling length, which represents the minimum length for optimal light transmission through the core of a DC-PCF, is consistent for both X and Y polarizations and can be determined using equation (1).

$$L_c = \frac{\pi}{|\beta_e^i - \beta_o^i|} = \frac{\lambda}{2|n_e^i - n_o^i|} \quad (5.3.1)$$

where  $\beta_e^i$  and  $\beta_o^i$  represent the propagation constants of the even and odd modes,  $\lambda$  denotes the wavelength [298]. As depicted in Figure 5.3.7, the coupling length exhibits a gradual increase with rising frequency.

In accordance with the mode-coupling theory, the optical power transmitted between the cores of a DC-PCF changes with respect to the length (L) of the PCF, as described by the following expression:

$$I_i(\lambda) = \sin^2\left(\frac{\pi}{\lambda} \Delta n_{i,eo} L\right), \text{ with } i = x, y \quad (5.3.2)$$

where  $\Delta n_{i,eo}$ , represents the effective refractive index difference [299, 300]. According to Figure 5.3.8 we have observed that the proposed DC-PCF power transmission curve is sinusoidal.

The sensitivity of the proposed biosensor is assessed by analyzing the wavelength shift in the transmission spectra resulting from changes in various analytes. The sensitivity of the proposed DC-PCF for detecting malaria is defined as

$$S_\lambda (nmRIU^{-1}) = \Delta \lambda_{peak} / \Delta n_i \quad (5.3.3)$$

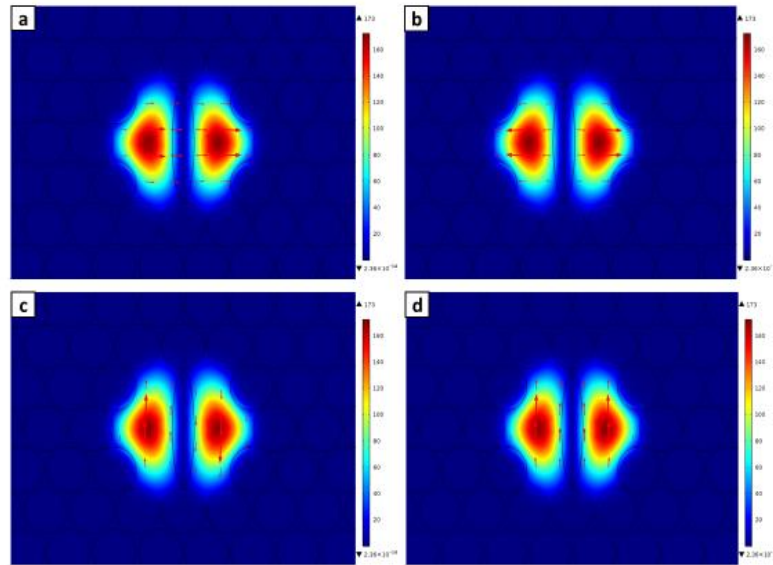


**Fig. 5.3.4** Distribution of electric field (a) even x-polarization, (b) odd x-polarization, (c) even y-polarization, and (d) odd y-polarization

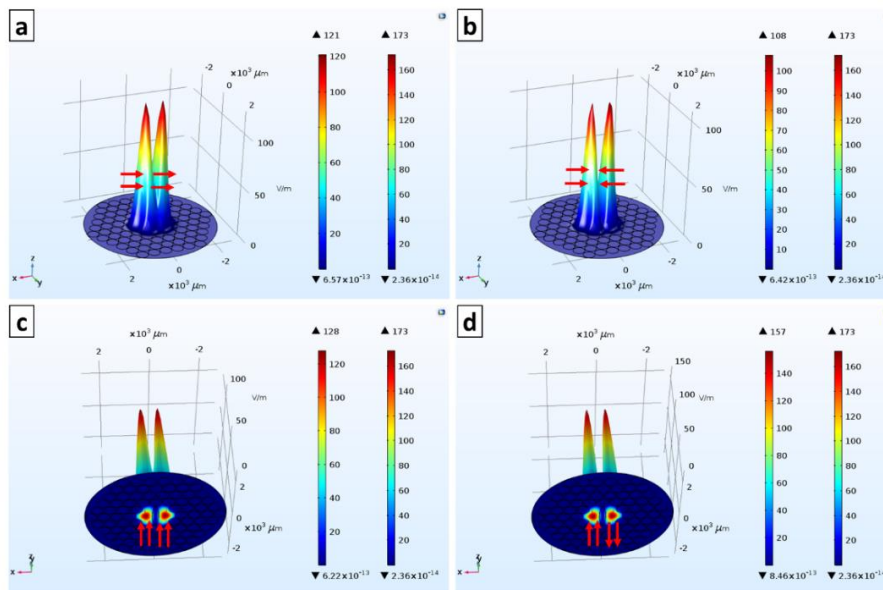


**Fig. 5.3.5** 3-D view of Electric field distribution for four distinct modes: (a) even x-polarization, (b) odd x-polarization, (c) even y-polarization, and (d) odd y-polarization

where  $\Delta\lambda_{peak}$  denotes the shift in peak wavelength and  $\Delta n_i$  represents the difference in R.I. for normal and different stages of RBCs and  $\left(\lambda_{peak} = \frac{\text{speed of light } (c)}{f_{peak}}\right)$  [301, 302]. Using Eq. (5.3.3), the presented biosensor achieves a maximum sensitivity across different stages, such as 12,00000 nm/RIU for the ring stage, 11,15263.15 nm/RIU for the trophozoite stage, and 11,13793.10 nm/RIU for the schizont stage under x-polarization. Similarly, under y-polarization, the sensitivity is observed to be 10,50000 nm/RIU for the ring stage, 10,54736.84 nm/RIU for the trophozoite stage, and 10,32758.62 nm/RIU for the schizont stage. Table 5.3.2 illustrates a sensitivity comparison between the proposed biosensor and the those already available in the literature [281, 303–305].

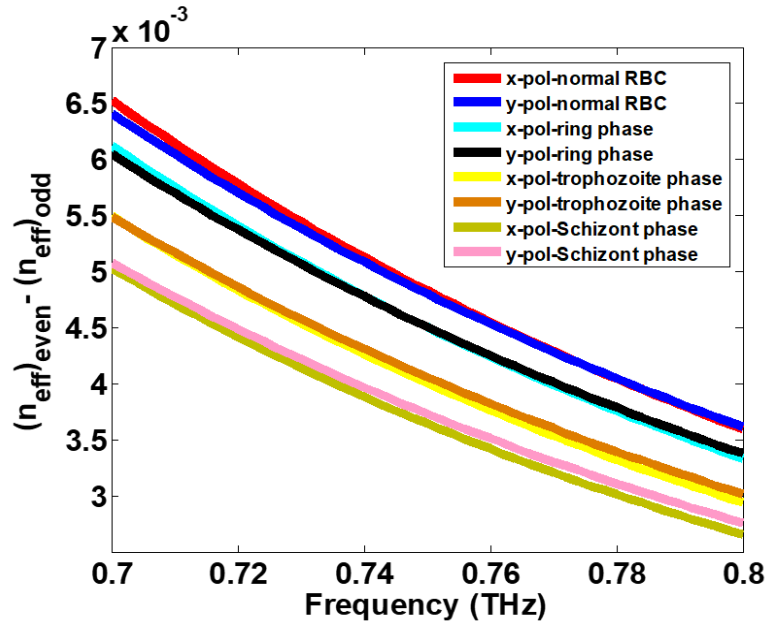


Fig. 5.3.6 Variations in  $\Delta n_{e0}$  with respect to frequency for different stages of RBCs

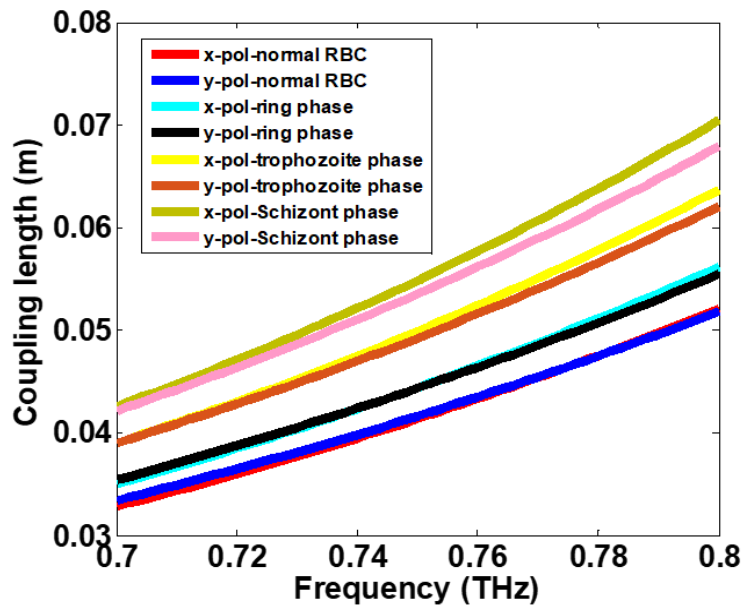


Fig. 5.3.7 Variations in coupling length with respect to frequency for different stages of RBCs

### 5.3.4 Impact of pitch variation on sensitivity

Figure 5.3.9 and 5.3.10 demonstrates the pitch variation in the transmission curve of DC-PCF for various stages of malaria infected RBCs, including the Ring stage, Trophozoite stage and Schizont stage. The maximum sensitivity achieved among these stages for three different pitch values under x and y polarization are shown in Figure 5.3.9 (a-c) and Figure 5.3.10 (a-c), respectively. It can be observed from Figure 5.3.9 (a-c) that under the x polarization, the proposed DC-PCF achieves a maximum sensitivity of 11,17142.85 nm/RIU at pitch ( $\Lambda$ ) = 498  $\mu\text{m}$ , 12,00000 nm/RIU at pitch ( $\Lambda$ ) = 500  $\mu\text{m}$ , and 11,35714.28 nm/RIU at pitch ( $\Lambda$ ) = 502  $\mu\text{m}$ , respectively. Similarly, it can be observed from Figure 5.3.10 (a-c) that under y-polarization, the proposed DC-PCF achieves a maximum sensitivity of 1024137.93 nm/RIU at pitch ( $\Lambda$ ) = 498  $\mu\text{m}$ , 10,54736.84 nm/RIU at pitch ( $\Lambda$ ) = 500  $\mu\text{m}$ , and 10,41034.48 nm/RIU at pitch ( $\Lambda$ ) = 502  $\mu\text{m}$ , respectively. Hence, optimizing the pitch demonstrates that the proposed DC-PCF

sensor achieves maximum sensitivity at  $\Lambda = 500 \mu\text{m}$ .

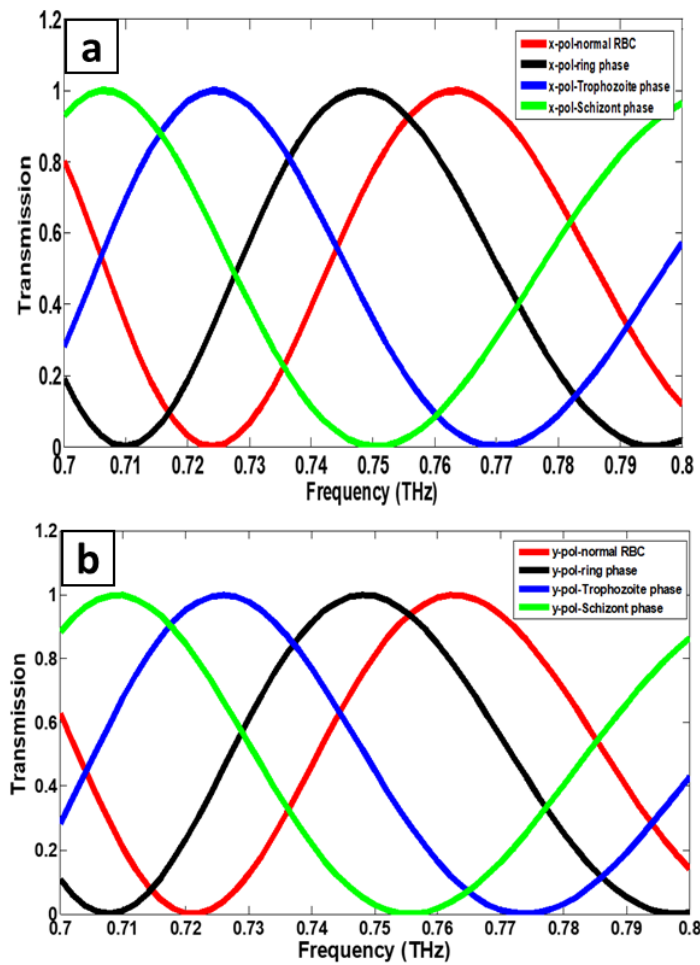


Fig. 5.3.8 Transmission curve with respect to frequency for (a) X and (b) Y-polarized light

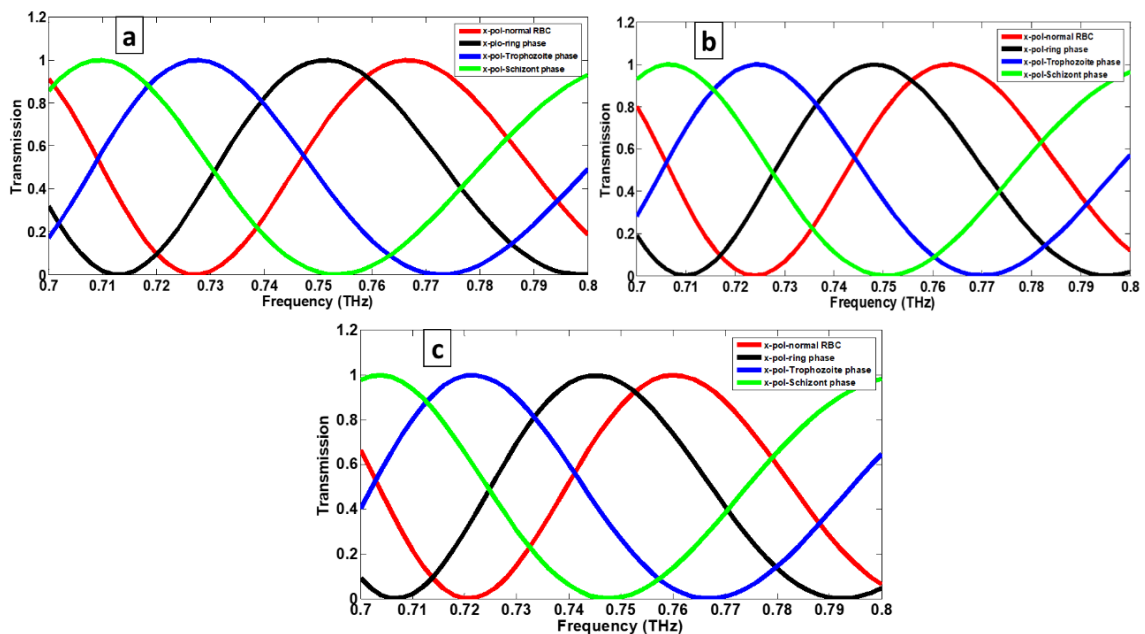


Fig. 5.3.9 Transmission curve with different pitch ( $\Lambda$ ), for various stages of malaria infected RBCs under x polarization (a)  $498 \mu\text{m}$  (b)  $500 \mu\text{m}$  and (c)  $502 \mu\text{m}$

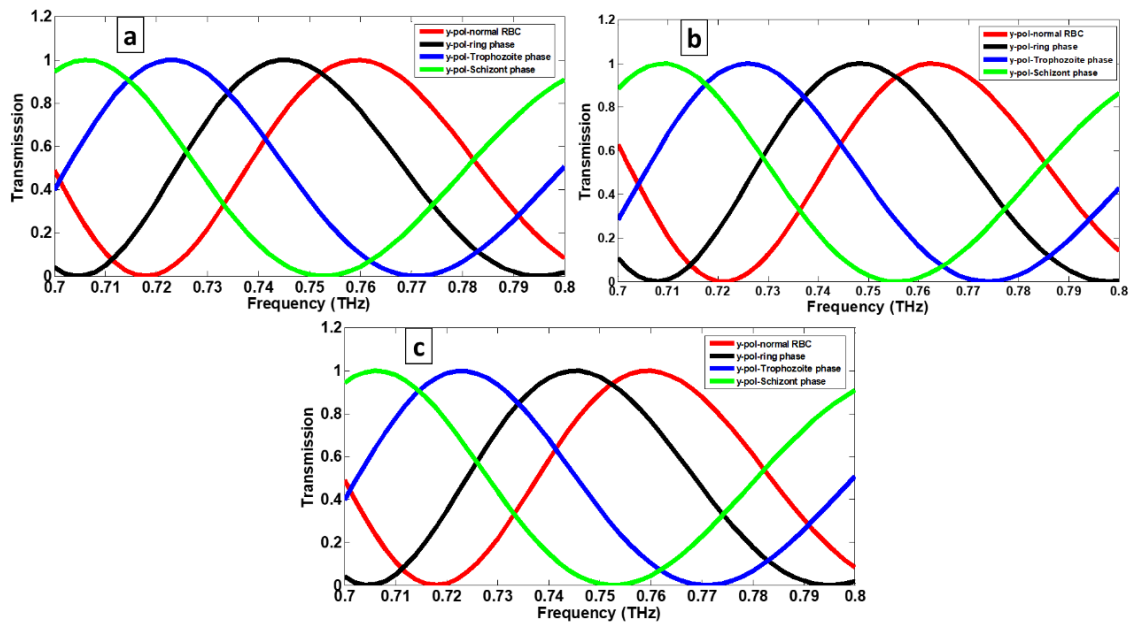


Fig. 5.3.10 Transmission curve with different pitch ( $\Lambda$ ), for various stages of malaria infected RBCs under y polarization (a) 498  $\mu\text{m}$  (b) 500  $\mu\text{m}$  and (c) 502  $\mu\text{m}$

TABLE 5.3.2 Comparison of the sensitivity between the sensor presented in this study and sensors reported in prior research

Reference	Sensing Application	Sensitivity (nm/RIU)	Background Material
[303]	Different cancerous cell identification	2360.12	Silica
[304]	D-shape open-loop PCF temperature sensor	3330	Silica
[305]	D-shaped PCF RI sensor	294.11	Silica
[281]	SPR based biosensor for malaria detection	14285.71	Silica
Proposed PCF	THz based DC-PCF for malaria detection	12,00000	TOPAS (cyclic olefin copolymer)

### 5.3.5 Summary

In this study, a novel biosensing approach to detect the malaria disease is presented by utilizing a DC-PCF technology and employing the FEM with COMSOL software. The shift in peak wavelength between normal and malaria-infected RBCs in the PCF biosensor, transmission spectrum can be used to diagnose malaria. To get the best possible outcomes, the PCF biosensor specifications have been optimized. Numerical analyses reveal that our biosensor exhibits remarkable sensitivity across different stages, such as 12,00000 nm/RIU for the ring stage, 11,15263.15 nm/RIU for the trophozoite stage, and 11,13793.10 nm/RIU for the schizont stage under x-polarization. Likewise, under y-polarization, sensitivities are observed to be 10,50000 nm/RIU for the ring stage, 10,54736.84 nm/RIU for the trophozoite stage, and 10,32758.62 nm/RIU for the schizont stage. Our results demonstrate that the proposed DC-PCF biosensor exhibits superior sensitivity compared to existing biosensors, to the best of our knowledge, and can thus, be considered as the most effective to detect malaria disease.

## CHAPTER 6

# DESIGN OF PHOTONIC CRYSTAL FIBER BASED PLASMONIC SENSOR FOR DIABETES DETECTION

### 6.1 Introduction

In 1993, Jorgenson et al. [306] introduced the use of SPR sensors with optical fibers, sparking huge interest in research over the years. These sensors exhibit exceptional sensitivity to variations in refractive index (RI), making them suitable for a wide range of applications such as fluid sensing [307, 308], environmental monitoring [309], food quality assessment [310, 311], label-free biosensing [312], and medical diagnostics. SPR takes place when the free electrons at the interface of a metal and a dielectric begin to oscillate collectively, leading to the formation of surface plasmon waves. When the energy of incoming light matches the energy of these electrons, SPR is excited, causing resonance. This resonance is highly sensitive to even the smallest changes in the surrounding environment's RI, leading to shifts in the SPP mode. By combining SPR with PCF, scientists can develop highly efficient and versatile optical based sensors with a wide range of uses.

In recent years, photonic crystal fibers (PCFs) have become more popular for use in biosensors. Researchers are working to overcome problems such as light loss, birefringence, bending loss and dispersion in these fibers [313–319]. PCFs are particularly effective for detecting different chemicals and biological compounds, making them valuable in fields such as food safety [320, 321], environmental monitoring [322–326], and medical testing [327–329]. Their growing popularity is because of their high accuracy, smaller size, cheap and flexible manufacturing process.

Over the past few decades, numerous high-quality research studies have been carried out to design and develop SPR based sensors with exceptional sensitivity. In their study, Azab et al. [330] introduced a PCF designed with a triangular lattice configuration and 32 circular air holes embedded in the cladding, resulting in a high sensitivity of 200 nm/RIU. A PCF based on a hexagonal shape structure, incorporating 31 air holes in the cladding region, was designed using gold as the plasmonic material and demonstrated a high wavelength sensitivity of 1000 nm/RIU [331]. To improve sensing precision, Dash et al. [332] proposed a PCF made from polymethyl methacrylate (PMMA) and utilized indium tin oxide as the plasmonic material, resulting in a maximum sensitivity of 2000 nm/RIU. To overcome the requirement of inserting samples into the PCF, common in internal sensing techniques, Hasan et al. [333] introduced an SPR sensor based on an external sensing approach, utilizing fewer air holes in the cladding than earlier designs. Over the past few years, numerous researchers have examined D-shaped, H-shaped and alternative PCF designs with the aim of advancing SPR sensing capabilities. They have investigated SPR based sensors performance using different plasmonic materials, such as gold, silver, metallic oxides and graphene, to enhance overall sensing efficiency [334–

337]. The field of PCF-based sensing is advancing swiftly, offering opportunities to address current challenges and design novel SPR sensors based on PCF technology.

This work presents a simple PCF-based SPR sensor for diabetes detection. Once the PCF is filled with diabetic samples, variations in their RI lead to a shift in the SPR wavelength, as observed through confinement loss measurements. A noticeable shift in the resonance wavelength occurs between normal and diabetic samples when the SPP mode effectively couples with the core mode at resonance. This wavelength shift is influenced by the RI variations of diabetes sample. The proposed sensor sensitivity is evaluated by analyzing the shift in wavelength observed in the confinement loss spectrum corresponding to the RI differences between infected and normal diabetes sample. The modelling and analysis of the proposed PCF-SPR sensor are carried out using FEM and COMSOL Multiphysics software. This approach holds potential as an early detection technique diabetes.

## 6.2 Sensor design

Figure 6.1 (a) depicts the cross-sectional structure of the newly designed PCF-based biosensor tailored for the detection of diabetes. The design features a dual-layer arrangement of air holes in a hexagonal configuration, forming a triangular shape pattern embedded within a silica background. Both layers feature a mix of elliptical and circular air holes, where the elliptical holes have a major axis denoted by  $a$ , minor axis denoted by  $b$ , and the circular holes have a diameter denoted by  $d$ . The spacing between the lattice points, known as the lattice constant, is denoted by  $\Lambda$ . The proposed biosensor is typically fabricated using the widely adopted “stacking and drawing” technique [338]. A circular gold layer with a thickness of  $t_g$  is externally deposited onto the surface of the PCF. Various techniques, such as “wet chemical deposition,” “radio frequency sputtering,” and “thermal evaporation,” can be used for depositing this metal layer [339]. However, achieving a uniform metal coating through these conventional methods can be challenging. In this regard, chemical vapor deposition (CVD) emerges as a more effective method, offering a consistent and uniform metal layer at the nanometer scale [340]. Over the gold-coated surface, a biochemical layer of thickness  $t_{\text{diabetes}}$  is applied and functionalized to allow the incorporation of analyte samples for diabetes detection. Both experimental and theoretical investigations have demonstrated that the elective infiltration technique is suitable for injecting diabetes samples into this functionalized biochemical layer [341]. The proposed sensor employs a dual-layer hexagonal PCF structure with a single thin gold plasmonic layer, which avoids complex geometries, multiple sensing channels, or multilayer coatings. Such a configuration reduces structural complexity and simplifies the design process. To prevent energy loss from the PCF surface, a perfectly matched layer (PML) arranged in a circular configuration with a thickness  $t_{\text{PML}}$  is applied, accompanied by scattering boundary conditions to absorb outgoing radiation efficiently. Table 6.1 provides a summary of the optimized design parameters for the proposed PCF. Unless stated otherwise, these values remain constant throughout the simulation. Pure silica is taken as the background material, and its dispersion properties are determined based on the Sellmeier equation as [325].

$$n^2(\lambda) = 1 + \frac{b_1}{1 - \left(\frac{c_1}{\lambda^2}\right)} + \frac{b_2}{1 - \left(\frac{c_2}{\lambda^2}\right)} + \frac{b_3}{1 - \left(\frac{c_3}{\lambda^2}\right)} \quad (6.1)$$

In this context,  $n$  represents the RI of pure silica,  $\lambda$  denotes the wavelength and the Sellmeier coefficients  $b_1$ ,  $b_2$ ,  $b_3$ ,  $c_1$ ,  $c_2$ , and  $c_3$  are listed in Table 6.2.

The RI of air is taken as 1. Furthermore, the gold permittivity is determined using the Drude–Lorentz model, as described in [342]

$$\epsilon_{DL}(\omega) = \epsilon_{\infty} - \frac{\omega_D^2}{\omega(\omega + i\gamma_D)} - \frac{\Delta\epsilon \cdot \Omega_L^2}{(\omega^2 - \Omega_L^2) - i\Gamma_L\omega} \quad (6.2)$$

Table 6.3 lists the parameters of the Drude–Lorentz model, where  $\Gamma_L$  indicates the Lorentz oscillator’s spectral linewidth,  $\Omega_L$  corresponds to its oscillator strength,  $\Delta\epsilon$  acts as the weighting coefficient. Additionally,  $\gamma_D$  represents the damping frequency,  $\epsilon_{\infty}$  denotes the dielectric constant at high frequencies, and  $\omega_D$  indicates the plasmon frequency. Gold’s high ductility allows it to be stretched and compressed, thereby enhancing the excitation of SPR between the core and SPP mode. The RI of healthy person and a diabetic person are shown in Table 6.4 [343]. The experimental setup for assessing the accuracy of diabetes detection using the proposed sensor is depicted in Figure 6.1 (b). A broadband light source (BLS) is employed to transmit optical signals via a single-mode fiber (SMF). The biosensor is linked to the SMF through the Fujikura Splicer fusion splicing method. Diabetes samples of different concentrations are introduced into the sensing channel. Prior to testing new samples, the PCF biosensor probes should be rinsed thoroughly with deionized water. When diabetes samples come into contact with ligands within the sensing channel, various changes take place. This interaction between ligands and target molecules alters the optical properties of the guided mode in the PCF-SPR biosensor, resulting in a wavelength shift in the confinement loss curve. To begin the analysis, the optical spectrum analyzer (OSA) captures the transmitted light via SMF, and a connected computer processes the data to generate the final spectrum.

**TABLE 6.1**  
**DESIGN PARAMETERS USED FOR THE PROPOSED PCF BIOSENSOR**

$d(\mu m)$	$a(\mu m)$	$b(\mu m)$	$\Lambda(\mu m)$	$t_g(nm)$	$t_{diabetes}(\mu m)$	$t_{PML}(\mu m)$
$0.6 \times \Lambda$	0.5	0.25	2	40	1	1.2

**TABLE 6.2**  
**SELLMEIER COEFFICIENTS VALUES**

$b_1$	$b_2$	$b_3$	$c_1(\mu m^2)$	$c_2(\mu m^2)$	$c_3(\mu m^2)$
0.696166300	0.40794260 0	0.8974794 00	0.00467914 826	0.01351206 31	97.9340025

**TABLE 6.3**  
**DRUDE–LORENTZ MODEL PARAMETERS**

$\epsilon_{\infty}$	$\omega_D/2\pi$ (THz)	$\gamma_D/2\pi$ (THz)	$\Omega_L/2\pi$ (THz)	$\Gamma_L/2\pi$ (THz)	$\Delta\epsilon$
5.9673	2113.6	15.92	650.07	104.86	1.09

**TABLE 6.4**  
**RI OF HEALTHY PERSON AND A DIABETIC PERSON**

Diabetes samples	RI
Normal diabetes cell	1.350
Effected diabetes cell	1.410

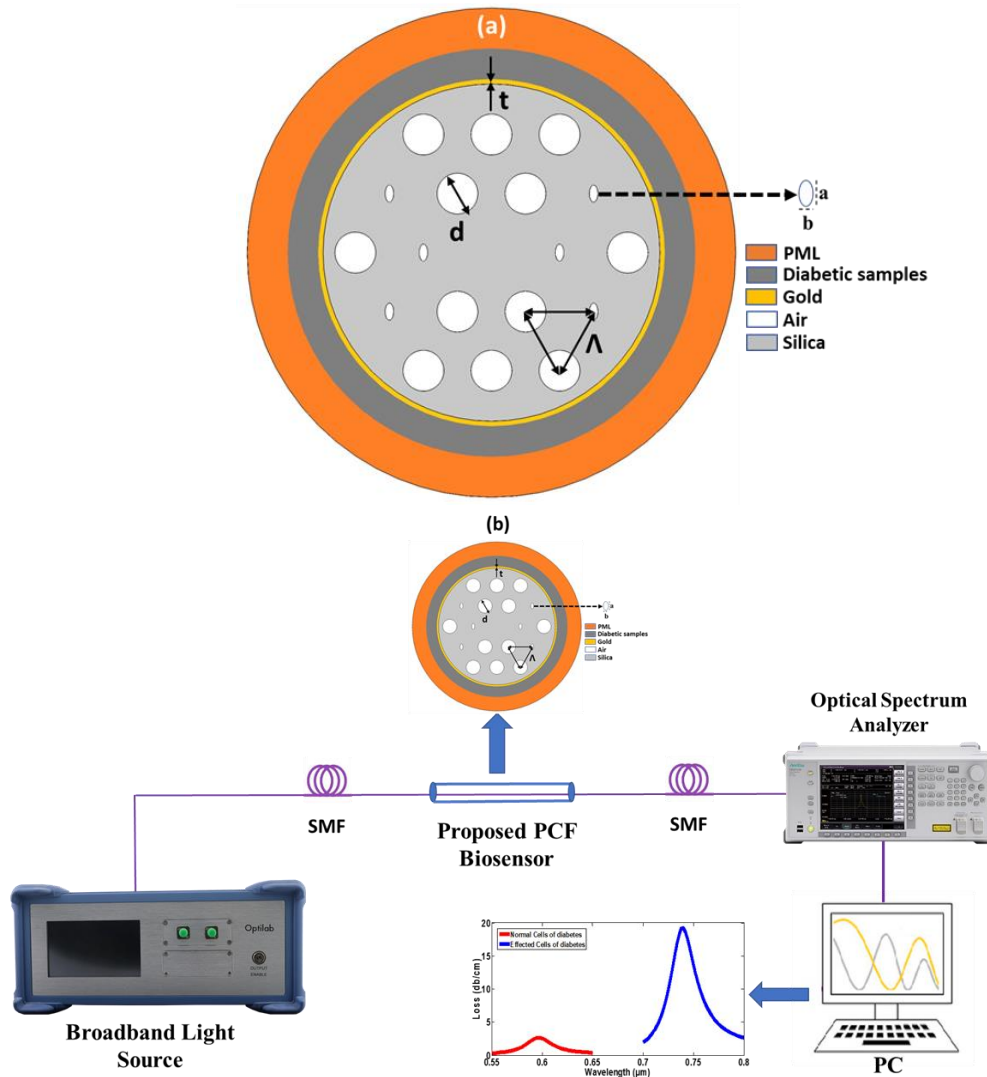


**Fig. 6.1 (a) Geometry illustration of the proposed PCF (b) schematic of the experimental setup for diabetes detection using the PCF-based SPR sensor**

### 6.3 Results Analysis

In the proposed PCF biosensor, gold is utilized as the key plasmonic material. Surface plasmon resonance (SPR) is triggered when the core mode and the surface plasmon polariton (SPP) mode become phase-matched, allowing energy to shift from the core mode to the SPP mode. This interaction results in a noticeable peak in the core mode's confinement loss at the specific resonance wavelength. The simulated design of the PCF biosensor is shown in Figure 2, highlighting light confinement in both the core and SPP modes. The electric field distribution is visualized, with arrows indicating the direction of the field. Figures 6.2 (a) and 6.2 (b) show

the core mode field under x and y polarization, respectively. Likewise, Figures 6.2 (c) and 6.2 (d) illustrate the SPP mode for x and y polarization light, respectively at a wavelength of 650 nm. Figure 6.3 presents a three-dimensional (3D) visualization of the electric field intensity across different modes.

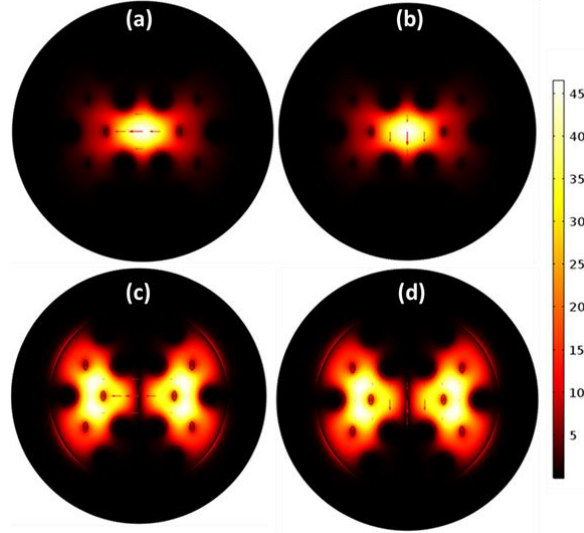


**Fig. 6.2 Distributions of electric field at the resonance wavelength of 596 nm for various polarization modes: (a) core mode with x-polarization, (b) core mode with y-polarization, (c) SPP mode with x-polarization, and (d) SPP mode with y-polarization**

Coupled-mode theory, as outlined in [343], offers a detailed explanation of the electric field patterns and the coupling behavior between modes in PCF-based SPR biosensors. The mathematical expressions for mode coupling are given as

$$\frac{dE_1}{dz} = i\beta_1 E_1 + i\kappa E_2 \quad (6.3)$$

$$\frac{dE_2}{dz} = i\beta_2 E_2 + i\kappa E_1 \quad (6.4)$$

here,  $\beta_1$  and  $\beta_2$  represent the propagation constants for the core mode and the SPP mode, respectively. Their corresponding mode field distributions are represented by  $E_1$  and  $E_2$ . The coupling coefficient is denoted by  $\kappa$ , and  $z$  indicates the propagation distance. When the core mode and SPP mode interact, the resulting propagation constant is represented by  $\beta$ . Under this coupling condition, the mode fields can be denoted as  $E_1 = A \exp(i\beta z)$  and  $E_2 = B \exp(i\beta z)$ . Substituting these expressions into equations (6.3) and (6.4) allows the calculation of the effective propagation constant  $\beta$ , as shown below.

$$\beta_{\pm} = \beta_{ave} \pm \sqrt{\delta^2 + \kappa^2} \quad (6.5)$$

Where,  $\beta_{ave} = \frac{(\beta_1 + \beta_2)}{2}$  and  $\delta = \frac{(\beta_1 - \beta_2)}{2}$ . Due to the complex nature of the propagation constants  $\beta_1$  and  $\beta_2$ , the detuning parameter  $\delta$  can be expressed as  $\delta = \delta_r + i\delta_i$ . When the phase-matching condition is met, the real components of  $\beta_1$  and  $\beta_2$  become equal, resulting in  $\delta_r = 0$ . Therefore, the relation becomes  $\delta^2 + \kappa^2 = -\delta_i^2 + \kappa$ . When  $\delta_i < \kappa$ , complete coupling occurs, whereas  $\delta_i > \kappa$  leads to incomplete coupling. An essential parameter for evaluating the

performance of a PCF-based SPR biosensor is the confinement loss of the core mode, which can be determined using the approach described in by [344]

$$\text{Loss(dB/cm)} = 8.686 \times \frac{2\pi}{\lambda} I_m(n_{\text{eff}}) \times 10^4 \quad (6.6)$$

here  $\lambda$  denotes the wavelength and  $I_m(n_{\text{eff}})$  represents the imaginary component of the effective refractive index (ERI).

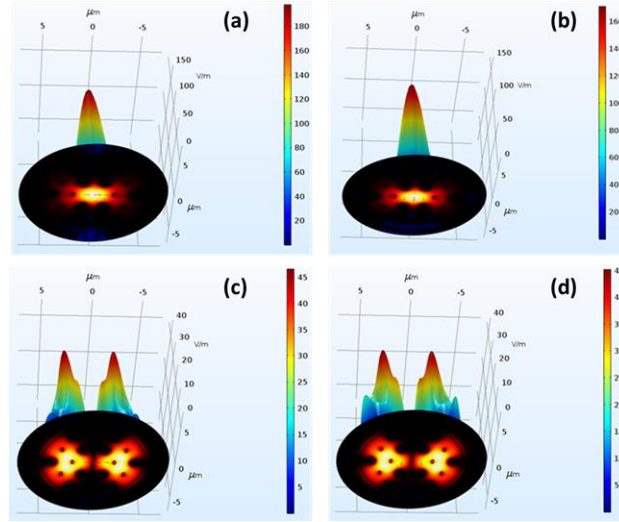


**Fig. 6.3 3D view of electric field profile for four distinct modes (a) core mode with x-polarization, (b) core mode with y-polarization, (c) SPP mode with x-polarization, and (d) SPP mode with y-polarization**

To detect diabetes, the proposed PCF-based biosensor is filled with samples from both normal and diabetic individuals, and the resonance wavelength is examined by analyzing the loss spectrum. The resonance wavelengths vary between the two sample types due to differences in their refractive indices. Figure 6.4 represents the confinement loss and ERI plots for both healthy and diabetic sample-infused PCF sensors. The intersection point of the ERI curves for the core mode and surface plasmon polariton (SPP) mode marks the resonance wavelength, indicating mode coupling. At this point, energy from the core mode couples into the SPP mode, leading to a peak in core mode loss. The resonance wavelengths for the normal and diabetic samples are found at 596 nm and 740 nm, respectively, with peak core losses measuring 2.662 dB/cm and 19.22 dB/cm, respectively.

It is clear that the resonance wavelength shift between normal and diabetic samples is highly responsive to variations in their respective RI. The wavelength sensitivity of the designed PCF biosensor is determined by evaluating the change in resonance wavelength relative to the RI difference between the normal and infected samples, as described in [345]

$$S_\lambda (nmRIU^{-1}) = \frac{\Delta \lambda_p}{\Delta n} \quad (6.7)$$

here,  $\Delta \lambda_p$  represents the change in resonance wavelength, while  $\Delta n$  denotes the variation in RI between the normal and infected samples. The proposed sensor achieves a sensitivity of 2400 nm/RIU, highlighting its strong potential for precise and dependable biomedical sensing

applications. Table 6.5 presents a sensitivity comparison between the proposed biosensor and those previously reported in the literature [346–349].

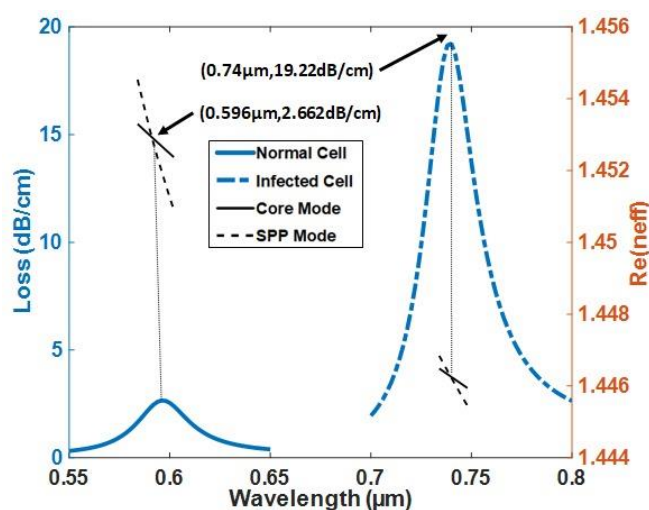


**Fig. 6.4** ERI and confinement loss curve corresponding to healthy and diabetic samples

**TABLE 6.5**

**COMPARISON OF THE SENSITIVITY OF THE SENSOR PROPOSED IN THIS STUDY WITH THAT OF SENSORS REPORTED IN PREVIOUS RESEARCH**

Reference	Sensing Application	Sensitivity (nm/RIU)
[346]	RI sensor based on D-shaped PCF	294.11
[347]	Photonic crystal biosensor for detecting cancerous cells based on RI variations	2360.12
[348]	Plasmonic PCF nano sensor coated with AZO	1950
[349]	SPR sensor utilizing a PCF featuring large microfluidic channels	2000
Proposed PCF	Diabetes detection using a PCF-based SPR sensor	2400

## 6.4 Summary

In this work, a SPR based PCF sensor has been successfully designed and simulated for efficient diabetes detection. By employing a dual-layer hexagonal shape structure and a thin gold coating as the plasmonic material, the sensor effectively utilizes the SPR phenomenon induced by the coupling of the SPP mode and the core mode under phase-matching conditions. The variation in RI of diabetes samples causes distinct shifts in the SPR resonance wavelength, enabling precise detection through confinement loss measurements. The wavelength at resonance for normal and diabetic samples are observed at 596 nm and 740 nm, respectively, with corresponding peak core losses of 2.662 dB/cm and 19.22 dB/cm. With a sensitivity of 2400 nm/RIU, the sensor demonstrates strong potential for precise and reliable biomedical sensing applications. Owing to its simplified structural design and cost-effective implementation, this PCF-based SPR sensor represents a promising solution for rapid, non-invasive, and sensitive diabetes detection applications.

## CHAPTER 7

### CONCLUSION, FUTURE SCOPE AND SOCIAL IMPACT

This chapter presents a concise summary of the findings derived from the ongoing research discussed throughout this thesis, along with key conclusions and recommendations for future investigations. The thesis encompasses the design, optimization, simulation, and performance evaluation of photonic crystal fiber (PCF) sensors for applications in physical, biomedical, and chemical sensing. Foundational concepts of PCFs and their roles in sensing were introduced in the earlier chapters, particularly in the introduction and literature review. The performance of the proposed sensor designs has been primarily assessed using mode coupling theory, transmission spectra, and wavelength interrogation techniques.

#### 7.1 Summary of the Work Done in the Thesis

The thesis begins with an overview of the evolution of fiber-optic sensors and the emergence of photonic crystal fibers as a transformative sensing platform. Traditional optical fibers, though effective for basic SPR sensing, exhibit structural and optical constraints that limit their advanced application. PCFs overcome these challenges by integrating the benefits of photonic crystals into optical fibers, enabling enhanced light guidance and sensitivity. The chapter establishes the groundwork for using PCF-based RI sensors in diverse domains, including physical, chemical, and biomedical sensing.

**Chapter 2** presents a comprehensive review of the theoretical foundations and prior work related to PCF-based sensing. It introduces critical concepts such as birefringence, mode coupling, and refractive index sensitivity, followed by an exploration of PCF-based surface plasmon resonance (SPR) sensors. The chapter highlights various applications including temperature monitoring, detection of blood components, malaria diagnosis, and sensing of fluidic analytes, showcasing the broad versatility of PCF structures in advanced sensing tasks.

In **Chapter 3**, a circular-shaped hollow-core PCF filled with ethanol is investigated for its optical properties over a wavelength range of 800–1600 nm. Through finite element method (FEM) simulations, the study demonstrates how the dispersion profile can be finely tuned by modifying the ethanol filling configuration. Achieved zero-dispersion wavelengths range from 880 nm to 1250 nm depending on the filling scenario. This tunable dispersion property makes the proposed structure highly suitable for nonlinear optics, sensing, telecommunications, and laser applications.

**Chapter 4** introduces a twin-core PCF (TC-PCF) structure optimized for temperature and chemical sensing. The sensor employs a vertically aligned elliptical air hole between two solid cores, enabling strong birefringence and efficient mode coupling. FEM-based simulations confirm the sensor's high performance, with a temperature sensitivity of approximately 21.5 pm/°C over 0–1200°C and a maximum chemical sensing sensitivity of 6667 nm/RIU with just 0.03 cm fiber length. The compact size, high sensitivity, and potential for easy fabrication emphasize the practical viability of the proposed TC-PCF design.

**Chapter 5** explores advanced biosensing applications using PCF designs in the terahertz (THz) frequency regime. FEM-based investigations show that TC-PCF and DC-PCF structures can effectively detect diseases such as various cancer types, malaria, and blood components by analyzing mode coupling behavior and refractive index differences. The proposed biosensors demonstrate superior sensitivity and design simplicity, making them highly suitable for early disease detection and biomedical diagnostics. These findings hold significant promise for future healthcare technologies.

**Chapter 6** proposes a novel PCF-based SPR sensor designed for diabetes monitoring. By incorporating a thin gold layer within a dual-layer hexagonal PCF structure, the sensor utilizes the SPR effect via coupling between the SPP and core-guided modes. FEM analysis confirms that changes in the refractive index of diabetes samples cause distinct resonance wavelength shifts. The sensor achieves a sensitivity of 2400 nm/RIU and offers advantages like simplicity, low cost, and non-invasive operation making it an effective tool for real-time diabetes detection.

## 7.2 Future Scope and Social Impact

With the growing integration of computational intelligence, PCF-based sensors are increasingly being explored in conjunction with machine learning algorithms, yielding promising outcomes. Advanced learning models such as artificial neural networks (ANNs) can predict sensor responses with high accuracy even without relying entirely on numerical simulations. This synergy between photonic design and data-driven models opens new avenues for faster, real-time, and adaptive sensing systems.

Building on the presented work, the following directions are suggested for future exploration:

- Development of SPR-PCF based biosensors for the detection of *Pseudomonas* bacteria, contributing to early diagnosis of infections in clinical and environmental applications.
- Design of PCF-based sensors for non-invasive glucose monitoring in blood and urine, which can be crucial for managing diabetes with higher sensitivity and convenience.
- Creation of a PCF-based biosensor for pregnancy detection, targeting hormone-level monitoring with precise optical sensitivity.
- Integration of deep learning frameworks with PCF sensor outputs to enable intelligent diagnostics, anomaly detection, and predictive healthcare systems.

## References

- [1] P. Yeh, A. Yariv, and E. Marom, "Theory of Bragg fiber," *JOSA*, vol. 68, no. 9, pp. 1196-1201, 1978.
- [2] T. Birks, P. S. J. Russell, and D. Atkin, "All-silica single-mode optical fiber with photonic crystal cladding: errata," *Optics letters*, vol. 22, no. 7, pp. 484-485, 1997.
- [3] A. M. Pinto and M. Lopez-Amo, "Photonic crystal fibers for sensing applications," *Journal of Sensors*, vol. 2012, no. 1, p. 598178, 2012.
- [4] E. Udd, "An overview of fiber-optic sensors," *review of scientific instruments*, vol. 66, no. 8, pp. 4015-4030, 1995.
- [5] J. Parikh Meera and P. Gharge Anuradha, "A Survey Paper of Optical Fiber Sensor," *International Journal on Recent and Innovation Trends in Computing and Communication*, vol. 2, no. 1, pp. 33-39, 2014.
- [6] H. K. Hisham, "Optical fiber sensing technology: basics, classifications and applications," *Am. J. Remote Sens*, vol. 6, no. 1, pp. 1-5, 2018.
- [7] P. M. Tracey, "Intrinsic fiber-optic sensors," *IEEE Transactions on Industry Applications*, vol. 27, no. 1, pp. 96-98, 1991.
- [8] D. Zhao *et al.*, "Bend sensors with direction recognition based on long-period gratings written in D-shaped fiber," *Applied optics*, vol. 43, no. 29, pp. 5425-5428, 2004.
- [9] J. Chen, B. Liu, and H. Zhang, "Review of fiber Bragg grating sensor technology," *Frontiers of Optoelectronics in China*, vol. 4, pp. 204-212, 2011.
- [10] M.-j. Yin, B. Gu, Q.-F. An, C. Yang, Y. L. Guan, and K.-T. Yong, "Recent development of fiber-optic chemical sensors and biosensors: Mechanisms, materials, micro/nano-fabrications and applications," *Coordination Chemistry Reviews*, vol. 376, pp. 348-392, 2018.
- [11] O. Butov, K. Golant, A. Tomashuk, M. Van Stralen, and A. Breuls, "Refractive index dispersion of doped silica for fiber optics," *Optics Communications*, vol. 213, no. 4-6, pp. 301-308, 2002.
- [12] J. Kirchhof, S. Unger, and A. Schwuchow, "Fiber lasers: materials, structures and technologies," in *Optical Fibers and Sensors for Medical Applications III*, 2003, vol. 4957: SPIE, pp. 1-15.
- [13] C. Yeh, "Optical waveguide theory," *IEEE Transactions on Circuits and Systems*, vol. 26, no. 12, pp. 1011-1019, 1979.
- [14] M. Saeed, "The influence of relative refractive index and core diameter on properties of single-mode optical fiber," *Journal of Education and Science*, vol. 29, no. 4, pp. 124.0-139.0, 2020.

- [15] A. Jian, L. Deng, S. Sang, Q. Duan, X. Zhang, and W. Zhang, "Surface plasmon resonance sensor based on an angled optical fiber," *IEEE Sensors Journal*, vol. 14, no. 9, pp. 3229-3235, 2014.
- [16] N. Mahnot, S. Maheshwary, and R. Mehra, "Photonic crystal fiber-an overview," *International Journal of Scientific & Engineering Research*, vol. 6, no. 2, pp. 2229-5518, 2015.
- [17] J. Ju, W. Jin, and M. Demokan, "Properties of a highly birefringent photonic crystal fiber," *IEEE photonics technology letters*, vol. 15, no. 10, pp. 1375-1377, 2003.
- [18] K. Saitoh and M. Koshiba, "Highly nonlinear dispersion-flattened photonic crystal fibers for supercontinuum generation in a telecommunication window," *Optics Express*, vol. 12, no. 10, pp. 2027-2032, 2004.
- [19] R. Sinha and S. K. Varshney, "Dispersion properties of photonic crystal fibers," *Microwave and optical technology letters*, vol. 37, no. 2, pp. 129-132, 2003.
- [20] H. Ademgil and S. Haxha, "Endlessly single mode photonic crystal fiber with improved effective mode area," *Optics Communications*, vol. 285, no. 6, pp. 1514-1518, 2012.
- [21] N. Mortensen, M. D. Nielsen, J. R. Folkenberg, A. Petersson, and H. R. Simonsen, "Improved large-mode-area endlessly single-mode photonic crystal fibers," *Optics Letters*, vol. 28, no. 6, pp. 393-395, 2003.
- [22] K. Suzuki, H. Kubota, S. Kawanishi, M. Tanaka, and M. Fujita, "Optical properties of a low-loss polarization-maintaining photonic crystal fiber," *Optics Express*, vol. 9, no. 13, pp. 676-680, 2001.
- [23] J. Kirchof *et al.*, "14 Photonic crystal fibers," in *Photonic crystals: Advances in design, fabrication, and characterization*, vol. 266: John Wiley & Sons, 2006.
- [24] T. Saini, A. Baili, A. Kumar, R. Cherif, M. Zghal, and R. Sinha, "Design and analysis of equiangular spiral photonic crystal fiber for mid-infrared supercontinuum generation," *Journal of modern optics*, vol. 62, no. 19, pp. 1570-1576, 2015.
- [25] M. B. Hossain, A. A.-M. Bulbul, M. A. Mukit, and E. Podder, "Analysis of optical properties for square, circular and hexagonal photonic crystal fiber," *Optics and Photonics Journal*, vol. 7, no. 11, pp. 235-243, 2017.
- [26] J. C. Knight, "Photonic crystal fibres," *nature*, vol. 424, no. 6950, pp. 847-851, 2003.
- [27] J. C. Knight, T. A. Birks, P. S. J. Russell, and J. G. Rarity, "Bragg scattering from an obliquely illuminated photonic crystal fiber," *Applied Optics*, vol. 37, no. 3, pp. 449-452, 1998.
- [28] C. M. Smith *et al.*, "Low-loss hollow-core silica/air photonic bandgap fibre," *Nature*, vol. 424, no. 6949, pp. 657-659, 2003.
- [29] A. Argyros, M. A. van Eijkelenborg, M. C. Large, and I. M. Bassett, "Hollow-core microstructured polymer optical fiber," *Optics letters*, vol. 31, no. 2, pp. 172-174, 2006.

- [30] G. Vienne *et al.*, "Ultra-large bandwidth hollow-core guiding in all-silica Bragg fibers with nano-supports," *Optics Express*, vol. 12, no. 15, pp. 3500-3508, 2004.
- [31] E. Pone *et al.*, "Drawing of the hollow all-polymer Bragg fibers," *Optics express*, vol. 14, no. 13, pp. 5838-5852, 2006.
- [32] B. Temelkuran, S. D. Hart, G. Benoit, J. D. Joannopoulos, and Y. Fink, "Wavelength-scalable hollow optical fibres with large photonic bandgaps for CO<sub>2</sub> laser transmission," *Nature*, vol. 420, no. 6916, pp. 650-653, 2002.
- [33] J. A. Harrington, "A review of IR transmitting, hollow waveguides," *Fiber & Integrated Optics*, vol. 19, no. 3, pp. 211-227, 2000.
- [34] Y. W. Shi, K. Ito, Y. Matsuura, and M. Miyagi, "Multiwavelength laser light transmission of hollow optical fiber from the visible to the mid-infrared," *Optics letters*, vol. 30, no. 21, pp. 2867-2869, 2005.
- [35] C. Charlton, B. Temelkuran, G. Dellemann, and B. Mizaikoff, "Midinfrared sensors meet nanotechnology: Trace gas sensing with quantum cascade lasers inside photonic band-gap hollow waveguides," *Applied Physics Letters*, vol. 86, no. 19, 2005.
- [36] F. Cox, A. Argyros, and M. Large, "Liquid-filled hollow core microstructured polymer optical fiber," *Optics Express*, vol. 14, no. 9, pp. 4135-4140, 2006.
- [37] Y. Hoo, W. Jin, H. Ho, J. Ju, and D. Wang, "Gas diffusion measurement using hollow-core photonic bandgap fiber," *Sensors and Actuators B: Chemical*, vol. 105, no. 2, pp. 183-186, 2005.
- [38] S. O. Konorov, A. B. Fedotov, A. M. Zheltikov, and R. B. Miles, "Phase-matched four-wave mixing and sensing of water molecules by coherent anti-Stokes Raman scattering in large-core-area hollow photonic-crystal fibers," *Journal of the Optical Society of America B*, vol. 22, no. 9, pp. 2049-2053, 2005.
- [39] S. Smolka, M. Barth, and O. Benson, "Highly efficient fluorescence sensing with hollow core photonic crystal fibers," *Optics Express*, vol. 15, no. 20, pp. 12783-12791, 2007.
- [40] M. Skorobogatiy, "Resonant Biochemical Sensors Based on Photonic Bandgap Waveguides and Fibers," in *Optical guided-wave Chemical and Biosensors II*: Springer, 2010, pp. 43-72.
- [41] C. De Matos, J. Taylor, T. P. Hansen, K. P. Hansen, and J. Broeng, "All-fiber chirped pulse amplification using highly-dispersive air-core photonic bandgap fiber," *Optics Express*, vol. 11, no. 22, pp. 2832-2837, 2003.
- [42] F. Poli, A. Cucinotta, and S. Selleri, *Photonic crystal fibers: properties and applications*. Springer Science & Business Media, 2007.
- [43] J. Knight, T. Birks, P. S. J. Russell, and J. De Sandro, "Properties of photonic crystal fiber and the effective index model," *Journal of the Optical Society of America A*, vol. 15, no. 3, pp. 748-752, 1998.

- [44] W. J. Wadsworth *et al.*, "Very high numerical aperture fibers," *IEEE Photonics Technology Letters*, vol. 16, no. 3, pp. 843-845, 2004.
- [45] W. Sun, X. Liu, H. Yu, Y. Jiang, Z. Hu, and Y. Zhu, "The high-numerical aperture photonic crystal fibers and application in astronomy," in *Optical Design and Testing IV*, 2010, vol. 7849: SPIE, pp. 282-287.
- [46] J. C. Baggett, T. M. Monro, K. Furusawa, V. Finazzi, and D. Richardson, "Understanding bending losses in holey optical fibers," *Optics Communications*, vol. 227, no. 4-6, pp. 317-335, 2003.
- [47] R. Cregan *et al.*, "Single-mode photonic band gap guidance of light in air," *science*, vol. 285, no. 5433, pp. 1537-1539, 1999.
- [48] J. Park, D.-E. Kang, B. Paulson, T. Nazari, and K. Oh, "Liquid core photonic crystal fiber with low-refractive-index liquids for optofluidic applications," *Optics Express*, vol. 22, no. 14, pp. 17320-17330, 2014.
- [49] J. Canning, E. Buckley, and K. Lyytikainen, "Propagation in air by field superposition of scattered light within a Fresnel fiber," *Optics letters*, vol. 28, no. 4, pp. 230-232, 2003.
- [50] C. Martelli, J. Canning, K. Lyytikainen, and N. Groothoff, "Water-core Fresnel fiber," *Optics Express*, vol. 13, no. 10, pp. 3890-3895, 2005.
- [51] S. Kim and C.-S. Kee, "Dispersion properties of dual-core photonic-quasicrystal fiber," *Optics Express*, vol. 17, no. 18, pp. 15885-15890, 2009.
- [52] Y. Ni, L. Zhang, L. An, J. Peng, and C. Fan, "Dual-core photonic crystal fiber for dispersion compensation," *IEEE photonics technology letters*, vol. 16, no. 6, pp. 1516-1518, 2004.
- [53] X.-h. Fang *et al.*, "Multiwatt octave-spanning supercontinuum generation in multicore photonic-crystal fiber," *Optics letters*, vol. 37, no. 12, pp. 2292-2294, 2012.
- [54] H. Chen *et al.*, "All-fiber-integrated high-power supercontinuum sources based on multi-core photonic crystal fibers," *IEEE Journal of Selected Topics in Quantum Electronics*, vol. 20, no. 5, pp. 64-71, 2014.
- [55] M. F. H. Arif, K. Ahmed, S. Asaduzzaman, and M. A. K. Azad, "Design and optimization of photonic crystal fiber for liquid sensing applications," *Photonic Sensors*, vol. 6, pp. 279-288, 2016.
- [56] R. Senthil, A. Soni, K. Bir, R. Senthil, and P. Krishnan, "Circular-pattern photonic crystal fiber for different liquids with high effective area and sensitivity," *Plasmonics*, vol. 14, pp. 1783-1787, 2019.
- [57] M. A. Habib, M. S. Anower, L. F. Abdulrazak, and M. S. Reza, "Hollow core photonic crystal fiber for chemical identification in terahertz regime," *Optical Fiber Technology*, vol. 52, p. 101933, 2019.

- [58] K. Ahmed and M. Morshed, "Design and numerical analysis of microstructured-core octagonal photonic crystal fiber for sensing applications," *Sensing and Bio-Sensing Research*, vol. 7, pp. 1-6, 2016.
- [59] S. Coen *et al.*, "White-light supercontinuum generation with 60-ps pump pulses in a photonic crystal fiber," *Optics Letters*, vol. 26, no. 17, pp. 1356-1358, 2001.
- [60] V. S. Chaudhary, D. Kumar, R. Mishra, and S. Sharma, "Twin core photonic crystal fiber for temperature sensing," *Materials Today: Proceedings*, vol. 33, pp. 2289-2292, 2020.
- [61] S. Wang, Y. Lu, W. Ma, N. Liu, and S. Fan, "D-shaped surface plasmon photonic crystal fiber temperature sensor," *Plasmonics*, vol. 17, no. 5, pp. 1911-1919, 2022.
- [62] H. Li *et al.*, "High-sensitivity temperature sensor based on photonic crystal fiber filled with ethanol and toluene," *ECS Journal of Solid State Science and Technology*, vol. 12, no. 12, p. 127007, 2023.
- [63] M. S. Karim *et al.*, "Quad core gold coated photonic crystal fiber temperature sensor based on surface plasmon resonance," *Sensing and Bio-Sensing Research*, vol. 39, p. 100548, 2023.
- [64] A. B. Siddik, S. Hossain, A. K. Paul, M. Rahman, and A. Mollah, "High sensitivity property of dual-core photonic crystal fiber temperature sensor based on surface plasmon resonance," *Sensing and Bio-Sensing Research*, vol. 29, p. 100350, 2020.
- [65] Q. Zhang *et al.*, "Research on D-shape PCF temperature sensor with simple structure and high sensitivity," *Optik*, vol. 323, p. 172228, 2025.
- [66] H. Abdullah *et al.*, "Theoretical analysis of highly temperature-sensitive fem based optical sensor in the infrared range," *Optik*, vol. 205, p. 164060, 2020.
- [67] D. Li, S. Pu, Y. Zhao, Y. Li, Z. Hao, and Z. Han, "Sensing properties of symmetrical side-polished photonic crystal fiber based on surface plasmon resonance," *Optik*, vol. 224, p. 165662, 2020.
- [68] Z. Du *et al.*, "High sensitivity photonic crystal fiber temperature and refractive index sensor based on surface plasmon resonance," *Indian Journal of Physics*, vol. 97, no. 9, pp. 2821-2826, 2023.
- [69] H. Chen, S. Li, J. Li, Y. Han, and Y. Wu, "High sensitivity of temperature sensor based on ultracompact photonics crystal fibers," *IEEE Photonics Journal*, vol. 6, no. 6, pp. 1-6, 2014.
- [70] X.-G. Li, Y. Zhao, X. Zhou, and L. Cai, "High sensitivity all-fiber Sagnac interferometer temperature sensor using a selective ethanol-filled photonic crystal fiber," *Instrumentation science & technology*, vol. 46, no. 3, pp. 253-264, 2018.
- [71] C. Du, Q. Wang, Y. Zhao, and J. Li, "Highly sensitive temperature sensor based on an isopropanol-filled photonic crystal fiber long period grating," *Optical Fiber Technology*, vol. 34, pp. 12-15, 2017.

- [72] Y. Cui, P. P. Shum, D. J. J. Hu, G. Wang, G. Humbert, and X.-Q. Dinh, "Temperature sensor by using selectively filled photonic crystal fiber Sagnac interferometer," *IEEE Photonics Journal*, vol. 4, no. 5, pp. 1801-1808, 2012.
- [73] R. K. Gangwar and V. K. Singh, "Refractive index sensor based on selectively liquid infiltrated dual core photonic crystal fibers," *Photonics and Nanostructures-Fundamentals and Applications*, vol. 15, pp. 46-52, 2015.
- [74] K. Ahmed *et al.*, "Highly sensitive twin resonance coupling refractive index sensor based on gold-and MgF<sub>2</sub>-coated nano metal films," *Biosensors*, vol. 11, no. 4, p. 104, 2021.
- [75] J. Wu, S. Li, X. Wang, M. Shi, X. Feng, and Y. Liu, "Ultra-high sensitivity refractive index sensor of a D-shaped PCF based on surface plasmon resonance," *Applied Optics*, vol. 57, no. 15, pp. 4002-4007, 2018.
- [76] E. Haque, S. Mahmuda, M. A. Hossain, N. H. Hai, Y. Namihira, and F. Ahmed, "Highly sensitive dual-core PCF based plasmonic refractive index sensor for low refractive index detection," *IEEE Photonics Journal*, vol. 11, no. 5, pp. 1-9, 2019.
- [77] E. Haque, M. A. Hossain, F. Ahmed, and Y. Namihira, "Surface plasmon resonance sensor based on modified D-shaped photonic crystal fiber for wider range of refractive index detection," *IEEE Sensors Journal*, vol. 18, no. 20, pp. 8287-8293, 2018.
- [78] A. K. Paul, A. K. Sarkar, A. B. S. Rahman, and A. Khaleque, "Twin core photonic crystal fiber plasmonic refractive index sensor," *IEEE Sensors Journal*, vol. 18, no. 14, pp. 5761-5769, 2018.
- [79] A. A. Rifat, R. Ahmed, G. A. Mahdiraji, and F. M. Adikan, "Highly sensitive D-shaped photonic crystal fiber-based plasmonic biosensor in visible to near-IR," *IEEE Sensors Journal*, vol. 17, no. 9, pp. 2776-2783, 2017.
- [80] E. Haque, M. Anwar Hossain, Y. Namihira, and F. Ahmed, "Microchannel-based plasmonic refractive index sensor for low refractive index detection," *Applied Optics*, vol. 58, no. 6, pp. 1547-1554, 2019.
- [81] M. Y. Azab, M. F. O. Hameed, G. A. Mahdiraji, F. R. M. Adikan, and S. Obayya, "Experimental and numerical characterization of a D-shaped PCF refractive index sensor," *Optical and Quantum Electronics*, vol. 54, no. 12, p. 846, 2022.
- [82] M. Tian, P. Lu, L. Chen, C. Lv, and D. Liu, "All-solid D-shaped photonic fiber sensor based on surface plasmon resonance," *Optics Communications*, vol. 285, no. 6, pp. 1550-1554, 2012.
- [83] A. Rifat *et al.*, "Surface plasmon resonance photonic crystal fiber biosensor: a practical sensing approach," *IEEE Photonics Technology Letters*, vol. 27, no. 15, pp. 1628-1631, 2015.
- [84] G. An, S. Li, W. Qin, W. Zhang, Z. Fan, and Y. Bao, "High-sensitivity refractive index sensor based on D-shaped photonic crystal fiber with rectangular lattice and nanoscale gold film," *Plasmonics*, vol. 9, pp. 1355-1360, 2014.

- [85] J. N. Dash and R. Jha, "Highly sensitive D shaped PCF sensor based on SPR for near IR," *Optical and Quantum Electronics*, vol. 48, pp. 1-7, 2016.
- [86] A. A. Rifat, G. A. Mahdiraji, D. M. Chow, Y. G. Shee, R. Ahmed, and F. R. M. Adikan, "Photonic crystal fiber-based surface plasmon resonance sensor with selective analyte channels and graphene-silver deposited core," *Sensors*, vol. 15, no. 5, pp. 11499-11510, 2015.
- [87] M. R. Hasan *et al.*, "Spiral photonic crystal fiber-based dual-polarized surface plasmon resonance biosensor," *IEEE Sensors Journal*, vol. 18, no. 1, pp. 133-140, 2017.
- [88] M. R. Momota and M. R. Hasan, "Hollow-core silver coated photonic crystal fiber plasmonic sensor," *Optical materials*, vol. 76, pp. 287-294, 2018.
- [89] A. M. i. Maidi, M. A. Kalam, and F. Begum, "Photonic crystal fibre for blood components sensing," *Sensing and Bio-Sensing Research*, vol. 41, p. 100565, 2023.
- [90] A. A.-M. Bulbul, R. H. Jibon, S. Biswas, S. T. Pasha, and M. A. Sayeed, "Photonic crystal fiber-based blood components detection in THz regime: Design and simulation," *Sensors International*, vol. 2, p. 100081, 2021.
- [91] M. R. Islam, A. Iftekher, F. Noor, M. R. H. Khan, M. T. Reza, and M. M. Nishat, "AZO-coated plasmonic PCF nanosensor for blood constituent detection in near-infrared and visible spectrum," *Applied Physics A*, vol. 128, no. 1, p. 86, 2022.
- [92] V. S. Chaudhary, D. Kumar, G. P. Mishra, S. Sharma, and S. Kumar, "Plasmonic biosensor with gold and titanium dioxide immobilized on photonic crystal fiber for blood composition detection," *IEEE Sensors Journal*, vol. 22, no. 9, pp. 8474-8481, 2022.
- [93] S. Singh and V. Kaur, "Photonic crystal fiber sensor based on sensing ring for different blood components: design and analysis," in *2017 Ninth international conference on ubiquitous and future networks (ICUFN)*, 2017: IEEE, pp. 399-403.
- [94] M. T. Islam, M. G. Moctader, K. Ahmed, and S. Chowdhury, "Benzene shape photonic crystal fiber based plasma sensor: design and analysis," *Photonic Sensors*, vol. 8, pp. 263-269, 2018.
- [95] K. Ahmed *et al.*, "Refractive index-based blood components sensing in terahertz spectrum," *IEEE Sensors Journal*, vol. 19, no. 9, pp. 3368-3375, 2019.
- [96] M. B. Hossain and E. Podder, "Design and investigation of PCF-based blood components sensor in terahertz regime," *Applied Physics A*, vol. 125, no. 12, p. 861, 2019.
- [97] V. Kaur and S. Singh, "Design approach of solid-core photonic crystal fiber sensor with sensing ring for blood component detection," *Journal of Nanophotonics*, vol. 13, no. 2, pp. 026011-026011, 2019.
- [98] P. Sharma and P. Sharan, "Design of photonic crystal based ring resonator for detection of different blood constituents," *Optics communications*, vol. 348, pp. 19-23, 2015.

- [99] A. Shafkat, A. N. Z. Rashed, H. M. El-Hageen, and A. M. Alatwi, "Design and analysis of a single elliptical channel photonic crystal fiber sensor for potential malaria detection," *Journal of Sol-gel science and technology*, vol. 98, pp. 202-211, 2021.
- [100] V. S. Chaudhary, D. Kumar, and S. Kumar, "Gold-immobilized photonic crystal fiber-based SPR biosensor for detection of malaria disease in human body," *IEEE sensors journal*, vol. 21, no. 16, pp. 17800-17807, 2021.
- [101] R. Srivastava, Y. K. Prajapati, S. Pal, and S. Kumar, "Micro-channel plasmon sensor based on a D-shaped photonic crystal fiber for malaria diagnosis with improved performance," *IEEE Sensors Journal*, vol. 22, no. 15, pp. 14834-14841, 2022.
- [102] D. Pysz *et al.*, "Stack and draw fabrication of soft glass microstructured fiber optics," *Bulletin of the Polish Academy of Sciences. Technical Sciences*, vol. 62, no. 4, pp. 667-682, 2014.
- [103] V. Cremers, R. L. Puurunen, and J. Dendooven, "Conformality in atomic layer deposition: Current status overview of analysis and modelling," *Applied Physics Reviews*, vol. 6, no. 2, 2019.
- [104] N. Singh, A. Saxena, and N. Valecha, "Field evaluation of the ICT malaria Pf/Pv immunochromatographic test for diagnosis of Plasmodium falciparum and P. vivax infection in forest villages of Chhindwara, central India," *Tropical Medicine & International Health*, vol. 5, no. 11, pp. 765-770, 2000.
- [105] A. J. De Langen, J. Van Dillen, P. d. Witte, S. Mucheto, N. Nagelkerke, and P. Kager, "Automated detection of malaria pigment: feasibility for malaria diagnosing in an area with seasonal malaria in northern Namibia," *Tropical Medicine & International Health*, vol. 11, no. 6, pp. 809-816, 2006.
- [106] V. Wongchotigul *et al.*, "The use of flow cytometry as a diagnostic test for malaria parasites," *Southeast Asian journal of tropical medicine and public health*, vol. 35, pp. 552-559, 2004.
- [107] O. Kanyi, M. Ajayi, S. Ezeugwu, E. Afocha, and B. Iwalokun, "Comparison of Rapid Diagnostic Test (RDT), Polymerase Chain Reaction (PCR) and microscopy methods in the diagnosis of malaria among airport workers in Lagos," *Nigerian Journal of Science and Environment*, vol. 13, no. 1, pp. 18-24, 2016.
- [108] B. K. Sandhya, S. S. Apurba, E. Nagaraj, S. Mannur, and S. S. Anand, "Laboratory diagnosis of malaria by conventional peripheral blood smear examination with Quantitative Buffy Coat (QBC) and Rapid Diagnostic Tests (RDT)-A comparative study," *International Journal of Collaborative Research on Internal Medicine & Public Health*, vol. 4, no. 10, p. 1746, 2012.
- [109] S. Sharma, V. S. Chaudhary, and D. Kumar, "Design of chemical sensor based on dual core photonic crystal fiber," *Materials today: proceedings*, vol. 33, pp. 2122-2124, 2020.
- [110] M. S. Hossain, M. S. H. Mollah, M. H. Rahman, and S. Sen, "Design and performance analysis of PCF-based octagonal chemical sensor to detect benzene, ethanol, and water in terahertz spectrum," *Results in Optics*, vol. 14, p. 100599, 2024.

- [111] M. S. Islam *et al.*, "A novel approach for spectroscopic chemical identification using photonic crystal fiber in the terahertz regime," *IEEE Sensors Journal*, vol. 18, no. 2, pp. 575-582, 2017.
- [112] H. Ademgil, "Highly sensitive octagonal photonic crystal fiber based sensor," *Optik*, vol. 125, no. 20, pp. 6274-6278, 2014.
- [113] H. Ademgil and S. Haxha, "PCF based sensor with high sensitivity, high birefringence and low confinement losses for liquid analyte sensing applications," *Sensors*, vol. 15, no. 12, pp. 31833-31842, 2015.
- [114] S. Asaduzzaman, K. Ahmed, T. Bhuiyan, and T. Farah, "Hybrid photonic crystal fiber in chemical sensing," *SpringerPlus*, vol. 5, pp. 1-11, 2016.
- [115] B. K. Paul, M. S. Islam, K. Ahmed, and S. Asaduzzaman, "Alcohol sensing over O+ E+ S+ C+ L+ U transmission band based on porous cored octagonal photonic crystal fiber," *Photonic Sensors*, vol. 7, no. 2, pp. 123-130, 2017.
- [116] S. Asaduzzaman and K. Ahmed, "Microarray-core based circular photonic crystal fiber for high chemical sensing capacity with low confinement loss," *Optica Applicata*, vol. 47, no. 1, 2017.
- [117] B. K. Paul, K. Ahmed, S. Asaduzzaman, and M. S. Islam, "Folded cladding porous shaped photonic crystal fiber with high sensitivity in optical sensing applications: design and analysis," *Sensing and Bio-Sensing Research*, vol. 12, pp. 36-42, 2017.
- [118] E. Ozbay, I. Bulu, K. Aydin, H. Caglayan, and K. Guven, "Physics and applications of photonic crystals," *Photonics Nanostruct. Fundam. Appl.*, vol. 2, pp. 87-95, 2004.
- [119] J. Broeng, D. Mogilevstev, S. E. Barkou, and A. Bjarklev, "Photonic Crystal Fibers: A New Class of Optical Waveguides," *Opt. Fiber Technol.*, vol. 5, pp. 305-330, 1999.
- [120] P. S. J. Russell, "Photonic-crystal fibers," *J. Light. Technol.*, vol. 24, pp. 4729-4749, 2006.
- [121] R. K. Sinha and S. K. Varshney, "Dispersion properties of photonic crystal fibers," *Microw. Opt. Technol. Lett.*, vol. 37, pp. 129-132, 2003.
- [122] C. Martelli, J. Canning, K. Lyytikainen, and N. Groothoff, "Water-core Fresnel fiber," *Opt. Express*, vol. 13, p. 3890, 2005.
- [123] S. Yiou *et al.*, "Stimulated Raman scattering in an ethanol core microstructured optical fiber," *Opt. Express*, vol. 13, p. 4786, 2005.
- [124] C. Zhang *et al.*, "Transformation of a transmission mechanism by filling the holes of normal silica-guiding microstructure fibers with nematic liquid crystal," *Opt. Lett.*, vol. 30, p. 2372, 2005.
- [125] T. T. Alkeskjold *et al.*, "Highly tunable large-core single-mode liquid-crystal photonic bandgap fiber," *Appl. Opt.*, vol. 45, pp. 2261-2264, 2006.

- [126] B. Eggleton, C. Kerbage, P. Westbrook, R. Windeler, and A. Hale, "Microstructured optical fiber devices," *Opt. Express*, vol. 9, p. 698, 2001.
- [127] C. Kerbage *et al.*, "Highly tunable birefringent microstructured optical fiber," *Opt. Lett.*, vol. 27, p. 842, 2002.
- [128] F. M. Cox, A. Argyros, and M. C. J. Large, "Liquid-filled hollow core microstructured polymer optical fiber," *Opt. Express*, vol. 14, p. 4135, 2006.
- [129] R. K. Gangwar and V. K. Singh, "Highly Sensitive Surface Plasmon Resonance Based D-Shaped Photonic Crystal Fiber Refractive Index Sensor," *Plasmonics*, vol. 12, pp. 1367–1372, 2017.
- [130] R. K. Gangwar and V. K. Singh, "Refractive index sensor based on selectively liquid infiltrated dual core photonic crystal fibers," *Photonics Nanostruct. Fundam. Appl.*, vol. 15, pp. 46–52, 2015.
- [131] K. J. Lee *et al.*, "Refractive index sensor based on a polymer fiber directional coupler for low index sensing," *Opt. Express*, vol. 22, p. 17497, 2014.
- [132] R. K. Gangwar, V. Bhardwaj, and V. K. Singh, "Magnetic field sensor based on selectively magnetic fluid infiltrated dual-core photonic crystal fiber," *Opt. Eng.*, vol. 55, p. 026111, 2016.
- [133] M. M. Hossain *et al.*, "Chloroform infiltrate temperature sensor using asymmetric circular dual-core photonic crystal fiber," *J. Biomed. Photonics Eng.*, vol. 4, p. 030302, 2018.
- [134] F. Q. Shi *et al.*, "A dual-parameter sensor based on the asymmetry of alcohol filling the photonic crystal fiber in Sagnac loop," *IEEE Sens. J.*, vol. 18, pp. 6188–6195, 2018.
- [135] C. Zhou *et al.*, "Geometrically structural parameters insensitive fiber sensor for detection of ethanol concentration," *IEEE Photonics Technol. Lett.*, vol. 30, pp. 2037–2039, 2018.
- [136] M. Suganthy *et al.*, "Analysis of optical sensitivity of analytes in aqua solutions," *Optik*, vol. 178, pp. 970–977, 2019.
- [137] Y. Liu *et al.*, "Compact tunable multibandpass filters based on liquid-filled photonic crystal fibers," *Opt. Lett.*, vol. 39, p. 2148, 2014.
- [138] M. Benhaddad, F. Kerrou, and O. Benabbes, "Design and analysis of non-linear properties of photonic crystal fiber with various doping concentration," *J. Phys. Conf. Ser.*, vol. 987, 2018.
- [139] S. Shakya, "Machine Learning Based Nonlinearity Determination for Optical Fiber Communication-Review," *J. Ubiquitous Comput. Commun. Technol.*, vol. 2019, pp. 121–127, 2019.
- [140] K. P., "MIMO Based High Speed Optical Fiber Communication System," *J. Electron. Informatics*, vol. 2019, pp. 107–116, 2019.
- [141] Z. Liu, M.-L. V. Tse, C. Wu, D. Chen, C. Lu, and H.-Y. Tam, "Intermodal coupling

- of supermodes in a twin-core photonic crystal fiber and its application as a pressure sensor,” *Opt. Express*, vol. 20, no. 19, p. 21749, 2012, doi: 10.1364/oe.20.021749.
- [142] P. Dhara and V. K. Singh, “Effect of MMF stub on the sensitivity of a photonic crystal fiber interferometer sensor at 1550 nm,” *Opt. Fiber Technol.*, vol. 21, pp. 154–159, 2015, doi: 10.1016/j.yofte.2014.11.008.
- [143] Q. Xu, Y. Zhao, H. Xia, S. Lin, and Y. Zhang, “Ultrashort polarization splitter based on dual-core photonic crystal fibers with gold wire,” *Opt. Eng.*, vol. 57, no. 04, p. 1, 2018, doi: 10.1117/1.oe.57.4.046104.
- [144] K. Saitoh, N. J. Florous, M. Koshiba, and M. Skorobogatiy, “Design of narrow band-pass filters based on the resonant-tunneling phenomenon in multi-core photonic crystal fibers,” *Opt. Express*, vol. 13, no. 25, p. 10327, 2005, doi: 10.1364/opex.13.010327.
- [145] J. Lægsgaard, O. Bang, and A. Bjarklev, “Photonic crystal fiber design for broadband directional coupling,” *Opt. Lett.*, vol. 29, no. 21, p. 2473, 2004, doi: 10.1364/ol.29.002473.
- [146] M. Koshiba, K. Saitoh, and Y. Sato, “Coupling characteristics of dual-core photonic crystal fiber couplers,” *Opt. Express*, vol. 11, no. 24, pp. 3188–3195, 2003, [Online]. Available: [http://www.opticsexpress.org/abstract.cfm?URI=oe-11-24-3188%5Cnhttp://www.opticsinfobase.org/DirectPDFAccess/13F3090A-BDB9-137E-C94291D5283CA923\\_78078.pdf?da=1&id=78078&seq=0%5Cnhttp://www.opticsinfobase.org/oe/abstract.cfm?URI=oe-11-24-3188](http://www.opticsexpress.org/abstract.cfm?URI=oe-11-24-3188%5Cnhttp://www.opticsinfobase.org/DirectPDFAccess/13F3090A-BDB9-137E-C94291D5283CA923_78078.pdf?da=1&id=78078&seq=0%5Cnhttp://www.opticsinfobase.org/oe/abstract.cfm?URI=oe-11-24-3188)
- [147] M. F. O. Hameed, R. T. Balat, A. M. Heikal, M. M. Abo-Elkhier, M. I. Abo El Maaty, and S. S. A. Obayya, “Polarization-Independent Surface Plasmon Liquid Crystal Photonic Crystal Multiplexer-Demultiplexer,” *IEEE Photonics J.*, vol. 7, no. 5, pp. 1–10, 2015, doi: 10.1109/JPHOT.2015.2480538.
- [148] L. Rindorf and O. Bang, “Sensitivity of photonic crystal fiber grating sensors: biosensing, refractive index, strain, and temperature sensing,” *J. Opt. Soc. Am. B*, vol. 25, no. 3, p. 310, 2008, doi: 10.1364/josab.25.000310.
- [149] S. Revathi, S. R. Inabathini, and J. Pal, “Pressure and temperature sensor based on a dual core photonicquasi-crystal fiber,” *Optik (Stuttg.)*, vol. 126, no. 22, pp. 3395–3399, 2015, doi: 10.1016/j.ijleo.2015.07.141.
- [150] S. Jegadeesan, M. Dhamodaran, and S. S. Shanmugapriya, “Numerical analysis of dual-core photonic crystal fiber based temperature and pressure sensor for oceanic applications,” *Opt. Appl.*, vol. 49, no. 2, pp. 249–264, 2019, doi: 10.5277/oa190206.
- [151] D. Chen, G. Hu, and L. Chen, “Pressure/temperature sensor based on a dual-core photonic crystal fiber,” *Asia Commun. Photonics Conf. Exhib. ACP 2011*, vol. 8307, pp. 1–10, 2011, doi: 10.1117/12.904029.
- [152] A. A. Rifat, G. A. Mahdiraji, Y. M. Sua, R. Ahmed, Y. G. Shee, and F. R. M. Adikan, “Highly sensitive multi-core flat fiber surface plasmon resonance refractive index sensor,” *Opt. Express*, vol. 24, no. 3, p. 2485, 2016, doi: 10.1364/oe.24.002485.

- [153] Z. Wang, T. Taru, T. A. Birks, J. C. Knight, Y. Liu, and J. Du, "Coupling in dual-core photonic bandgap fibers: theory and experiment," *Opt. Express*, vol. 15, no. 8, p. 4795, 2007, doi: 10.1364/oe.15.004795.
- [154] P. S. J. Russell, "Photonic-crystal fibers," *J. Light. Technol.*, vol. 24, no. 12, pp. 4729–4749, 2006, doi: 10.1109/JLT.2006.885258.
- [155] A. Ortigosa-Blanch *et al.*, "Highly Birefringent Photonic Crystal Fibers," *Opt. Photonics News*, vol. 12, no. 12, p. 17, 2001, doi: 10.1364/opn.12.12.000017.
- [156] T. Martynkien *et al.*, "Highly birefringent microstructured fibers with enhanced sensitivity to hydrostatic pressure," *Opt. Express*, vol. 18, no. 14, p. 15113, 2010, doi: 10.1364/oe.18.015113.
- [157] B. Gauvreau, A. Hassani, M. Fassi Fehri, A. Kabashin, and M. A. Skorobogatiy, "Photonic bandgap fiber-based Surface Plasmon Resonance sensors," *Opt. Express*, vol. 15, no. 18, pp. 11413–11426, 2007, doi: 10.1364/oe.15.011413.
- [158] L. M. Rodrigues and B. A. Marinkovic, "Effects of Fused Silica Addition on Thermal Expansion, Density, and Hardness of Alumix-231 Based Composites," *Materials (Basel)*, vol. 15, no. 10, 2022, doi: 10.3390/ma15103476.
- [159] V. S. Chaudhary, D. Kumar, R. Mishra, and S. Sharma, "Twin core photonic crystal fiber for temperature sensing," *Mater. Today Proc.*, vol. 33, no. xxxx, pp. 2289–2292, 2020, doi: 10.1016/j.matpr.2020.04.197.
- [160] H. Yu, Y. Wang, J. Ma, Z. Zheng, Z. Luo, and Y. Zheng, "Fabry-perot interferometric high-temperature sensing up to 1200 °c based on a silica glass photonic crystal fiber," *Sensors (Switzerland)*, vol. 18, no. 1, 2018, doi: 10.3390/s18010273.
- [161] S. Geerthana, A. S. Raja, and D. S. Sundar, "Design and optimization of photonic crystal fiber with improved optical characteristics," *J. Nonlinear Opt. Phys. Mater.*, vol. 24, no. 4, 2015, doi: 10.1142/S0218863515500514.
- [162] M. Hossain, E. Podder, A. Adhikary, and A. Al-Mamun, "Optimized Hexagonal Photonic Crystal Fibre Sensor for Glucose Sensing," *Adv. Res.*, vol. 13, no. 3, pp. 1–7, 2018, doi: 10.9734/air/2018/38972.
- [163] S. Kim, Y. S. Lee, C. G. Lee, Y. Jung, and K. Oh, "Hybrid square-lattice photonic crystal fiber with broadband single-mode operation, high birefringence, and normal dispersion," *J. Opt. Soc. Korea*, vol. 19, no. 5, pp. 449–455, 2015, doi: 10.3807/JOSK.2015.19.5.449.
- [164] V. Chaudhary and D. Kumar, "Design and analysis of refractive index sensor based on dual-core photonic crystal fiber (DC-PCF) with rectangular air hole lattice structure," *Lect. Notes Electr. Eng.*, vol. 546, pp. 207–213, 2020, doi: 10.1007/978-981-13-6159-3\_22.
- [165] A. M. R. Pinto and M. Lopez-Amo, "Photonic crystal fibers for sensing applications," *J. Sensors*, vol. 2012, 2012, doi: 10.1155/2012/598178.
- [166] D. Chen, M. L. V. Tse, and H. Y. Tam, "Optical properties of photonic crystal fibers with a fiber core of arrays of sub-wavelength circular air holes: Birefringence and

- dispersion,” *Prog. Electromagn. Res.*, vol. 105, pp. 193–212, 2010, doi: 10.2528/PIER10042706.
- [167] O. S., N. Seifouri, M. A., Abadi, and M. S. E., “Low Nonlinear Effects Index-Guiding Nanostructured Photonic Crystal fiber,” *Int. J. Chem. Mol. Nucl. Mater. Metall. Eng.*, vol. 9, no. 2, pp. 253–257, 2015.
- [168] K. R. Priya, A. S. Raja, and D. S. Sundar, “Design of a dual-core liquid-filled photonic crystal fiber coupler and analysis of its optical characteristics,” *J. Opt. Technol.*, vol. 83, no. 9, p. 569, 2016, doi: 10.1364/jot.83.000569.
- [169] M. B. Hossain, A. A.-M. Bulbul, M. A. Mukit, and E. Podder, “Analysis of Optical Properties for Square, Circular and Hexagonal Photonic Crystal Fiber,” *Opt. Photonics J.*, vol. 07, no. 11, pp. 235–243, 2017, doi: 10.4236/opj.2017.711021.
- [170] H. Ademgil, “Highly sensitive octagonal photonic crystal fiber based sensor,” *Optik (Stuttg.)*, vol. 125, no. 20, pp. 6274–6278, 2014, doi: 10.1016/j.ijleo.2014.08.018.
- [171] E. K. Akowuah, T. Gorman, H. Ademgil, S. Haxha, G. K. Robinson, and J. V. Oliver, “Numerical analysis of a photonic crystal fiber for biosensing applications,” *IEEE J. Quantum Electron.*, vol. 48, no. 11, pp. 1403–1410, 2012, doi: 10.1109/JQE.2012.2213803.
- [172] A. A. Rifat, G. A. Mahdiraji, Y. M. Sua, R. Ahmed, Y. G. Shee, and F. R. M. Adikan, “Highly sensitive multi-core flat fiber surface plasmon resonance refractive index sensor,” *Opt. Express*, vol. 24, no. 3, p. 2485, 2016, doi: 10.1364/oe.24.002485.
- [173] V. S. Chaudhary and D. Kumar, “TOPAS based porous core photonic crystal fiber for terahertz chemical sensor,” *Optik (Stuttg.)*, vol. 223, no. August, p. 165562, 2020, doi: 10.1016/j.ijleo.2020.165562.
- [174] W.-P. Huang, “Coupled-mode theory for optical waveguides: an overview,” *J. Opt. Soc. Am. A*, vol. 11, no. 3, p. 963, 1994, doi: 10.1364/josaa.11.000963.
- [175] K. Saitoh, Y. Sato, and M. Koshiba, “Coupling characteristics of dual-core photonic crystal fiber couplers,” *Opt. Express*, vol. 11, no. 24, p. 3188, 2003, doi: 10.1364/oe.11.003188.
- [176] Z. Wang, T. Taru, T. A. Birks, J. C. Knight, Y. Liu, and J. Du, “Coupling in dual-core photonic bandgap fibers: theory and experiment,” *Opt. Express*, vol. 15, no. 8, p. 4795, 2007, doi: 10.1364/oe.15.004795.
- [177] A. Ortigosa-Blanch *et al.*, “Highly Birefringent Photonic Crystal Fibers,” *Opt. Photonics News*, vol. 12, no. 12, p. 17, 2001, doi: 10.1364/opn.12.12.000017.
- [178] B. Gauvreau, A. Hassani, M. Fassi Fehri, A. Kabashin, and M. A. Skorobogatiy, “Photonic bandgap fiber-based Surface Plasmon Resonance sensors,” *Opt. Express*, vol. 15, no. 18, p. 11413, 2007, doi: 10.1364/oe.15.011413.
- [179] Z. K. Fan, S. B. Fang, S. G. Li, and Z. Y. Wei, “Refractive index sensor based on high-order surface plasmon resonance in gold nanofilm coated photonic crystal fiber,” *Chinese Phys. B*, vol. 28, no. 9, 2019, doi: 10.1088/1674-1056/ab327a.

- [180] P. Bing, J. Yao, Y. Lu, and Z. Li, "A surface-plasmon-resonance sensor based on photonic-crystal-fiber with large size microfluidic channels," *Opt. Appl.*, vol. 42, no. 3, pp. 493–501, 2012, doi: 10.5277/oa120306.
- [181] G. An *et al.*, "Extra-broad Photonic Crystal Fiber Refractive Index Sensor Based on Surface Plasmon Resonance," *Plasmonics*, vol. 12, no. 2, pp. 465–471, 2017, doi: 10.1007/s11468-016-0286-2.
- [182] C. Liu *et al.*, "Birefringent PCF-Based SPR Sensor for a Broad Range of Low Refractive Index Detection," *IEEE Photonics Technol. Lett.*, vol. 30, no. 16, pp. 1471–1474, 2018, doi: 10.1109/LPT.2018.2856859.
- [183] M. J. Bin Murshed Leon and A. S. Disha, "A simple structure of PCF based sensor for sensing sulfur dioxide gas with high sensitivity and better birefringence," *Sensors Int.*, vol. 2, 2021, doi: 10.1016/j.sintl.2021.100115.
- [184] M. Al Mahfuz *et al.*, "Highly sensitive photonic crystal fiber plasmonic biosensor: Design and analysis," *Opt. Mater. (Amst.)*, vol. 90, pp. 315–321, 2019, doi: 10.1016/j.optmat.2019.02.012.
- [185] M. A. Mollah, M. Yousufali, I. M. Ankan, M. M. Rahman, H. Sarker, and K. Chakrabarti, "Twin core photonic crystal fiber refractive index sensor for early detection of blood cancer," *Sens. Bio-Sensing Res.*, vol. 29, no. April, p. 100344, 2020, doi: 10.1016/j.sbsr.2020.100344.
- [186] S. Soylemez, Y. A. Udum, M. Kesik, C. Gündođdu Hizliateş, Y. Ergun, and L. Toppare, "Electrochemical and optical properties of a conducting polymer and its use in a novel biosensor for the detection of cholesterol," *Sensors Actuators, B Chem.*, vol. 212, pp. 425–433, 2015, doi: 10.1016/j.snb.2015.02.045.
- [187] D. Sun, T. Guo, Y. Ran, Y. Huang, and B. O. Guan, "In-situ DNA hybridization detection with a reflective microfiber grating biosensor," *Biosens. Bioelectron.*, vol. 61, pp. 541–546, 2014, doi: 10.1016/j.bios.2014.05.065.
- [188] G. An, S. Li, Y. An, H. Wang, and X. Zhang, "Glucose sensor realized with photonic crystal fiber-based Sagnac interferometer," *Opt. Commun.*, vol. 405, pp. 143–146, 2017, doi: 10.1016/j.optcom.2017.08.003.
- [189] "World health organization, Cancer," [Online]. Available: <https://www.who.int/news-room/fact-sheets/detail/cancer>
- [190] Clark LC, "Implantable gas-containing biosensor and method for measuring an analyte such as glucose," *Biotechnol. Adv.*, vol. 5, no. 2, p. 343, 1987, doi: 10.1016/0734-9750(87)90513-1.
- [191] L. Hajba and A. Guttman, "Circulating tumor-cell detection and capture using microfluidic devices," *TrAC - Trends Anal. Chem.*, vol. 59, pp. 9–16, 2014, doi: 10.1016/j.trac.2014.02.017.
- [192] F. R. Li, Q. Li, H. X. Zhou, H. Qi, and C. Y. Deng, "Detection of circulating tumor cells in breast cancer with a refined immunomagnetic nanoparticle enriched assay and nested-RT-PCR," *Nanomedicine Nanotechnology, Biol. Med.*, vol. 9, no. 7, pp. 1106–

- 1113, 2013, doi: 10.1016/j.nano.2013.03.002.
- [193] T. Li, Q. Fan, T. Liu, X. Zhu, J. Zhao, and G. Li, "Detection of breast cancer cells specially and accurately by an electrochemical method," *Biosens. Bioelectron.*, vol. 25, no. 12, pp. 2686–2689, 2010, doi: 10.1016/j.bios.2010.05.004.
- [194] S. L. Shupeng Liu *et al.*, "Surface-enhanced Raman spectroscopy measurement of cancerous cells with optical fiber sensor," *Chinese Opt. Lett.*, vol. 12, no. s1, pp. S13001-313003, 2014, doi: 10.3788/col201412.s13001.
- [195] U. Neugebauer, J. H. Clement, T. Bocklitz, C. Krafft, and J. Popp, "Identification and differentiation of single cells from peripheral blood by Raman spectroscopic imaging," *J. Biophotonics*, vol. 3, no. 8–9, pp. 579–587, 2010, doi: 10.1002/jbio.201000020.
- [196] C. Ribaut *et al.*, "Cancer biomarker sensing using packaged plasmonic optical fiber gratings: Towards in vivo diagnosis," *Biosens. Bioelectron.*, vol. 92, pp. 449–456, 2017, doi: 10.1016/j.bios.2016.10.081.
- [197] N. Ayyanar, G. Thavasi Raja, M. Sharma, and D. Sriram Kumar, "Photonic Crystal Fiber-Based Refractive Index Sensor for Early Detection of Cancer," *IEEE Sens. J.*, vol. 18, no. 17, pp. 7093–7099, 2018, doi: 10.1109/JSEN.2018.2854375.
- [198] N. R. Ramanujam *et al.*, "Enhanced sensitivity of cancer cell using one dimensional nano composite material coated photonic crystal," *Microsyst. Technol.*, vol. 25, no. 1, pp. 189–196, 2019, doi: 10.1007/s00542-018-3947-6.
- [199] A. A. Rifat *et al.*, "Surface Plasmon Resonance Photonic Crystal Fiber Biosensor: A Practical Sensing Approach," *IEEE Photonics Technol. Lett.*, vol. 27, no. 15, pp. 1628–1631, 2015, doi: 10.1109/LPT.2015.2432812.
- [200] S. Poonam and S. Preeta, "Design of Photonic Crystal-Based Biosensor for Detection of Glucose Concentration in Urine," *IEEE Sens. J.*, vol. 15, no. 2, pp. 1035–1042, 2015.
- [201] V. Kaur and S. Singh, "Design approach of solid-core photonic crystal fiber sensor with sensing ring for blood component detection," *J. Nanophotonics*, vol. 13, no. 02, p. 1, 2019, doi: 10.1117/1.jnp.13.026011.
- [202] E. Podder, M. B. Hossain, R. H. Jibon, A. A. M. Bulbul, and H. S. Mondal, "Chemical sensing through photonic crystal fiber: sulfuric acid detection," *Front. Optoelectron.*, vol. 12, no. 4, pp. 372–381, 2019, doi: 10.1007/s12200-019-0903-8.
- [203] K. Ahmed *et al.*, "Refractive Index-Based Blood Components Sensing in Terahertz Spectrum," *IEEE Sens. J.*, vol. 19, no. 9, pp. 3368–3375, 2019, doi: 10.1109/JSEN.2019.2895166.
- [204] M. S. Islam, M. Faisal, and S. M. A. Razzak, "Dispersion flattened extremely high-birefringent kagome lattice elliptic core photonic crystal fiber in THz regime," *Opt. Quantum Electron.*, vol. 51, no. 1, 2019, doi: 10.1007/s11082-019-1744-9.
- [205] F. A. Mou, M. M. Rahman, M. R. Islam, and M. I. H. Bhuiyan, "Development of a photonic crystal fiber for THz wave guidance and environmental pollutants detection," *Sens. Bio-Sensing Res.*, vol. 29, 2020, doi: 10.1016/j.sbsr.2020.100346.

- [206] A. A. M. Bulbul, F. Imam, M. A. Awal, and M. A. P. Mahmud, "A novel ultra-low loss rectangle-based porous-core pcf for efficient THz waveguidance: design and numerical analysis," *Sensors (Switzerland)*, vol. 20, no. 22, pp. 1–18, 2020, doi: 10.3390/s20226500.
- [207] D. Vigneswaran, N. Ayyanar, M. Sharma, M. Sumathi, M. R. Mani, and K. Porsezian, "Salinity sensor using photonic crystal fiber," *Sensors Actuators, A Phys.*, vol. 269, pp. 22–28, 2018, doi: 10.1016/j.sna.2017.10.052.
- [208] M. M. Rahman, F. A. Mou, M. I. H. Bhuiyan, and M. R. Islam, "Photonic crystal fiber based terahertz sensor for cholesterol detection in human blood and liquid foodstuffs," *Sens. Bio-Sensing Res.*, vol. 29, 2020, doi: 10.1016/j.sbsr.2020.100356.
- [209] M. De, A. K. Pathak, and V. K. Singh, "Single channel photonic crystal fiber based high sensitive petrol adulteration detection sensor," *Optik (Stuttg.)*, vol. 183, pp. 539–546, 2019, doi: 10.1016/j.ijleo.2019.03.001.
- [210] Y. E. Monfared, M. Hajati, C. Liang, S. Yang, and M. Qasymeh, "Quasi-D-Shaped Fiber Optic Plasmonic Biosensor for High-Index Analyte Detection," *IEEE Sens. J.*, vol. 21, no. 1, pp. 17–23, 2021, doi: 10.1109/JSEN.2019.2945003.
- [211] Y. Esfahani Monfared, "Refractive Index Sensor Based on Surface Plasmon Resonance Excitation in a D-Shaped Photonic Crystal Fiber Coated by Titanium Nitride," *Plasmonics*, vol. 15, no. 2, pp. 535–542, 2020, doi: 10.1007/s11468-019-01072-y.
- [212] Y. E. Monfared, "Overview of recent advances in the design of plasmonic fiber-optic biosensors," *Biosensors*, vol. 10, no. 7, 2020, doi: 10.3390/BIOS10070077.
- [213] B. M. Fischer *et al.*, "Terahertz time-domain spectroscopy and imaging of artificial RNA," *Opt. Express*, vol. 13, no. 14, p. 5205, 2005, doi: 10.1364/opex.13.005205.
- [214] A. Roitberg, E. J. Heilweil, and A. G. Markelz, "Pulsed terahertz spectroscopy of DNA, bovine serum albumin and collagen between 0.1 and 2.0 THz," *Chem. Phys. Lett.*, vol. 320, no. 1–2, pp. 42–48, 2000.
- [215] B. M. Fischer, M. Walther, and P. U. Jepsen, "Far-infrared vibrational modes of DNA components studied by terahertz time-domain spectroscopy," *Phys. Med. Biol.*, vol. 47, no. 21, pp. 3807–3814, 2002, doi: 10.1088/0031-9155/47/21/319.
- [216] C. Yu, S. Fan, Y. Sun, and E. Pickwell-Macpherson, "The potential of terahertz imaging for cancer diagnosis: A review of investigations to date.," *Quant. Imaging Med. Surg.*, vol. 2, no. 1, pp. 33–45, 2012, doi: 10.3978/j.issn.2223-4292.2012.01.04.
- [217] A. Rahman, A. K. Rahman, and B. Rao, "Early detection of skin cancer via terahertz spectral profiling and 3D imaging," *Biosens. Bioelectron.*, vol. 82, pp. 64–70, 2016, doi: 10.1016/j.bios.2016.03.051.
- [218] H. Cheon, H. J. Yang, and J. H. Son, "Toward Clinical Cancer Imaging Using Terahertz Spectroscopy," *IEEE J. Sel. Top. Quantum Electron.*, vol. 23, no. 4, 2017, doi: 10.1109/JSTQE.2017.2704905.
- [219] E. Arik, C. Koral, H. Altan, and O. Esentürk, "A new method for alcohol content

- determination of fuel oils by terahertz spectroscopy,” *Int. Conf. Infrared, Millimeter, Terahertz Waves, IRMMW-THz*, 2013, doi: 10.1109/IRMMW-THz.2013.6665885.
- [220] J. Sultana, M. S. Islam, K. Ahmed, A. Dinovitser, B. W.-H. Ng, and D. Abbott, “Terahertz detection of alcohol using a photonic crystal fiber sensor,” *Appl. Opt.*, vol. 57, no. 10, p. 2426, 2018, doi: 10.1364/ao.57.002426.
- [221] M. M. Rahman, F. A. Mou, A. Al Mahmud, M. I. H. Bhuiyan, and M. R. Islam, “Photonic Crystal Fiber based Terahertz Sensor for Alcohol Detection in Beverages: Design and Analysis,” *3rd IEEE Int. Conf. Telecommun. Photonics, ICTP 2019*, 2019, doi: 10.1109/ICTP48844.2019.9041767.
- [222] B. K. Paul, K. Ahmed, V. Dhasarathan, and T. K. Nguyen, “Oligoporous-core Quasi cladding photonic crystal fiber based micro-sensor for alcohol detection,” *Phys. B Condens. Matter*, vol. 584, 2020, doi: 10.1016/j.physb.2020.412104.
- [223] M. M. A. Eid, A. N. Z. Rashed, A. A. M. Bulbul, and E. Podder, “Mono-Rectangular Core Photonic Crystal Fiber (MRC-PCF) for Skin and Blood Cancer Detection,” *Plasmonics*, vol. 16, no. 3, pp. 717–727, 2021, doi: 10.1007/s11468-020-01334-0.
- [224] M. F. Huq Arif, M. Mobarak Hossain, M. M. Rahman, P. K. Mithun Kumar, and S. M. Khaled, “Photonic crystal based liquid sensor: A theoretical analysis for formalin detection,” *2018 Jt. 7th Int. Conf. Informatics, Electron. Vis. 2nd Int. Conf. Imaging, Vis. Pattern Recognition, ICIEV-IVPR 2018*, pp. 295–299, 2019, doi: 10.1109/ICIEV.2018.8640998.
- [225] A. A. M. Bulbul, R. H. Jibon, S. K. Das, T. Roy, A. Saha, and M. B. Hossain, “PCF Based Formalin Detection by Exploring the Optical Properties in THz Regime,” *Nanosci. Nanotechnology-Asia*, vol. 11, no. 3, pp. 314–321, 2020, doi: 10.2174/2210681210999200525171303.
- [226] M. S. Islam *et al.*, “Broadband Characterization of Glass and Polymer Materials Using THz-TDS,” *Int. Conf. Infrared, Millimeter, Terahertz Waves, IRMMW-THz*, vol. 2019-Septe, 2019, doi: 10.1109/IRMMW-THz.2019.8874013.
- [227] B. K. Paul, K. Ahmed, D. Vigneswaran, F. Ahmed, S. Roy, and D. Abbott, “Quasi-photonic crystal fiber-based spectroscopic chemical sensor in the terahertz spectrum: Design and analysis,” *IEEE Sens. J.*, vol. 18, no. 24, pp. 9948–9954, 2018, doi: 10.1109/JSEN.2018.2872892.
- [228] M. A. Jabin *et al.*, “Surface Plasmon Resonance Based Titanium Coated Biosensor for Cancer Cell Detection,” *IEEE Photonics J.*, vol. 11, no. 4, 2019, doi: 10.1109/JPHOT.2019.2924825.
- [229] V. Chaudhary and S. Singh, “Twin core photonic crystal fiber based temperature sensor with improved sensitivity over a wide range of temperature,” *Opt. Quantum Electron.*, vol. 55, no. 1, 2023, doi: 10.1007/s11082-022-04304-4.
- [230] M. Aslam Mollah, M. Yousufali, M. Rifat Bin Asif Faysal, M. Rabiul Hasan, M. B. Hossain, and I. S. Amiri, “Highly sensitive photonic crystal fiber salinity sensor based on Sagnac interferometer,” *Results Phys.*, vol. 16, 2020, doi: 10.1016/j.rinp.2020.103022.

- [231] S. Singh and Y. K. Prajapati, "Novel Bottom-Side Polished PCF-Based Plasmonic Biosensor for Early Detection of Hazardous Cancerous Cells," *IEEE Trans. Nanobioscience*, pp. 1–1, 2023, doi: 10.1109/tnb.2023.3233990.
- [232] G. P. Mishra, D. Kumar, V. S. Chaudhary, and G. Murmu, "Cancer cell detection by a heart-shaped dual-core photonic crystal fiber sensor," *Appl. Opt.*, vol. 59, no. 33, p. 10321, 2020, doi: 10.1364/ao.409221.
- [233] A. Yasli, "Cancer Detection with Surface Plasmon Resonance-Based Photonic Crystal Fiber Biosensor," *Plasmonics*, vol. 16, no. 5, pp. 1605–1612, 2021, doi: 10.1007/s11468-021-01425-6.
- [234] S. Singh and V. Kaur, "Photonic crystal fiber sensor based on sensing ring for different blood components: Design and analysis," *Int. Conf. Ubiquitous Futur. Networks, ICUFN*, pp. 399–403, 2017, doi: 10.1109/ICUFN.2017.7993816.
- [235] P. Sharma and P. Sharan, "Design of photonic crystal based ring resonator for detection of different blood constituents," *Opt. Commun.*, vol. 348, pp. 19–23, 2015, doi: 10.1016/j.optcom.2015.03.015.
- [236] K. Ahmed *et al.*, "Refractive Index-Based Blood Components Sensing in Terahertz Spectrum," *IEEE Sens. J.*, vol. 19, no. 9, pp. 3368–3375, 2019, doi: 10.1109/JSEN.2019.2895166.
- [237] G. Barshtein, "Biochemical and Biophysical Properties of Red Blood Cells in Disease," *Biomolecules*, vol. 12, no. 7, 2022, doi: 10.3390/biom12070923.
- [238] C. Bray *et al.*, "Erythrocyte sedimentation rate and C-reactive protein measurements and their relevance in clinical medicine," *Wis. Med. J.*, vol. 115, no. 6, pp. 317–321, 2016.
- [239] M. P. Spencer, "Systemic circulation.," *Annu. Rev. Physiol.*, vol. 28, pp.311–346, 1966, doi:10.1146/annurev.ph.28.030166.001523.
- [240] M. S. Islam *et al.*, "A novel approach for spectroscopic chemical identification using photonic crystal fiber in the terahertz regime," *IEEE Sens. J.*, vol. 18, no. 2, pp. 575–582, 2018, doi: 10.1109/JSEN.2017.2775642.
- [241] B. Fischer, M. Hoffmann, H. Helm, G. Modjesch, and P. U. Jepsen, "Chemical recognition in terahertz time-domain spectroscopy and imaging," *Semicond. Sci. Technol.*, vol. 20, no. 7, 2005, doi: 10.1088/0268-1242/20/7/015.
- [242] B. M. Fischer, H. Helm, and P. U. Jepsen, "Chemical recognition with broadband THZ spectroscopy," *Proc. IEEE*, vol. 95, no. 8, pp. 1592–1604, 2007, doi: 10.1109/JPROC.2007.898904.
- [243] M. Walther, B. M. Fischer, A. Ortner, A. Bitzer, A. Thoman, and H. Helm, "Chemical sensing and imaging with pulsed terahertz radiation," *Anal. Bioanal. Chem.*, vol. 397, no. 3, pp. 1009–1017, 2010, doi: 10.1007/s00216-010-3672-1.
- [244] P. U. Jepsen, U. Møller, and H. Merbold, "Investigation of aqueous alcohol and sugar solutions with reflection terahertz time-domain spectroscopy," *Opt. Express*, vol. 15, no. 22, p. 14717, 2007, doi: 10.1364/oe.15.014717.

- [245] P. U. Jepsen, J. K. Jensen, and U. Møller, "Characterization of aqueous alcohol solutions in bottles with THz reflection spectroscopy," *Opt. Express*, vol. 16, no. 13, p. 9318, 2008, doi: 10.1364/oe.16.009318.
- [246] E. Arik, C. Koral, H. Altan, and O. Esentürk, "A new method for alcohol content determination of fuel oils by terahertz spectroscopy," *Int. Conf. Infrared, Millimeter, Terahertz Waves, IRMMW-THz*, 2013, doi: 10.1109/IRMMW-THz.2013.6665885.
- [247] M. Nagel, P. Haring Bolivar, M. Brucherseifer, H. Kurz, A. Bosserhoff, and R. Büttner, "Integrated THz technology for label-free genetic diagnostics," *Appl. Phys. Lett.*, vol. 80, no. 1, pp. 154–156, 2002, doi: 10.1063/1.1428619.
- [248] B. M. Fischer *et al.*, "Terahertz time-domain spectroscopy and imaging of artificial RNA," *Opt. Express*, vol. 13, no. 14, p. 5205, 2005, doi: 10.1364/opex.13.005205.
- [249] J. Zhang and D. Grischkowsky, "Waveguide terahertz time-domain spectroscopy of nanometer water layers," *Opt. Lett.*, vol. 29, no. 14, p. 1617, 2004, doi: 10.1364/ol.29.001617.
- [250] C. Yu, S. Fan, Y. Sun, and E. Pickwell-Macpherson, "The potential of terahertz imaging for cancer diagnosis: A review of investigations to date.," *Quant. Imaging Med. Surg.*, vol. 2, no. 1, pp. 33–45, 2012, doi: 10.3978/j.issn.2223-4292.2012.01.04.
- [251] A. Rahman, A. K. Rahman, and B. Rao, "Early detection of skin cancer via terahertz spectral profiling and 3D imaging," *Biosens. Bioelectron.*, vol. 82, pp. 64–70, 2016, doi: 10.1016/j.bios.2016.03.051.
- [252] D. J.S., M. B.P., F. C.I., and G. R.A., "Beyond mammography: New frontiers in breast cancer screening," *Am. J. Med.*, vol. 126, no. 6, pp. 472–479, 2013.
- [253] H. Cheon, H. J. Yang, and J. H. Son, "Toward Clinical Cancer Imaging Using Terahertz Spectroscopy," *IEEE J. Sel. Top. Quantum Electron.*, vol. 23, no. 4, 2017, doi: 10.1109/JSTQE.2017.2704905.
- [254] K. I. Zaytsev *et al.*, "Medical diagnostics using terahertz pulsed spectroscopy," *J. Phys. Conf. Ser.*, vol. 486, no. 1, 2014, doi: 10.1088/1742-6596/486/1/012014.
- [255] A. Roitberg, E. J. Heilweil, and A. G. Markelz, "Pulsed terahertz spectroscopy of DNA, bovine serum albumin and collagen between 0.1 and 2.0 THz," *Chem. Phys. Lett.*, vol. 320, no. 1–2, pp. 42–48, 2000.
- [256] B. M. Fischer, M. Walther, and P. U. Jepsen, "Far-infrared vibrational modes of DNA components studied by terahertz time-domain spectroscopy," *Phys. Med. Biol.*, vol. 47, no. 21, pp. 3807–3814, 2002, doi: 10.1088/0031-9155/47/21/319.
- [257] Y. He, P. I. Ku, J. R. Knab, J. Y. Chen, and A. G. Markelz, "Protein dynamical transition does not require protein structure," *Phys. Rev. Lett.*, vol. 101, no. 17, 2008, doi: 10.1103/PhysRevLett.101.178103.
- [258] S. Asaduzzaman, K. Ahmed, T. Bhuiyan, and T. Farah, "Hybrid photonic crystal fiber in chemical sensing," *Springerplus*, vol. 5, no. 1, 2016, doi: 10.1186/s40064-016-2415-y.

- [259] S. Sen, S. Chowdhury, K. Ahmed, and S. Asaduzzaman, "Design of a porous cored hexagonal photonic crystal fiber based optical sensor with high relative sensitivity for lower operating wavelength," *Photonic Sensors*, vol. 7, no. 1, pp. 55–65, 2017, doi: 10.1007/s13320-016-0384-y.
- [260] R. Kanmani, K. Ahmed, S. Roy, F. Ahmed, B. Kumar Paul, and M. S. Mani Rajan, "The performance of hosting and core materials for slotted core Q-PCF in terahertz spectrum," *Optik (Stuttg.)*, vol. 194, 2019, doi: 10.1016/j.ijleo.2019.163084.
- [261] E. Podder, M. B. Hossain, R. H. Jibon, A. A. M. Bulbul, and H. S. Mondal, "Chemical sensing through photonic crystal fiber: sulfuric acid detection," *Front. Optoelectron.*, vol. 12, no. 4, pp. 372–381, 2019, doi: 10.1007/s12200-019-0903-8.
- [262] E. Podder, M. B. Hossain, M. E. Rahaman, A. A. M. Bulbul, and K. Ahmed, "Design and optimization of terahertz blood components sensor using photonic crystal fiber," *Sens. Bio-Sensing Res.*, vol. 30, 2020, doi: 10.1016/j.sbsr.2020.100386.
- [263] D. Vijayalakshmi, C. T. Manimegalai, and P. Selvakumar, "Bi-core photonic crystal fiber for blood component detection," *J. Opt.*, vol. 52, no. 1, pp. 42–49, 2023, doi: 10.1007/s12596-022-00848-6.
- [264] "Topas advanced polymer. accessed: 15 th march, 2021." [online]. available:<https://topas.com/markets/electronics/more-electronics-apps>.
- [265] R. T. Bise and D. J. Trevor, "Sol-gel derived microstructured fiber: Fabrication and characterization," *Conf. Opt. Fiber Commun. Tech. Dig. Ser.*, vol. 3, pp. 269–271, 2005, doi: 10.1109/ofc.2005.192772.
- [266] A. Ghazanfari, W. Li, M. C. Leu, and G. E. Hilmas, "A novel freeform extrusion fabrication process for producing solid ceramic components with uniform layered radiation drying," *Addit. Manuf.*, vol. 15, pp. 102–112, 2017, doi: 10.1016/j.addma.2017.04.001.
- [267] H. Ebendorff-Heidepriem, J. Schuppich, A. Dowler, L. Lima-Marques, and T. M. Monro, "3D-printed extrusion dies: a versatile approach to optical material processing," *Opt. Mater. Express*, vol. 4, no. 8, p. 1494, 2014, doi: 10.1364/ome.4.001494.
- [268] W.-P. Huang, "Coupled-mode theory for optical waveguides: an overview," *J. Opt. Soc. Am. A*, vol. 11, no. 3, p. 963, 1994, doi: 10.1364/josaa.11.000963.
- [269] V. Chaudhary and S. Singh, "Highly sensitive twin core photonic crystal fiber for hazardous cancer cell detection in THz frequency regime," *Opt. Quantum Electron.*, pp. 1–17, 2023, doi: 10.1007/s11082-023-05462-9.
- [270] V. Chaudhary and S. Singh, "Twin core photonic crystal fiber based temperature sensor with improved sensitivity over a wide range of temperature," *Opt. Quantum Electron.*, vol. 55, no. 1, 2023, doi: 10.1007/s11082-022-04304-4.
- [271] V. Chaudhary and D. Kumar, "Design and analysis of refractive index sensor based on dual-core photonic crystal fiber (DC-PCF) with rectangular air hole lattice structure," *Lect. Notes Electr. Eng.*, vol. 546, pp. 207–213, 2020, doi: 10.1007/978-

981-13-6159-3\_22.

- [272] N. A. Elmahdy, M. F. O. Hameed, and S. S. A. Obayya, "Refractive index sensor based on plasmonic D-shaped photonic crystal fiber with pyramid grating," *Opt. Quantum Electron.*, vol. 54, no. 11, 2022, doi: 10.1007/s11082-022-04102-y.
- [273] M. R. Islam, A. N. M. Iftekher, F. Noor, M. R. H. Khan, M. T. Reza, and M. M. Nishat, "AZO-coated plasmonic PCF nanosensor for blood constituent detection in near-infrared and visible spectrum," *Appl. Phys. A Mater. Sci. Process.*, vol. 128, no. 1, 2022, doi: 10.1007/s00339-021-05220-2.
- [274] M. Y. Azab, M. F. O. Hameed, G. A. Mahdiraji, F. R. M. Adikan, and S. S. A. Obayya, "Experimental and numerical characterization of a D-shaped PCF refractive index sensor," *Opt. Quantum Electron.*, vol. 54, no. 12, 2022, doi: 10.1007/s11082-022-04232-3.
- [275] F. Meng, H. Wang, and D. Fang, "Research on D-Shape Open-Loop PCF Temperature Refractive Index Sensor Based on SPR Effect," *IEEE Photonics J.*, vol. 14, no. 3, 2022, doi: 10.1109/JPHOT.2022.3166822.
- [276] M. Al Mahfuz *et al.*, "Highly sensitive photonic crystal fiber plasmonic biosensor: Design and analysis," *Opt. Mater. (Amst.)*, vol. 90, pp. 315–321, 2019, doi: 10.1016/j.optmat.2019.02.012.
- [277] L. M. Rodrigues and B. A. Marinkovic, "Effects of Fused Silica Addition on Thermal Expansion, Density, and Hardness of Alumix-231 Based Composites," *Materials (Basel)*, vol. 15, no. 10, 2022, doi: 10.3390/ma15103476.
- [278] S. Soylemez, Y. A. Udum, M. Kesik, C. Gündođdu Hizliateş, Y. Ergun, and L. Toppare, "Electrochemical and optical properties of a conducting polymer and its use in a novel biosensor for the detection of cholesterol," *Sensors Actuators, B Chem.*, vol. 212, pp. 425–433, 2015, doi: 10.1016/j.snb.2015.02.045.
- [279] D. Sun, T. Guo, Y. Ran, Y. Huang, and B. O. Guan, "In-situ DNA hybridization detection with a reflective microfiber grating biosensor," *Biosens. Bioelectron.*, vol. 61, pp. 541–546, 2014, doi: 10.1016/j.bios.2014.05.065.
- [280] G. An, S. Li, Y. An, H. Wang, and X. Zhang, "Glucose sensor realized with photonic crystal fiber-based Sagnac interferometer," *Opt. Commun.*, vol. 405, pp. 143–146, 2017, doi: 10.1016/j.optcom.2017.08.003.
- [281] V. S. Chaudhary, D. Kumar, and S. Kumar, "Gold-Immobilized Photonic Crystal Fiber-Based SPR Biosensor for Detection of Malaria Disease in Human Body," *IEEE Sens. J.*, vol. 21, no. 16, pp. 17800–17807, 2021, doi: 10.1109/JSEN.2021.3085829.
- [282] S. Bendib and B. C., "Photonic Crystals for Malaria Detection," *J. Biosens. Bioelectron.*, vol. 09, no. 03, 2018, doi: 10.4172/2155-6210.1000257.
- [283] K. Ahmed *et al.*, "Refractive Index-Based Blood Components Sensing in Terahertz Spectrum," *IEEE Sens. J.*, vol. 19, no. 9, pp. 3368–3375, 2019, doi: 10.1109/JSEN.2019.2895166.
- [284] A. A. M. Bulbul, R. H. Jibon, S. K. Das, T. Roy, A. Saha, and M. B. Hossain, "PCF

- Based Formalin Detection by Exploring the Optical Properties in THz Regime,” *Nanosci. Nanotechnology-Asia*, vol. 11, no. 3, pp. 314–321, 2020, doi: 10.2174/2210681210999200525171303.
- [285] M. S. Islam, M. Faisal, and S. M. A. Razzak, “Dispersion flattened extremely high-birefringent kagome lattice elliptic core photonic crystal fiber in THz regime,” *Opt. Quantum Electron.*, vol. 51, no. 1, 2019, doi: 10.1007/s11082-019-1744-9.
- [286] V. Kaur and S. Singh, “Design approach of solid-core photonic crystal fiber sensor with sensing ring for blood component detection,” *J. Nanophotonics*, vol. 13, no. 02, p. 1, 2019, doi: 10.1117/1.jnp.13.026011.
- [287] F. A. Mou, M. M. Rahman, M. R. Islam, and M. I. H. Bhuiyan, “Development of a photonic crystal fiber for THz wave guidance and environmental pollutants detection,” *Sens. Bio-Sensing Res.*, vol. 29, 2020, doi: 10.1016/j.sbsr.2020.100346.
- [288] E. Podder, M. B. Hossain, R. H. Jibon, A. A. M. Bulbul, and H. S. Mondal, “Chemical sensing through photonic crystal fiber: sulfuric acid detection,” *Front. Optoelectron.*, vol. 12, no. 4, pp. 372–381, 2019, doi: 10.1007/s12200-019-0903-8.
- [289] S. Poonam and S. Preeta, “Design of Photonic Crystal-Based Biosensor for Detection of Glucose Concentration in Urine,” *IEEE Sens. J.*, vol. 15, no. 2, pp. 1035–1042, 2015.
- [290] A. A. Rifat *et al.*, “Surface Plasmon Resonance Photonic Crystal Fiber Biosensor: A Practical Sensing Approach,” *IEEE Photonics Technol. Lett.*, vol. 27, no. 15, pp. 1628–1631, 2015, doi: 10.1109/LPT.2015.2432812.
- [291] B. K. Paul, K. Ahmed, D. Vigneswaran, F. Ahmed, S. Roy, and D. Abbott, “Quasi-photonic crystal fiber-based spectroscopic chemical sensor in the terahertz spectrum: Design and analysis,” *IEEE Sens. J.*, vol. 18, no. 24, pp. 9948–9954, 2018, doi: 10.1109/JSEN.2018.2872892.
- [292] R. T. Bise and D. J. Trevor, “Sol-gel derived microstructured fiber: Fabrication and characterization,” *Conf. Opt. Fiber Commun. Tech. Dig. Ser.*, vol. 3, pp. 269–271, 2005, doi: 10.1109/ofc.2005.192772.
- [293] A. Ghazanfari, W. Li, M. C. Leu, and G. E. Hilmas, “A novel freeform extrusion fabrication process for producing solid ceramic components with uniform layered radiation drying,” *Addit. Manuf.*, vol. 15, pp. 102–112, 2017, doi: 10.1016/j.addma.2017.04.001.
- [294] H. Ebendorff-Heidepriem, J. Schuppich, A. Dowler, L. Lima-Marques, and T. M. Monro, “3D-printed extrusion dies: a versatile approach to optical material processing,” *Opt. Mater. Express*, vol. 4, no. 8, p. 1494, 2014, doi: 10.1364/ome.4.001494.
- [295] P. Y. Liu *et al.*, “Cell refractive index for cell biology and disease diagnosis: Past, present and future,” *Lab Chip*, vol. 16, no. 4, pp. 634–644, 2016, doi: 10.1039/c5lc01445j.
- [296] Y. K. Park *et al.*, “Refractive index maps and membrane dynamics of human red blood

- cells parasitized by *Plasmodium falciparum*,” *Proc. Natl. Acad. Sci. U. S. A.*, vol. 105, no. 37, pp. 13730–13735, 2008, doi: 10.1073/pnas.0806100105.
- [297] W.-P. Huang, “Coupled-mode theory for optical waveguides: an overview,” *J. Opt. Soc. Am. A*, vol. 11, no. 3, p. 963, 1994, doi: 10.1364/josaa.11.000963.
- [298] V. Chaudhary and S. Singh, “Hexagonal lattice twin core photonic crystal fiber based chemical sensor,” *Proc. 10th Int. Conf. Signal Process. Integr. Networks, SPIN 2023*, pp. 164–167, 2023, doi: 10.1109/SPIN57001.2023.10117365.
- [299] V. Chaudhary and S. Singh, “Twin core photonic crystal fiber based temperature sensor with improved sensitivity over a wide range of temperature,” *Opt. Quantum Electron.*, vol. 55, no. 1, 2023, doi: 10.1007/s11082-022-04304-4.
- [300] V. Chaudhary and S. Singh, “Highly sensitive twin core photonic crystal fiber for hazardous cancer cell detection in THz frequency regime,” *Opt. Quantum Electron.*, pp. 1–17, 2023, doi: 10.1007/s11082-023-05462-9.
- [301] M. A. Jabin *et al.*, “Surface Plasmon Resonance Based Titanium Coated Biosensor for Cancer Cell Detection,” *IEEE Photonics J.*, vol. 11, no. 4, 2019, doi: 10.1109/JPHOT.2019.2924825.
- [302] V. Chaudhary and D. Kumar, “Design and analysis of refractive index sensor based on dual-core photonic crystal fiber (DC-PCF) with rectangular air hole lattice structure,” *Lect. Notes Electr. Eng.*, vol. 546, pp. 207–213, 2020, doi: 10.1007/978-981-13-6159-3\_22.
- [303] A. Panda and P. Puspa Devi, “Photonic crystal biosensor for refractive index based cancerous cell detection,” *Opt. Fiber Technol.*, vol. 54, 2020, doi: 10.1016/j.yofte.2019.102123.
- [304] F. Meng, H. Wang, and D. Fang, “Research on D-Shape Open-Loop PCF Temperature Refractive Index Sensor Based on SPR Effect,” *IEEE Photonics J.*, vol. 14, no. 3, 2022, doi: 10.1109/JPHOT.2022.3166822.
- [305] M. Y. Azab, M. F. O. Hameed, G. A. Mahdiraji, F. R. M. Adikan, and S. S. A. Obayya, “Experimental and numerical characterization of a D-shaped PCF refractive index sensor,” *Opt. Quantum Electron.*, vol. 54, no. 12, 2022, doi: 10.1007/s11082-022-04232-3.
- [306] R. C. Jorgenson and S. S. Yee, “A fiber-optic chemical sensor based on surface plasmon resonance,” *Sensors Actuators B. Chem.*, vol. 12, no. 3, pp. 213–220, 1993, doi: 10.1016/0925-4005(93)80021-3.
- [307] S. Long *et al.*, “Sensing absorptive fluids with backside illuminated grating coupled SPR sensor fabricated by nanoimprint technology,” *Sensors Actuators A Phys.*, vol. 337, 2022, doi: 10.1016/j.sna.2022.113416.
- [308] V. Kaur and S. Singh, “Design of titanium nitride coated PCF-SPR sensor for liquid sensing applications,” *Opt. Fiber Technol.*, vol. 48, pp. 159–164, 2019, doi: 10.1016/j.yofte.2018.12.015.
- [309] W. M. E. M. M. Daniyal, Y. W. Fen, N. I. M. Fauzi, H. S. Hashim, N. S. M. Ramdzan,

- and N. A. S. Omar, "Recent Advances in Surface Plasmon Resonance Optical Sensors for Potential Application in Environmental Monitoring," *Sensors Mater.*, vol. 32, no. 12, pp. 4191–4200, 2020, doi: 10.18494/SAM.2020.3204.
- [310] S. Balbinot, A. M. Srivastav, J. Vidic, I. Abdulhalim, and M. Manzano, "Plasmonic biosensors for food control," *Trends Food Sci. Technol.*, vol. 111, pp. 128–140, 2021, doi: 10.1016/j.tifs.2021.02.057.
- [311] J. Zhou *et al.*, "Surface plasmon resonance (SPR) biosensors for food allergen detection in food matrices," *Biosens. Bioelectron.*, vol. 142, 2019, doi: 10.1016/j.bios.2019.111449.
- [312] X. Fan, "Sensitive surface plasmon resonance label-free biosensor on a fiber end-facet," *Light Sci. Appl.*, vol. 11, no. 1, 2022, doi: 10.1038/s41377-022-01025-x.
- [313] P. S. J. Russell, "Photonic-crystal fibers," *J. Light. Technol.*, vol. 24, no. 12, pp. 4729–4749, 2006, doi: 10.1109/JLT.2006.885258.
- [314] S. A. Cerqueira Jr, "Recent progress and novel applications of photonic crystal fibers," *Reports Prog. Phys.*, vol. 73, no. 2, p. 24401, 2010.
- [315] M. E. Rahaman, M. M. Hossain, H. Shekhar Mondal, R. Saha, and A. Saif Muntaseer, "Theoretical analysis of large negative dispersion photonic crystal fiber with small confinement loss," *Appl. Opt.*, vol. 59, no. 28, p. 8925, 2020, doi: 10.1364/ao.397420.
- [316] M. E. Rahaman, H. S. Mondal, M. B. Hossain, M. M. Hossain, M. S. Ahsan, and R. Saha, "Simulation of a highly birefringent photonic crystal fiber in terahertz frequency region," *SN Appl. Sci.*, vol. 2, no. 8, 2020, doi: 10.1007/s42452-020-03210-2.
- [317] R. Saha, M. M. Hossain, M. E. Rahaman, and H. S. Mondal, "Design and analysis of high birefringence and nonlinearity with small confinement loss photonic crystal fiber," *Front. Optoelectron.*, vol. 12, no. 2, pp. 165–173, 2019, doi: 10.1007/s12200-018-0837-6.
- [318] W. Urbanczyk *et al.*, "Photonic crystal fibers for sensing applications," *2008 IEEE/LEOS Winter Top. Meet. Ser.*, pp. 196–197, 2008, doi: 10.1109/LEOSWT.2008.4444468.
- [319] V. Chaudhary and S. Singh, "Effect of Selectively-Filled-Ethanol on Dispersion Characteristics of Circular Shaped Hollow Core Photonic Crystal Fiber," pp. 429–437, 2023, doi: 10.1007/978-981-19-7753-4\_33.
- [320] F. Iqbal *et al.*, "Alcohol sensing and classification using PCF-based sensor," *Sens. Bio-Sensing Res.*, vol. 30, 2020, doi: 10.1016/j.sbsr.2020.100384.
- [321] A. A. Rifat, G. Amouzad Mahdiraji, D. M. Chow, Y. G. Shee, R. Ahmed, and F. R. M. Adikan, "Photonic crystal fiber-based surface plasmon resonance sensor with selective analyte channels and graphene-silver deposited core," *Sensors (Switzerland)*, vol. 15, no. 5, pp. 11499–11510, 2015, doi: 10.3390/s150511499.
- [322] Y. Zhao, Z. Q. Deng, and J. Li, "Photonic crystal fiber based surface plasmon resonance chemical sensors," *Sensors Actuators, B Chem.*, vol. 202, pp. 557–567, 2014, doi: 10.1016/j.snb.2014.05.127.

- [323] M. E. Rahaman *et al.*, “Sensing Toxic Carbonyl Compounds in Cigarette Smoke by Photonic Crystal Fiber,” *2020 11th Int. Conf. Comput. Commun. Netw. Technol. ICCCNT 2020*, 2020, doi: 10.1109/ICCCNT49239.2020.9225607.
- [324] M. E. Rahaman, M. B. Hossain, H. S. Mondal, R. Saha, M. M. Hossain, and M. S. Ahsan, “Highly sensitive photonic crystal fiber liquid sensor in terahertz frequency range,” *Mater. Today Proc.*, vol. 43, pp. 3815–3820, 2021.
- [325] V. Chaudhary and S. Singh, “Twin core photonic crystal fiber based temperature sensor with improved sensitivity over a wide range of temperature,” *Opt. Quantum Electron.*, vol. 55, no. 1, 2023, doi: 10.1007/s11082-022-04304-4.
- [326] V. Chaudhary and S. Singh, “Hexagonal lattice twin core photonic crystal fiber based chemical sensor,” *Proc. 10th Int. Conf. Signal Process. Integr. Networks, SPIN 2023*, pp. 164–167, 2023, doi: 10.1109/SPIN57001.2023.10117365.
- [327] B. Lee, S. Roh, and J. Park, “Current status of micro- and nano-structured optical fiber sensors,” *Opt. Fiber Technol.*, vol. 15, no. 3, pp. 209–221, 2009, doi: 10.1016/j.yofte.2009.02.006.
- [328] V. Chaudhary and S. Singh, “Highly sensitive twin core photonic crystal fiber for hazardous cancer cell detection in THz frequency regime,” *Opt. Quantum Electron.*, pp. 1–17, 2023, doi: 10.1007/s11082-023-05462-9.
- [329] V. Chaudhary, S. Singh, V. S. Chaudhary, and D. Kumar, “Design and Optimization of Terahertz Based D-shaped Photonic Crystal Fiber for Blood Component Detection,” *IEEE Sens. J.*, 2024, doi: 10.1109/JSEN.2024.3437245.
- [330] M. Y. Azab, M. F. O. Hameed, A. M. Heikal, S. S. A. Obayya, and M. A. Swillam, “Surface plasmon photonic crystal fiber biosensor for glucose monitoring,” *2017 Int. Appl. Comput. Electromagn. Soc. Symp. - Italy, ACES 2017*, 2017, doi: 10.23919/ROPACES.2017.7916401.
- [331] A. A. Rifat, G. A. Mahdiraji, Y. G. Shee, M. J. Shawon, and F. R. M. Adikan, “A Novel Photonic Crystal Fiber Biosensor Using Surface Plasmon Resonance,” *Procedia Eng.*, vol. 140, pp. 1–7, 2016, doi: 10.1016/j.proeng.2015.08.1107.
- [332] Dash, J. Narayan, and R. Jha, “SPR biosensor based on polymer PCF coated with conducting metal oxide,” *IEEE Photonics Technol. Lett.*, vol. 26, no. 6, pp. 595–598, 2016.
- [333] M. R. Hasan, S. Akter, A. A. Rifat, S. Rana, and S. Ali, “A highly sensitive gold-coated photonic crystal fiber biosensor based on surface plasmon resonance,” *Photonics*, vol. 4, no. 1, 2017, doi: 10.3390/photonics4010018.
- [334] H. Han *et al.*, “A large detection-range plasmonic sensor based on an h-shaped photonic crystal fiber,” *Sensors (Switzerland)*, vol. 20, no. 4, 2020, doi: 10.3390/s20041009.
- [335] M. E. Rahaman, R. Saha, M. S. Ahsan, and I. B. Sohn, “Design and performance analysis of a D-shaped PCF and surface plasmon resonance based glucose sensor,” *4th Int. Conf. Electr. Eng. Inf. Commun. Technol. iCEEiCT 2018*, pp. 325–329, 2018, doi:

10.1109/CEEICT.2018.8628080.

- [336] Q. Liu *et al.*, “Surface plasmon resonance sensor based on photonic crystal fiber with indium tin oxide film,” *Opt. Mater. (Amst.)*, vol. 102, 2020, doi: 10.1016/j.optmat.2020.109800.
- [337] X. Guo, L. Han, F. Liu, and S. Li, “Refractive index sensing characteristics of dual-core PCF based on surface plasmon resonance,” *Optik (Stuttg.)*, vol. 218, 2020, doi: 10.1016/j.ijleo.2020.164796.
- [338] D. Pysz *et al.*, “Stack and draw fabrication of soft glass microstructured fiber optics,” *Bull. Polish Acad. Sci. Tech. Sci.*, vol. 62, no. 4, pp. 667–682, 2014, doi: 10.2478/bpasts-2014-0073.
- [339] A. A. Rifat *et al.*, “Photonic crystal fiber based plasmonic sensors,” *Sensors Actuators, B Chem.*, vol. 243, pp. 311–325, 2017, doi: 10.1016/j.snb.2016.11.113.
- [340] J. Boehm, A. François, H. Ebendorff-Heidepriem, and T. M. Monro, “Chemical Deposition of Silver for the Fabrication of Surface Plasmon Microstructured Optical Fibre Sensors,” *Plasmonics*, vol. 6, no. 1, pp. 133–136, 2011, doi: 10.1007/s11468-010-9178-z.
- [341] K. Nielsen, D. Noordegraaf, T. Sørensen, A. Bjarklev, and T. P. Hansen, “Selective filling of photonic crystal fibres,” *J. Opt. A Pure Appl. Opt.*, vol. 7, no. 8, pp. L13–L20, 2005, doi: 10.1088/1464-4258/7/8/02.
- [342] G. P. Mishra, D. Kumar, V. S. Chaudhary, and G. Murmu, “Cancer cell detection by a heart-shaped dual-core photonic crystal fiber sensor,” *Appl. Opt.*, vol. 59, no. 33, p. 10321, 2020, doi: 10.1364/ao.409221.
- [343] M. H. Sani, A. Ghanbari, and H. Saghaei, “High-sensitivity biosensor for simultaneous detection of cancer and diabetes using photonic crystal microstructure,” *Opt. Quantum Electron.*, vol. 54, no. 1, 2022, doi: 10.1007/s11082-021-03371-3.
- [344] R. Zakaria, W. Kam, Y. S. Ong, S. F. A. Z. Yusoff, H. Ahmad, and W. S. Mohammed, “Fabrication and simulation studies on D-shaped optical fiber sensor via surface plasmon resonance,” *J. Mod. Opt.*, vol. 64, no. 14, pp. 1443–1449, 2017, doi: 10.1080/09500340.2017.1293858.
- [345] M. A. Jabin *et al.*, “Surface Plasmon Resonance Based Titanium Coated Biosensor for Cancer Cell Detection,” *IEEE Photonics J.*, vol. 11, no. 4, 2019, doi: 10.1109/JPHOT.2019.2924825.
- [346] M. Y. Azab, M. F. O. Hameed, G. A. Mahdiraji, F. R. M. Adikan, and S. S. A. Obayya, “Experimental and numerical characterization of a D-shaped PCF refractive index sensor,” *Opt. Quantum Electron.*, vol. 54, no. 12, 2022, doi: 10.1007/s11082-022-04232-3.
- [347] A. Panda and P. Puspa Devi, “Photonic crystal biosensor for refractive index based cancerous cell detection,” *Opt. Fiber Technol.*, vol. 54, 2020, doi: 10.1016/j.yofte.2019.102123.
- [348] M. R. Islam, A. N. M. Iftekher, F. Noor, M. R. H. Khan, M. T. Reza, and M. M. Nishat,

“AZO-coated plasmonic PCF nanosensor for blood constituent detection in near-infrared and visible spectrum,” *Appl. Phys. A Mater. Sci. Process.*, vol. 128, no. 1, 2022, doi: 10.1007/s00339-021-05220-2.

- [349] P. Bing, J. Yao, Y. Lu, and Z. Li, “A surface-plasmon-resonance sensor based on photonic-crystal-fiber with large size microfluidic channels,” *Opt. Appl.*, vol. 42, no. 3, pp. 493–501, 2012, doi: 10.5277/oa120306.



**DELHI TECHNOLOGICAL UNIVERSITY**  
*Formerly Delhi College of Engineering*  
Shahbad Daultapur, Main Bawana Road, Delhi –42

---

## Plagiarism Verification

**Thesis Title:** Design and Analysis of Photonic Crystal Fiber for Sensing Applications

**Name of the Scholar:** Vishal Chaudhary

**Supervisor:** Dr. Sonal Singh

**Designation:** Assistant Professor

**Department:** Electronics and Communication Engineering

This is to report that the above thesis was scanned for similarity detection. Process and outcomes are given below:

**Software Used:** Turnitin

**Submission ID:** trn:oid:::1:3501973663

**Similarity Index:** 36%

**Self Publication(s) Similarity Index:** 28%

**Final Total Similarity Index:** 8%

**Total Word Count:** 52,594

**Date:** March, 09 2026

---

**Signature of Supervisor**

---

**Signature of Candidate**

# CURRICULUM VITAE

**VISHAL CHAUDHARY**

**Address:** Diwan Bazar  
Behind Post Office,  
Gorakhpur-273001  
U.P. (India)

**E-mail:** vishalchaudhary719@gmail.com

**Contact No.:** +91-8756255807

## OBJECTIVE

- To work hard with full determination and dedication to achieve organizational as well as personal goals.

## PROFESSIONAL QUALIFICATIONS

- **PhD (Electronics & Communication Engineering)**, Delhi Technological University, Delhi, India (Formerly Delhi College of Engineering).  
**Mode of PhD:** Full Time, **Broad Area of Specialization:** Photonics  
**Date of Registration:** 02/08/2021, **Date of Awarded:** Thesis Submitted
- **M.Tech. in Digital Systems** from Madan Mohan Malaviya University of Technology, Gorakhpur, U.P., India (Formerly Madan Mohan Malaviya Engineering College Gorakhpur) with a CGPA of 8.06 (2016-18).
- **B.Tech. in Electronics & Communication Engineering** from Feroze Gandhi Institute of Engineering & Technology, Raebareli, affiliated to Uttar Pradesh Technical University with an aggregate of 64.96% in 2015.

## ACADEMIC QUALIFICATIONS

- Secured 67.4% in Intermediate (U.P. Board) in 2011.
- Secured 60.1% in High School (U.P. Board) in 2009.

## WORK EXPERIENCE

- **Working as Assistant Professor** in the Department of Electronics and Communication Engineering at **JSS University, Noida** since **15 July 2025**.
- **02 years Worked** as an **Assistant Professor** in the department of Electronics and Communication Engineering in **Netaji Subhas Institute of Technology, Bihta Patna, Bihar, India** since **15-Jan-2019 To 07-Jan-2021**.

### International Journal

1. **Vishal Chaudhary** and Sonal Singh, “Design of photonic crystal fiber-based plasmonic sensor for diabetes detection,” *Journal of Computational Electronics*, vol. 25, no. 29, 2026, doi: 10.1007/s10825-025-02475-3 [SCI, Impact Factor: 2.5].
2. **Vishal Chaudhary** and Sonal Singh, “Design and optimization of a terahertz photonic crystal fiber based biosensor to detect malaria disease,” *Journal of Computational Electronics*, vol. 24, no. 1, 2025, doi: 10.1007/s10825-024-02255-5 [SCI, Impact Factor: 2.5].
3. **Vishal Chaudhary**, Sonal Singh, Vijay Shanker Chaudhary and Dharmendra Kumar “Design and Optimization of Terahertz Based D-shaped Photonic Crystal Fiber for Blood Component Detection” *IEEE Sensors Journal* <https://doi.org/10.1109/JSEN.2024.3437245> [SCI, Impact Factor: 4.5].
4. **Vishal Chaudhary** and Sonal Singh, “Twin core photonic crystal fiber-based temperature sensor with improved sensitivity over a wide range of temperature” *Optical and Quantum Electronics*, vol. 55, no. 1, 2023, doi: 10.1007/s11082-022-04304-4 [SCI, Impact Factor: 4.0].
5. **Vishal Chaudhary** and Sonal Singh, “Highly sensitive twin core photonic crystal fiber for hazardous cancer cell detection in THz frequency regime,” *Optical and Quantum Electronics*, vol. 55, no. 1174, 2023, doi: 10.1007/s11082-023-05462-9. [SCI, Impact Factor: 4.0].
6. Vijay Shanker Chaudhary, **Vishal Chaudhary**, and Dharmendra Kumar “Highly Negative Dispersion Compensating Dual Core Photonic Crystal Fiber” *International Journal of advanced research in Science and Engineering (IJARSE-18)* Vol. No-1, pp. 343-346 (2018) (UGC Approved).

### International conferences

1. **Vishal Chaudhary** and Sonal Singh, “Dual-core photonic crystal fiber for blood cancer detection in THz frequency regime” **4th International Symposium on Electrical, Electronics and Information Engineering (ISEEIE 2024)** held in University of Leicester, Leicester, UK, 28-30 August, 2024.
2. **Vishal Chaudhary**, Kirti Dalal, Asbah Masih, and Vijay Shanker Chaudhary, “Bi-Core Photonic Crystal Fiber Based Chemical Sensor in THz Frequency Regime,” **IEEE Work. Recent Adv. Photonics, WRAP 2023**.

3. **Vishal Chaudhary** and Sonal Singh, “Hexagonal lattice twin core photonic crystal fiber based chemical sensor” **10<sup>th</sup> International Conference on Signal Processing and Integrated Networks (SPIN 2023) held in Noida, Uttar Pradesh, India, 23-24 March, 2023.**
4. **Vishal Chaudhary** and Sonal Singh, “Effect of selectively-filled-ethanol on dispersion characteristics of circular shaped Hollow Core Photonic Crystal Fiber” **4th International Conference on Communication, Computing and Electronics Systems 2022 Lecture Notes in Electrical Engineering 977, (Scopus-Index Springer Conference Proceedings).**
5. **Vishal Chaudhary** and Dharmendra Kumar, “Design and analysis of Refractive index sensor based on Dual Core Photonic crystal fiber (DC-PCF) with rectangular air hole lattice structure,” **International Conference on Optical & Wireless Technologies 2018 (OWT 2018) held in Jaipur, INDIA, 10-11 February. (Scopus-Index Springer Conference Proceedings).**
6. Vijay Shanker Chaudhary, **Vishal Chaudhary**, and Dharmendra Kumar “Highly Negative Dispersion Compensating Dual Core Photonic Crystal Fiber” **International Conference on Recent Innovations in Science and Engineering (ICRISE-18) held at Buddha Institute of Technology GIDA, Gorakhpur (India) on 1st - 2nd April 2018.**
7. Aparna Singh, **Vishal Chaudhary**, Vijay Shanker Chaudhary, and Dharmendra Kumar “Design of Dual Core Photonic Crystal Fiber (DC-PCF) Based Temperature Sensor with Rectangular Lattice Structure” **2018 5th IEEE Uttar Pradesh Section International Conference on Electrical, Electronics and Computer Engineering (UPCON).**

## TECHNICAL WORKSHOPS, TRAINING & ACHIEVEMENTS

- I was honored with **commendable research awards** at Delhi Technological University for my research work in August 2024 and September 2025.
- **Attended Two-Days Workshop titled "Hands-on Training on Latex" scheduled on 26<sup>th</sup> and 27<sup>th</sup> September 2022 being organized by ECE Department, Delhi Technological University, Delhi.**
- **Participation in webinar entitled, “Engineering The Future In The Post-COVID Era” delivered by Prof. S. K. Ramesh, Professor of Electrical and Computer Engineering California State University Northridge, USA and organized by IEEE Student Branch MNNIT Allahabad (September 2020).**

- **Participation in Short Term Course (STC)** on “Advanced Modeling of Microwave and Photonics Devices” (AMMPD-2018) sponsored by TEQIP-III, organized at MMMUT, GKP.
- **Participated in the “Malaviya Research Conclave-2017” (MRC-2017)** organized at MMMUT, GKP.
- **Participation in One Week Short Term Course** on “Modeling and Simulation of Microelectronics Devices and Circuits” (MSMDC-2016) sponsored by TEQIP-II, organized at MMMUT, GKP.
- **Training** at “BHARAT SANCHAR NIGAM LIMITED” (A Govt. Of India Enterprise) Gorakhpur SSA, UP (June-July 2014).
- **Training Course** on “EMBEDDED SYSTEMS IN AVR MICROCONTROLLER” (Technocrats/October 2013).
- **Training** at “SIGNAL & TELECOM DEPARTMENT” North Eastern Railway, Gonda (June-July 2013).
- **Qualified GATE Exam** in 2016 with a Gate score 244.

## RESPONSIBILITIES

- **Reviewer of Journals:** Optical and Quantum Electronics, Journal of Computational Electronics, Plasmonics, Sensing and Imaging, Microsystem Technologies.
- **Coordinate “Two Days National Seminar on Recent Advancements in Wireless Communication”** Organized by Department of Electronics and Communication Engineering NSIT, Bihta, Patna – (801118)
- Sports Club-FGIET, Carom In-Charge.
- Singing Club-FGIET, Senior Member.
- MASPUM- Technocrats, a team of five, project-design.

## TECHNICAL EXPERTIES

- **Languages:** Proficiency in MS-OFFICE, MATLAB, COMSOL MULTIPHYSICS SOFTWARE, OPTI-SYSTEM SOFTWARE.

## PERSONAL INFORMATION

<b>Date of birth</b>	:	24 July 1994
<b>Fathers Name</b>	:	Sri J. P. Chaudhary
<b>Sex</b>	:	Male
<b>Marital status</b>	:	Unmarried
<b>Language Known</b>	:	Hindi, English
<b>Nationality</b>	:	India

## RESEARCH AND PROJECT

- Master's thesis entitled "**Design and Analysis of Dual Core Photonic Crystal Fiber for Various Applications**"

**Description:** Photonic crystal fiber (PCF) is a new class of optical fiber that uses photonic crystals to form the cladding around the core of the cable. In PCF, on the other hand, light is trapped in the core, providing a much better wave guide to photons than conventional optical fiber.

- **Designed a** Refractive Index Sensor based on dual core photonic crystal fiber (DC-PCF) with rectangular air hole lattice structure by using COMSOL Multiphysics software.
- **Designed a** Temperature Sensor based on dual core photonic crystal fiber (DC-PCF) with rectangular air hole lattice structure by using COMSOL Multiphysics software.
- Automatic plant irrigation system (Major Project 2015), using DTMF.
- Automatic plant irrigation system (Mini Project 2014), using 8051 microcontroller.